novel analytical approaches to characterize particles in biopharmaceuticals
Grabarek, A.D.

Citation
Grabarek, A. D. (2021, October 21). *novel analytical approaches to characterize particles in biopharmaceuticals*. Retrieved from https://hdl.handle.net/1887/3217865

Novel analytical approaches to characterize particles in biopharmaceuticals

Adam Grabarek

Novel analytical approaches to characterize particles in biopharmaceuticals

Proefschrift

ter verkrijging van

de graad van doctor aan de Universiteit Leiden,

op gezag van rector magnificus prof.dr.ir. H. Bijl,

volgens besluit van het college voor promoties

te verdedigen op donderdag 21 oktober

klokke 15:00 uur

door

Adam Dariusz Grabarek

geboren te Warschau, Polen

in 1990

Promotor: Prof. dr. Wim Jiskoot

Co-promotor: dr. Andrea Hawe

Promotiecommissie:

Prof. dr. Hubertus Irth, Leiden University, LACDR, chair

Prof. dr. Joke A. Bouwstra, Leiden University, LACDR, secretary

Prof. dr. Henderik Frijlink, Groningen University

Prof. dr. Anne Juppo, University of Helsinki

Prof. dr. Olivia Merkel, Ludwig Maximilian University of Munich

Prof. dr. Gerard van Westen, Leiden University, LACDR

Prof. dr. David Volkin, University of Kansas

To Louise

Table of contents

Chapter 1

General introduction and thesis outline

Biopharmaceuticals as a quickly developing and expanding class of medicines

Biopharmaceuticals are a still emerging class of therapeutics, with insulin being the first recombinant human protein product approved in 1982[1]. Their origin dates back to 1890 when Emil Behring and Shibasaburo Kitasato demonstrated on guinea pigs the curing effects of sera from mammals previously exposed to sub-lethal doses of *Clostridium tetani* or *diphtheria toxin*[2]. Despite this early research on serum therapies, translation into successful human trials was difficult to achieve because of the inconsistencies between produced therapeutic sera. The breakthrough came in the mid-1890s, when Paul Ehrlich developed standardized methods for the production of high-quality anti-diphtheria serum in larger animals, which became the first international standard reference preparation[3]. Since then, the advancement in our understanding and technological progress within the fields of medicine and pharmaceutics has allowed for optimization of the purity of protein drug products and for a more detailed characterization of the active pharmaceutical ingredients (APIs).

With the advent of recombinant DNA technologies and emergence of other new technologies, the portfolio of biopharmaceuticals has expanded rapidly during the past few decades. Today the class encompasses a range of therapeutic modalities, such as hormones, cytokines, fusion proteins, monoclonal antibodies (mAbs), antibody-drug conjugates, viral vectors and living cells. Currently, mAbs are the dominant class within biopharmaceuticals with a market value of approximately $115 billion as of 2018[4]. However, the elaborate manufacturing process, high susceptibility to degradation and difficult analytical characterization of biopharmaceuticals result in ongoing concerns with respect to quality, safety and efficacy of these drug products[5,6]. These concerns escalate for advanced therapy medicinal products (ATMPs), which include gene therapy products, cell-based products and tissue-engineered products. The intrinsic complexity of viruses, cells and tissues pose even greater technical challenges in delivering safe and effective medicinal products[7].

Protein-based biopharmaceuticals and their formulation aspects

Therapeutic proteins are usually formulated in a liquid or lyophilized state, most commonly designed for parenteral administration[8]. The therapeutic efficacy of proteins is mostly dependent on their native three-dimensional structure. However, the inherent conformational instability of proteins poses a threat to their therapeutic activity[9]. Protein (partial) unfolding and decline in colloidal stability leads inevitably to aggegation[10]. Aggregation of proteins may follow different types of pathways and lead to the formation of a variety of aggregates, which may differ in several aspects, such as size, morphology and reversibility[10-13]. Formation of protein aggregates can occur during protein expression and purification, formulation and filling, storage, transportation and upon administration to patients[14].

In order to achieve sufficient stability of native protein structures, formulation development is essential during the development of these drug products. The goal of designing a formulation for a drug candidate is to prevent instability, achieve a sufficient shelf-life and make the drug product convenient for administration, e.g., formulating as a subcutaneous instead of an intravenous injeciton[15]. The conformational integrity of protein molecules is maintained by three main stabilizing forces: hydrophobic interactions, electrostatic interactions and hydrogen bonding[16,17]. Each of these factors can be weakened or strengthened by altering the formulation variables, such as pH, ionic strength and inclusion of specific excipients in protein formulations[18,19]. The substances used for stabilization of proteins include, among others, surfactants, buffering agents, amino acids, salts, polyols and sugars. Despite the availability of a large number of chemical compounds from each category, only a few dozens of different substances are usually considered during formulation development[20]. Four groups of excipients frequently used in drug products formulations are briefly described below.

> To successfully control the pH of protein formulations, and other pH dependent physical properties of the solution (e.g., solubility, viscosity and phase separation[21-23]), buffering agents are typically used. The excellent buffering capacity of some amino acids (e.g., histidine) or multivalent salts (e.g., phosphate

salts) make them popular excipients used in mAb-based formulations. Optimization of solution pH according to the specific mAbs formulation increases the stability of the liquid drug product. The highest conformational and colloidal stability of protein is achieved within a narrow range of pH at which the overall surface charges guarantee favorable electrostatic interactions[24-27]. Furthermore, in low pH solutions proteins are more susceptible to cleavage or isomerization, whereas at higher pH values deamidation and oxidation rates of proteins increase and lead to formation of chemical degradants[5,28,29].

➢ Salts are also frequently included in formulations, e.g., to achieve tonicity, to increase protein stability, and/or as viscosity-reducing agent[30,31]. One of the types of interactions of salts with proteins are long-range protein-protein electrostatic interactions. In a solution where the pH is close to the isoelectric point (pI value) of a protein, the overall surface charge is close to neutral, reducing the electrostatic interactions between molecules. This may be favorable for reducing the viscosity of a protein solution, but also promotes short-range hydrophobic interactions leading to protein unfolding and non-native aggregation[32]. A charged protein state exhibits greater colloidal stability due to the protein-protein electrostatic repulsion. However, addition of salt leads to charge-screening effects upon which hydrophobic intermolecular interactions become enhanced[32,33].

➢ Nonreducing sugars, such as sucrose and trehalose, are another class of commonly used excipients in protein formulations. The commonality of using these excipients relates to their excellent stabilizing properties in liquid and lyophilized products. Preferential exclusion of sucrose from protein surfaces via hydrogen bonding increases the hydration shell of protein molecules, which in turn promotes a more compact native state and thereby increases their molecular conformational stability[34,35]. However, the quality of sugars must be also considered, as even pharmaceutical-grade sucrose may contain nanoparticulate impurities which have been shown to destabilize mAbs[36-38].

➢ Surfactants are often included in protein formulations to minimize the damage induced by interfacial stress[39-43]. The most commonly used surfactants in protein formulations are polysorbate 20 (Tween 20) and polysorbate 80 (Tween 80), and to a lesser extent poloxamer 188 (Pluronic F-68). Their relatively low toxicity profile and excellent stabilizing properties at low concentrations contribute to their popularity[44,45]. Polysorbates (PS) are non-ionic amphiphilic molecules comprising a sorbitan (hydrophilic) head group linked to four polyethylene glycol (PEG) chains. Each of these chains is esterified with a fatty acid side chain which vary among different types of polysorbates[46]. However, the complex manufacturing process, challenges associated with purification, and chemical instability of PS result in products of a highly heterogeneous chemical mixture[46]. Surfactants are believed to have a dual stabilizing effect on protein molecules[40,46]. Competitive adsorption to hydrophobic interfaces is believed to be the prevalent stabilization mechanism[39-41]. The other stabilization mechanism is the direct binding of PS to protein molecules[40,41,47]. It has been suggested that PS acts as a chaperone, which can catalyze the correct folding of proteins and shield their hydrophobic patches[47,48]. Despite the excellent stabilizing properties of PS, numerous studies have also reported destabilizing effects of PS degradants[43,49,50]. The main degradation pathways for PS are oxidation and (enzymatic) hydrolysis[51]. The latter yields free fatty acids that can form insoluble hydrophobic particles. Improved characterization methods are currently being developed to achieve greater selectivity for impurities in PS, which would allow for better evaluation of their stability and batch-to-batch variability.

Advancing analytical tools for characterization of particles in biopharmaceuticals

Monitoring the stability of protein-based therapeutics can be performed by a plethora of analytical techniques intended for particle characterization. The hydrodynamic diameter of a mAb monomer is ca. 5 – 12 nm, depending on the hydration shell[52]. However, protein instability leads to physical and chemical changes of the native monomers, resulting in their self-association and the formation of proteinaceous particles[5]. The risks associated with the formation of protein aggregates in therapeutic drug products is not limited to the loss of clinical efficacy. Unwanted immunogenicity is an additional concern, as perturbed protein structures have been shown to be more immunogenic compared to native protein monomers[53-56]. Nano-meter and micro-meter sized protein aggregates are also potentially more immunogenic than the native monomer. However, *in vitro* and *in vivo* immunogenicity studies have so far delivered conflicting results[57-61]. Nevertheless, the presence of aggregated interferon and human growth factor in drug products has been linked with adverse immunological responses in human patients[62-65]. In addition to proteinaceous particles, nonproteinaceous particles originating from excipients, primary packaging material, manufacturing processes and production environment can also pose threats to the integrity of drug products[66]. Silicone oil droplets deriving from the coatings of internal surfaces of pre-filled syringes or rubber particles shed from vial stoppers may increase the kinetics of protein aggregation[67,68], or lead to blockage of small (micro-) blood vessels within the lungs[69,70].

The heterogeneity of particulate impurities in protein-based formulations prompt for their classification in several different ways, e.g., based on size (nano-, micro-meter or larger than 100 µm sized particles) or origin (extrinsic, intrinsic or inherent particles according to USP <1790> and extrinsic or intrinsic according to Ph. Eur.5.17.2)[12,66,71]. Specifications set by pharmacopeial monographs for parenteral biopharmaceuticals are primarily focused on particle sizes and provide acceptable limits of particulates sized above 10 and 25 µm within a specified unit of drug product[72-74]. The commentary from Carpenter et al. in 2009 was one of the first to address the safety concerns arising from sub-visible (1 – 100 µm in size) particles in biopharmaceutical formulations, as well as the challenges associated with

characterization of these impurities[14]. One year later, Demeule et al. published a critical evaluation of three characterization techniques for micro-meter sized particles for characterization of protein aggregates: light obscuration (LO), flow imaging microscopy (FIM) and electric sensing zone (ESZ)[75]. The authors addressed several challenges associated with these techniques, and other research groups further explored limitations of these techniques with respect to protein formulations[66,76-82]. For example, the small difference between the refractive index (RI) of proteinaceous particles and (protein-containing) formulation buffers results in underestimation of recorded particle concentrations when using optical-based techniques. The underestimation is augmented in case of formulations with high protein concentration or presence of sugars, where the refractive index differences between protein aggregates and the matrix are particularly small[78]. Furthermore, the evaluation of statistical significance of measured particle concentrations in samples with low particle load should be performed. Even when considering a well homogenized sample and high precision measurements, experimental data of particle concentrations within single digits determined by using LO comprise high statistical variances[83]. One must also note the variability of determined particle concentration and size between different techniques (or even between different instruments of the same technique[84]) for a single sample[75,85]. Such discrepancies are to be expected due to the different measuring principles of each technique for detection and characterization of particles as well as differences in the size range covered. For instance, LO is known for underestimation of particle concentrations compared to FIM due to different sensitivities of the two techniques[85,86]; and samples with translucent particles will have higher particle counts and sizes reported by ESZ compared to optical-based techniques[81].

Currently, the content of particles within the lower micro-meter and nano-meter size range present in drug products is not regulated. However, regulatory authorities recommend the assessment of these particles within drug products[87]. In comparison to the characterization of micro-meter sized particles, quantification and sizing of particles within the nanometer-size range is associated with many more challenges. Nonetheless, substantial advancements in the fields of microscopy, nanotechnology and microfluidics

have delivered promising techniques for characterization of nano-meter sized particles. Transmission electron microscopy, scanning electron microscopy and atomic force microscopy are powerful techniques for visualization and sizing of particles over a broad size range. However, the low throughput of these methods, their high costs and laborious sample preparation requirements limit their usage for formulation screening and protein aggregate characterization[88]. Light-scattering based techniques are currently the methods of choice for evaluating the formation of nanoparticles in protein-based formulations. Dynamic light scattering (DLS), static light scattering (SLS), laser diffraction (LD) and nanoparticle tracking analysis (NTA) are techniques which utilize the events of particle-light interactions (i.e., Mie scattering, Rayleigh scattering, diffraction) for measurements of particle size and counts. DLS and NTA measure the scattered light of particles under Brownian motion in a low-Reynold number liquid and determine their diffusion coefficients[89-91]. The hydrodynamic diameter of particles can then be calculated from the Stokes-Einstein equation, assuming that the measured particles are of spherical shape and the viscosity, RI and temperature are known[92]. Orthogonal to light scattering-based techniques are resonant mass measurement (RMM) and resistive pulse sensing (RPS). RMM measures the size and concentration of particles passing near a resonating cantilever suspended within a microfluidic system[93,94]. If the density of particles is known, the volumetric diameter can be obtained. Instruments measuring particles by using RPS, operate on the basis of the Coulter principle that was originally employed in cell counters for sizing and quantifying cells using impedance measurements[95-97]. In microfluidic RPS (MRPS), sample material is loaded into chips with microfluidic passages and particles are directed through the orifice of a nanoconstriction. Each passage of particle induces a change in the electric current and its magnitude is directly related to the volumetric diameter of the particle[98].

Robust and accurate characterization of protein drug products requires development and qualification of the applied analytical methods[99]. For example, the particle characterization methods must be proven to reliably detect and/or quantify protein degradants. Thus, forced degradation studies to induce the formation of degradants in protein formulations are essential in the development of biotherapeutics[100,101]. These

studies mimic (exaggerated) real-life conditions to which drug products can be exposed to and usually involve freezing, thawing, thermal stress, mechanical stress, light exposure, oxidative stress or interaction with specific components present in the primary packaging. Evaluation of mechanical stress, such as stirring, pumping or shaking, on protein stability is necessary, as this type of stress is the most common one to which biopharmaceutical products are exposed to during processing and handling[102]. In solution under quiescent storage, monomeric proteins exist in an equilibrium between native folded and unfolded structures[103]. However, the balance can be disrupted upon exposure to interfaces, such as liquid-liquid, air-liquid and solid-liquid[104,105]. Manufacturing and transportation induce a plethora of interfacial stresses, which may cause perturbation of the native protein structure, leading to protein aggregation[106,107]. The main degradants formed in protein formulations exposed to mechanical stress have been shown to be proteinaceous particles[100,108-110]. Consequently, methods for reliable detection of particulate impurities in drug products are required for selection of the most optimal surfactant (concentrations) and evaluation of the stability of protein formulations against these stress conditions.

The increasing number of available characterization techniques and the exponential growth of collected data requires improved data processing and analysis approaches to gain a better understanding of the outcome of performed analytics. Artificial intelligence and its subfield machine learning are becoming integrated in the biopharmaceutical field for evaluation of the large quantities of generated data[111]. The main objective of machine learning is to discover patterns and trends in collected data in order to obtain relationships between variables and set predictions. Depending on the needs and available data, machine learning models can be based on linear regression algorithms or utilize deep convolutional neural networks (CNNs). Logistic regression and decision tree models require modest processing power to perform predictions or weighed selections. In contrast, application of high-performance processor cores (i.e., graphics processing units [GPUs]) becomes necessary when parsing data with CNNs. These models consist of sophisticated architectures with multiple numbers of hidden layers and interconnected nodes for extraction of features from highly structured data. The teaching of machine learning algorithms can be done via two different approaches: unsupervised or supervised

learning. In unsupervised machine learning, principal component analysis (PCA) is commonly used for data clustering and segregation of different patterns[112]. Simplification of high-dimensional data by feature elimination and extraction, while retaining trends and patterns, allows for projection of correlations between certain variables, such as particle morphology, Raman spectrum and polymorphic states of a compound[113]. On the contrary, the supervised learning approach requires knowledge on the input fed into the model for learning. Labelled datasets must be provided to the model for training during which specific relationships between the input and output data are being recognized. For the testing of the model, new (i.e., not used during training) unlabeled data is inputted and the predictions (results) are made based on the previous learning process. Models based on artificial neural networks (ANNs) are particularly favored for the supervised learning approach. These networks consist of a group of interconnected nodes in which algorithms apply non-linear transformations to learn specific features or patterns in the received data[114]. To further improve model performance, ANNs were developed into CNNs in which the input and output layers are connected to multiple locally linked hidden layers[111]. The connectivity and distribution of units within each layer allows for generating simple local features and hierarchically combining them into complex high dimensional objects. The intricacy of CNNs makes them extremely useful for image classification where extraction of complex patterns allows for, e.g., identification of proteinaceous particles formed by different types of stress factors[115,116]. Similarly, CNNs were used for discrimination between types of particles, such as silicone oil droplets and protein aggregates[117].

Cell-based medicinal products and new challenges in formulation and analytical characterization

Cell-based medicinal products (CBMPs) are therapeutics that are rapidly gaining importance in the treatment of chronic and life-threatening diseases, for which often no other treatment options are available. Several CBMPs have reached the market and a few thousand CBMPs are currently in clinical development[118]. Cell therapy products involve somatic cells of autologous (patient) or of allogenic (healthy donors) origin. The APIs of these products are (mainly) living cells which have been submitted to substantial

manipulation to achieve the desired therapeutic effect[119]. Irrespective of the class of therapeutics cells, manufacturing and administration of these products are associated with multiple processing steps that may include the addition/removal of various raw materials, several handling steps, cryopreservation and transportation. Cells as living units respond to their local environment and interact with each other[120]. The sensitivity of cells to external stimuli (stress factors) makes them uniquely fragile and susceptible to abrupt death (necrosis), resulting in a release of intracellular components and formation of debris particles. Formulation development for CBMPs may help to achieve maximal stability and efficacy of these therapeutics. Several of the current common additives used for stabilization of cells, such as dimethylsufoxide (DMSO) and human serum albumin (HSA), have multiple drawbacks and examining alternative excipients is required[121]. The complexity of CBMPs combined with the intricate features of living and dead cells pose greater challenges for analytical characterization compared to protein-based products. Therefore, gaining better understanding of the critical quality attributes of CBMPs, and the development of robust, low-volume and high-throughput analytical methods is essential in order to achieve safe, effective and high-quality formulations.

Subvisible particle analysis of CBMPs is very challenging because of the presence of cells in the size range of interest. Nonetheless, particulate impurities, whether process- or cell-derived, remain a concern and should be accurately characterized[118,122]. The concern is amplified by the fact that only large-pore filters (≥ 70 μm pore size) can be used during manufacturing to remove particles (if present). Process and product particle impurities and contaminants within the micro-meter size range, cannot be removed by filtration without compromising quality and potentially efficacy of the product. Consequently, control measures must be in place to prevent or minimize particulate contamination from sources like instruments, raw materials, processes, environment and people[123]. Verification of the particle load in CBMPs from a quality (e.g., to demonstrate batch-to-batch consistency and stability), safety and potentially efficacy perspective is prudent[118]. This involves micrometer-size particle characterization not only with respect to the cell concentration and cell viability, but also potential particulate impurities. FIM is emerging as an attractive tool for

characterization of particles in cell suspensions, owing to its capability of generating high-resolution images and processing samples with a high particle load[124].

Aims and outline of the thesis

The objective of this thesis is to investigate novel analytical approaches for the characterization of particulates in biopharmaceutical products, in particular therapeutic proteins and CBMPs. **Chapter 2** focuses on the comparison of the novel MRPS against the three other more established nanoparticle characterization techniques for biopharmaceutical product characterization, namely RMM, NTA and DLS. It includes an assessment of the applicability of each of these techniques and describes their advantages and limitations. **Chapter 3** continues to focus on nanoparticle characterization techniques, specifically tunable RPS and MRPS, which require a minimum electrical conductivity of the samples. The colloidal stability of a mAb formulation is assessed upon spiking histidine and sodium chloride. **Chapter 4** explores the *in vitro* immunogenicity of nanoparticulate impurities found in pharmaceutical-grade sucrose. **Chapter 5** describes the implementation of shaking, free-fall and syringe pump stress methods for the evaluation of mAbs stability and particle formation. Moreover, the performance of two grades of polysorbate 80 is compared with respect to their stabilizing properties towards a model mAb upon mechanical stress. Chapter 6 and 7 describe the characterization of particulate impurities in CBMPs. In **Chapter 6** a novel method, based on FIM and machine learning, was introduced to detect and quantify antibody-coated magnetic beads (Dynabeads) within cell suspensions. In **Chapter 7** the developed FIM method was used alongside other cell characterization techniques for the assessment of cell stability after exposure to different thawing temperatures, freeze-thawing and shaking stress. **Chapter 8** summarizes the work performed in this thesis and gives an outlook on further potential developments in the field of particle analysis within protein- and cell-based medicinal products.

References:

1. Quianzon CC, Cheikh I. History of insulin. J Community Hosp Intern Med Perspect. 2012;2(2). doi:10.3402/jchimp.v2i2.18701.

2. Kaufmann SHE. Immunology's Coming of Age. Front Immunol. 2019;10:684. doi:10.3389/fimmu.2019.00684.

3. Bosch F, Rosich L. The contributions of Paul Ehrlich to pharmacology: a tribute on the occasion of the centenary of his Nobel Prize. Pharmacology. 2008;82(3):171-179. doi:10.1159/000149583.

4. Lu R-M, Hwang Y-C, Liu I-J, et al. Development of therapeutic antibodies for the treatment of diseases. J Biomed Sci. 2020;27(1):1. doi:10.1186/s12929-019-0592-z.

5. Mahler H-C, Friess W, Grauschopf U, Kiese S. Protein aggregation: pathways, induction factors and analysis. J Pharm Sci. 2009;98(9):2909-2934. doi:10.1002/jps.21566.

6. Crommelin DJA, Storm G, Verrijk R, Leede L de, Jiskoot W, Hennink WE. Shifting paradigms: biopharmaceuticals versus low molecular weight drugs. Int. J. Pharm. 2003;266(1-2):3-16. doi:10.1016/S0378-5173(03)00376-4.

7. Crommelin DJA, Mastrobattista E, Hawe A, Hoogendoorn KH, Jiskoot W. Shifting Paradigms Revisited: Biotechnology and the Pharmaceutical Sciences. J Pharm Sci. 2019. doi:10.1016/j.xphs.2019.08.010.

8. Jameel F, Hershenson S. Formulation and process development strategies for manufacturing biopharmaceuticals. Hoboken N.J.: Wiley; 2010.

9. Manning MC, Patel K, Borchardt RT. Stability of protein pharmaceuticals. Pharm Res. 1989;6(11):903-918. doi:10.1023/a:1015929109894.

10. Roberts CJ. Therapeutic protein aggregation: mechanisms, design, and control. Trends in biotechnol. 2014;32(7):372-380. doi:10.1016/j.tibtech.2014.05.005.

11. Amin S, Barnett GV, Pathak JA, Roberts CJ, Sarangapani PS. Protein aggregation, particle formation, characterization & rheology. Curr Opin Colloid Interface Sci. 2014;19(5):438-449. doi:10.1016/j.cocis.2014.10.002.

12. Narhi LO, Schmit J, Bechtold-Peters K, Sharma D. Classification of protein aggregates. J Pharm Sci. 2012;101(2):493-498. doi:10.1002/jps.22790.

13. Arosio P, Rima S, Morbidelli M. Aggregation mechanism of an IgG2 and two IgG1 monoclonal antibodies at low pH: from oligomers to larger aggregates. Pharm Res. 2013;30(3):641-654. doi:10.1007/s11095-012-0885-3.

14. Carpenter JF, Randolph TW, Jiskoot W, et al. Overlooking subvisible particles in therapeutic protein products: gaps that may compromise product quality. J Pharm Sci. 2009;98(4):1201-1205. doi:10.1002/jps.21530.

15. Wang W. Advanced protein formulations. Protein Sci. 2015;24(7):1031-1039. doi:10.1002/pro.2684.

16. Nick Pace C, Scholtz JM, Grimsley GR. Forces stabilizing proteins. FEBS Letters. 2014;588(14):2177-2184. doi:10.1016/j.febslet.2014.05.006.

17. Fitzpatrick AW, Knowles TPJ, Waudby CA, Vendruscolo M, Dobson CM. Inversion of the balance between hydrophobic and hydrogen bonding interactions in protein folding and aggregation. PLoS Comput Biol. 2011;7(10):e1002169. doi:10.1371/journal.pcbi.1002169.

18. Wang T, Kumru OS, Yi L, et al. Effect of Ionic Strength and pH on the Physical and Chemical Stability of a Monoclonal Antibody Antigen-Binding Fragment. J Pharm Sci. 2013;102(8):2520-2537. doi:10.1002/jps.23645.

19. Kamerzell TJ, Esfandiary R, Joshi SB, Middaugh CR, Volkin DB. Protein-excipient interactions: mechanisms and biophysical characterization applied to protein formulation development. Adv Drug Deliv Rev. 2011;63(13):1118-1159. doi:10.1016/j.addr.2011.07.006.

20. Chi EY. Excipients Used in Biotechnology Products; 2016. Wiley Online Books. p.146-170

21. Lewus RA, Levy NE, Lenhoff AM, Sandler SI. A comparative study of monoclonal antibodies. 1. Phase behavior and protein-protein interactions. Biotechnol Prog. 2015;31(1):268-276. doi:10.1002/btpr.2011.

22. Jiang J, Xiong YL, Chen J. pH Shifting alters solubility characteristics and thermal stability of soy protein isolate and its globulin fractions in different pH, salt concentration, and temperature conditions. J Agric Food Chem. 2010;58(13):8035-8042. doi:10.1021/jf101045b.

23. Yadav S, Shire SJ, Kalonia DS. Viscosity Behavior of High-Concentration Monoclonal Antibody Solutions: Correlation with Interaction Parameter and Electroviscous Effects. J Pharm Sci. 2012;101(3):998-1011. doi:10.1002/jps.22831.

24. Tian X, Langkilde AE, Thorolfsson M, Rasmussen HB, Vestergaard B. Small-angle x-ray scattering screening complements conventional biophysical analysis: comparative structural and biophysical analysis of monoclonal antibodies IgG1, IgG2, and IgG4. J Pharm Sci. 2014;103(6):1701-1710. doi:10.1002/jps.23964.

25. Sarangapani PS, Weaver J, Parupudi A, et al. Both Reversible Self-Association and Structural Changes Underpin Molecular Viscoelasticity of mAb Solutions. J Pharm Sci. 2016;105(12):3496-3506. doi:10.1016/j.xphs.2016.08.020.

26. Lim JY, Kim NA, Lim DG, Eun C-y, Choi D, Jeong SH. Biophysical stability of hyFc fusion protein with regards to buffers and various excipients. Int J Biol Macromol. 2016;86:622-629. doi:10.1016/j.ijbiomac.2016.02.006.

27. Koepf E, Schroeder R, Brezesinski G, Friess W. The missing piece in the puzzle: Prediction of aggregation via the protein-protein interaction parameter A*2. Eur J Pharm Biopharm. 2018;128:200-209. doi:10.1016/j.ejpb.2018.04.024.

28. Usami A, Ohtsu A, Takahama S, Fujii T. The effect of pH, hydrogen peroxide and temperature on the stability of human monoclonal antibody. J Pharm Biomed Anal. 1996;14(8):1133-1140. doi:10.1016/S0731-7085(96)01721-9.

29. Lu X, Nobrega RP, Lynaugh H, et al. Deamidation and isomerization liability analysis of 131 clinical-stage antibodies. mAbs. 2019;11(1):45-57. doi:10.1080/19420862.2018.1548233.

30. Chi EY, Krishnan S, Randolph TW, Carpenter JF. Physical Stability of Proteins in Aqueous Solution: Mechanism and Driving Forces in Nonnative Protein Aggregation. Pharm Res. 2003;20(9):1325-36. doi: 10.1023/a:1025771421906

31. Arosio P, Jaquet B, Wu H, Morbidelli M. On the role of salt type and concentration on the stability behavior of a monoclonal antibody solution. Biophys Chem. 2012;168-169:19-27. doi:10.1016/j.bpc.2012.05.004.

32. Chi EY, Krishnan S, Kendrick BS, Chang BS, Carpenter JF, Randolph TW. Roles of conformational stability and colloidal stability in the aggregation of recombinant human granulocyte colony-stimulating factor. Protein Sci. 2003;12(5):903-913. doi:10.1110/ps.0235703.

33. Bauer KC, Göbel M, Schwab M-L, Schermeyer M-T, Hubbuch J. Concentration-dependent changes in apparent diffusion coefficients as indicator for colloidal stability of protein solutions. Int. J. Pharm. 2016;511(1):276-287. doi:10.1016/j.ijpharm.2016.07.007.

34. Timasheff SN. Protein hydration, thermodynamic binding, and preferential hydration. Biochemistry. 2002;41(46):13473-13482. doi:10.1021/bi020316e.

35. Timasheff SN, Xie G. Protein-solvent preferential interactions, protein hydration, and the modulation of biochemical reactions by solvent components. PNAS. 2002;99(105):9721-9726.

36. Weinbuch D, Cheung JK, Ketelaars J, et al. Nanoparticulate Impurities in Pharmaceutical-Grade Sugars and their Interference with Light Scattering-Based Analysis of Protein Formulations. Pharm Res. 2015;32(7):2419-2427. doi:10.1007/s11095-015-1634-1.

37. Weinbuch D, Ruigrok M, Jiskoot W, Hawe A. Nanoparticulate Impurities Isolated from Pharmaceutical-Grade Sucrose Are a Potential Threat to Protein Stability. Pharm Res. 2017;34(12):2910-2921. doi:10.1007/s11095-017-2274-4.

38. Wu Y, Levons J, Narang AS, Raghavan K, Rao VM. Reactive impurities in excipients: profiling, identification and mitigation of drug-excipient incompatibility. AAPS PharmSciTech. 2011;12(4):1248-1263. doi:10.1208/s12249-011-9677-z.

39. Agarkhed M, O'Dell C, Hsieh M-C, Zhang J, Goldstein J, Srivastava A. Effect of Surfactants on Mechanical, Thermal, and Photostability of a Monoclonal Antibody. AAPS PharmSciTech. 2018;19(1):79-92. doi:10.1208/s12249-017-0845-7.

40. Arsiccio A, Pisano R. Surfactants as stabilizers for biopharmaceuticals: An insight into the molecular mechanisms for inhibition of protein aggregation. Eur J Pharm Biopharm. 2018;128:98-106. doi:10.1016/j.ejpb.2018.04.005.

41. Bam NB, Cleland JL, Yang J, et al. Tween protects recombinant human growth hormone against agitation-induced damage via hydrophobic interactions. J Pharm Sci. 1998;87(12):1554-1559. doi:10.1021/js980175v.

42. Deechongkit S, Wen J, Narhi LO, et al. Physical and biophysical effects of polysorbate 20 and 80 on darbepoetin alfa. J Pharm Sci. 2009;98(9):3200-3217. doi:10.1002/jps.21740.

43. Wang W, Wang YJ, Wang DQ. Dual effects of Tween 80 on protein stability. Int. J. Pharm.. 2008;347(1-2):31-38. doi:10.1016/j.ijpharm.2007.06.042.

44. Wang S, Wu G, Zhang X, et al. Stabilizing two IgG1 monoclonal antibodies by surfactants: Balance between aggregation prevention and structure perturbation. Eur J Pharm Biopharm. 2017;114:263-277. doi:10.1016/j.ejpb.2017.01.025.

45. Singh SK, Mahler H-C, Hartman C, Stark CA. Are Injection Site Reactions in Monoclonal Antibody Therapies Caused by Polysorbate Excipient Degradants? J Pharm Sci. 2018;107(11):2735-2741. doi:10.1016/j.xphs.2018.07.016.

46. Martos A, Koch W, Jiskoot W, et al. Trends on Analytical Characterization of Polysorbates and Their Degradation Products in Biopharmaceutical Formulations. J Pharm Sci. 2017;106(7):1722-1735. doi:10.1016/j.xphs.2017.03.001.

47. Bam NB, Cleland JL, Randolph TW. Molten Globule Intermediate of Recombinant Human Growth Hormone: Stabilization with Surfactants. 1996;12:801-809.

48. Krielgaard L, Jones LS, Randolph TW, et al. Effect of tween 20 on freeze-thawing- and agitation-induced aggregation of recombinant human factor XIII. J Pharm Sci. 1998;87(12):1597-1603. doi:10.1021/js980126i.

49. Kishore RSK, Pappenberger A, Dauphin IB, et al. Degradation of polysorbates 20 and 80: studies on thermal autoxidation and hydrolysis. J Pharm Sci. 2011;100(2):721-731. doi:10.1002/jps.22290.

50. Larson NR, Wei Y, Prajapati I, et al. Comparison of Polysorbate 80 Hydrolysis and Oxidation on the Aggregation of a Monoclonal Antibody. J Pharm Sci. 2020;109(1):633-639. doi:10.1016/j.xphs.2019.10.069.

51. Kranz W, Wuchner K, Corradini E, Berger M, Hawe A. Factors Influencing Polysorbate's Sensitivity Against Enzymatic Hydrolysis and Oxidative Degradation. J Pharm Sci. 2019;108(6):2022-2032. doi:10.1016/j.xphs.2019.01.006.

52. Hawe A, Hulse WL, Jiskoot W, Forbes RT. Taylor dispersion analysis compared to dynamic light scattering for the size analysis of therapeutic peptides and proteins and their aggregates. Pharm Res. 2011;28(9):2302-2310. doi:10.1007/s11095-011-0460-3.

53. Jiskoot W, Randolph TW, Volkin DB, et al. Protein instability and immunogenicity: roadblocks to clinical application of injectable protein delivery systems for sustained release. J Pharm Sci. 2012;101(3):946-954. doi:10.1002/jps.23018.

54. Moussa EM, Panchal JP, Moorthy BS, et al. Immunogenicity of Therapeutic Protein Aggregates. J Pharm Sci. 2016;105(2):417-430. doi:10.1016/j.xphs.2015.11.002.

55. Sharma B. Immunogenicity of therapeutic proteins. Part 1: impact of product handling. Biotechnol Adv. 2007;25(3):310-317. doi:10.1016/j.biotechadv.2007.01.005.

56. Sharma B. Immunogenicity of therapeutic proteins. Part 3: impact of manufacturing changes. Biotechnol Adv. 2007;25(3):325-331. doi:10.1016/j.biotechadv.2007.01.007.

57. Jiskoot W, Kijanka G, Randolph TW, et al. Mouse Models for Assessing Protein Immunogenicity: Lessons and Challenges. J Pharm Sci. 2016;105(5):1567-1575. doi:10.1016/j.xphs.2016.02.031.

58. Kijanka G, Bee JS, Korman SA, et al. Submicron Size Particles of a Murine Monoclonal Antibody Are More Immunogenic Than Soluble Oligomers or Micron Size Particles Upon Subcutaneous Administration in Mice. J Pharm Sci. 2018;107(11):2847-2859. doi:10.1016/j.xphs.2018.06.029.

59. Fathallah AM, Chiang M, Mishra A, et al. The Effect of Small Oligomeric Protein Aggregates on the Immunogenicity of Intravenous and Subcutaneous Administered Antibodies. J Pharm Sci. 2015;104(11):3691-3702. doi:10.1002/jps.24592.

60. Ahmadi M, Bryson CJ, Cloake EA, et al. Small amounts of sub-visible aggregates enhance the immunogenic potential of monoclonal antibody therapeutics. Pharm Res. 2015;32(4):1383-1394. doi:10.1007/s11095-014-1541-x.

61. Rombach-Riegraf V, Karle AC, Wolf B, et al. Aggregation of human recombinant monoclonal antibodies influences the capacity of dendritic cells to stimulate adaptive T-cell responses in vitro. PLoS ONE. 2014;9(1):e86322. doi:10.1371/journal.pone.0086322.

62. Moore WV, Leppert P. Role of aggregated human growth hormone (hGH) in development of antibodies to hGH. J Clin Endocrinol Metab. 1980;51(4):691-697. doi:10.1210/jcem-51-4-691.

63. Bertolotto A, Deisenhammer F, Gallo P, Sölberg Sørensen P. Immunogenicity of interferon beta: differences among products. J Neurol. 2004;251 Suppl 2:II15-II24. doi:10.1007/s00415-004-1204-7.

64. Ryff JC. Clinical investigation of the immunogenicity of interferon-alpha 2a. J Interferon Cytokine Res. 1997;17 Suppl 1:S29-33.

65. Barnard JG, Babcock K, Carpenter JF. Characterization and Quantitation of Aggregates and Particles in Interferon-β Products: Potential Links Between Product Quality Attributes and Immunogenicity. J Pharm Sci. 2013;102(3):915-928. doi:10.1002/jps.23415.

66. Narhi LO, Corvari V, Ripple DC, et al. Subvisible (2-100 μm) Particle Analysis During Biotherapeutic Drug Product Development: Part 1, Considerations and Strategy. J Pharm Sci. 2015;104(6):1899-1908. doi:10.1002/jps.24437.

67. Jones LS, Kaufmann A, Middaugh CR. Silicone oil induced aggregation of proteins. J Pharm Sci. 2005;94(4):918-927. doi:10.1002/jps.20321.

68. Bee JS, Chiu D, Sawicki S, et al. Monoclonal antibody interactions with micro- and nanoparticles: adsorption, aggregation, and accelerated stress studies. J Pharm Sci. 2009;98(9):3218-3238. doi:10.1002/jps.21768.

69. Bukofzer S, Ayres J, Chavez A, et al. Industry Perspective on the Medical Risk of Visible Particles in Injectable Drug Products. PDA J Pharm Sci Technol. 2015;69(1):123. doi:10.5731/pdajpst.2015.01037.

70. Salvatore T, Davis N, Detrimental Effects of Particulate Matter on the Pulmonary Circulation. JAMA. 1971;217(1):81-82. doi:10.1001/jama.1971.03190010063029

71. Corvari V, Narhi LO, Spitznagel TM, et al. Subvisible (2-100 μm) particle analysis during biotherapeutic drug product development: Part 2, experience with the application of subvisible particle analysis. J. Biol. Stand. 2015;43(6):457-473. doi:10.1016/j.biologicals.2015.07.011.

72. Ph.Eur. 2.9.19. General, particulate contamination: sub-visible particles. In: The European Pharmacopoeia,. 7th ed. 2011.

73. USP <1788>. Methods for the determination of particulate matter in injections and ophthalmic solutions. In: The United States Pharmacopoeia, National Formulary. 2012

74. USP <788>. Particulate Matter in Injections. In: The United States Pharmacopoeia, National Formulary. 2009.

75. Demeule B, Messick S, Shire SJ, Liu J. Characterization of particles in protein solutions: reaching the limits of current technologies. The AAPS journal. 2010;12(4):708-715. doi:10.1208/s12248-010-9233-x.

76. Zölls S, Weinbuch D, Wiggenhorn M, et al. Flow imaging microscopy for protein particle analysis--a comparative evaluation of four different analytical instruments. The AAPS journal. 2013;15(4):1200-1211. doi:10.1208/s12248-013-9522-2.

77. Weinbuch D, Jiskoot W, Hawe A. Light obscuration measurements of highly viscous solutions: sample pressurization overcomes underestimation of subvisible particle counts. The AAPS journal. 2014;16(5):1128-1131. doi:10.1208/s12248-014-9629-0.

78. Zölls S, Gregoritza M, Tantipolphan R, et al. How subvisible particles become invisible-relevance of the refractive index for protein particle analysis. J Pharm Sci. 2013;102(5):1434-1446. doi:10.1002/jps.23479.

79. Scherer TM, Leung S, Owyang L, Shire SJ. Issues and challenges of subvisible and submicron particulate analysis in protein solutions. The AAPS journal. 2012;14(2):236-243. doi:10.1208/s12248-012-9335-8.

80. Ríos Quiroz A, Finkler C, Huwyler J, Mahler H-C, Schmidt R, Koulov AV. Factors Governing the Accuracy of Subvisible Particle Counting Methods. J Pharm Sci. 2016;105(7):2042-2052. doi:10.1016/j.xphs.2016.03.044.

81. Ripple DC, Montgomery CB, Hu Z. An interlaboratory comparison of sizing and counting of subvisible particles mimicking protein aggregates. J Pharm Sci. 2015;104(2):666-677. doi:10.1002/jps.24287.

82. Cavicchi RE, Carrier MJ, Cohen JB, et al. Particle shape effects on subvisible particle sizing measurements. J Pharm Sci. 2015;104(3):971-987. doi:10.1002/jps.24263.

83. Gühlke M, Hecht J, Böhrer A, et al. Taking Subvisible Particle Quantitation to the Limit: Uncertainties and Statistical Challenges With Ophthalmic Products for Intravitreal Injection. J Pharm Sci. 2020;109(1):505-514. doi:10.1016/j.xphs.2019.10.061.

84. Matter A, Koulov A, Singh S, et al. Variance Between Different Light Obscuration and Flow Imaging Microscopy Instruments and the Impact of Instrument Calibration. J Pharm Sci. 2019;108(7):2397-2405. doi:10.1016/j.xphs.2019.02.019.

85. Ripple DC, Hu Z. Correcting the Relative Bias of Light Obscuration and Flow Imaging Particle Counters. Pharm Res. 2016;33(3):653-672. doi:10.1007/s11095-015-1817-9.

86. Sharma DK, King D, Oma P, Merchant C. Micro-flow imaging: flow microscopy applied to sub-visible particulate analysis in protein formulations. The AAPS journal. 2010;12(3):455-464. doi:10.1208/s12248-010-9205-1.

87. U.S. Department of Health and Human Services FaDA, Center for Drug Evaluation and Research, Center for Biologics Evaluation and Research. In: Guidance for industry: immunogenicity assessment for therapeutic protein products; 2014. Available at: http://www.fda.gov/Drugs/GuidanceComplianceRegulatoryInformation/Guidances/default.htm. Accessed March 30, 2021.

88. Robson A-L, Dastoor PC, Flynn J, et al. Advantages and Limitations of Current Imaging Techniques for Characterizing Liposome Morphology. Front Pharmacol. 2018;9:80. doi:10.3389/fphar.2018.00080.

89. Gross J, Sayle S, Karow AR, Bakowsky U, Garidel P. Nanoparticle tracking analysis of particle size and concentration detection in suspensions of polymer and protein samples: Influence of experimental and data evaluation parameters. Eur J Pharm Biopharm. 2016;104:30-41. doi:10.1016/j.ejpb.2016.04.013.

90. Filipe V, Hawe A, Jiskoot W. Critical evaluation of Nanoparticle Tracking Analysis (NTA) by NanoSight for the measurement of nanoparticles and protein aggregates. Pharm Res. 2010;27(5):796-810. doi:10.1007/s11095-010-0073-2.

91. Bhattacharjee S. DLS and zeta potential - What they are and what they are not? J. Control. Release. 2016;235:337-351. doi:10.1016/j.jconrel.2016.06.017.

92. Einstein A. Investigations on the theory of the Brownian movement. 1956.

93. Panchal J, Kotarek J, Marszal E, Topp EM. Analyzing subvisible particles in protein drug products: a comparison of dynamic light scattering (DLS) and resonant mass measurement (RMM). The AAPS journal. 2014;16(3):440-451. doi:10.1208/s12248-014-9579-6.

94. Burg TP, Godin M, Knudsen SM, et al. Weighing of biomolecules, single cells and single nanoparticles in fluid. Nature. 2007;446(7139):1066-1069. doi:10.1038/nature05741.

95. Fraikin J-L, Teesalu T, McKenney CM, Ruoslahti E, Cleland AN. A high-throughput label-free nanoparticle analyser. Nat Nanotechnol. 2011;6(5):308-313. doi:10.1038/nnano.2011.24.

96. Barnard JG, Rhyner MN, Carpenter JF. Critical evaluation and guidance for using the Coulter method for counting subvisible particles in protein solutions. J Pharm Sci. 2012;101(1):140-153. doi:10.1002/jps.22732.

97. Kozak D, Broom M, Vogel R. High resolution particle characterization to expedite development and regulatory acceptance of nanomedicines. Curr Drug Deliv. 2015;12(1):115-120. doi:10.2174/1567201811666140922110647.

98. Maxwell JC. A Treatise on Electricity and Magnetism. Oxford, UK.: Clarendon Press, Oxford, UK; 1891; p. 95-109.

99. Tiwari G, Tiwari R. Bioanalytical method validation: An updated review. Pharm Methods. 2010;1(1):25-38. doi:10.4103/2229-4708.72226.

100. Halley J, Chou YR, Cicchino C, et al. An Industry Perspective on Forced Degradation Studies of Biopharmaceuticals: Survey Outcome and Recommendations. J Pharm Sci. 2020;109(1):6-21. doi:10.1016/j.xphs.2019.09.018.

101. Hawe A, Wiggenhorn M, van de Weert M, Garbe JHO, Mahler H-C, Jiskoot W. Forced degradation of therapeutic proteins. J Pharm Sci. 2012;101(3):895-913. doi:10.1002/jps.22812.

102. Nejadnik MR, Randolph TW, Volkin DB, et al. Postproduction Handling and Administration of Protein Pharmaceuticals and Potential Instability Issues. J Pharm Sci. 2018;107(8):2013-2019. doi:10.1016/j.xphs.2018.04.005.

103. Roberts CJ. Kinetics of Irreversible Protein Aggregation: Analysis of Extended Lumry–Eyring Models and Implications for Predicting Protein Shelf Life. J Phys Chem B. 2003;107(5):1194-1207. doi:10.1021/jp026827s.

104. Bee JS, Schwartz DK, Trabelsi S, et al. Production of particles of therapeutic proteins at the air–water interface during compression/dilation cycles. Soft Matter. 2012;8(40):10329. doi:10.1039/c2sm26184g.

105. Li J, Krause ME, Chen X, et al. Interfacial Stress in the Development of Biologics: Fundamental Understanding, Current Practice, and Future Perspective. The AAPS journal. 2019;21(3):44. doi:10.1208/s12248-019-0312-3.

106. Her C, Carpenter JF. Effects of Tubing Type, Formulation, and Postpumping Agitation on Nanoparticle and Microparticle Formation in Intravenous Immunoglobulin Solutions Processed With a Peristaltic Filling Pump. J Pharm Sci. 2020;109(1):739-749. doi:10.1016/j.xphs.2019.05.013.

107. Kiese S, Papppenberger A, Friess W, Mahler H-C. Shaken, not stirred: mechanical stress testing of an IgG1 antibody. J Pharm Sci. 2008;97(10):4347-4366. doi:10.1002/jps.21328.

108. Le Basle Y, Chennell P, Tokhadze N, Astier A, Sautou V. Physicochemical Stability of Monoclonal Antibodies: A Review. J Pharm Sci. 2020;109(1):169-190. doi:10.1016/j.xphs.2019.08.009.

109. Gikanga B, Eisner DR, Ovadia R, Day ES, Stauch OB, Maa Y-F. Processing Impact on Monoclonal Antibody Drug Products: Protein Subvisible Particulate Formation Induced by

Grinding Stress. PDA J Pharm Sci Technol. 2017;71(3):172-188. doi:10.5731/pdajpst.2016.006726.

110.   Mahler H-C, Müller R, Friess W, Delille A, Matheus S. Induction and analysis of aggregates in a liquid IgG1-antibody formulation. Eur J Pharm Biopharm. 2005;59(3):407-417. doi:10.1016/j.ejpb.2004.12.004.

111.   Narayanan H, Dingfelder F, Butté A, Lorenzen N, Sokolov M, Arosio P. Machine Learning for Biologics: Opportunities for Protein Engineering, Developability, and Formulation. Trends Pharmacol Sci. 2021;42(3):151-165. doi:10.1016/j.tips.2020.12.004.

112.   Jolliffe IT, Cadima J. Principal component analysis: a review and recent developments. Philos Trans A Math Phys Eng Sci. 2016;374(2065):20150202. doi:10.1098/rsta.2015.0202.

113.   Sekulovic A, Verrijk R, Rades T, et al. Simultaneous automated image analysis and Raman spectroscopy of powders at an individual particle level. J Pharm Biomed Anal. 2021;193:113744. doi:10.1016/j.jpba.2020.113744.

114.   Krough A. What are artificial neural networks. Nat Biotechnol. 2008;26(2):195-197.

115.   Daniels AL, Calderon CP, Randolph TW. Machine learning and statistical analyses for extracting and characterizing "fingerprints" of antibody aggregation at container interfaces from flow microscopy images. Biotechnol Bioeng. 2020;117(11):3322-3335. doi:10.1002/bit.27501.

116.   Calderon CP, Daniels AL, Randolph TW. Deep Convolutional Neural Network Analysis of Flow Imaging Microscopy Data to Classify Subvisible Particles in Protein Formulations J Pharm Sci. 2018;107(4):999-1008. doi:10.1016/j.xphs.2017.12.008.

117.   Chen XG, Graužinytė M, van der Vaart AW, Boll B. Applying Pattern Recognition as a Robust Approach for Silicone Oil Droplet Identification in Flow-Microscopy Images of Protein Formulations. J Pharm Sci. 2020. doi:10.1016/j.xphs.2020.10.044.

118.   Jere D, Sediq AS, Huwyler J, Vollrath I, Kardorff M, Mahler H-C. Challenges for Cell-Based Medicinal Products From a Pharmaceutical Product Perspective. J Pharm Sci. 2020. doi:10.1016/j.xphs.2020.11.040.

119.   Mount NM, Ward SJ, Kefalas P, Hyllner J. Cell-based therapy technology classifications and translational challenges. Philos Trans R Soc Lond , B, Biol Sci. 2015;370(1680):20150017. doi:10.1098/rstb.2015.0017.

120.   Hoogendoorn KH, Crommelin DJA, Jiskoot W. Formulation of Cell-Based Medicinal Products: A Question of Life or Death? J Pharm Sci. 2020. doi:10.1016/j.xphs.2020.07.002.

121.   Li R, Johnson R, Yu G, McKenna DH, Hubel A. Preservation of cell-based immunotherapies for clinical trials. Cytotherapy. 2019;21(9):943-957. doi:10.1016/j.jcyt.2019.07.004.

122.   Clarke D, Harati D, Martin J, et al. Managing particulates in cellular therapy. Cytotherapy. 2012;14(9):1032-1040. doi:10.3109/14653249.2012.706709.

123.   Clarke D, Stanton J, Powers D, et al. Managing particulates in cell therapy: Guidance for best practice. Cytotherapy. 2016;18(9):1063-1076. doi:10.1016/j.jcyt.2016.05.011.

Chapter 2

Critical evaluation of microfluidic resistive pulse sensing for quantification and sizing of nanometer- and micrometer-sized particles in biopharmaceutical products

Adam D. Grabarek[1,2], Daniel Weinbuch[1], Wim Jiskoot[1,2]*, Andrea Hawe[1]*

[1]*Coriolis Pharma, Fraunhoferstrasse 18 b, 82152 Martinsried, Germany*

[2]*Leiden Academic Centre for Drug Research, Leiden University, The Netherlands*

*corresponding authors

Abstract

The objective was to evaluate performance, strengths and limitations of the microfluidic resistive pulse sensing (MRPS) technique for the characterization of particles in the size range from about 50 to 2000 nm. MRPS, resonant mass measurement (RMM), nanoparticle tracking analysis (NTA) and dynamic light scattering (DLS) were compared for the analysis of nanometer-sized polystyrene (PS) beads, liposomes, bacteria and protein aggregates. An electrical conductivity of at least 3 mS/cm (equivalent to 25 mM NaCl) was determined as a key requirement for reliable analysis with MRPS. Particle size distributions of PS beads determined by MRPS, NTA and RMM correlated well. However, counting precision varied significantly among the techniques, and was best for RMM followed by MRPS and NTA. As determined by measuring single and mixed PS bead populations, MRPS showed the highest peak resolution for sizing. RMM and MRPS were superior over DLS and NTA for the characterization of stressed protein samples. Finally, MRPS proved to be the only analytical technique able to characterize both bacteria and liposomes. In conclusion, MRPS is an orthogonal technique alongside other established techniques for a comprehensive analysis of a sample´s particle size distribution and particle concentration.

Introduction

Particles ranging from a few nanometers up to several hundred micrometers receive substantial attention in the biopharmaceutical industry, for example, as unwanted particulate impurities in drug products, as drug delivery systems (e.g., liposomes) and as active pharmaceutical ingredients (APIs, e.g., virus-like particles, viruses, exosomes, bacteria, cells)[1,2].

Particulate impurities found in therapeutic protein drug products can have various sources and may include environmental contaminants, impurities related to excipients or degradants of excipients, and proteinaceous particles formed due to instability of the API[3]. Particulate impurities can impair product stability, quality and safety, and may cause serious adverse effects in patients, such as capillary occlusion, hypersensitivity reactions and neutralizing antibody formation[4-6]. The wide size range and heterogeneous distribution of protein aggregates and other impurities pose a great challenge in protein drug development and quality control. Since no current analytical technique is able to comprehensively characterize the entire protein aggregate population, several complementary methods must be utilized[7-9]. Even though regulatory authorities increasingly demand the characterization of protein therapeutics within the nanometer size range[10], technical limitations of currently available instruments with respect to robustness and low throughput make the development and validation of methods to size and quantify particles within this range extremely challenging[11,12].

Drug delivery systems within the nanometer size range (e.g., liposomes, polymer-based nanoparticles) are often applied to control the biodistribution profile of small and large molecules, to promote their selective and specific targeted release, or to protect the API from proteolytic degradation upon administration[1,13]. The efficacy and safety of nanoparticulate formulations depend to a significant extent on their size, quantity and heterogeneity[14]. In addition, utilization of genetically engineered microbes and viruses has become a promising tool for therapies against life-threatening diseases, such as cancer[15]. For all of these therapeutic agents, adequate particle characterization methods are required for the determination of product quality.

Currently, common techniques used for particle characterization in the nanometer and low micrometer size ranges include transmission electron microscopy[9,16], flow cytometry[12], dynamic light scattering (DLS)[17,18], asymmetrical flow field-flow fractionation[19], resonant mass measurement (RMM)[18,20,21] and nanoparticle tracking analysis (NTA)[22-25]. Each of these techniques has its own strengths and limitations, based on a distinct measurement principle, and covers a specific size range[9,23,26]. Despite the availability of several methods, our ability to characterize particle populations within the nanometer and low micrometer size ranges is limited and analytical gaps remain[27].

Resistive pulse sensing has been widely reported as a technique for characterization of single molecules as well as particles sizing up to several micrometers[28]. It is based on the electrical sensing zone technique, or Coulter principle, where the size of a particle is measured based on the resistance change it induces upon passage through a small orifice. The technique was primarily developed for counting and sizing of human cells. With the advancement of microfluidics, microfluidic resistive pulse sensing (MRPS) based methods have been developed. The MRPS technology is employed in nCS1, which utilizes disposable polydimethylsiloxane (PDMS) cartridges for particle sizing and counting. The covered size range is cartridge dependent and ranges from about 50 to 2000 nm. In order to characterize particles within this range, four types of cartridges are available, namely TS-300 (50-300 nm), TS-400 (65-400 nm), TS-900 (130-900 nm) and TS-2000 (250- 2000 nm). The principal component of the cartridge is the sensing electrode, which is fixed between a fluidic resistor and a nanoconstriction. The motion of the analyte with suspended particles is controlled within the microfluidic channels with pressurized air. Particles are directed through the orifice of the nanoconstriction where a single passage induces a change in the electric current. This event is characterized by an induced nanoconstriction resistance (ΔR) which changes the fluid potential (ΔV) in contact with the sensing electrode. Its magnitude then depends, accordingly to the Maxwell's equation[29], on the occupied volume by the particle at the constriction, and thus particle size, as described in more detail elsewhere[30].

Recently, Barnett et al. performed a comparison of nCS1 to light scattering-based techniques, such as DLS and size exclusion chromatography with multi-angle static light

scattering, for the characterization of silicone oil droplets and protein particles in formulations exposed to various stress conditions[31]. In our study, we extended the investigation of MRPS by exploring the potential and limitations of nCS1 for the characterization of various types of nanometer-sized particles with special focus on biological applications. In addition, a direct comparison of MRPS with other submicron particle characterization techniques, i.e., DLS, NTA and RMM, which are commonly applied during biopharmaceutical drug product development, was performed to assess each method's strengths and weaknesses.

Materials and Methods

Materials

Polysorbate 20, sodium chloride and ten-fold concentrated phosphate buffer saline (PBS) were obtained from Sigma-Aldrich (Steinheim, Germany). Dibasic and monobasic sodium phosphate was purchased from VWR (Bruchsal, Germany). In-house Milli-Q water (resistivity 18.2 MΩ cm) was dispensed from an Advantage A10 purification system (Millipore, Newark, New Jersey). All diluents used in the study were freshly filtered using a 0.1 µm Millex-VV syringe filter unit (Millipore, Schwalback, Germany) and dilutions were performed under laminar air flow conditions.

Polystyrene (PS) nanometer standard beads with diameters of 203 ± 5 nm (PS203nm), 297 ± 7 nm (PS297nm), 495 ± 8 nm (PS495nm), 799 ± 9 nm (PS799nm) and 1030 ± 9 nm (PS1030nm) were purchased from Fisher Scientific (Ulm, Germany). Dilutions of the PS beads were performed in formulation buffer containing 0.1% w/v polysorbate 20, unless otherwise stated.

Preparation of proteinaceous particles

Bovine serum albumin (BSA) (Sigma-Aldrich, Steinheim, Germany; LOT 193829) was used to generate proteinaceous particles. A 10 mg/mL protein solution was prepared by dissolving lyophilized BSA in single strength PBS (pH adjusted to 4.75 with 1 M HCl). The solution was filtered by using a 0.1-µm polyethersulfone syringe filter and 1-mL aliquots were artificially stressed in 2-mL Eppendorf tubes by using a Thermomixer (Eppendorf, Hamburg, Germany) at 67 °C/1400 rpm for 5 min. In order to homogenize the sample, aliquots were pooled into a Falcon tube and subsequently aliquoted into 1.5-mL Eppendorf tubes for long term storage at -80 °C. Thawed aliquots were measured with Micro-Flow Imaging and DLS to demonstrate vial-to-vial consistency (n=3) as well particle stability at room temperature over 8 hours (data not shown). To obtain optimal proteinaceous particle concentrations for each analytical technique, the thawed samples were diluted with PBS (pH 7.4).

Preparation of liposomes

Negatively charged liposomes (-21 mV, determined with Zetasiser nano ZS), composed of distearoyl phophatidylcholine, distearoyl phosphatidylglycerol and cholesterol, were kindly provided by Naomi Benne (Leiden Academic Centre for Drug Research) and were prepared as described elsewhere[32].

Preparation of probiotic bacterial samples

Pharmaceutical-grade probiotic bacteria containing two strains of Lactobacillus (*L. helveticus* R-52 and *L. rhamnosus* R-11) were purchased as Lacidofil from Institut Rosell Inc., Montreal, CA. About 40 mg of the capsule's dry powder blend was dissolved in 10 mL of 150 mM NaCl in a 15-mL Falcon tube (VWR, Bruchsal, Germany) and mixed at 10 rpm for 15 min by using a rotating mixer. Volume-based dilutions in 150 mM NaCl were performed and samples were measured within 2 hours post preparation.

Dynamic light scattering (DLS)

DLS was performed by using a Zetasizer Nano ZS (Malvern Instruments, Worcestershire, UK) equipped with a 633-nm He-Ne laser set at an angle of 173°. Single-use PS semi-micro

cuvettes with a 10-mm path length (Brand, Wertheim, Germany) were filled with 0.5 ml of sample for each measurement. The attenuator was set automatically depending on the particle concentration. Samples were equilibrated to a working temperature of 25 $^{\circ}$C for 60 seconds prior to each analysis. The Z-average diameter (Z-ave), polydispersity index (PDI) and intensity-weighted size distribution were derived from the autocorrelation function by using the Dispersion Technology Software version 6.01 with CONTIN smoothing algorithm. Each measurement was performed in triplicate.

Nanoparticle tracking analysis (NTA)

NTA data was obtained with a NanoSight (Model LM20, Malvern Instrument, Malvern, UK) instrument with a 405-nm laser (blue), a sample chamber and a Viton fluoroelastomer O-ring. Samples were injected into the chamber by using a 1-mL silicone-free syringe and the purging volume was 0.3 mL. A video capture was initiated immediately after injection and a triplicate measurement of 60-second replicates was performed. All measurements were collected at room temperature with camera levels set to optimal values and 200 valid tracks must have been recorded for a valid measurements. Data collection and evaluation was done with the NanoSight software version 3.2, unless otherwise stated.

Resonant mass measurement (RMM)

Particles were analyzed with a Archimedes system (Malvern Instrument, Malvern, UK) equipped with a Hi-Q Micro Sensor (Malvern Instrument) operated by a ParticleLab software version 2.01. Prior to each set of measurements, the instrument was calibrated with PS1030nm followed by a measurement of Milli-Q water to confirm cleanliness of the system. Between sample measurements two "sneeze" operations were performed and the system was flushed for 5 minutes with Milli-Q water to avoid carry-over. Samples were loaded for 40 seconds and the limit of detection (LOD) was determined automatically by the software. A density value of 1.05 g/cm^3 was used for PS beads, 1.34 g/cm^3 for protein particles and 1.16 g/cm^3 for bacteria[33], and solely negatively buoyant particles were considered. Measurements were performed in triplicate and for each replicate 150 nL was analyzed, where a minimum of 50 particle counts were recorded.

Microfluidic resistive pulse sensing (MRPS)

Microfluidics-based resistive pulse sensing measurements were performed by using an nCS1 instrument (Spectradyne, Torrence, USA) equipped with disposable PDMS cartridges: TS-400 (size range 65-400 nm), TS-900 (size range 125-900 nm) and TS-2000 (size range 250-2000 nm). A running buffer of PBS (pH 7.4) with 1% w/v polysorbate 20 was used to generate an appropriate ionic electrical current in the analyte and ensure an appropriate flow of particles leaving the cartridge to the waste reservoirs. The running buffer does not have contact with the analyte prior to the nano-constriction, thereby avoiding cross-contamination. Approximately 3 µL of sample was used for each measurement and not less than 500 particles were counted per analysis. To achieve appropriate sizing of the analyzed particles, a calibration step for each cartridge was required. Calibration was performed by using PS beads (495 ± 8 nm) diluted in analyte's diluent consisting of 0.1% polysorbate 20. Collected data was analyzed by using nCS1 Data Analyzer (Spectradyne, Torrence, USA). Filters were applied for data analysis in order to exclude false-positive signals. The used filters excluded detected particle events characterized by user defined transit time, signal-to-noise ratio, peak symmetry and/or diameter.

Conductivity measurements

Electric conductivities of samples were measured in triplicate at 25 °C by using a SevenCompact S230 basic conductivity meter (Mettler Toledo, Columbus, USA), calibrated with a 1.413 µS/cm standard

Results

Impact of conductivity on sample analysis by MRPS

At first, the impact of conductivity on the MRPS technique's performance for particle sizing and counting was investigated. A consistent precision of measurement of the mean diameter and concentration of PS1030nm beads suspended in solutions with a conductivity ranging from ~3 mS/cm (equivalent to 25 mM NaCl) up to ~17 mS/cm (150 mM NaCl) could be achieved, independent of pH and ionic species (Figure 1). Below ~3 mS/cm, however,

there is a notable decrease in the measured mean diameter as well as an increase in particle count. The higher baseline noise (Figure 2 A, 2 B and Supplementary figure S1) increases the limit of detection. The overestimated particle concentration at low electrical conductivity is related to the measuring principle of MRPS. Media with low ionic strength lead to an increased detected transit time of a particle passing through the nanoconstriction, as shown in Figure 2 C (see also discussion section).
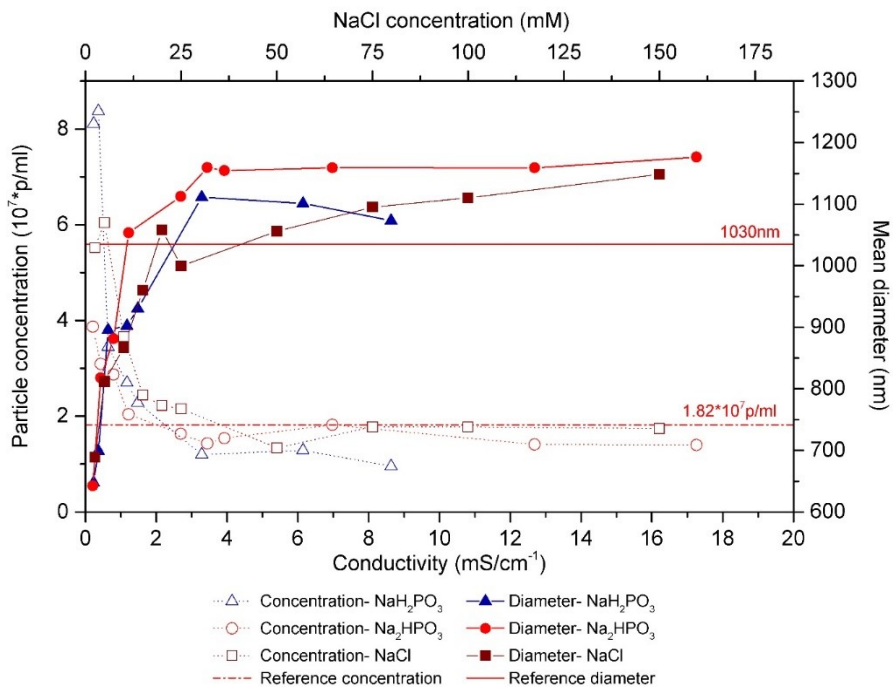

Figure 1: Sizing and quantification of PS1030 beads suspended in solutions with increasing ionic strength using cartridge TS-2000. The top x-axis shows the molar concentration of NaCl corresponding to the electrical conductivity values at the bottom x-axis. Each data point represents a single measurement. Horizontal solid and dashed lines indicate the reference particle size and concentration, respectively, specified by the manufacturer.
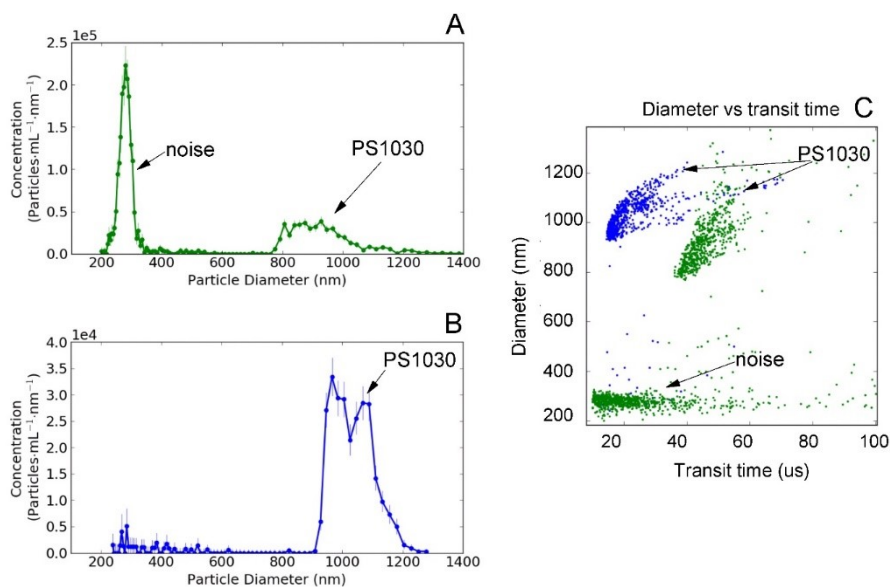
Figure 2: Particle size distribution characterized with MRPS (nCS1 equipped with a TS-2000 cartridge) for PS1030nm beads suspended in Na2HPO4 solution with low Na2HPO4 concentration (5 mM) (a) and high Na2HPO4 concentration (150 mM) (b). Scatter plot of measured diameter versus transit time for PS1030nm at high (blue) and low (green) Na2HPO4 concentration (c).

Repeatability of sizing and counting of monodisperse nanoparticles by MRPS

Repeatability was assessed by comparing the detected particle concentration, mean and mode diameter size in nm, as well as peak centroid of five replicate measurements of PS495nm and PS1030nm suspended in single strength PBS with 0.1% polysorbate 20 (conductivity ~14 mS/cm) by using TS-900 and TS-2000 cartridges, respectively. The results obtained from measurements performed with one single cartridge (intra-cartridge variability) and with multiple cartridges (inter-cartridge variability) from a single batch were used to calculate the CV% of replicate measurements (Table 1). For each of the measured parameters, the variance of the replicate intra- and inter-cartridge measurements was statistically equal (one-sided ANOVA, *p< 0.05 confidence level) for both cartridge types.

Table 1. Comparison of MRPS repeatability in sizing and counting of PS495nm and PS1030nm in five replicate measurements using single (intra) and multiple (inter) cartridges for two types of cartridges (TS-2000 and TS-900). PS beads were suspended in PBS (pH 7.4) with 0.1% w/v polysorbate 20.

Measurement	Cartridge type	Bead size (nm)	Particle concentration (p/ml)	Mean diameter (nm)	Mode diameter (nm)	Centroid (nm)
			Coefficient of variation (%)			
Inter	TS-2000	1030 ± 9	6.45	5.18	7.27	4.71
Intra			7.11	3.42	5.53	6.34
Inter	TS-900	495 ± 8	13.98	5.11	5.14	5.06
Intra			19.42	4.10	4.20	4.48

Accuracy and precision of MRPS compared to DLS, NTA and RMM using monodisperse nanoparticles

Accuracy and precision for sizing and counting of triplicate measurements of monodisperse PS beads were compared for DLS, NTA, RMM and MRPS. Because of the differences in the working size ranges of each technique, two distinct PS bead sizes were selected to perform a cross comparison between all four techniques.

Size accuracy was determined based on comparing the mean size diameter, peak maximum, and particle size distribution defined as span, calculated as $((D_{90}-D_{10})/D_{50})$, and percentile values at 10%, 50% and 90% (D_{10}, D_{50}, D_{90}). Sizing precision of each technique was evaluated based on the standard deviation of the above mentioned values over the replicate measurements. The estimated particle concentration of the PS standard sizing beads was calculated based on the size-, density- and mass-concentration values specified by the manufacturer. This approach was chosen because, to the best of our knowledge, there are no certified counting standard beads available in the required size range.

As the concentration of the PS sizing beads is not traceable, and the concentration is based on an estimation, absolute counting accuracy could not be tested. Therefore, a relative comparison between the techniques in particle counting and examination of the precision in determination of particle concentration was done instead. The stated particle concentration limits for TS-900 and TS-2000 are estimates based on the PS bead specifications from the manufacturer.

For both PS bead populations, a good agreement in the determined mean diameter and maximum peak position was found among all evaluated techniques (Table 2). DLS measurements of both PS bead standards resulted in ca. 10% greater size values compared to the single particle counting techniques. RMM provided lowest span value for a single population of PS beads and with it the highest accuracy in characterization of the particle size distribution. All techniques showed similar particle size distribution percentile values, indicating similar accuracy in sizing of PS beads in the presented setting. Percentiles of obtained distributions are not presented for DLS as it is not recommended calculating these value because of the inherent errors present in the deconvolution of the correlation function used for particle measurements [34].

*Table 2. Descriptors of particle size distributions obtained from measuring single populations of PS203nm and PS799nm beads with DLS, NTA, RMM and MRPS. Values are presented as mean values of replicate measurements and errors are standard deviations of the triplicate measurements. Span represents width of the size distribution ((D$_{90}$-D$_{10}$)/D$_{50}$). *Parameters of main peak reported*

Technique	Bead diameter size (nm)	Mean diameter (nm)	Peak max (nm)	D$_{10}$ (nm)	D$_{50}$ (nm)	D$_{90}$ (nm)	Span
DLS*		234 ± 5	220 ± 0	-	-	-	-
NTA	203	193 ± 1	198 ± 2	166 ± 1	194 ± 1	213 ± 3	0.25 ± 0.06
MRPS		187 ± 7	178 ± 6	162 ± 2	182 ± 1	222 ± 2	0.33 ± 0.01
DLS*		879 ± 5	825 ± 0	-	-	-	-
RMM	799	805 ± 1	792 ± 4	747 ± 4	780 ± 1	822 ± 2	0.10 ± 0.01
MRPS		799 ± 15	758 ± 3	737 ± 12	792 ± 12	886 ± 10	0.19 ± 0.01

PS495nm beads were measured with the three techniques within the estimated concentration range from $1*10^6$ p/ml up to $1*10^{10}$ p/ml (Figure 3 A). All techniques showed strong linearity (>0.98) for measured bead concentrations within their working counting range.

For MRPS a concentration range of approximately $5*10^7$-$1*10^{10}$ p/ml could be covered with cartridge TS-900 and of $5*10^6$-$5*10^9$ p/ml with cartridge TS-2000. Consequently, MRPS was the only technique able to cover the entire concentration spectrum, showing a superior dynamic range compared to RMM and NTA. Although it was possible to carry out measurements at lower tested concentrations, the required number of measured particles stated in Materials and Methods section could not be reached within a practical timeframe (Figure 3 A, empty symbols).
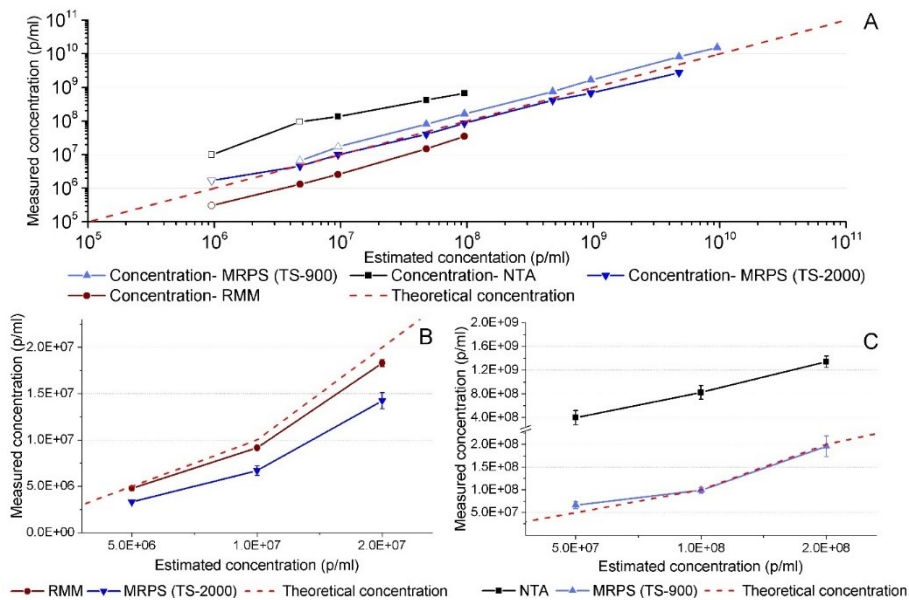

Figure 3: (A) Relation between theoretically estimated and measured concentration of PS495nm obtained by NTA, RMM and MRPS. Empty symbols represent measured samples with a particle concentration below the recommended concentration range for the given technique

Because of the limitations of RMM and NTA to detect PS495nm beads (see discussion section), we further investigated PS799nm and PS203nm beads to compare the relative accuracy and precision in quantification of nm-sized particles between MRPS, NTA and RMM. The PS beads were analyzed at three dilutions. For PS799nm, RMM reported higher measured particle concentrations compared to MRPS by 50% for the two lowest and by 25% for the one highest estimated concentrations (Figure 3 B). NTA determined a much higher particle concentration of PS203nm for all three dilutions compared to MRPS and showed

particle concentrations up to 8 fold higher compared to the estimated concentrations calculated based on manufacturer specifications (Figure 3 C).

The technique with the highest repeatability in determining particle concentration was RMM, which showed an average deviation of 3±2% for replicate measurements among the three concentrations. Precision in particle count for MRPS was dependent on the used cartridge and an average 5±3% and 10±3% deviation was found for TS-2000 and TS-900, respectively. NTA was the technique with the lowest precision in particle counting for which the deviation varied from 8% to 30% for the highest and lowest estimated PS bead concentration, respectively.

Size resolution of MRPS in comparison with DLS, NTA and RMM

In order to compare the size resolution and the ability to discriminate multimodal particle size distributions, PS297nm, PS495nm and PS799nm beads were analyzed individually and as mixtures (Figure 4). Gaussian curves were plotted for each distribution and the peak max, peak start and peak end was obtained. In addition, full width at half maximum (FWHM), which refers to the width of the peak at 50% of the peak height, was considered (Supplementary table S1). Furthermore, the impact of the polydispersity on the measured size distribution was investigated. The particle size distributions for the single particle counting techniques (NTA, RMM and MRPS) are presented in 10 nm bins, whereas DLS results are presented as a series of logarithmically spaced size bin values derived by the used software.
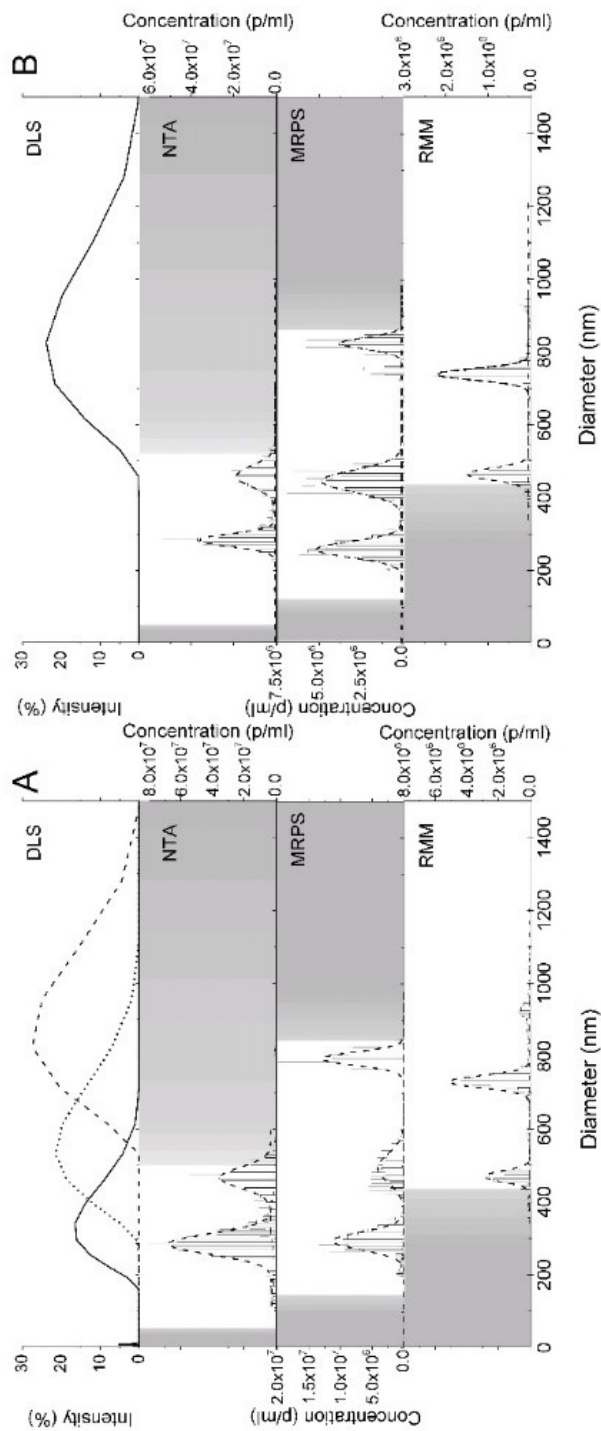
Figure 4: Particle size distributions of PS297nm, PS495nm and PS799nm beads (particle number ratio of 2:1:1) measured individually (A) and as mixture (B) with DLS, NTA, MRPS and RMM. Beads were dispersed in PBS (pH 7.4) + 0.1% w/v polysorbate 20 (RMM samples were free from polysorbate 20). Grey areas indicate particle sizes out of the approximate optimum working size range (white areas) for each technique, taking into account factors influencing the measurement, such as physical properties of particles (density, RI) and diluent (density, RI and conductivity).

Figure 4 A presents the particle size distributions of triplicate measurements of three monomodal bead populations (beads measured individually) performed by DLS, NTA, RMM and MRPS. For the characterization of nanometer-sized PS beads, DLS and MRPS proved to be superior to RMM or NTA with respect to the covered sizing range. Although DLS could cover the full size range presented in Figure 4 A, the technique showed the broadest peaks for monodisperse beads with FWHM values 5- to 15-fold greater compared to MRPS. It must be noted that DLS does not count individual particles but provides an intensity-weighted distribution of the overall population, which is naturally weighted according to the light scattering intensity of each particle fraction. Therefore, the obtained size distributions obtained with DLS will vary significantly to the other single particle analysis techniques and a direct comparison should not be performed. For NTA, RMM and MRPS the determined mean size diameter and FWHM values correlated well. Of note, RMM showed the highest precision in determination of particle size distribution.

Figure 4 B presents particle size distribution of multimodal PS bead suspensions (beads analyzed as mixture). Measurements with DLS showed only one single peak with a Z-average diameter of 785 nm. So, resolving different size populations at equal molar ratio was not possible, as shown before[35], and the strong bias towards larger particles in the intensity-weighted distribution provided by DLS displays the technique's inaccuracy in characterization of polydisperse samples. For the remaining techniques, the difference in mean size between each PS bead population was enough to resolve the different bead sizes present in the mixture. For NTA and RMM mean size diameter and peak max for each population group agreed well between both the measurements of individual and mixed beads with values falling within 5% of each other. For MRPS measurements of multimodal populations the determined mean size diameter of PS799nm beads was used to calibrate the cartridge. The variation in mean size diameter of PS297nm and PS495nm between monomodal and multimodal populations was 7% and 14%, respectively.

For quantitative determination of each technique's size resolution we used equation 1, which is commonly applied in chromatography to determine the degree of separation of

two solutes[36] and was used in a recent study on validation of the nanoparticle tracking analysis method[24]:

$$Rs = \frac{tR2 - tR1}{\frac{W1 + W2}{2}} \qquad (1)$$

Where, tR1 and tR2 are local maxima of peak 1 and peak 2, and W1 and W2 are peak width at baseline of these peaks. MRPS showed the highest R_s values compared to NTA and RMM, indicating high resolution capabilities in characterization of polydisperse samples.

Applications of MRPS for analysis of pharmaceutically relevant particulate formulations in comparison to RMM, DLS and NTA

Protein aggregates

The stressed BSA formulation was diluted by a factor of 25-, 50-, 100-, 250- and 500-fold in PBS and the dilutions were studied with DLS, NTA, RMM and MRPS within the suitable working range with respect to particle concentration for each technique (Figure 5). At each dilution level DLS showed multiple peaks, including a peak at ca. 10 nm deriving from BSA monomer and smaller aggregates. Subpopulations of particles above 20 nm were not resolved and the PDI value was above 0.9.
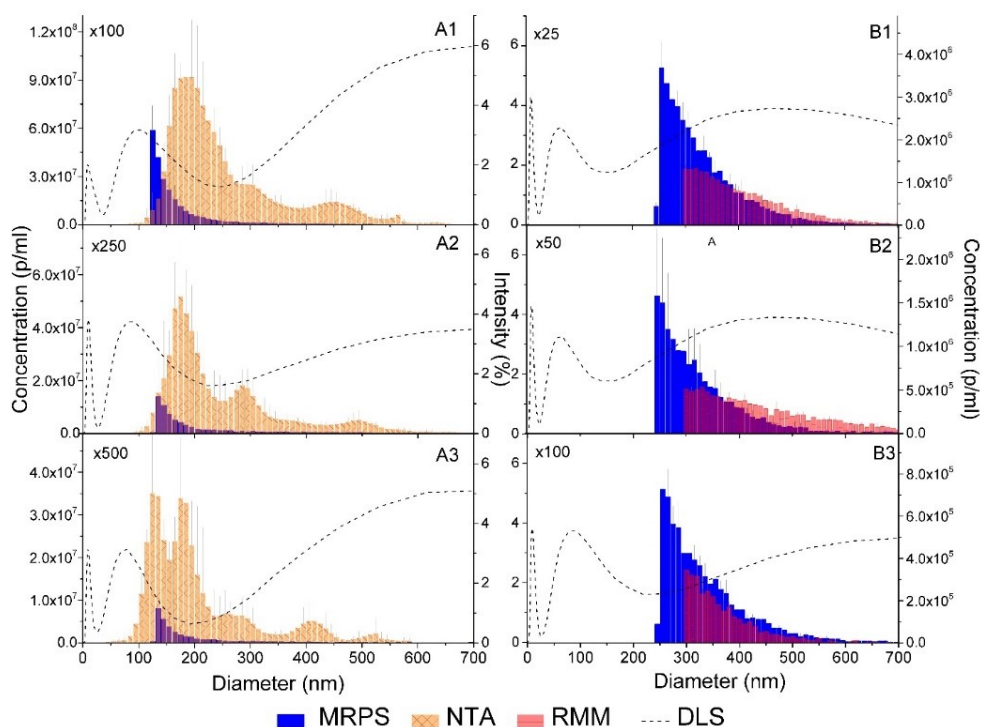
Figure 5: Particle size distribution of stressed BSA. A1-A3 show PSD determined with DLS, MRPS (TS-900) and NTA at 100-, 250- and 500-fold dilutions. B1-B3 show PSD determined with DLS, MRPS (TS-2000) and RMM at 25-, 50- and 100-fold dilutions. Middle Y-axes relate to determined intensity with DLS, whereas Y-axes on the left and right side represent the measured concentration for each bin size and their scale is adjusted to each graph. Error bars represent the standard deviation of triplicate measurements.

Figure 5 A1-A3 presents the particle size distributions of stressed BSA samples at 100-, 250- and 500-fold dilution, each measured with DLS, MRPS and NTA. The shape of the distribution determined with NTA shifted towards smaller sized particles for each subsequent dilution, whereas MRPS produced a consistent asymmetrical particle size distribution with a cut-off at a fixed lower limit of size detection. MRPS and RMM showed highly similar particle size distributions above 300 nm for protein aggregates at all three different dilutions (Figure 5 B1-B3).

The decrease in sensitivity of NTA for smaller particles within samples that also contain a higher number of larger particles, led to an underestimation in the concentration of particles below 200 nm. Nonetheless, compared to MRPS, NTA reported an approximately 10-fold higher determined particle concentration within the same measured size range for

each dilution. MRPS measured higher concentrations of particles above 300 nm compared to RMM, however the difference was below 18%.

Liposomes

Measurement of liposomes diluted 5000-fold in PBS was performed by using DLS, NTA and MRPS (Figure 6 A). DLS showed a Z-average diameter of 165 nm with a PDI of 0.09, indicating a homogenous particle size distribution. NTA showed a similar mean size diameter (159 nm) as DLS, with a relatively low average polydispersity of the size distribution (span-0.69) for each replicate. The mean size diameter determined with MRPS was 97 nm, which is significantly lower compared to the values obtained with the two light scattering-based techniques. Furthermore, MRPS produced a wider size distribution (span-1.23), suggesting a higher sensitivity towards the smallest and largest particles within the population.
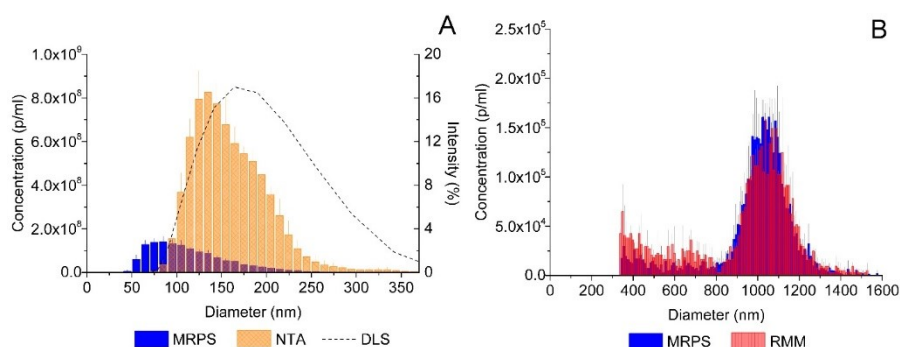

Figure 6: A) Particle size distribution of liposomes from NTA, DLS and MRPS (TS-400). For MRPS and NTA the determined particle concentration is reported on the left y-axis and the measured intensity with DLS is reported on the right y-axis. The diameter is shown in a logarithmic scale (x-axis). B) Particle size distribution of Lactobacilli determined by MRPS (TS-2000) and RMM. Error bars represent the standard deviation of the triplicate measurements.

Quantification of the number of liposomes was carried out with NTA and MRPS. The reported mean particle concentration with NTA was 5.5-fold greater when compared to MRPS, which confirms the data obtained from measurement of PS beads (Table 2 and Figure 3).

Lactobacilli

A commercially available product, containing a mixture of *Lactobacilli helveticus* and *Lactobacilli rhamnosus*, was used to examine the suitability of MRPS for counting and sizing microorganisms, and the performance of MRPS was compared to that of RMM (Figure 6 B). The mean size for the bacteria population was 1037 nm according to MRPS, which correlates well with the mean diameter of 1075 nm obtained with RMM.

Both techniques showed a similar concentration of *Lactobacilli*. The particle concentration within the size range 800-1600 nm, the expected size of the bacteria, was $3.52*10^6$ and $3.48*10^6$ p/ml for MRPS and RMM, respectively. Particles detected below ca. 800 nm are most likely cell debris or particulate matter originating from the stock material and were not included in the calculation.

Discussion

We evaluated the MRPS technique for particle characterization to provide insights into its limitations and advantages. The electrical conductivity of the analyzed sample showed to be one of the most important factors for correct analysis with MRPS. An underestimation of the particle diameter and an overestimation of particle counts at low ionic strength (below 3 mS/cm) of the analyte suspension were observed. Lower reported diameter sizes for PS beads in samples with low electrical conductivity relate to the relatively lower induced ΔR at the nanoconstriction upon particle passage at the orifice. This translates to a weaker output signal due to the decreased double-layer capacitance of the sensing electrode[37]. In addition, the thermal noise is increased at low ionic strength due to the reduced measurement bandwidth, leading to a higher baseline noise and increased number of false-positives (Supplementary figure S1) as well as a loss of particle detection at the lower end of the sizing range (Figure 2 A and 2 B). It must be noted that the conductivity threshold of 3 mS/cm applies solely to the TS-2000 cartridge and will increase in smaller cartridges which are equipped with a nanoconstriction of smaller orifice dimensions.

The apparent particle concentration increased in samples with a conductivity below 3 mS/cm. MRPS determines particle concentration based on the mean transit time of single particle passages via a high current density surrounding the nanoconstriction. This high current density is significantly reduced at a low concentration of ionic species, and therefore the magnitude of this electric field is reduced for a prolonged time and a higher transit time is detected by the software (Figure 2 C).

The cartridges are fabricated by using a micro-molding technique, where each batch is produced with a single mold with defined microfluidic channels. For accurate size determination it is recommended by the manufacture to spike in a reference standard (e.g., NIST PS beads) into the sample for a required size calibration. However, biological material, such as proteins, tend to irreversibly adsorb to PS beads, which may alter the size distribution of the PS particles as well as that of the analyte[38]. Moreover, the bead size may overlap with the size of particles in the sample. Because of the high intra-cartridge sizing precision shown within our study (Table 1), the size calibration measurement of each cartridge was performed after the sample measurement.

Furthermore, the accuracy and precision of the four particle characterization techniques was evaluated using PS203nm and PS799nm. The mean diameter size values obtained with NTA, RMM and MRPS are slightly lower compared to DLS and in better agreement to the reference value. This trend was expected, as the dispersed particles scatter incident light proportional to at least the 2nd power of their radii (depending on the particle size, wavelength of the used laser and type of scattering) leading to a bias towards larger particles size in DLS[39]. A similar trend was observed by other authors who performed sizing comparisons between DLS and NTA[22] or DLS and tunable resistive pulse sensing technique[40]. Furthermore, for both bead populations, MRPS, NTA and RMM showed a highly similar span values, indicating a similar accuracy in determination of the size distribution for monodisperse populations. The variation coefficient of the mean size determined with MRPS for PS beads was ca. 3-5%, which is superior to the repeability of NTA measurements stated in the literature (6.3% and 10% with software version 3.0 and 2.3, respectively)[24].

However, values above 3% are inferior to that of RMM (0.3%) and DLS (1.1%)[18], and to the results presented in Table 2.

DLS does not quantify particles, but is a qualitative technique for assessing particle size distributions with a high sensitivity, or bias, to larger aggregates/particles within an analyzed sample. Therefore, DLS was not considered for the comparison of the techniques with respect to particle quantification. The particle concentration determined by MRSP, NTA and RMM varied for each sample to a significant degree. Such deviations in determined particle concentrations from different methods have been previously reported and a number of factors could contribute to these[26,41]. Firstly, in all current techniques for submicron particle measurements, a notably small sample volume is analyzed and therefore the extrapolation factor of particle counts to particles/mL is relatively high. For example, in our setup, NTA analyzes up to 0.08 nL per replicate – generating an extrapolation factor of about $1*10^9$. The analyzed volume with MRPS is cartridge dependent. The TS-900 cartridge samples approximately 10 nL per replicate, yielding an extrapolation factor of about $1*10^5$. With the TS-2000 cartridge and also with RMM, 150 nL were analyzed, resulting in an extrapolation of particle count of approximately $1.5*10^4$. For comparison, methods used for characterization of micron sized particles, e.g., flow imaging microscopy, measure from 0.15 up to 0.8 mL of sample and particle counts are corrected to particles/mL by a factor of 6.5 - 1.25.

Secondly, an additional source of discrepancies in particle count between each technique could be the different measuring principle used to determine the absolute particle concentration. NTA takes the average count of particles per frame and then divides it by the interrogated volume determined by the cell dimensions. RMM and MRPS measure the particle concentration based on the single transit time of a particle through a microfluidic channel and a high current density, respectively. The different algorithms and models used in each method can introduce errors that may lead to imprecision in the obtained particle concentrations.

For the evaluation of size resolution, a mixture of three differently sized PS beads at a number ratio of 2:1:1 was considered as a suitable polydisperse model sample with no

overlap between particle size distributions of the three sets. The difference in mean size diameter between the PS297nm and PS799nm is above 2.5-fold, thus allowing to compare how well each instrument will be able to handle samples consisting of a broad range of particle sizes. Hence, for techniques with high resolution, the distinction of each population should be evident. In this study, we did not study other ratios of PS beads or the impact of concentration of distinct bead populations on the overall particle size distribution. Apart from DLS, all evaluated techniques showed good separation of peaks, with MRPS having the highest R_s value (Supplementary table S1). The incapability of resolving PS bead populations with DLS was expected, as discussed above. In the literature, NTA has been used to characterize PS particles from 30 nm up to 1000 nm in diameter[22,25,42]. However, the short wavelength laser used in our study limited the technique´s measurement capability of PS799nm due to the multiple scattering points present on a single particle, resulting in an interference that impedes correct particle tracking. Consequently, samples containing large particles may require additional sample preparation, e.g., filtration or centrifugation, prior to measurement with NTA for reliable characterization of the particle size distribution in the nanometer size range, as shown before for polydisperse protein aggregates[25]. RMM detects particles entering a microfluidic channel where they alter the resonance frequency of the suspended resonating cantilever[20]. The low density of PS beads (1.05 g/cm^3) suspended in PBS affects the lower limit of size detection and increases it automatically to 460 nm. This shows a critical limitation of RMM for the characterization of heterogeneous samples with particulate matter of low or unknown density where a significant error in the observed particle size distribution and particle concentration may be introduced.

Artificially stressed BSA samples were submitted to dilution and the proteinaceous particles were characterized by the four evaluated techniques. As different dilution factors may alter the protein particle concentration and/or size distribution[25], in our study comparative characterization was performed by measuring samples submitted to identical dilutions. MRPS showed to be capable of analyzing polydisperse proteinaceous samples on particle-by-particle basis to which sample dilution had not effect on the determined particle size distributions, as opposed to NTA or DLS. The bell shape distribution towards particles of larger sizes (clearly visible in Figure 5 A and 5 B) for protein aggregates seen with NTA has

been observed in the past by other authors[22,25,43]. Factors contributing to an inaccurate determination of particle size distribution by NTA for polydisperse samples include: 1) the relatively low particle counts obtained from a single measurement, as well as 2) the loss in sensitivity for smaller, weakly scattering particles, therefore showing bias towards a limited particle population. The derived Z-average diameter from DLS is an intensity-based overall average size based on a specific fit to the raw correlation function data. Therefore, the obtained data did not provide accurate information on particle populations within the sample, as this technique is not suitable for such polydisperse samples[18]. RMM and MRPS presented highly similar results for the proteinaceous samples with respect to particle size distribution and particle concentration.

For liposomes, DLS and NTA determined a higher mean size diameter of the population compared to MRPS, due to the above discussed bias of these techniques. Similar to protein aggregates, the difference in refractive index between buffer and liposomes is relatively small, resulting in a low light scattering intensity. Thus, the smallest particles within the population will not be detected with the two light scattering-based techniques and the reported distribution will be shifted to higher particle sizes. Additionally, the loss of sensitivity with NTA towards the smallest and largest particles within a polydisperse sample is indicated by the 2-fold smaller span value for liposome samples compared to MRPS (Supplementary table S2). Furthermore, the liposome concentration determined by NTA was significantly higher as compared to MRPS, which is in agreement with the results for PS beads (Figure 3). Previously reported comparative analysis between NTA and the resistive pulse sensing (RPS) technique, also showed an approximate 10-fold overestimation in concentration by NTA and the heavy influence of the operator settings on the quantitative assessment [44].

Characterization of bacterial cells using RMM and RPS was previously reported in the literature [33,45,46]. The two instruments determine the mean particle diameter via two distinct measuring principles using particle mass or volume, respectively. The obtained mean diameter values with RMM and MRPS vary from the cell dimensions of rod-shaped *Lactobacilli* stated in literature determined by using electron microscopy (*L. helveticus* – 6.0

x 0.7-0.9 µm and *L. rhamnosus* 2.0-4.0 x 0.8-1.0 µm)[47]. The measured diameters acquired with both used techniques refer to the volume-equivalent spherical diameter, which is characterized by:

$$d_V = \left(\frac{6}{\pi}V\right)^{\frac{1}{3}}$$

(2)

Where d_V is the diameter of a sphere with the same volume (*V*) as the particle. Using equation 2 and the reference bacteria dimensions to calculate d_V, we would expect the volumetric mean diameter to be in the range between 1.2 and 1.9 µm. Therefore, both MRPS and RMM may underestimate the mean size of elongated particles. These results align with the work carried out by Cavicchi et al., who showed a significant underestimation of d_V with the electrical sensing zone instrument for rod-shaped micrometer-sized particles[48]. The shape of particles would also have an impact on the reported mean diameter with DLS or NTA. Further investigation of the influence of particle shape and morphology on reported mean particle size and concentration with nanoparticle characterization techniques is therefore recommended.

Each of the evaluated technique in this study operates on a distinct principle. The suitability of each technique depends on the intended application, i.e., type of sample, required read-out and purpose of the analysis. In Table 3 we compare the four techniques to assist the reader in selecting the most appropriate technique for a given experimental setup. For instance, for a rapid and qualitative determination of the presence of particles, DLS can be recommended. However, for quantitative characterization of particle size distribution and particle concentration, single particle counting techniques (NTA, RMM, MRPS) are preferred. The other main factors to consider are the physical properties of the analyzed particles (e.g., size, refractive index, density, shape) and sample (e.g., viscosity, conductivity, particle concentration). As an example, highly concentrated protein solutions come along with a high viscosity and a high refractive index. In this case, the performance of light scattering-based techniques, such as NTA and DLS, is compromised, and RMM and MRPS

may be superior. With respect to highly viscous samples, software operating DLS, NTA and RMM allows the user to input the analyzed sample's viscosity. So far, such an option does not exist for the software operating MRPS and therefore, calibration beads of known size and concentration must be spiked into the sample to perform the required calibration.

Table 3. Comparison of the four evaluated techniques.

	DLS	NTA	RMM	MRPS
Technique characteristics				
Size determination based on	Intensity fluctuations of scattered light from particles moving under Brownian motion	Tracking the position of individual light-scattering particles moving under Brownian motion	Frequency shift of resonating cantilever	Electrical resistance increase in orifice
Approximate size range based on the literature [17,21]	1 – 1000 nm	30 – 1000 nm	300 – 5000 nm	50 – 2000 nm
Reported diameter	Hydrodynamic	Hydrodynamic	Volumetric	Volumetric
Approximate particle concentration range (#/mL) based on the literature [17,21]	$1*10^8 – 1*10^{12}$	$1*10^7 – 1*10^9$	$3*10^5 – 3*10^7$	$5*10^6 – 1*10^{11}$
Quantification and extrapolation factor for particle concentration	Not quantitative	Quantitative ~10^8	Quantitative ~10^4	Quantitative ~10^4 (TS-900) or ~10^5 (TS-2000)
Accuracy in size distribution determination of polydisperse particles	Low	Medium	High	High
Size resolution	Low	Medium	High	High
Technique's operative considerations				
Required information for (data) analysis	Refractive index, viscosity and temperature	Viscosity and temperature	Particle density	Conductivity
Additional requirements	-	-	System is vulnerable for blockage	Addition of polysorbate may be required for measurement
Consumables	Disposable or reusable cuvettes/plates	None	Microfluidic sensor	Microfluidic cartridges
Calibration	Not applicable	Not applicable	Required per sensor	Required per cartridge
Large particulate impurities or contaminants	Have significant influence on results	Easily detected and have large influence on results	May block the system and difficult to remove; little to significant impact on results	Filtered out at cartridge entry, no impact on results

Conclusions

MRPS showed to be a useful orthogonal technique for particle sizing and counting alongside DLS, NTA and RMM, which are frequently used in the (bio-)pharmaceutical field.. For measurements with nCS1 the sample of interest must have electrical conductivity above ~3 mS/cm for proper sizing and counting. Sizing of PS standard beads with each of the four techniques showed comparable results. Particle concentrations obtained by MRPS and RMM were similar, whereas NTA showed 5- to 10-fold higher particle counts. Apart from DLS, all techniques were able to resolve different size populations in polydisperse samples. The applicability of MRPS was further illustrated by the successful characterization of relevant samples, including protein aggregates, liposomes and bacteria. In conclusion, we have shown that MRPS is a valuable technique for analyzing particles in the nanometer- and low micrometer-size range.

References:

1. Tyagi P, Subramony JA. Nanotherapeutics in oral and parenteral drug delivery: Key learnings and future outlooks as we think small. J Control Release 2018;272:159-168.

2. Singh SK, Afonina N, Awwad M, Bechtold-Peters K, Blue JT, Chou D, Cromwell M, Krause HJ, Mahler HC, Meyer BK, Narhi L, Nesta DP, Spitznagel T. An industry perspective on the monitoring of subvisible particles as a quality attribute for protein therapeutics. J Pharm Sci 2010;99(8):3302-3321.

3. Narhi LO, Corvari V, Ripple DC, Afonina N, Cecchini I, Defelippis MR, Garidel P, Herre A, Koulov AV, Lubiniecki T, Mahler HC, Mangiagalli P, Nesta D, Perez-Ramirez B, Polozova A, Rossi M, Schmidt R, Simler R, Singh S, Spitznagel TM, Weiskopf A, Wuchner K. Subvisible (2-100 mum) particle analysis during biotherapeutic drug product development: part 1, considerations and strategy. J Pharm Sci 2015;104(6):1899-1908.

4. Kijanka G, Bee JS, Bishop SM, Que I, Lowik C, Jiskoot W. Fate of multimeric oligomers, submicron, and micron size aggregates of monoclonal antibodies upon subcutaneous injection in mice. J Pharm Sci 2016;105(5):1693-1704.

5. Roberts CJ. Protein aggregation and its impact on product quality. Curr Opin Biotechnol 2014;30:211-217.

6. Moussa EM, Panchal JP, Moorthy BS, Blum JS, Joubert MK, Narhi LO, Topp EM. Immunogenicity of therapeutic protein aggregates. J Pharm Sci 2016;105(2):417-430.

7. Weinbuch D, Jiskoot W, Hawe A. Light obscuration measurements of highly viscous solutions: sample pressurization overcomes underestimation of subvisible particle counts. AAPS J. 2014;16(5):1128-1131.

8. USP<788>. Particulate matter in injections. United States Pharmacopoeia, Natl. Formul. 2006.

9. Zolls S, Tantipolphan R, Wiggenhorn M, Winter G, Jiskoot W, Friess W, Hawe A. Particles in therapeutic protein formulations, Part 1: overview of analytical methods. J Pharm Sci 2012;101(3):914-935.

10. U.S. Department of Health and Human Services FaDA, Center for Drug Evaluation and Research, Center for Biologics Evaluation and Research. In: Guidance for industry: immunogenicity assessment for therapeutic protein products; 2014. Available at: http://www.fda.gov/Drugs/GuidanceComplianceRegulatoryInformation/Guidances/default.htm. Accessed March 30, 2018.

11. Carpenter JF, Randolph TW, Jiskoot W, Crommelin DJ, Middaugh CR, Winter G, Fan YX, Kirshner S, Verthelyi D, Kozlowski S, Clouse KA, Swann PG, Rosenberg A, Cherney B. Overlooking subvisible particles in therapeutic protein products: gaps that may compromise product quality. J Pharm Sci 2009;98(4):1201-1205.

12. Zhang L, Shi S, Antochshuk V. Closing the gap: counting and sizing of particles across submicron range by flow cytometry in therapeutic protein products. J Pharm Sci 2017;106(11):3215-3221.

13. Chuang S-Y, Lin C-H, Huang T-H, Fang J-Y. Lipid-based nanoparticles as a potential delivery approach in the treatment of rheumatoid arthritis. J Nanomater 2018;8(1):42.

14. Desai N. Challenges in development of nanoparticle-based therapeutics. AAPS J. 2012;14(2):282-295.

15. Kim OY, Park HT, Dinh NTH, Choi SJ, Lee J, Kim JH, Lee S-W, Gho YS. Bacterial outer membrane vesicles suppress tumor by interferon-γ-mediated antitumor response. Nat Commun 2017;8(1):626.

16. van der Pol E, Coumans FA, Grootemaat AE, Gardiner C, Sargent IL, Harrison P, Sturk A, van Leeuwen TG, Nieuwland R. Particle size distribution of exosomes and microvesicles determined by transmission electron microscopy, flow cytometry, nanoparticle tracking analysis, and resistive pulse sensing. J Thromb Haemost. 2014;12(7):1182-92

17. Bhattacharjee S. DLS and zeta potential – What they are and what they are not? J Control Release 2016;235:337-351.

18. Panchal J, Kotarek J, Marszal E, Topp EM. Analyzing subvisible particles in protein drug products: a comparison of dynamic light scattering (DLS) and resonant mass measurement (RMM). AAPS J. 2014;16(3):440-451.

19. Hawe A, Romeijn S, Filipe V, Jiskoot W. Asymmetrical flow field-flow fractionation method for the analysis of submicron protein aggregates. J Pharm Sci 2012;101(11):4129-4139.

20. Burg TP, Godin M, Knudsen SM, Shen W, Carlson G, Foster JS, Babcock K, Manalis SR. Weighing of biomolecules, single cells and single nanoparticles in fluid. Nature 2007;446:1066.

21. Godin M, Bryan AK, Burg TP, Babcock K, Manalis SR. Measuring the mass, density, and size of particles and cells using a suspended microchannel resonator. Appl Phys Lett 2007;91(12):123121.

22. Filipe V, Hawe A, Jiskoot W. Critical evaluation of nanoparticle tracking analysis (NTA) by NanoSight for the measurement of nanoparticles and protein aggregates. Pharm. Res. 2010;27(5):796-810.

23. Zhao H, Diez M, Koulov A, Bozova M, Bluemel M, Forrer K. Characterization of aggregates and particles using emerging techniques In Hanns-Christian Mahler WJ, eds. *Analysis of Aggregates and Particles in Protein Pharmaceuticals*, ed., John Wiley & Sons, Inc.; 2012:133-167.

24. Kestens V, Bozatzidis V, De Temmerman P-J, Ramaye Y, Roebben G. Validation of a particle tracking analysis method for the size determination of nano- and microparticles. J Nanopart Res 2017;19(8):271.

25. Tian X, Nejadnik MR, Baunsgaard D, Henriksen A, Rischel C, Jiskoot W. A comprehensive evaluation of nanoparticle tracking analysis (NanoSight) for characterization of proteinaceous submicron particles. J Pharm Sci 2016;105(11):3366-3375.

26. Rios Quiroz A, Lamerz J, Da Cunha T, Boillon A, Adler M, Finkler C, Huwyler J, Schmidt R, Mahler HC, Koulov AV. Factors Governing the Precision of Subvisible Particle Measurement Methods - A

Case Study with a Low-Concentration Therapeutic Protein Product in a Prefilled Syringe. Pharm Res 2016;33(2):450-461.

27. Filipe V, Hawe A, Carpenter JF, Jiskoot W. Analytical approaches to assess the degradation of therapeutic proteins. Trends Analyt Chem 2013;49:118-125.

28. Song Y, Zhang J, Li D. Microfluidic and nanofluidic resistive pulse sensing: A review. Micromachines 2017;8(7):204.

29. Maxwell JC. *A treatise on electricity and magnetism, 3rd ed*., New York: Dover Publications, Inc.; 1954:419-425.

30. Fraikin J-L, Teesalu T, McKenney CM, Ruoslahti E, Cleland AN. A high-throughput label-free nanoparticle analyser. Nat Nanotechnol 2011;6:308.

31. Barnett GV, Perhacs JM, Das TK, Kar SR. Submicron Protein Particle Characterization using Resistive Pulse Sensing and Conventional Light Scattering Based Approaches. Pharm Res 2018;35(3):58.

32. Varypataki EM, van der Maaden K, Bouwstra J, Ossendorp F, Jiskoot W. Cationic Liposomes Loaded with a Synthetic Long Peptide and Poly(I:C): a Defined Adjuvanted Vaccine for Induction of Antigen-Specific T Cell Cytotoxicity. AAPS J. 2015;17(1):216-226.

33. Lewis CL, Craig CC, Senecal AG. Mass and density measurements of live and dead Gram-negative and Gram-positive bacterial populations. Appl Environ Microbiol 2014;80(12):3622-3631.

34. Malvern Panalytical. 2016 D90, D50, D10, and span – for DLS? Available at: http://www.materials-talks.com/blog/2016/08/25/d90-d50-d10-and-span-for-dls/. Accessed March 23, 2018

35. Engelsman JD, Kebbel F, Garidel P. Laser light scattering-based techniques. In Mahler H-C, Jiskoot W, eds. *Analysis of Aggregates and Particles in Protien Pharmaceuticals, ed.,* New Jersey, USA: John Wiley & Sons.; 2012:43-49.

36. Foley JP. Resolution equations for column chromatography. Analyst 2012;116(12):1275-1279.

37. Bard AJ, Faulkner LR. *Electrochemical methods: Fundamentals and applications. ed*., Wiley.; 2000

38. Nejadnik MR, Jiskoot W 2015. Measurement of the average mass of proteins adsorbed to a nanoparticle by using a suspended microchannel resonator. J Pharm Sci 104(2):698-704.

39. Yguerabide J, Yguerabide EE. Light-scattering submicroscopic particles as highly fluorescent analogs and their use as tracer labels in clinical and biological applications: I. theory. Anal Biochem. 1998;262(2):137-156.

40. Pal AK, Aalaei I, Gadde S, Gaines P, Schmidt D, Demokritou P, Bello D. High resolution characterization of engineered nanomaterial dispersions in complex media using tunable resistive pulse sensing technology. ACS Nano 2014;8(9):9003-9015.

41. Anderson W, Kozak D, Coleman VA, Jamting AK, Trau M. A comparative study of submicron particle sizing platforms: accuracy, precision and resolution analysis of polydisperse particle size distributions. J Colloid Interface Sci 2013;405:322-330.

42. Kestens V, Bozatzidis V, De Temmerman P-J, Ramaye Y, Roebben G. Validation of a particle tracking analysis method for the size determination of nano- and microparticles. J. Nanoparticle Res 2017;19(8):271.

43. Vasudev R, Mathew S, Afonina N. Characterization of submicron (0.1-1 mum) particles in therapeutic proteins by nanoparticle tracking analysis. J Pharm Sci 2015;104(5):1622-1631.

44. Maas SLN, de Vrij J, van der Vlist EJ, Geragousian B, van Bloois L, Mastrobattista E, Schiffelers RM, Wauben MHM, Broekman MLD, Nolte-'t Hoen ENM. Possibilities and limitations of current technologies for quantification of biological extracellular vesicles and synthetic mimics. J Control Release 2015;200:87-96.

45. Yu ACS, Loo JFC, Yu S, Kong SK, Chan T-F. Monitoring bacterial growth using tunable resistive pulse sensing with a pore-based technique. Appl Microbiol Biotechnol 2014;98(2):855-862.

46. Cermak N, Becker JW, Knudsen SM, Chisholm SW, Manalis SR, Polz MF. Direct single-cell biomass estimates for marine bacteria via Archimedes' principle. ISME J 2016;11:825.

47. Schleifer K-H. Phylum XIII. Firmicutes Gibbons and Murray 1978, 5 (Firmacutes [sic] Gibbons and Murray 1978, 5). In De Vos P, Garrity GM, Jones D, Krieg NR, Ludwig W, Rainey FA, Schleifer K-H, Whitman WB, editors. *Bergey's Manual® of Systematic Bacteriology: Volume Three The Firmicutes, ed.,* New York, NY: Springer New York.; 2009:19-1317.

48. Cavicchi RE, Carrier MJ, Cohen JB, Boger S, Montgomery CB, Hu Z, Ripple DC. Particle shape effects on subvisible particle sizing measurements. J Pharm Sci 2017;104(3):971-987.

Supplementary materials
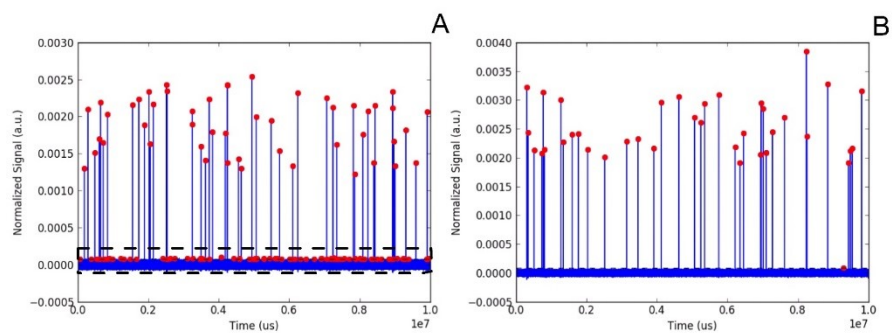
Supplementary figure S1: Output signal versus time for PS1030nm suspended in Na_2HPO_4 solution with low Na_2HPO_4 concentration (5mM) (A) and high Na_2HPO_4 concentration (150mM) (B). Events marked with red circle represent particle detection. Selected events in the dashed black rectangle represent detected false-positive events.

Supplementary table S1: Characterization of mono- and multimodal dispersions of beads using DLS, NTA, RMM and MRPS

Technique	PS beads	Mean diameter (nm)	Peak start (nm)	Peak max (nm)	Peak end (nm)	FWHM (nm)	R_s
DLS	Mono PS297nm	337 ± 5	181 ± 15	342 ± 0	647 ± 56	249 ± 21	
	Mono PS495nm	561 ± 3	326 ± 27	531 ± 0	1006 ± 88	382 ± 37	-
	Mono PS799nm	879 ± 5	615 ± 0	825 ± 0	1281 ± 0	467 ± 7	
	Multi	833 ± 8	507 ± 41	825 ± 0	1348 ± 117	508 ± 38	
NTA	Mono PS297nm	289 ± 2	181 ± 66	288 ± 5	391 ± 37	70 ± 21	
	Multi PS297nm	282 ± 19	235 ± 17	285 ± 0	338 ± 25	45 ± 17	1.38
	Mono PS495nm	432 ± 5	301 ± 15	451 ± 23	561 ± 30	86 ± 39	
	Multi PS495nm	459 ± 19	391 ± 25	455 ± 0	535 ± 36	71 ± 18	
RMM	Mono PS495nm	511 ± 1	440 ± 0	480 ± 0	517 ± 3	35 ± 1	
	Multi PS495nm	502 ± 1	433 ± 5	470 ± 0	513 ± 6	39 ± 4	3.56
	Mono PS799nm	830 ± 6	720 ± 17	760 ± 0	810 ± 0	33 ± 4	
	Multi PS799nm	812 ± 2	727 ± 6	760 ± 0	810 ± 0	37 ± 6	
MRPS	Mono PS297nm	296 ± 15	258 ± 15	285 ± 17	355 ± 10	50 ± 8	
	Multi PS297nm	260 ± 11	261 ± 11	251 ± 6	311 ± 23	43 ± 8	2.41
	Mono PS495nm	499 ± 34	438 ± 30	498 ± 47	578 ± 37	77 ± 9	
	Multi PS495nm	466 ± 20	401 ± 15	428 ± 12	498 ± 20	59 ± 14	
	Mono PS799nm	799 ± 15	765 ± 20	792 ± 12	832 ± 15	37 ± 10	4.71
	Multi PS799nm	801 ± 43	772 ± 42	798 ± 38	832 ± 49	34 ± 5	

Supplementary table S2: Span of particle size distribution of PS beads and liposomes measured with MRPS and NTA. Mean values and standard deviations of triplicate measurements (n=3)

Technique	PS297nm beads	Liposomes
	Span	
MRPS	0.33 ± 0.01	1.12 ± 0.04
NTA	0.25 ± 0.06	0.67 ± 0.01

Chapter 3

Electrolyte induced formation of submicron particles in heat stressed monoclonal antibody and implications for analytical strategies

Andreas Stelzl[1], Adam D. Grabarek[2,4], Stefan Schneid[3], Wim Jiskoot[2,4], Tim Menzen[2], Gerhard Winter[1]*

[1]*Pharmaceutical Technology and Biopharmaceutics, Ludwig-Maximilians Universität München, Germany*

[2]*Coriolis Pharma Research GmbH, Fraunhoferstr. 18 b, 82152 Martinsried, Germany*

[3]*Bayer AG, Pharmaceuticals, Formulation Development Parenterals, Friedrich-Ebert-Str. 475, 42096 Wuppertal, Germany*

[4]*Leiden Academic Centre for Drug Research, Leiden University, The Netherlands*

Abstract

Within this study, the performance and limitations of tunable resistive pulse sensing (TRPS) was evaluated to characterize submicron particles in unstressed and heat stressed monoclonal antibody (mAb) solutions. These were compared with microfluidic resistive pulse sensing (MRPS), resonant mass measurement (RMM), and nanoparticle tracking analysis (NTA). For TRPS and MRPS measurements, adjustment of ionic strength was required but seen critical for protein formulations. Influences of sodium chloride concentration and pH on colloidal stability with respect to submicron particle levels were investigated.

Heat stress caused a sharp increase in particle levels between 250-900 nm, observable in all four techniques. Due to reduced colloidal stability, indicated by increased attractive forces and reduced aggregation onset temperatures in the presence of sodium chloride, protein aggregation was observed in heat stressed mAb only after the addition of sodium chloride. Achieving adequate ionic strength by replacing sodium chloride with other electrolytes similarly resulted in reduced colloidal stability and protein aggregation. It is recommended that protein samples prone for aggregation in the presence of high ionic strength should not be analyzed by RPS measurements after the addition of electrolytes. However, protein samples containing already required ionic strength can be analyzed by any of the four techniques.

Introduction

Biopharmaceuticals, such as monoclonal antibodies, can undergo several routes of degradation due to the complexity of the molecules[1,2]. Among other degradation pathways, the formation of protein aggregates can be detrimental for product quality[3]. Submicron aggregates, despite being often overlooked, are an important category of aggregates due to their potential role in protein immunogenicity[4,5]. However, submicron particle analysis in biopharmaceutical products in the size range of $0.1 - 1$ µm is increasingly expected by regulatory agencies[6]. Resonant mass measurement (RMM) and nanoparticle tracking analysis (NTA) are two commonly used methods to quantify the particle level in the submicron size range, but both come with certain drawbacks[7]. NTA is able to detect particles between $50 - 1000$ nm based on the scattering of light and is therefore biased towards larger particles if heterogeneous particle populations are measured[7]. Depending on the used sensor, RMM is able to detect particles between $100 - 4000$ nm based on their mass, which is then converted it into particle size based on the density of the particle and the density of the fluid[7]. Due to differences in particle detection and subsequent differences in particle characterization, the comparison of results obtained by RMM or NTA can be difficult. For example, a difference of 1-2 orders of magnitude in particle concentration was observed for the same sample when analyzed with both techniques[8]. Additionally, a low reproducibility in particle sizing and quantification compared to established micrometer-sized particle analysis techniques is reported[8].

Owing to improvements in micro- and nano-fabrication[9,10], resistive pulse sensing (RPS) was introduced as new technique for submicron particle analysis. Hereby, the detection of particles in solutions relies on the Coulter counter principle (electrical sensing zone), which detects particles based on changes in the electric field between two electrodes upon particle passage through a sensing orifice[11], thereby overcoming technical limitations of RMM and NTA as discussed above. Studies have shown great accuracy of RPS in characterizing concentration and size of polystyrene bead mixtures or exosomal vesicles, giving RPS a potential advantage over other techniques[12,13].

With tunable resistive pulse sensing (TRPS, IZON Ltd., Christchurch, New Zealand) and microfluidic resistive pulse sensing (MRPS, Spectradyne LLC., Torrance, CA, USA) two RPS-based instruments are currently available for submicron particle characterization. TRPS uses a stretchable nanopore and MRPS a microfluidic channel to create a nano-constriction, which separates both electrodes and can therefore be used as sensing zone. Despite their structural differences, both techniques rely on sufficient ionic strength present in the sample solution[11,14] in order to establish a stable electric current between both electrodes. Thus, particles are detected as drop in electrical resistance by crossing the nano-constriction between both electrodes. For samples with low conductivity, it is recommended to add electrolytes during sample preparation by i.e., dilution in phosphate buffered saline (PBS)[14-16] or by spiking-in electrolytes from a stock solution.

Applicability of RPS for different biopharmaceutical samples including protein formulations was previously presented[17]. In the present study, we investigated the comparability of TRPS to other submicron particle measurement techniques, namely RMM, NTA and MRPS, for the analysis of biopharmaceuticals. Therefore, particle concentrations in the size ranges between 250 - 900 nm and 600 – 900 nm present in an unstressed and heat stressed monoclonal antibody (mAb) formulation were evaluated by using the four instruments and the results were compared. Additionally, the effect of adding electrolytes to (un-)stressed protein formulations prior to particle analysis on the formation of sub-micron proteinaceous particles was critically investigated. A guide to choose a suitable submicron particle characterization technique for biopharmaceuticals based on the conductivity of the samples concludes the paper.

Materials and Methods

Materials

Calcium chloride, glacial acetic acid, L-arginine hydrochloride, L-lysine monohydrochloride, L-methionine, polysorbate 80, sodium acetate, sodium chloride (NaCl), sodium sulfate, and sucrose were purchased from Merck KGaA (Darmstadt, Germany). L-histidine, L-histidine monohydrochloride monohydrate and sodium succinate hexahydrate were purchased from

Alfa Aesar (Kandel, Germany). Magnesium chloride hexahydrate, monosodium phosphate dihydrate, and potassium chloride were obtained from Applichem (Darmstadt, Germany). Citric acid was obtained from USBiological Life Sciences (Hamburg, Germany), disodium phosphate dihydrate from Bernd Kraft (Duisburg, Germany), and sodium citrate from Caesar&Lorentz GmbH (Hilden, Germany). In-house highly purified water (conductivity 0.055 µs/cm) was dispensed from an Arium®Pro purification system (Sartorius, Göttingen, Germany). All diluents used in the study were freshly filtered through a 0.02-µm Anotop 25 syringe filter (Anopore membrane, Whatman, Maidstone, UK).

A mAb (Bayer AG, Leverkusen, Germany), belonging to the IgG1 subclass in 10 mM histidine buffer at pH 5.5 with 130 mM glycine, 5% sucrose, 20 mM methionine, and 0.05% polysorbate 80 was used as model protein. The identical formulation not containing the mAb was used as placebo throughout the study. Different formulations of mAb at pH 4.5 and pH 6.5 were prepared via dialysis at room temperature by using a Spectra/Por® 8000 MWCO dialysis tubing (Spectrum laboratories Inc., Rancho Dominguez, USA). A 100-fold excess of the respective histidine/glycine based formulation was used and media exchanges were performed 2 h and 4 h after the start of the dialysis. Dialysis was performed for a total duration of 24 h.

Coating solution and calibration beads (350 nm, polystyrene) for TRPS measurements were purchased from IZON Ltd. (Oxford, UK) and calibration beads for MRPS (496 nm, polystyrene) and RMM (994 nm, polystyrene) were obtained from Fisher Scientific (Ulm, Germany).

Preparation of proteinaceous particles

All mAb solutions were filtered through a 0.22-µm polyethersulfone (PES) syringe filter prior to use. To generate heat stressed samples, the mAb solution was incubated at 50 °C for 72 h (Eppendorf Thermomix, Hamburg, Germany). Prior to analysis, heat stressed and unstressed samples were diluted to 5 mg/mL mAb concentration by using 0.02-µm filtered placebo solution. The diluted samples were subsequently filtered through a 5-µm PES membrane filter in order to remove large aggregates, if any, which may cause blockages

during submicron particle analysis. Furthermore, the samples were aliquoted for particle analysis and individually spiked with 1 M sodium chloride (0.02-µm filtered) stock solution to a target concentration of 50 mM sodium chloride (e.g., 190 µL sample + 10 µL electrolyte) prior to analysis. Analysis on all four submicron particle characterization techniques as well as micrometer-sized particle analysis were performed within a single working day, but particle analysis was performed not later than 2 min after the addition of sodium chloride to each individual aliquot.

Evaluation of electrolytes to increase conductivity in low-ionic-strength samples for RPS

Stock solutions of eight different electrolytes, $CaCl_2$, KCl, $MgCl_2$, NaCl, Na_2SO_4, histidine buffer pH 6.0, citrate buffer pH 6.0, and phosphate buffer pH 6.0 were prepared as spiking solutions. Concentrations were chosen to reach a conductivity of 4.5 mS/cm after 20-fold dilution and the respective values are given in Table 2. Ten microliter electrolyte stock solution or placebo were added to 190 µL 0.22-µm filtered (PES-membrane) mAb at 5 mg/mL. Because of solubility limits of histidine, required at a relatively high concentration due to low conductivity of histidine solutions, the histidine stock solution was prepared at 450 mM and 20 µL were spiked into 40 µL 5 mg/mL mAb, accounting for a 3-fold dilution of histidine solution. Aggregation onset temperatures were analyzed by using a Prometheus NT.48.

Additionally, submicron particles were characterized by using RMM and NTA after spiking 200 µL placebo, 150 mM sodium chloride, or 450 mM histidine to 400 µL unstressed or heat stressed mAb to investigate the aggregation behavior of the heat stressed mAb in the presence of a high histidine concentration instead of sodium chloride.

Table 2: Conductivity and solute concentration at 4.5mS/cm for various excipients.

Substance class	Electrolyte	Measured conductivity at 50 mM	Calculated concentration at 4.5 mS/cm
		[mS/cm]	[mM]
Inorganic salt	$CaCl_2$	2.1	109.2
	KCl	6.2	36.1
	$MgCl_2$	2.2	104.2
	NaCl	4.5	50.0
	Na_2SO_4	8.5	26.6
Buffer component	Citrate buffer, pH 6.0	8.6	26.2
	Histidine buffer, pH 6.0	1.5	150.0
	Phosphate buffer, pH 6.0	2.4	93.4

Tunable resistive pulse sensing (TRPS)

Submicron particles were analyzed by tunable resistive pulse sensing (TRPS) on a qNano Gold system (IZON, Oxford, UK). A nanopore NP300 with an analysis range of 150 - 900 nm was fitted to the qNano Gold system and submicron particle counts were recorded and evaluated in a similar manner as in our previous study (manuscript in preparation). Three technical replicates per sample were measured.

Microfluidic resistive pulse sensing (MRPS)

A nCS1 system equipped with disposable TS-900 (125 – 900 nm) polydimethylsiloxane cartridges (Spectradyne, Torrance, CA, USA) was used for MRPS measurements. Phosphate buffered saline at pH 7.4 containing 1% polysorbate 20 was used as running buffer to generate an appropriate electrical current. For each sample, the loading volume was 3 μL and at least 500 particles were recorded per measurement. Three technical replicates per sample were analyzed. Size calibration with polystyrene beads (496 nm) was performed for each cartridge after a sample measurement to ensure appropriate sizing. False-positive signals were excluded in data analysis (Data Analysis software V2.4.0.202, Spectradyne) by

applying filters based on transit time, signal-to-noise ratio, peak symmetry, and/or diameter, following the manufacturer's recommendation.

Resonant mass measurement (RMM)

An Archimedes system equipped with a Hi-Q Micro sensor (Malvern Instrument, Malvern, UK) was used for RMM. The system was calibrated with polystyrene beads (994 nm) prior to each set of measurements. Between each sample measurement, 2 sneeze operations were performed, and the system was flushed with highly purified water to ensure system cleanliness. The lower limit of detection (LOD) was determined automatically by ParticleLab software version 2.01. Density was set to 1.05 g/cm³ for polystyrene beads and to 1.34 g/cm³ for protein particles. Only negatively buoyant particles and measurements with at least 50 particle counts were used for data evaluation. Three sub-runs were performed per measurement. Three technical replicates were measured of each sample, yielding nine replicates in total.

Nanoparticle tracking analysis (NTA)

A NanoSight (Model LM20, Malvern Instrument, Malvern, UK) was used to obtain NTA data at a wavelength of 405 nm (blue laser). Purging volume of the sample chamber was 0.3 mL. By using a video capture, three sub-runs of 60 s each were performed per measurement immediately after injection at room temperature. Three technical replicates were measured of each sample, yielding nine replicates in total. The camera levels were set to optimal values and 200 valid tracks were defined as lower limit for valid measurements. NanoSight software version 3.2 was used for data evaluation.

Dynamic light scattering (DLS)

Aggregation onset temperature ($T_{agg,onset}$) and diffusion interaction parameter (k_D) measurements were performed by using a DynaPro plate reader III (Wyatt, Santa Barbara, CA, USA) with a sample volume of 20 µL in 384-well plates (Corning Inc., Corning, NY, USA). Prior to analysis, samples were centrifuged at 2000 g for 2 min and sealed with 5 µL silicone oil to prevent evaporation and centrifuged again for 2 min at 2000 g.

k_D was determined in duplicate with 3-10 mg/mL mAb and different sodium chloride concentrations ranging from 0-150 mM. The diffusion coefficient was obtained from 20 acquisitions at 5 s/acquisition with the attenuation level set to Auto at 25 °C. k_D was evaluated by using Dynamic V7.8.2 software.

$T_{agg,onset}$ of the mAb was determined in formulations containing 5 mg/mL mAb (0.22-μm PES membrane filtered) at pH 4.5, 5.5, or 6.5 after adding 0, 50, and 150 mM sodium chloride. Samples were equilibrated at 25 °C and temperature was increased linearly to 85 °C at a rate of 0.1 °C/min. DLS was measured and each data point was recorded with 3 acquisitions of 3 s per acquisition with the attenuation level set to Auto. $T_{agg,onset}$ was determined in Dynamics V7.8.2 software.

Temperature of aggregation

A Prometheus® NT.48 (NanoTemper Technologies, Munich, Germany) was used to study thermal unfolding and aggregation of mAb formulations. Standard glass capillaries (NanoTemper) were filled with the respective formulation and placed in the Prometheus NT.48 in duplicates. Temperature was ramped from 20 – 95 °C at 1 °C/min. Protein aggregation was detected by measuring the back-reflection intensity of a light beam passing twice through the capillary[18]. The aggregation onset temperature, $T_{agg,onset}$, was calculated with PR.ThermControl V2.1 software (NanoTemper) from the increase in scattering signal detected with the back-reflection optics.

Micrometer-sized particle (SVP) analysis

mAb samples were analyzed for the presence of micrometer-sized particles (sized within the range of 1 – 80 μm) with a FlowCam 8100 (Fluid Imaging Technologies, Inc., Scarborough, ME, USA). The system was equipped with a 10x magnification and a FOV80 flow-cell (80 μm × 700 μm). A sample volume of 150 μL was used for the analysis and the images were collected with a flow rate of 0.15 mL/min with an auto image frame rate of 28 frames/second. A distance of 3 μm to the nearest neighbor and thresholds of 10 and 13 for light and dark pixels, respectively, were used for particle detection. Particle size was

reported as equivalent spherical diameter (ESD) by using VisualSpreadsheet® 4.7.6 software for data collection and evaluation.

Size exclusion chromatography (SEC)

A Dionex Ultimate 3000 system (Thermo Scientific, Dreieich, Germany) was used for SEC. Ten microgram of mAb were injected on a Waters Acquity UPLC® Protein BEH SEC column, 200Å, 1.7 µm, 4.6 × 150 mm column (Waters Corporation, Milford, MA, USA) and the elution of the protein was detected at 280 nm with a VWD-3400RS UV detector (Thermo Fisher, Dreieich, Germany). The running buffer consisted of 50 mM sodium phosphate (pH 6.5) with 300 mM sodium chloride at a flowrate of 0.3 mL/min. The chromatograms were integrated with Chromeleon V7.2 (Thermo Fisher) and the relative area of the high-molecular-weight species (i.e., small soluble aggregates) was calculated in percentage.

Viscosity

The viscosity of the prepared samples was measured by a mVROC viscometer (Rheosense Inc., San Ramon, CA, USA) using a RA05-100-087 flow cell with a 50 µm flow channel at 20 °C. Prepared samples were filled into a 250-µL Hamilton syringe, without introducing any air bubbles. All measurements were performed at a flow rate of 250 mL/min and a corresponding shear rate of 3160 s^{-1}. Control software V2.6 was used for data recording.

Protein concentration

Protein concentration was determined on a NanoDrop One (Thermo Scientific) by measuring the absorbance at 280 nm with a baseline subtraction at 340 nm. Protein concentrations were calculated using a mass extinction coefficient of 13.7 at 280 nm for a 1% w/v IgG solution.

Conductivity measurements

Electric conductivity of samples was measured in triplicate at 20 °C by using an Inolab Cond Level 2 P conductivity meter equipped with a TetraCon 325 electrode (WTW, Weilheim, Germany) calibrated with a 100 µS/cm standard.

Results and discussion

Comparison of submicron particle characterization techniques

Submicron particle concentrations in placebo, unstressed and heat stressed protein (5 mg/mL mAb) samples were determined by using four different submicron particle characterization techniques. Particle size distributions were compared as obtained and particle concentrations were compared in the ranges between 250 - 900 nm and 600 - 900 nm.

Particle size distribution

The average particle size distributions of three replicates measured for unstressed and heat stressed mAb with any of the four particle characterization methods are shown in Figure 1. A bin size of 10 nm was applied to the obtained data for all four methods, however, the scale of the y-axis was varied in order to compare the observed particle size distributions due to differences in the observed particle concentration between the four analytical methods as discussed in section 0. Quantitative descriptors of the particle size distributions of unstressed and heat stressed mAb as such as mean diameter, mode of the peak and D10/D50/D90 values, corresponding to the diameters below which 10%, 50% and 90% of the particles are measured, are provided in

Table 3[19,20]. TRPS and MRPS measurements revealed a narrow particle size distribution with the vast majority of particles detected below 400 nm. RMM revealed substantial particle concentrations for particles above 600 nm, which were hardly detected with both RPS techniques. However, the high LOD values determined with heat stressed mAb samples resulted in no detected particles below 500 nm. Placebo and unstressed samples resulted in much lower LOD values in RMM measurements compared to heat stressed mAb formulations, however no particles below 250 nm were detected. NTA showed the broadest size distribution ranging from 150 nm to 900 nm with a large fraction of particles being larger than 400 nm.
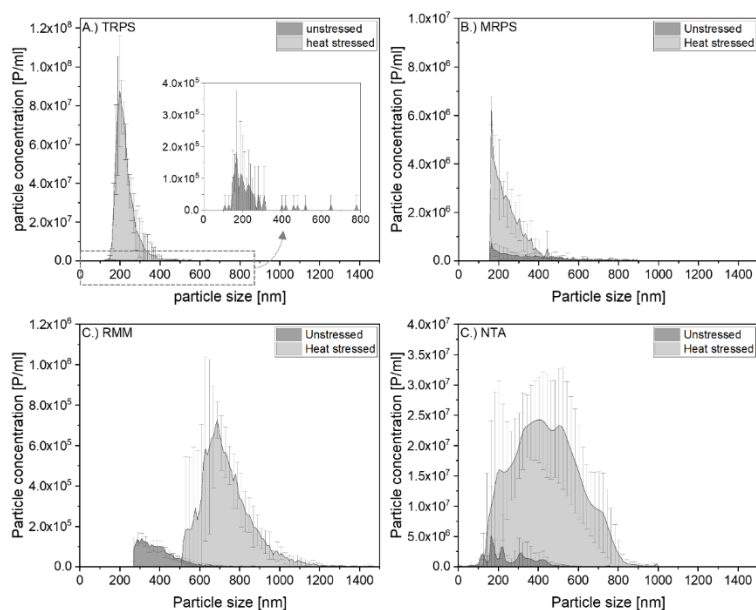
Figure 1: Particle size distribution of unstressed and heat stressed mAb formulation determined by A.) TRPS, B.) MRPS, C.) RMM, and D.) NTA. Error bars represent mean ± standard deviation (10 nm bin size) of three technical replicates. Samples were analyzed at 5 mg/mL protein concentration, except for RMM analysis of heat stressed mAb (2.5 mg/mL). All samples were spiked with 50 mM sodium chloride prior to particle analysis.

Table 3: Quantitative descriptors of the particle size distributions of unstressed and heat stressed mAb formulation

		Mean diameter	Mode	D10*	D50*	D90*
		[nm]	[nm]	[nm]	[nm]	[nm]
Unstressed	TRPS	232	170	150	195	305
	MRPS	358	165	170	305	625
	RMM	369	290	280	350	470
	NTA	258	165	125	225	410
Heat stressed	TRPS	226	200	175	210	280
	MRPS	250	165	165	225	355
	RMM	733	690	590	710	890
	NTA	441	405	225	430	655

* D10/D50/D90 correspond to the diameters below which 10%, 50% and 90% of the particles are measured

Particle concentration in the size ranges 250-900 nm and 600-900 nm

The comparison of particle concentrations for placebo, unstressed and heat stressed mAb formulations obtained by the four different techniques is shown in Figure 2 and Figure S1 (supplementary data). In contrast to Hubert et al.[8], particle concentrations were compared in the limited size ranges from 250 nm to 900 nm and 600 nm to 900 nm, to eliminate biases due to different size ranges inherent to the four methods.

All submicron particle characterization techniques detected an increase in particle concentration after three days of heat stress at 50 °C compared to an unstressed protein control (Figure 2 and Supplementary figure S1). A narrow standard deviation of the analyzed replicates indicated a high precision in concentration determination for all four methods. However, absolute particle concentrations differed between the four measurement techniques. Between $250 - 900$ nm, MRPS and TRPS detected particle concentrations of 6.5×10^7 and 2.0×10^8 particles/mL in heat stressed mAb samples, respectively, whereas no increase in particle concentration was observed in the size range from $600 - 900$ nm. In the $250 - 900$ nm size range, particle concentration in heat stressed mAb samples was highest in NTA with 9.6×10^8 particles/mL and lowest in RMM with 2×10^7 particles/mL. Both methods also detected a significant increase in particle levels in the size range above 600 nm. Overall, particle levels in heat stressed mAb samples detected by NTA were found to be 7.5- to 30-fold higher than particle levels obtained by RMM in the size ranges from 600 nm to 900 nm and 250 nm to 900 nm, respectively. An increase in particle concentration after heat stress in the $250 - 900$ nm size range was observed with a minimum of 3-fold in RMM and up to 35-fold in NTA compared to the unstressed mAb samples. In the size range from 600-900 nm, the difference in particle concentration between unstressed and heat stressed mAb was up to three orders of magnitude.

In general, placebo formulations showed the lowest particle concentrations with up to two orders of magnitude lower concentrations measured than in unstressed protein samples. However, especially for clean samples, particle concentrations and particle size distributions relied on less than 50 detected particles for TRPS and RMM. In placebo samples, for example, less than 10 particles were typically detected within a measurement time of

10 min (TRPS) or in a measurement volume of 150 nL (RMM). After heat stress, all results derived from any of the four instruments relied on at least 500 particles per measurement for evaluation of the particle size distribution and the particle concentration.

The substantial differences in the submicron particle levels in stressed formulations detected by the four techniques was not only influenced by a high LOD value in RMM, as described in the previous section, but also by differences in particle detection between the methods[7]. For example, differences in particle concentration between RMM and NTA have been reported previously for various protein formulations with higher particle concentrations being detected in NTA, whereas RMM and MRPS showed only minor differences in particle concentration in stressed BSA samples[8,17,22,24]. Comparability of the particle concentrations obtained by either of the four methods is restricted by the underlying physical parameters that are used to detect particles in solution. Additionally, an adjustment of the ionic strength was required for TRPS and MRPS measurements, but is seen critical for protein formulations. Influences of sodium chloride concentration and pH on colloidal stability with respect to submicron particle formation was therefore investigated.
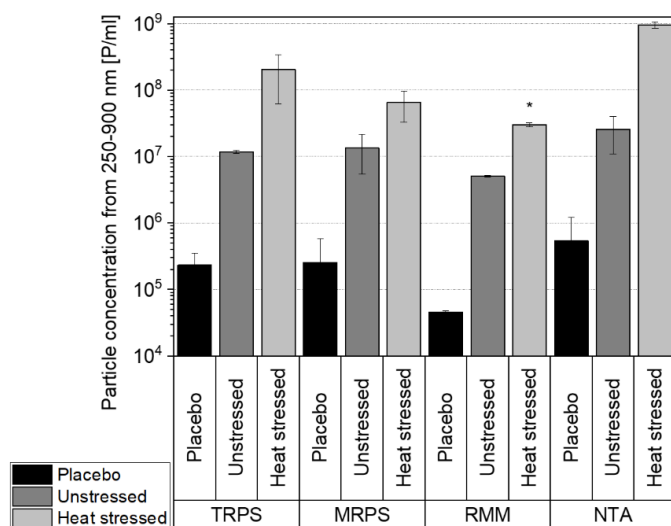
Figure 2: Comparison of particle concentrations in the size range from 250-900 nm measured by four submicron particle characterization techniques for placebo, unstressed and heat stressed mAb formulations. Error bars represent mean ± standard deviation of three technical replicates. * Particle concentration was analyzed at 5 mg/mL protein concentration, except for RMM analysis of heat stressed mAb (2-fold diluted sample was analyzed and particle concentration was corrected for dilution afterwards). All samples were spiked with 50 mM sodium chloride prior to particle analysis.

Dimers, oligomers and micrometer-sized particles

Particle concentrations in a size range above 1 µm were measured with flow imaging microscopy (Supplementary figure S2). Total particle concentrations in placebo and unstressed mAb samples were below 400 particles/mL above 1 µm. A slight increase to 1200 particles/mL was detected after heat stress.

The content of dimers and oligomers (Supplementary figure S2) as well as viscosity (1.4 ± 0.1 mPas) and protein concentration remained unchanged after heat stress.

Sodium chloride-induced aggregation through spiking to heat stressed mAb

The addition of electrolytes can be necessary to provide sufficient ionic strength for both RPS methods to achieve reliable results[17]. To investigate the effect of adding electrolytes,

RMM and NTA were used to analyze the submicron particle concentration in samples with and without electrolyte addition (Figure3). Increasing ionic strength in unstressed mAb samples resulted in no change in submicron particle concentration in NTA measurements and only in a minor increase in particle concentration in RMM measurements. The addition of sodium chloride to heat stressed samples led to immediate particle formation, resulting in a 25-fold increase in particle concentration in RMM measurements for the entire size range measured. In NTA, the particle concentration in heat stressed mAb without sodium chloride spiking was already close to the upper limit of the measurement range of 10^{10} particles/mL[23], but an increase was still observed upon addition of sodium chloride prior to particle analysis.

In order to understand the aggregation phenomenon in heat stressed mAb solutions after adding sodium chloride, protein interactions and thermal stability of the mAb was investigated. At pH 5.5, the mAb is positively charged (isoelectric point (IEP): 8.2) and thus net repulsive electrostatic forces inhibit attractive interactions and thus stabilize the molecules from forming aggregates. Shielding positive charges by ions has been found as a cause of protein aggregation[24]. We found that the k_D was only slightly negative with -7.5 mL/g at pH 5.5 (without sodium chloride), indicating weak attractive forces between antibody molecules (Figure 4)[25]. However, k_D rapidly dropped to more negative values upon addition of small amounts of sodium chloride. At 50 mM sodium chloride, the concentration needed for RPS measurements, k_D was reduced to -29 mL/g. The decrease in k_D in the presence of sodium chloride indicates an increase in net attractive protein interactions, probably because of a decrease in repulsive electrostatic interactions. The increase in attractive protein interactions is a likely cause for aggregation of the heat stressed mAb as discussed in the previous sections.

To further assess aggregation behavior of the mAb, $T_{agg,onset}$ was determined for antibody formulations at different pH values (pH 4.5, 5.5, and 6.5) and at different sodium chloride levels (0, 50, and 150 mM sodium chloride) by temperature-ramped DLS and Prometheus measurements. An increase in pH towards the IEP of the protein reduces the net-charge of the protein whereas decreasing pH results in higher net-charge[26]. Increased net-charge was

reported to show the highest degree of repulsion and the addition of sodium chloride was furthermore found to decrease repulsive forces (via charge shielding) for various antibodies[26]. We therefore hypothesize that at lower pH (i.e., higher net charge and therewith stronger repulsive forces between protein molecules), protein aggregation should occur at higher temperatures or at higher sodium chloride concentrations compared to mAb solutions at higher pH.

Without sodium chloride, aggregation was found only in pH 6.5 samples (Figure 5A), whereas aggregate formation was not observed at pH 4.5 and 5.5. Increasing the ionic strength by adding 50 mM sodium chloride led to aggregation in pH 5.5 and 6.5 samples (Figure 5B) with a $T_{agg,onset}$ reduced from > 95 °C and 76.5 °C to 76.3 °C and 72.6 °C, respectively. At pH 4.5 only a weak scattering signal was detected at 50 mM sodium chloride, suggesting that less aggregation occurred compared to the formulations at higher pH value. At a concentration of 150 mM sodium chloride (Figure 5C), the charge shielding effects of sodium chloride supposedly overpowered electrostatic repulsion between mAb molecules, resulting in aggregation in all samples to a comparable extent. Similar trends were found in $T_{agg,onset}$ determined by using DLS (supplementary data, Figure S3).

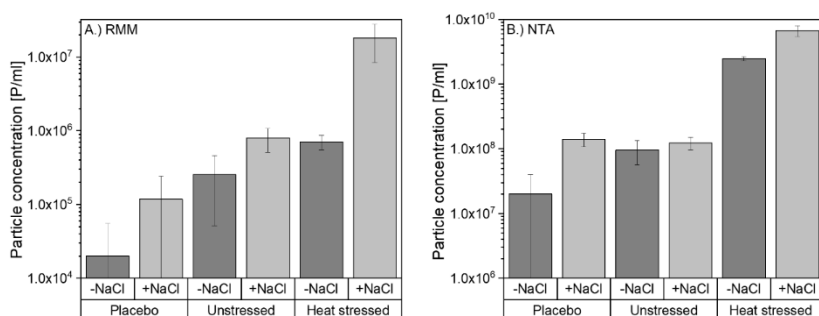*Figure 3: Submicron particle concentration with and without sodium chloride spiking, as determined by A.) RMM and B.) NTA. Mean ± standard deviation of triplicate measurements for the entire size range measured.*
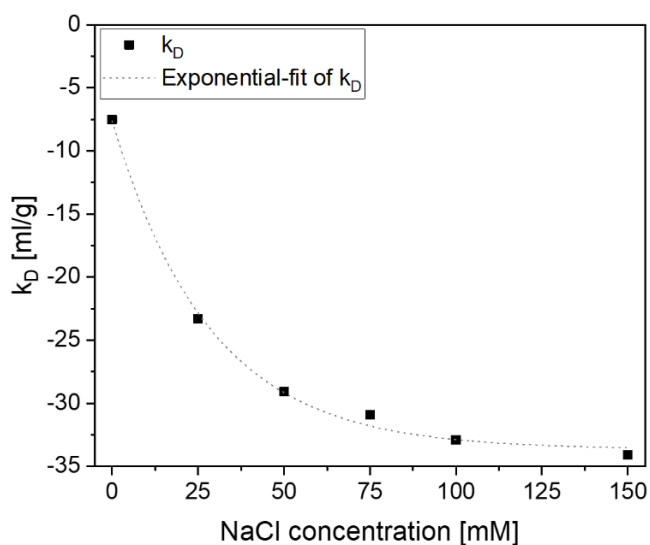
Figure 4: Dependence of kD as a function of sodium chloride concentration in the mAb formulation at pH 5.5.
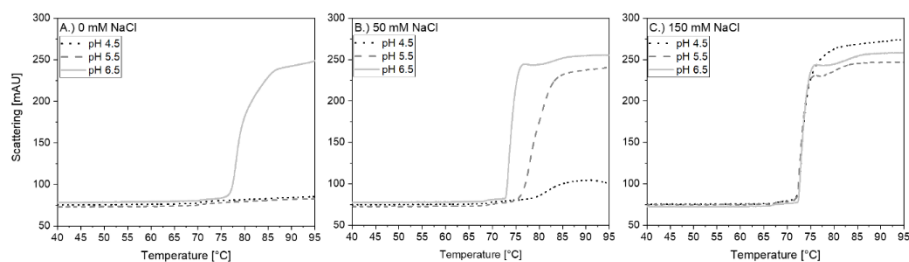

Figure 5: Scattering signal in Prometheus measurements at different formulation pHs and sodium chloride concentrations: A.) 0 mM sodium chloride, B.) 50 mM sodium chloride, C.) 150 mM sodium chloride.

Evaluation of other electrolytes as alternative to sodium chloride

Addition of alternative electrolytes, which provide sufficient conductivity to allow submicron particle analysis by using RPS without inducing so strong mAb aggregation, was evaluated. Tested electrolytes include inorganic salts and buffer components (Table 1).

All tested electrolytes showed a similar scattering signal compared to sodium chloride with aggregation onset temperatures ranging from 69.9 °C to 74.4 °C (Figure 6). None of the tested electrolytes revealed a significantly different result compared to sodium chloride.

The spiking of histidine, replacing sodium chloride as spiking solution, was investigated since histidine was already present in the formulation at a lower concentration. RMM and NTA measurements were conducted after spiking placebo, 150 mM sodium chloride, or 450 mM histidine into unstressed or heat stressed mAb formulation. Thereby, the conductivity was either unchanged when placebo was added to the sample or the conductivity was increased to a level suitable for both RPS techniques with an addition of 150 mM histidine or 50 mM sodium chloride to the sample after spiking with either of the electrolytes. Both, RMM and NTA, showed an increase in submicron particle concentration in heat stressed mAb samples in the presence of additional histidine (Figure 7). The behavior was similar to sodium chloride spiking: Particle formation was not observed when the conductivity was not changed by spiking in placebo solution, and particle formation was not observed in unstressed mAb upon addition of placebo, sodium chloride or histidine.
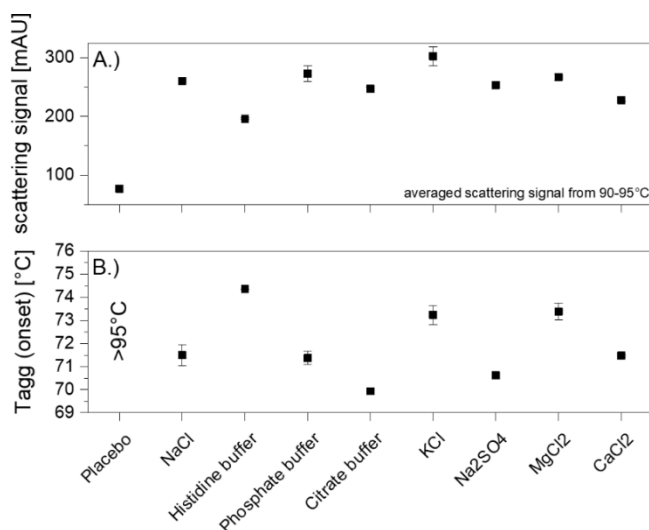

Figure 6: Aggregation of the mAb at pH 5.5 with different electrolytes at a conductivity of 4.5 mS/cm or placebo as control in Prometheus measurements. A.) Averaged light scattering signal in the temperature range from 90 °C to 95 °C, B.) Aggregation onset temperature.
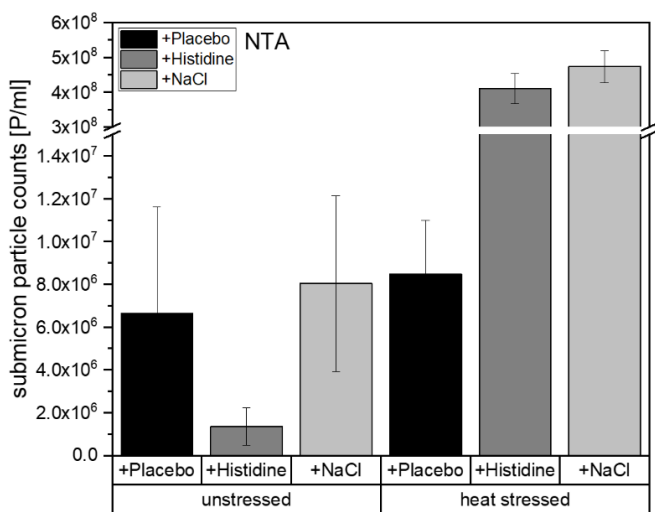
Figure 7: Submicron particle concentrations from NTA with placebo, histidine, or sodium chloride spiking to unstressed or heat stressed mAb. Mean ± standard deviation of triplicate measurements.

Conclusion and selection guide for submicron particle characterization methods

Four submicron particle characterization techniques were compared with regards to their capabilities of quantifying and characterizing submicron particles in proteinaceous samples. Based on previously published work[17], an electrical conductivity exceeding 3 mS/cm or 4.5 mS/cm is required for MRPS or TRPS measurements, respectively, and by spiking-in electrolytes from a stock solution, suitable measurement conditions could be achieved for samples of low ionic strength. A sharp increase in SMPs after three days of heat stress at 50°C compared to unstressed mAb samples was observed by each submicron particle characterization technique and replicates yielded in a narrow standard deviation indicating a high precision in concentration determination for all four methods. Predominantly smaller particles below 400 nm were detected by both RPS techniques, whereas a larger fraction of particles above 500 nm were detected in

RMM and NTA. A pronounced increase in submicron particle levels up to 2×10^7 to 1×10^9 particles per milliliter in the size range from $250 - 900$ nm was observed after heat stress, depending on the characterization technique. However, only a minor increase micrometer-sized particles and unchanged dimer and oligomer content were observed. SMP quantification during formulation development is therefore an important parameter to assess aggregation behavior of protein formulations without eventually waiting until aggregates have grown larger.

However, as a conductivity level of larger than 4.5 mS/cm is required for both RPS techniques, electrolyte addition was needed to meet this requirement. The addition of sodium chloride caused protein aggregation in heat stressed mAb samples due to reduced colloidal stability indicated by increased protein-protein interactions and decreased aggregation onset temperatures. The formation of submicron particles in heat stressed mAb samples was observed in RMM and NTA analysis after ionic strength adjustment compared to samples without addition of sodium chloride. The use of other inorganic salt or buffer components, such as histidine, for increasing ionic strength resulted in similar $T_{agg,\,onset}$ temperatures and submicron particle formation after spiking to heat stressed mAb samples. Therefore, the addition of electrolytes in order to increase conductivity of the sample for RPS measurement is not recommended.

Since RPS methods require a certain conductivity for particle detection, we recommend to first determine the conductivity of the sample and in case this complies with the mandatory requirements for RPS analysis, any of the four methods is suitable for submicron particle analysis[17]. If the requirements are not met, only RMM and NTA can be recommended for the quantification of submicron particles since the measurement principle is independent of the ionic strength, giving those two methods an advantage over RPS methods.

References:

1. Le Basle, Y., et al., Physicochemical Stability of Monoclonal Antibodies: A Review. J Pharm Sci, 2020. 109(1): p. 169-190.

2. Mahler, H.C., et al., Protein aggregation: pathways, induction factors and analysis. J Pharm Sci, 2009. 98(9): p. 2909-34.

3. Roberts, C.J., Protein aggregation and its impact on product quality. Curr Opin Biotechnol, 2014. 30: p. 211-7.

4. Kijanka, G., et al., Submicron Size Particles of a Murine Monoclonal Antibody Are More Immunogenic Than Soluble Oligomers or Micron Size Particles Upon Subcutaneous Administration in Mice. J Pharm Sci, 2018. 107(11): p. 2847-2859.

5. Moussa, E.M., et al., Immunogenicity of Therapeutic Protein Aggregates. J Pharm Sci, 2016. 105(2): p. 417-430.

6. U.S. Department of health and human services FDA (Center for Drug Evaluation and Research and Center for Biologics Evaluation and Research), Guidance for Industry: Immunogenicity Assessment for Therapeutic Protein Products. 2014.

7. Hawe, A., et al., Subvisible and Visible Particle Analysis in Biopharmaceutical Research and Development, in Biophysical Characterization of Proteins in Developing Biopharmaceuticals. 2015. p. 261-286.

8. Hubert, M., et al., A Multicompany Assessment of Submicron Particle Levels by NTA and RMM in a Wide Range of Late-phase Clinical and Commercial Biotechnology-Derived Protein Products. J Pharm Sci, 2019.

9. Song, Y., J. Zhang, and D. Li, Microfluidic and Nanofluidic Resistive Pulse Sensing: A Review. Micromachines (Basel), 2017. 8(7).

10. Kozak, D., et al., Advances in Resistive Pulse Sensors: Devices bridging the void between molecular and microscopic detection. Nano Today, 2011. 6(5): p. 531-545.

11. Rhyner, M.N., The Coulter principle for analysis of subvisible particles in protein formulations. AAPS J, 2011. 13(1): p. 54-8.

12. Anderson, W., et al., A comparative study of submicron particle sizing platforms: accuracy, precision and resolution analysis of polydisperse particle size distributions. J Colloid Interface Sci, 2013. 405: p. 322-30.

13. van der Pol, E., et al., Particle size distribution of exosomes and microvesicles determined by transmission electron microscopy, flow cytometry, nanoparticle tracking analysis, and resistive pulse sensing. J Thromb Haemost, 2014. 12(7): p. 1182-92.

14. Anderson, W., et al., Observations of Tunable Resistive Pulse Sensing for Exosome Analysis: Improving System Sensitivity and Stability. Langmuir, 2015. 31(23): p. 6577-87.

15. Vogel, R., et al., A standardized method to determine the concentration of extracellular vesicles using tunable resistive pulse sensing. J Extracell Vesicles, 2016. 5: p. 31242.

16. Maas, S.L., et al., Possibilities and limitations of current technologies for quantification of biological extracellular vesicles and synthetic mimics. J Control Release, 2015. 200: p. 87-96.

17. Grabarek, A.D., et al., Critical Evaluation of Microfluidic Resistive Pulse Sensing for Quantification and Sizing of Nanometer- and Micrometer-Sized Particles in Biopharmaceutical Products. J Pharm Sci, 2019. 108(1): p. 563-573.

18. Söltl F., et al., Analysis of formulation-dependent colloidal and conformational stability of monoclonal antibodies. 2016.

19. Allen, T., Particle Size Measurement, Volume 1: Powder Sampling and Particle Size Determination. 2003, Elsevier B.V.

20. Matteucci, M.E., et al., Drug Nanoparticles by Antisolvent Precipitation: Mixing Energy versus Surfactant Stabilization. Langmuir, 2006. 22.

21. Barnard, J.G., K. Babcock, and J.F. Carpenter, Characterization and quantitation of aggregates and particles in interferon-beta products: potential links between product quality attributes and immunogenicity. J Pharm Sci, 2013. 102(3): p. 915-28.

22. Yoneda, S., et al., Quantitative Laser Diffraction for Quantification of Protein Aggregates: Comparison With Resonant Mass Measurement, Nanoparticle Tracking Analysis, Flow Imaging, and Light Obscuration. J Pharm Sci, 2019. 108(1): p. 755-762.

23. Hawe, A., et al., Submicrometer, micrometer and visible particle analysis in biopharmaceutical research and development, in Biophysical Characterization of Proteins in Developing Biopharmaceuticals. 2020. p. 285-310.

24. Arosio, P., et al., On the role of salt type and concentration on the stability behavior of a monoclonal antibody solution. Biophys Chem, 2012. 168-169: p. 19-27.

25. Shi, S., et al., Method qualification and application of diffusion interaction parameter and virial coefficient. Int J Biol Macromol, 2013. 62: p. 487-93.

26. Lehermayr, C., et al., Assessment of net charge and protein-protein interactions of different monoclonal antibodies. J Pharm Sci, 2011. 100(7): p. 2551-62.
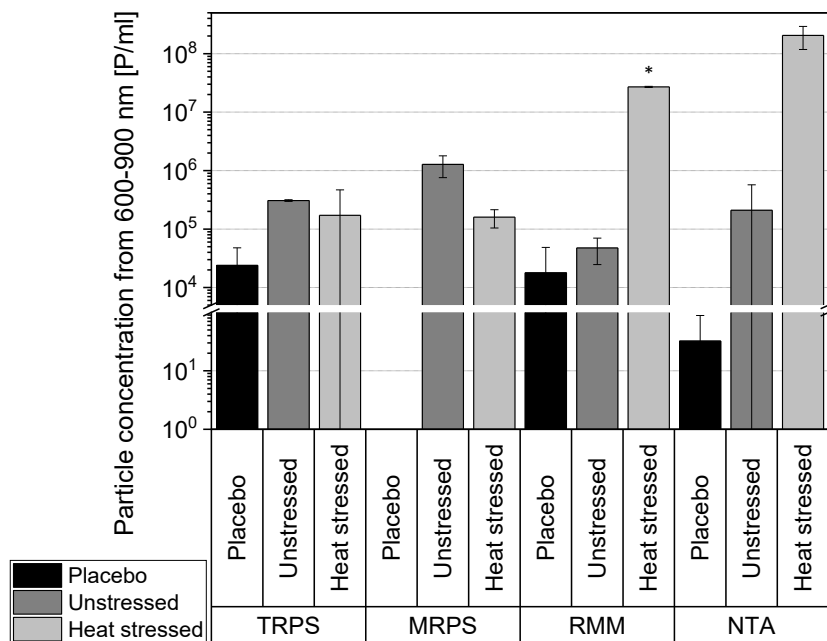
*Supplementary figure S1: Comparison of particle concentrations in the size range from 600-900 nm measured by four different submicron particle characterization techniques for placebo, unstressed and heat stressed mAb formulations. Error bars represent mean ± standard deviation of three technical replicates. * Particle concentration was analyzed at 5 mg/mL protein concentration, except for RMM analysis of heat stressed mAb (2-fold diluted sample was analyzed and particle concentration was corrected for dilution afterwards). All samples were spiked with 50 mM sodium chloride prior to particle analysis.*
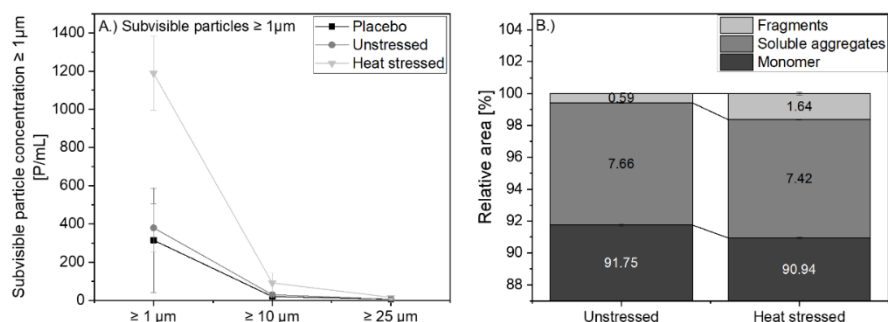
Supplementary figure S2: A.) Subvisible particle concentrations obtained by FlowCam analysis, B.) Relative area of monomers, soluble aggregates, and fragments obtained by size exclusion chromatography. Placebo and unstressed samples were measured at t0, heat stressed samples after 3 days at 50°C.
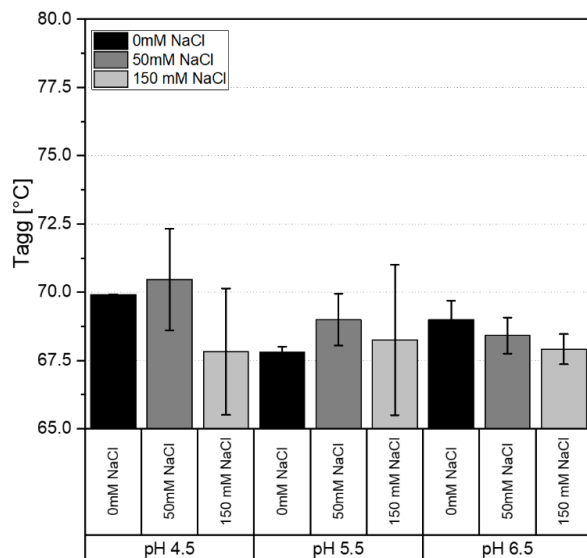
Supplementary figure S3: $T_{agg,\ onset}$ of the mAb at different formulation pHs and sodium chloride concentrations, as determined by using dynamic light scattering.

Chapter 4

Immunological evaluation in vitro of nanoparticulate impurities isolated from pharmaceutical-grade sucrose

Adam D. Grabarek*[1,2], Myriam Nabhan*[3], Isabella Turbica[3], Andrea Hawe[2], Marc Pallardy[3], Wim Jiskoot**[1,2]

[1]Coriolis Pharma, Fraunhoferstrasse 18 b, 82152 Martinsried, Germany

[2]Leiden Academic Centre for Drug Research, Leiden University, The Netherlands

[3]Inserm, Inflammation, Microbiome and Immunosurveillance, Université Paris-Saclay, Châtenay-Malabry, France

Equal contribution

**corresponding author*

Abstract

Sucrose is a commonly used stabilizing excipient in protein formulations. However, recent studies have indicated the presence of nanoparticulate impurities (NPIs) in the size range of 100 – 200 nm in pharmaceutical-grade sucrose. Furthermore, isolated NPIs have been shown to induce protein aggregation when added to monoclonal antibody formulations. Moreover, nanoparticles are popular vaccine delivery systems used to increase the immunogenicity of antigens. Therefore, we hypothesized that NPIs may have immunostimulatory properties. In this study, we evaluated the immunomodulatory effects of NPIs in presence and absence of trastuzumab *in vitro* with monocyte-derived dendritic cells (moDCs). Exposure of trastuzumab, the model IgG used in this study, to NPIs led to an increase in concentration of proteinaceous particles in the sub-micron range. When added to moDCs, the NPIs alone or in presence of trastuzumab did not affect cell viability or cytotoxicity. Moreover, no significant effect on the expression of surface markers, and cytokine and chemokine production was observed. Our findings showed, surprisingly, no evidence of any immunomodulatory activity of NPIs. As this study was limited to a single IgG formulation and to *in vitro* immunological read-outs, further work is required to fully understand the immunogenic potential of NPIs.

Introduction

Protein pharmaceuticals are prone to physical and chemical instability.[1] This may result in deterioration of protein drug product quality and pose potential safety concerns, such as unwanted immunogenicity.[2] To inhibit protein degradation, protein pharmaceuticals typically contain a combination of stabilizing excipients.[3] Sucrose is a commonly used excipient in both liquid and lyophilized protein formulations because of its excellent stabilizing properties.[4, 5]

Recently, it has been found that pharmaceutical-grade sucrose contains nanoparticulate impurities (NPIs) in the size range of 100 – 200 nm.[6] Based on analytical characterization, the nanoparticles were suggested to be agglomerates of various compounds, including dextran (with presence of β-glucans), inorganic metal salts and fluorescent compounds, potentially originating from raw materials and production processes.[6] Furthermore, NPIs have been shown to destablize several marketed monoclonal antibodies (mAbs).[7] Introduction of NPIs isolated from pharmaceutical-grade sucrose to the mAbs resulted in immediate or delayed formation of protein aggregates and particles. Therefore, it is recommended to use sucrose low in NPI content to reduce instability risks for biopharmaceutical drug products.

Immunogenicity of protein biopharmaceuticals is an ongoing concern and may be linked to multiple sources related to the medicinal product, the patient and the treatment regimen.[8] Impurities in drug products, such as proteinaceous particles, have been shown to evoke immune responses in *in vitro* and *in vivo* models.[9] The presence of metal ions can result in the formation of immunogenic protein-metal complexes or metal ion-catalyzed oxidized protein species, including aggregates.[10–12] Furthermore, polysaccharides such as glucans have been explored as adjuvants to improve vaccine immunogenicity.[13] Various types of ß-glucans have been shown to increase the immunogenicity of antigens.[14, 15] Although glucan-related contaminants can been found in therapeutic mAb products at a much lower concentrations compared to concentrations tested in vaccine formulations with glucan-

based adjuvants (100-1000 µg/mL), immune-related adverse reactions upon administration might still occur.[16, 17]

Based on the above, we hypothesized that NPIs in absence or presence of protein, or protein aggregates generated from the presence of NPIs, may act as a danger signal and induce the activation of innate immune cells such as dendritic cells. To test this hypothesis, we evaluated the effect of NPIs in presence and absence of trastuzumab (humanized mAb, isotype IgG1) on human dendritic cells, which are pivotal in the establishment of a CD4$^+$ T-cell dependent immune response leading to the production of high affinity anti-drug antibodies detected in patients' sera.[18]

Materials and methods

Materials

The humanized mAb, isotype IgG1, trastuzumab (Herzuma®) was purchased from Leiden University Medical Centre (Leiden, The Netherlands). Pharmaceutical-grade surcose was purchased from VWR (Bruchsal, Germany) and RPMI 1640 medium was supplied by ThermoFisher Scientific (Waltham, USA). Polyvinylidene fluoride (PDVF) syringe filters with a pore size of 0.22 µm were purchased from Merck (Darmstadt, Germany). Labeled monoclonal antibodies used for flow cytometry were purchased from BD Biosciences (New Jersey, USA). A cytokine and chemokine multiplex assay (U-PLEX) was purchased from MSD (Rockville, USA). Highly purified water (conductivity: 18.2 mUΩ*cm) obtained from a Milli-Q® Advantage A10 system (Merck, Newark, USA) was used throughout the study.

Preparation of NPIs

Preparation of NPIs was performed as described before.[7] Briefly, a 50% w/v of sucrose solution in water was prepared and submitted to an ultra-/dia-filtration process by using a Minimate II Tangential Flow Filtration (TFF) system (Pall, Crailsheim, Germany) equipped with a 30-kDa TFF capsule (Pall). Diafiltration of the sucrose solution was performed against 20 volumes of water. Further, the sucrose-free retentate (confirmed by DLS, data not shown) was upconcentrated 1000-fold and filtered by using a 0.22-µm PDVF filter.

Upconcentrated stock retentate containing NPIs at a concentration 1×10^{11} particles/mL (as determined by NTA) was stored at -80 °C until needed.

Water without addition of sucrose was submitted to the same process described above and served as a control sample (Ctl) throughout the study.

Sample preparation

Stock suspensions of NPIs (two-fold higher in concentration compared to the target concentration) were prepared in RPMI medium and spiked into trastuzumab samples to target concentrations stated in the results section. Trastuzumab was diluted with RPMI medium to 2 mg/mL. Further addition of NPIs and RPMI medium was performed to reach a final protein concentration of 1 mg/mL. Trastuzumab was incubated in presence of NPIs or control (water) for 1 hour at room temperature. The formulations were added to moDC suspensions to reach a target IgG concentration of 0.1 mg/mL.[19]

Nanoparticle tracking analysis (NTA)

NanoSight (Model LM20, Malvern Instrument, Malvern, UK) instrument equipped with a 405-nm laser (blue) was used to quantify and determine the size of nanometer sized particles (size range~50 – 1000 nm). Samples were injected into the chamber by using a 1-mL silicone-free syringe and the purging volume was 0.3 mL. A video capture was initiated immediately after injection and a triplicate measurement of 60-second replicates was performed. All measurements were collected at room temperature with camera levels set to optimal values until at least 100 valid tracks were recorded.

Flow imaging microscopy (FIM)

MFI 5200 (ProteinSimple, USA) was used for characterization and quantification of particles ≥ 1 µm in equivalent circular diameter. The system was equipped with a silane-coated high-resolution 100-µm flow cell. RPMI medium was used to perform optimization of illumination after a 0.17-mL purge volume and 0.28 mL of sample was analyzed within each measurement, resulting in a ca. 2.89 min measurement time. The number of image frames stored per measurement was between 138 and 1133, dependent on the particle

concentration within each sample. Data were processed by using MVAS V2.3 software and each sample was measured once.

Generation of human monocyte-derived dendritic cells (moDCs)

Human peripheral blood mononuclear cells were purified from buffy coats obtained from Etablissement Français du Sang (EFS Rennes, France) by density centrifugation on a Ficoll gradient (lymphocyte separation medium; GE Healthcare, Buc, France). Healthy donors gave their written consent for the use of blood donation for research purposes. MoDC preparation was performed as described before.[20] Briefly, monocytes were isolated from the mononuclear fraction by magnetic positive selection with MidiMacs separation columns and anti-CD14 antibodies coated on magnetic beads (Miltenyi Biotec, Bergish Gladbach, Germany). Monocytes were cultured at 1×10^6 cells/mL in the presence of GM-CSF (550 U/mL) and IL-4 (550 U/mL) (Miltenyi Biotec) in RPMI-1640 25 mM HEPES GlutaMAX™ supplemented with 10% fetal calf serum, antibiotics and 1% pyruvate at 37 °C in humidified air containing 5% CO_2. Within 4 days, monocytes had differentiated into moDCs with an immature phenotype.

Treatment of moDCs

After differentiation, immature moDCs were treated with water (negative control, water treated the same way as NPIs) or NPIs (10^8, 10^9 or 10^{10} NPIs/mL) in 12-well plates. Additionally, moDCs were treated with trastuzumab (100 μg/mL) alone or in presence of NPIs (10^{10} NPIs/mL). Lipopolysaccharide (LPS from Escherichia coli 055:B5 strain, at a final concentration of 25 ng/mL; Sigma-Aldrich, St. Louis, USA) served as a positive maturation control. All treated moDC samples were incubated at a final concentration of 10^6 cells/mL in 1 mL at 37°C in humidified air containing 5% CO_2 for 24 hours prior to analysis.

Flow cytometric analysis of moDC maturation

MoDC viability and phenotype were analyzed by using flow cytometry. Cell viability was assessed in preliminary experiments by staining with propidium iodide (PI) (Invitrogen, California, USA), used at a final concentration of 625 ng.mL^{-1}, on a small fraction of moDC

cultures. For the phenotypic analysis, the surface labeling procedure was as follows: 2×10^5 cells/mL were washed in cold phosphate-buffered saline (PBS) supplemented with 0.5% bovine serum albumin (BSA) and stained with monoclonal antibodies (mAbs) in the dark, on ice for 20 min. The following mAbs were used: allophycocyanin (APC)-labeled mouse anti-human CD86 (555660, BD Biosciences, New Jersey, USA) and anti-human CXCR4 (555976, 12G5, BD Biosciences); fluorescein isothiocyanate (FITC)-labeled mouse anti-human CD80 (5557226, L307.4, BD Biosciences) and anti-human PD-L1 (558065, MIH1 BD Biosciences); phycoerythrin (PE)-labeled mouse anti-human CD83 (556855, HB15e, BD Biosciences). Appropriate isotype controls (mouse IgG1κ or IgG2aκ, BD Biosciences) were used at the same concentration to determine non-specific staining. Cells were analyzed on an Attune Nxt (Invitrogen) by using FlowJo software (version 10; FlowJo LLC, Oregon, USA), and we used a gating strategy to exclude dead cells, based on the FSC/SSC criteria. The data acquisitions were performed on a minimum of 10,000 living cells. Results are expressed as the relative fluorescence intensity (RFI), by using the corrected mean fluorescence intensity (cMFI), as follows: cMFI=MFI–MFI of isotype control; RFI = cMFI of treated cells/cMFI of untreated cells.

Quantification of cytokines and chemokines in cell culture supernatants

Culture supernatants were analyzed by using Meso Scale Discovery (MSD, Rockville, MA, USA) multiplex assay, according to the manufacturer's instructions, to assess the concentrations of the following cytokines and chemokines: IL-1β, IL-6, IL-8, IL-10, IL-12/23p40, CCL2 (MCP-1), CCL3 (MIP-1α), CCL4 (MIP-1β), IFN-β, TNFα. The quantification ranges were: IL-1β: 0.91-3,730 pg/mL, IL-6: 0.51-2,080 pg/mL, IL-8: 0.50-2,050 pg/mL, IL-10: 0.90-3,700 pg/mL, IL-12/23p40: 5.57-22,800 pg/mL, CCL2: 1.45-5,920 pg/mL, CCL3: 1.46-6,000 pg/mL, CCL4: 0.45-1,860 pg/mL, IFN-β: 21.97-90,000 pg/mL, TNFα: 0.89-3,650 pg/mL. Each plate was imaged on a Meso Quickplex SQ120 (MSD) according to manufacturer's instructions. The analysis software (Discovery Workbench, MSD) provided with the platform contains the quantification, detection ranges and quality criteria for the standard curve, which were applied automatically during analysis.

Statistical analysis

ANOVA with post hoc Tukey's analysis was used to assess statistical significance, with $P <$ 0.05 considered significant. Data were analyzed on Graphpad Prism software (La Jolla, CA, USA).

Results and discussion

Particle characterization

Isolated NPIs from sucrose were added to trastuzumab to a target concentration of 1×10^{10} NPIs/mL (based on dilution). This concentration was chosen as a worst-case scenario, as it is slightly above the maximum concentration of NPIs that might be present in an isosmotic sucrose formulation.[6] The resulting mixture was incubated for 1 hour at room temperature prior to analysis. A noticeable higher concentration of nanometer sized particles was detected by NTA for the trastuzumab formulation spiked with NPIs as compared to NPIs alone and the non-treated IgG sample (Figure 1), indicating the formation of nanometer sized trastuzumab aggregates. Nanometer sized IgG aggregates previously were shown to be highly immunogenic *in vivo*[21] and an assessment of risks imposed by such particles with respect to the clinical performance of drug products is recommended by regulatory agencies.[22] On the other hand, no increase in micron sized particles in MFI was measured upon addition of NPIs to the trastuzumab formulation. These results vary from the results of a previous study, where the originator drug product (Herceptin®) was used, and the addition of NPIs induced the formation of micron sized particles.[7] Even though the concentration of NPIs was adjusted based on a NTA method used in both studies, the composition of NPIs used in our study could have differed from the NPIs used in the study of Weinbuch et al., because we used a different batch. Additionally, the different IgG behavior in presence of NPIs could be explained by the different formulation composition used in this study and/or the slightly different glycosylation profiles between Herceptin® and Herzuma®.[23, 24]
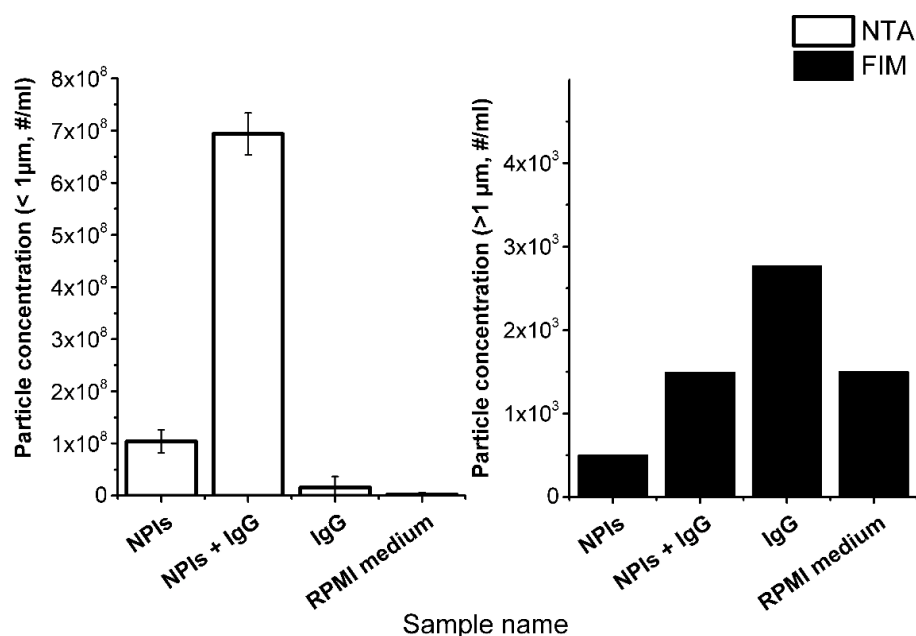
*Figure 1: **Nanometer sized and micron sized particle concentrations determined by using a) NTA and b) FIM, respectively.** Samples measured with NTA were diluted 100-fold in RPMI medium prior to measurement and stated concentrations are not corrected for dilution. Error bars represent standard deviation of triplicate measurements. FIM analysis was performed as single measurements of undiluted samples. NPIs: nanoparticulate impurities, IgG: trastuzumab.*

Previously performed Glucatell assays with the isolated NPIs indicated a prominent presence of (1→3)-β-D-glucans (10 ng/mL per $1x10^{10}$ NPIs/mL),[25] which are well-known immunomodulatory agents.[26] β-glucans are believed to trigger the innate immunity via dectin-1, Toll-like receptors 2 and 6, and complement receptor 3, which are transmembrane receptors abundantly found on myeloid cells, such as dendritic cells.[27] However, opposed to endotoxin levels, glucans are not regulated in terms of maximum permitted concentrations in pharmaceutical products and their levels in IgG formulations is rarely tested.[28, 29] Whereas the immunostimulatory effect of β-glucans is considered relatively low, they can act as adjuvants in presence of other immunogenic species, such as proteinaceous particles.[30, 31]

Effect of NPIs alone on moDC phenotype

To investigate the effect of NPIs on moDC maturation, we analyzed the expression of moDC surface markers after 24 hours of stimulation with different concentrations of NPIs (10^8, 10^9 and 10^{10} NPIs/mL). The toxicity of NPIs was first analyzed by using PI staining and we observed that cell viability was unaffected at all tested concentrations and remained above 75% (data not shown). Surface markers CD83 and CD86 were highly up-regulated after incubation with LPS for 24 hours, indicating that moDCs could undergo maturation. However, the NPIs at the three tested concentrations did not modulate CD83 and CD86 expression compared to water, processed as NPIs and used as control, and untreated cells (Figure 2). On the basis of these observations, the following experiments were carried out with 10^{10} NPIs/mL (maximal concentration which could be prepared).
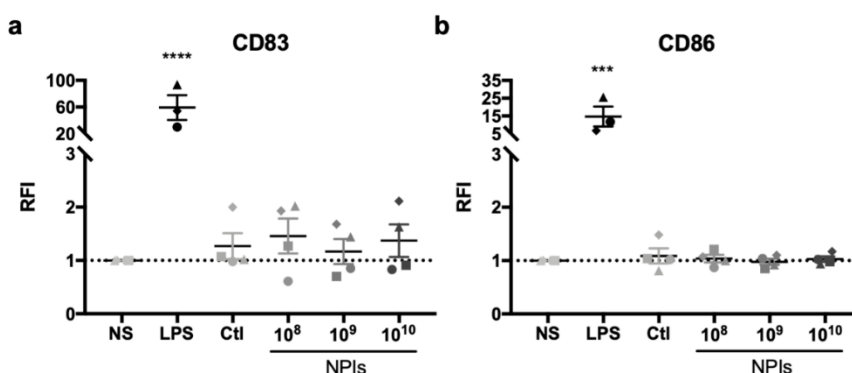
*Figure 2: **Effect of NPIs on the expression of moDC surface markers.** Immature moDCs were treated for 24 hours with NPIs (10^8, 10^9 and 10^{10} particles/mL), water or LPS (25 ng/mL). Cells were then collected, washed and analyzed by flow cytometry for expression of surface maturation markers a) CD83 and b) CD86. Results are expressed as relative fluorescence intensity (RFI) compared to non-stimulated cells and represent the mean ± SEM of 4 independent experiments. ***p<0.001, ****p<0.0001 ; one-way ANOVA followed by Tukey's analysis. NS: non-stimulated cells; LPS: lipopolysaccharide; Ctl: control water treated as NPIs; NPIs: nanoparticulate impurities.*

Effect of NPIs and trastuzumab aggregates on moDC maturation

To evaluate if nanometer sized particles generated after adding NPIs to a trastuzumab solution modulate the phenotype of moDCs, we first analyzed the expression of surface markers. NPIs and trastuzumab aggregates had no significant effect on the expression of

CD80, CD83, CD86, PD-L1 and CXCR4 compared to the corresponding controls: control water alone, NPIs alone, trastuzumab alone and trastuzumab mixed with water after 24 hours of incubation (Figure 3 and Supplementary figure S1). NPIs in absence and presence of trastuzumab did not increase inflammatory cytokine and chemokine production (Figure 4). These results indicate that NPI-induced aggregates of trastuzumab have little impact on antigen-presenting cells.
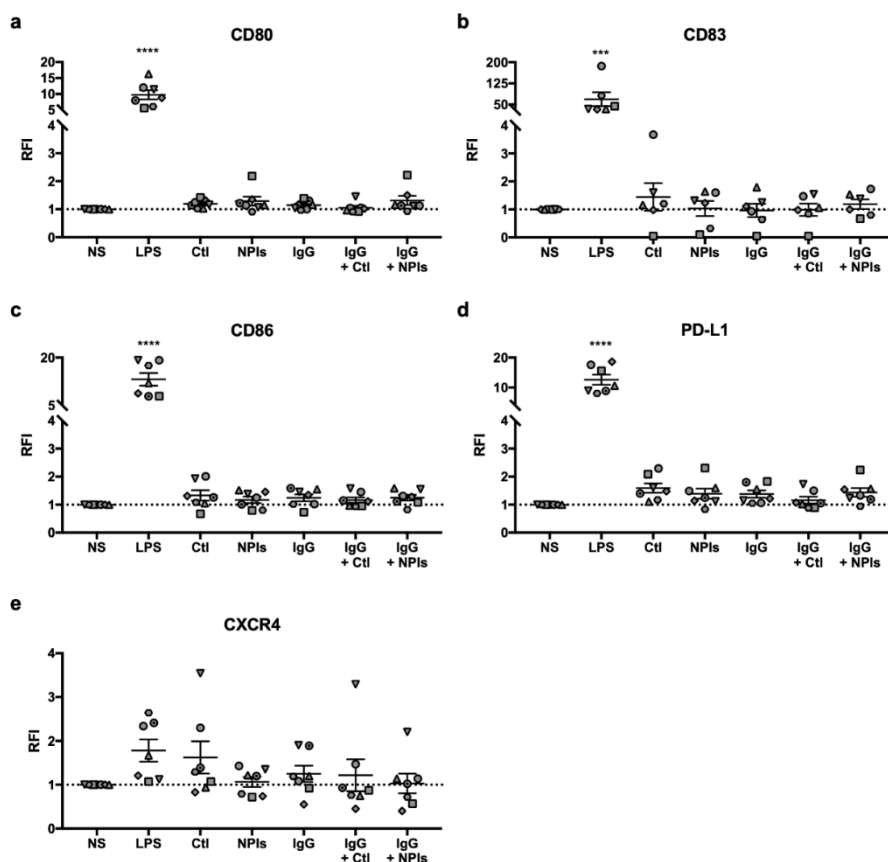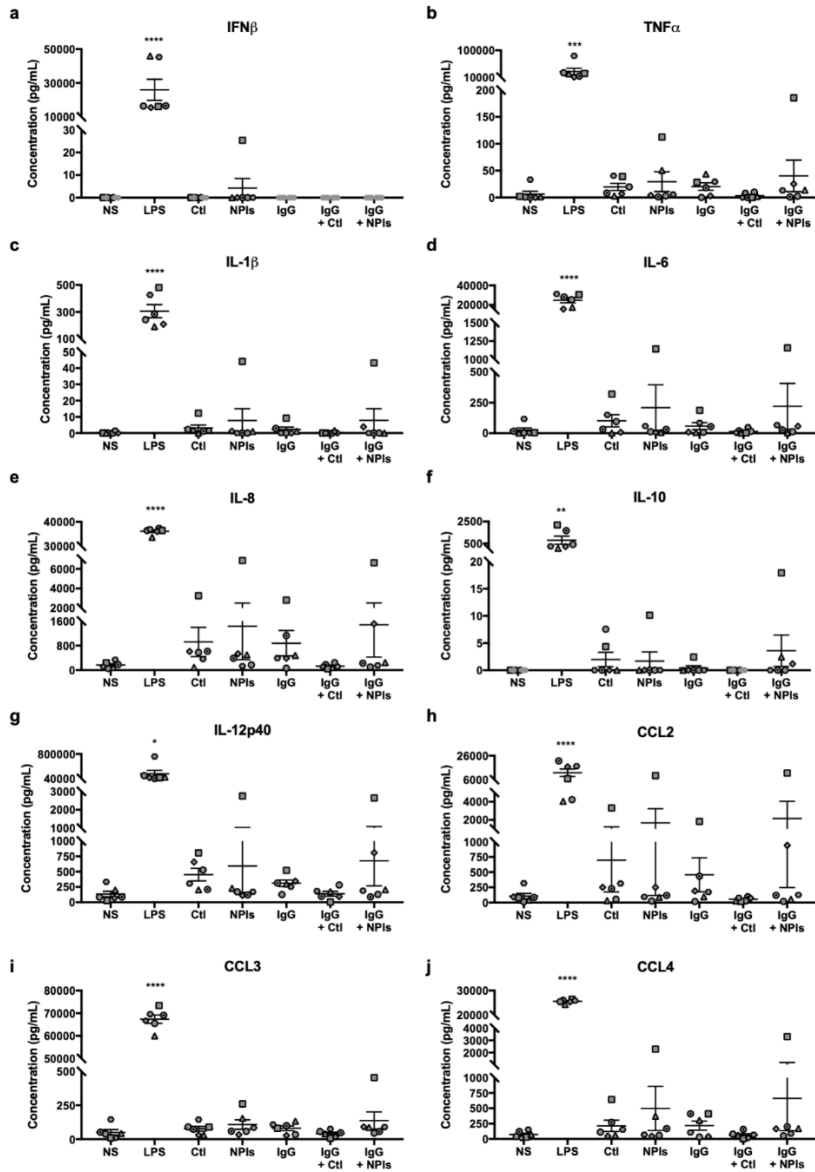

*Figure 3: **Effect of NPIs and trastuzumab on the expression of moDC surface markers.** Immature moDC were treated for 24 hours with a mixture of NPIs (10^{10} NPIs/mL) and trastuzumab (100 µg/mL) or corresponding controls or LPS (25 ng/mL). Cells were then collected, washed and analyzed by flow cytometry for expression of surface maturation markers. Results are expressed as relative fluorescence intensity (RFI) compared to non-stimulated cells and represent the mean ± SEM of 6 or 7 independent experiments with values for each donor represented by one given symbol. ***p<0.001, ****p<0.0001 ; one-way ANOVA followed by Tukey's analysis. NS: non-stimulated cells; LPS: lipopolysaccharide; Ctl: control water treated as NPIs; NPIs: nanoparticulate impurities, IgG: trastuzumab.*

*Figure 4: **Effect of NPIs and trastuzumab on moDC cytokine and chemokine secretion.** Immature moDC were treated for 24 hours with a mixture of NPIs (10¹⁰ NPIs/mL) and trastuzumab (100 µg/mL) or corresponding controls or LPS (25 ng/mL). Cytokine and chemokine concentrations in culture supernatants were analyzed induplicate by using an electroluminescent multiplex assay. Detection limits are indicated in the Methods section. Results of 6 independent experiments are presented with values for each donor represented by one given symbol. *p<0.05, **p<0.01, ***p<0.001, ****p<0.0001 ; one-way ANOVA followed by Tukey's analysis. NS: non-stimulated cells; LPS: lipopolysaccharide; Ctl: control water treated as NPIs; NPIs: nanoparticulate impurities, IgG: trastuzumab.*

The immunomodulatory properties of aggregated antibodies have often been studied following application of extreme stress conditions to protein formulations, such as heat- or stir-stress, resulting in formation of very high numbers of proteinaceous particles.[21, 32–34] In one of the studies, the high abundance of particles was determined to be a dominant factor in evoking an immune response *in vitro*.[32] Furthermore, forced degradation studies result in a mixture of variable aggregate sizes, which induced a strong moDC maturation. In fact, results from various studies comparing different size range-aggregates are controversial. Oligomeric, nanometer or micron sized antibody aggregates were found to have variable immunogenic potency *in vitro*[32–34] and *in vivo*.[8, 21, 35] In our case, a relatively low concentration of proteinaceous particles in the nanometer size range was formed within trastuzumab formulations in presence of NPIs, which were insufficient to activate moDCs in the experimental setting used in the current study.

The inherent immunogenicity of the monomeric protein and the physicochemical properties of protein aggregates are other important influencing factors in unwanted immunogenicity.[32, 34] Generation of immunogenicity *via* moDCs depends on the interactions of IgG aggregates and innate receptors such as immunoglobulin receptors (FcγRs), danger signal receptors (e.g., TLRs) or complement receptors.[19] Morgan et al. showed infliximab aggregates formed upon heat stress to induce full moDC maturation, as opposed to infliximab aggregates induced by mechanical stress.[19] Other protocols attempted to refine aggregate formation in order to expose moDCs to more homogeneous preparations and to induce low levels of aggregation of the total protein. For instance, applying stir stress to a trastuzumab preparation induced the formation of aggregates within the sub-micron and micron size range, while heat stress mainly induced the formation of oligomers. Both preparations induced moDC maturation, but aggregates generated via stir stress induced an increased maturation state.[33] Therefore, both the protein and the stress applied to induce aggregates will have a considerable effect on the immunogenic potential of protein therapeutics.

The weak immunostimulatory effect of NPIs in presence of trastuzumab aggregates could be rationalized by the minimal impact of NPIs on the monomeric IgG three-dimensional

structure.[7] Harsh artificial stress, such as heat or stir stress, generates aggregates consisting of altered protein structures which may increase the presentation of peptide sequences on the aggregate´s surface that are recognized by moDC receptors. For instance, heat-stressed infliximab activated moDCs by cross-linking of FcγRIIa receptors.[36] Overall, the studies cited above focused on the direct impact of the pure protein aggregates on immune cells, while in our work the potential effect of NPIs in presence of monoclonal antibodies was investigated.

Another explanation for the lack of moDC maturation seen in our study could be the relatively small size of the NPIs (100-200 nm). For example, for particulate vaccines an increase in mean particle diameter resulted in a stronger immune response.[37, 38] Similarly, many investigational applications of ß-glucans involve preparations consisting of particulates in the lower micron-size range. However, further studies are required to evaluate the impact of particle size and other physico-chemical attributes of protein aggregates on their immunogenicity.[39]

Conclusions

Surprisingly, NPIs derived from pharmaceutical-grade sucrose, when added to moDCs *in vitro* at a level of 1×10^{10} NPIs/mL, did not show immunomodulatory effects in absence or in presence of trastuzumab, even though the NPIs induced the formation of nanometer sized protein aggregates. It is worth noting, however, that the observations made in this study relate solely to *in vitro* models using one dendritic cell type, and are unlikely to fully predict the immunological potential of NPIs *in vivo*. Examination of the immunogenicity of the NPIs with other IgGs and protein formulations in both *in vitro* and *in vivo* models would be required to obtain a broader picture of the immunogenic risk of NPIs. However, with respect to pharmaceutical quality and stability the induction of aggregation and particles by NPIs remains critical and should be considered during drug product development.

References:

1. Roberts CJ. Therapeutic protein aggregation: mechanisms, design, and control. 2014. Trends Biotechnol. 32: 372–380.

2. Jiskoot W, Randolph TW, Volkin DB, et al. Protein instability and immunogenicity: roadblocks to clinical application of injectable protein delivery systems for sustained release. 2012. J Pharm Sci 101: 946–954.

3. Jameel F, Hershenson S. 2010. Formulation and process development strategies for manufacturing biopharmaceuticals, Hoboken N.J.: Wiley. p.955.

4. Timasheff SN. Protein hydration, thermodynamic binding, and preferential hydration. 2002. Biochemistry 41: 13473–13482.

5. Timasheff SN, Xie G. Protein-solvent preferential interactions, protein hydration, and the modulation of biochemical reactions by solvent components. 2002. Proceedings of the National Academy of Sciences of the United States of America 99: 9721–9726.

6. Weinbuch D, Cheung JK, Ketelaars J, et al. Nanoparticulate Impurities in Pharmaceutical-Grade Sugars and their Interference with Light Scattering-Based Analysis of Protein Formulations. 2015. Pharm Res 32: 2419–2427.

7. Weinbuch D, Ruigrok M, Jiskoot W, Hawe A. Nanoparticulate Impurities Isolated from Pharmaceutical-Grade Sucrose Are a Potential Threat to Protein Stability. 2017. Pharm Res 34: 2910–2921.

8. Jiskoot W, Kijanka G, Randolph TW, et al. Mouse Models for Assessing Protein Immunogenicity: Lessons and Challenges. 2016. J Pharm Sci 105: 1567–1575.

9. Moussa EM, Panchal JP, Moorthy BS, et al. Immunogenicity of Therapeutic Protein Aggregates. 2016. J Pharm Sci 105: 417–430.

10. Filipe V, Jiskoot W, Basmeleh AH, et al. Immunogenicity of different stressed IgG monoclonal antibody formulations in immune tolerant transgenic mice. 2012. mAbs 4: 740–752.

11. van Beers MMC, Sauerborn M, Gilli F, et al. Oxidized and aggregated recombinant human interferon beta is immunogenic in human interferon beta transgenic mice. 2011. Pharm Res 28: 2393–2402.

12. Torosantucci R, Mozziconacci O, Sharov V, et al. Chemical modifications in aggregates of recombinant human insulin induced by metal-catalyzed oxidation: covalent cross-linking via michael addition to tyrosine oxidation products. 2012. Pharm Res 29: 2276–2293.

13. Lukashevich I, Shirwan H. Novel. 2014. Technologies for Vaccine Development, Springer-Verlag Wien; p.3-32.

14. Irvine DJ, Hanson MC, Rakhra K, Tokatlian T. Synthetic Nanoparticles for Vaccines and Immunotherapy. 2015. Chem Rev 115: 11109–11146.

15. Gregory AE, Titball R, Williamson D. Vaccine delivery using nanoparticles. 2013. Front Cell Infect Microbiol 3: 13.

16. Ferwerda G, Meyer-Wentrup F, Kullberg B-J, et al. Dectin-1 synergizes with TLR2 and TLR4 for cytokine production in human primary monocytes and macrophages. 2008. Cell Microbiol 10: 2058–2066.

17. Wang M, Zhang L, Yang R, et al. Improvement of immune responses to influenza vaccine (H5N1) by sulfated yeast beta-glucan. 2016. Int J Biol Macromol 93: 203–207.

18. Jawa V, Terry F, Gokemeijer J, et al. T-Cell Dependent Immunogenicity of Protein Therapeutics Pre-clinical Assessment and Mitigation-Updated Consensus and Review 2020. 2020. Front Immunol 11: 1301.

19. Morgan H, Tseng S-Y, Gallais Y, et al. Evaluation of in vitro Assays to Assess the Modulation of Dendritic Cells Functions by Therapeutic Antibodies and Aggregates. 2019. Front Immunol 10: 601.

20. Gallais Y, Szely N, Legrand F-X, et al. Effect of growth hormone and IgG aggregates on dendritic cells activation and T-cells polarization. 2017. Immunol Cell Biol 95: 306–315.

21. Kijanka G, Bee JS, Korman SA, et al. Submicron Size Particles of a Murine Monoclonal Antibody Are More Immunogenic Than Soluble Oligomers or Micron Size Particles Upon Subcutaneous Administration in Mice. 2018. J Pharm Sci 107: 2847–2859.

22. U.S. Department of Health and Human Services FDA, Center for Biologics Evaluation and Research. In: Guidance for industry: immunogenicity assessment for therapeutic protein products; 2014. Available at: http://www.fda.gov/Drugs/GuidanceComplianceRegulatoryInformation/Guidances/default.htm. Accessed 30th June 2020.

23. Alsenaidy MA, Jain NK, Kim JH, et al. Protein comparability assessments and potential applicability of high throughput biophysical methods and data visualization tools to compare physical stability profiles. 2014. Front Pharmacol 5: 39.

24. U.S. Department of Health and Human Services FDA , Center For Drug Evaluation and Research. In: Complete Response BLA 761091 Trastuzumab-pkrb Celltrion, Inc;2017. Available at: https://www.accessdata.fda.gov/drugsatfda_docs/nda/2018/761091Orig1s000OtherR.pdf Accessed 30th June 2020.

25. Weinbuch D. 2016. Nanoparticulate impurities in pharmaceutical-grade sucrose are a potential threat to protein stability. Doctorate thesis, Leiden. p24 .

26. Goodridge HS, Wolf AJ, Underhill DM. Beta-glucan recognition by the innate immune system. 2009. Immunol Rev 230: 38–50.

27. Novak M, Vetvicka V. Beta-glucans, history, and the present: immunomodulatory aspects and mechanisms of action. 2008. J Immunotoxicol 5: 47–57.

28. Gefroh E, Hewig A, Vedantham G, et al. Multipronged approach to managing beta-glucan contaminants in the downstream process: control of raw materials and filtration with charge-modified nylon 6,6 membrane filters. 2013. Biotechnol Prog 29: 672–680.

29. Barton C, Vigor K, Scott R, et al. Beta-glucan contamination of pharmaceutical products: How much should we accept? 2016. Cancer Immunol Immunother 65: 1289–1301.

30. Vetvicka V, Vannucci L, Sima P. β-glucan as a new tool in vaccine development. 2020. Scand J Immunol 91: e12833.

31. Sonck E, Devriendt B, Goddeeris B, Cox E. Varying effects of different β-glucans on the maturation of porcine monocyte-derived dendritic cells. 2011. Clin Vaccine Immunol 18: 1441–1446.

32. Joubert MK, Hokom M, Eakin C, et al. Highly aggregated antibody therapeutics can enhance the in vitro innate and late-stage T-cell immune responses. 2012. J Biol Chem 287: 25266–25279.

33. Ahmadi M, Bryson CJ, Cloake EA, et al. Small amounts of sub-visible aggregates enhance the immunogenic potential of monoclonal antibody therapeutics. 2015. Pharm Res 32: 1383–1394.

34. Rombach-Riegraf V, Karle AC, Wolf B, et al. Aggregation of human recombinant monoclonal antibodies influences the capacity of dendritic cells to stimulate adaptive T-cell responses in vitro. 2014. PLoS ONE 9: e86322.

35. Fathallah AM, Chiang M, Mishra A, et al. The Effect of Small Oligomeric Protein Aggregates on the Immunogenicity of Intravenous and Subcutaneous Administered Antibodies. 2015. J Pharm Sci Sciences 104: 3691–3702.

36. Nabhan M, Legrand F-X, Le-Minh V, et al. The FcγRIIa-Syk Axis Controls Human Dendritic Cell Activation and T Cell Response Induced by Infliximab Aggregates. 2020. J Immunol 205: 2351–2361.

37. Benne N, van Duijn J, Kuiper J, et al. Orchestrating immune responses: How size, shape and rigidity affect the immunogenicity of particulate vaccines. 2016. J Control Release 234: 124–134.

38. Elder MJ, Webster SJ, Chee R, et al. β-Glucan Size Controls Dectin-1-Mediated Immune Responses in Human Dendritic Cells by Regulating IL-1β Production. 2017. Front Immunol 8: 791.

Supplementary materials
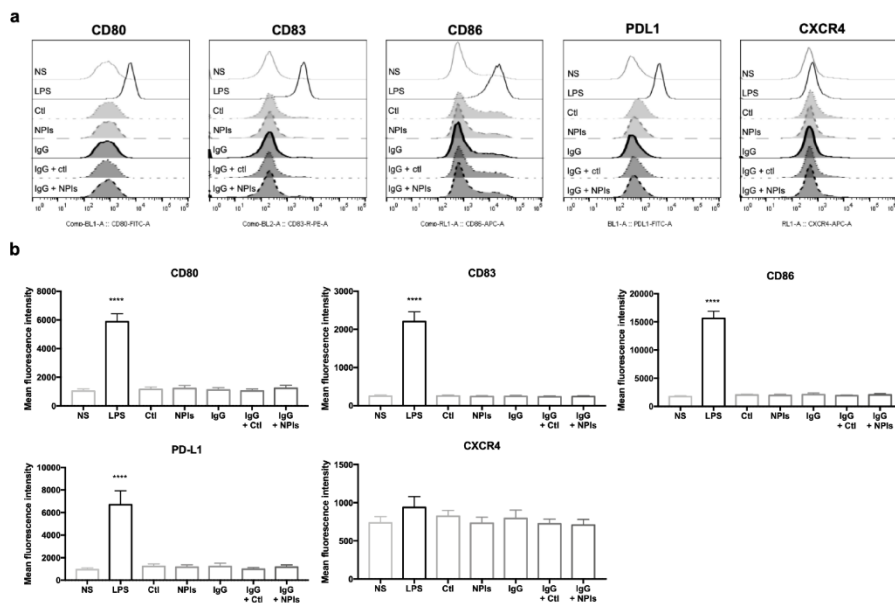
Supplementary figure S1: **Effect of NPIs and trastuzumab on the expression of moDC surface markers.** *Immature moDC were treated for 24 hours with a mixture of NPIs (10^{10} NPIs/mL) and trastuzumab (100 µg/mL) or corresponding controls or LPS (25 ng/mL). Cells were then collected, washed and analyzed by flow cytometry for expression of surface maturation markers. (a) Representative histograms of CD80, CD83, CD86, PD-L1, and CXCR4 expression. (b) Results are expressed as mean fluorescence intensity and represent the mean ± SEM of 6 or 7 independent experiments. ****p<0.0001 ; one-way ANOVA followed by Tukey's analysis. NS: non-stimulated cells; LPS: lipopolysaccharide; NPIs: nanoparticulate impurities, IgG: trastuzumab; Ctl: control water treated as NPIs.*

Chapter 5

What makes polysorbate functional? Impact of polysorbate 80 grade and quality on IgG stability during mechanical stress

Adam D. Grabarek[1,2], Ula Bozic[1], Jannik Rousel[1,2], Tim Menzen[1], Wendelin Kranz[1], Klaus Wuchner[3], Wim Jiskoot[1,2], Andrea Hawe[1]*

[1] Coriolis Pharma Research, Fraunhoferstr. 18b, 82152 Martinsried, Germany

[2] Leiden Academic Centre for Drug Research, Leiden University, The Netherlands

[3] Janssen Research & Development, Large Molecule Analytical Development, Schaffhausen, Switzerland

*corresponding author

Abstract

Polysorbate 80 (PS80) is a commonly used surfactant in therapeutic protein formulations to mitigate adsorption and interface-induced protein aggregation. Several PS80 grades and qualities are available on the market for parenteral application. The role of PS80 grade on protein stability remains debatable, and the impact of (partially) degraded PS on protein aggregation is not yet well understood. In our study, a monoclonal antibody (IgG) was subjected to three different mechanical stress conditions in the presence of multicompendial (MC) and Chinese pharmacopeia (ChP) grade PS80. Furthermore, IgG formulations were spiked with (partly) hydrolyzed PS80 to investigate the effect of PS80 degradants on protein stability. PS80 functionality was assessed by measuring the extent of protein aggregation and particle formation induced during mechanical stress by using size-exclusion chromatography, dynamic light scattering, backgrounded membrane imaging and flow imaging microscopy. No distinguishable differences in PS80 functionality between MC and ChP grade were observed in the three stress tests. However, with increasing degree of PS80 hydrolysis, higher counts of sub-visible particles were measured after stress. Furthermore, higher levels of PS80 degradants at a constant PS80 concentration may destabilize the IgG. In conclusion, MC and ChP grade PS80 are equally protective, but PS80 degradants compromise IgG stability.

Introduction

Manufacturing, handling and administration of biopharmaceutical products generates mechanical stress which can induce aggregation of proteins[1]. Protein aggregation deteriorates product quality and may compromise safety, e.g., by causing unwanted immune responses[2]. Aggregation is often driven by weak interactions between exposed hydrophobic patches of (partially) unfolded proteins[3]. A range of conditions, including pH shift, elevated temperature and mechanical stress, may induce protein unfolding and enhance the formation of protein aggregates. Therefore, the development of robust formulations consisting of excipients mitigating protein unfolding and aggregation is required to ensure the quality of protein drug products.

Proteins are amphiphilic molecules which have a high propensity to adsorb to interfaces and are susceptible to surface-mediated unfolding[4]. Surface active molecules, such as polysorbates (PS), are common excipients in drug product formulations to increase colloidal stability and minimize adsorption of proteins to interfaces[5,6]. PS are non-ionic surfactants containing mainly sorbitan polyoxyethylene (POE) fatty acid esters. The protective role of PS in protein formulations has been thoroughly investigated[7] and two main mechanisms have been elucidated: (1) PS acting as a chaperone for aggregation-prone hydrophobic sites on the protein surfaces (promoting the folded structure)[8,9] and (2) PS competing with proteins at interfaces (reducing interface exposure)[10,11]. Currently, polysorbate 20 (POE sorbitan monolaurate, PS20) and polysorbate 80 (POE sorbitan monooleate, PS80) are the most frequently used surfactants in marketed biopharmaceutical formulations. Both types are highly effective in preventing protein adsorption and aggregation and they have a well-known toxicity profile[12,13]. The longer monounsaturated chain in PS80, compared to PS20, makes PS80 more surface active with a lower critical micelle concentration (CMC). The binding properties of the two types of surfactants to proteins is highly dependent on the protein type[14,15]. The different physico-chemical properties of PS80 and PS20 translate to distinguishable properties in their functionality[16] as well as chemical stability[17].

The chemical properties are key towards the notable functionality of PS. Nonetheless, commercial PS products consist of a mixture of mono- and poly-esters of POE sorbitans

alongside substantial amounts of POE, sorbitan POE and isosorbide POE fatty acid esters, originating from the synthesis[18]. Significant variations in the chemical composition of PS can be present, not only between suppliers[19] but also between different lots of a single supplier[20]. In addition, PS is known to be susceptible to oxidative and hydrolytic (mainly enzymatic under pharmaceutical relevant conditions[21]) degradation, resulting in the formation of aldehydes, epoxides, free fatty acids (FFA) and other impurities, which adds on to their heterogeneity[20].

The European, United States, and Japanese Pharmacopeias have harmonized requirements for PS80 (multicompendial, MC-PS80), where a fraction of above 58% of esterified fatty acids must be oleic acid. Other fractions are specified to a much lower percentage and consist of palmitic, myristic, stearic, linoleic, and linolenic acid esters. In 2015, the Chinese Pharmacopeia (ChP) introduced much more stringent purity requirements for the fatty acid distribution with a minimum oleic acid content of 98% (ChP-PS80). However, there is currently little known on the impact of PS80 grade and quality on its protective role towards proteins exposed to mechanical stress. The highly distinctive compositions of the two PS80 grades led us to focus our study on the functionality of PS80.

In our study, we applied three different mechanical stress methods which allowed us to comprehensively understand the functionality of two different PS80 grades – MC-PS80 and ChP-PS80. In addition to shaking stress, which is commonly used in biopharmaceutical formulation development in forced degradation studies[22], we developed a free-fall test and a syringe pump test as alternative stress methods to assess protein stability in presence of MC-PS80 and ChP-PS80. Unintentional dropping of vials or syringes during transportation and handling may have detrimental effects on protein stability[23-25]. Here, we designed an apparatus with specifications according to the international organization for standardization (ISO) requirements for needle-based injection systems[26] to induce mechanical shock to vials filled with IgG formulations. Furthermore, to mimic the stress conditions during manufacturing, we developed a low-volume flow device equipped with two glass syringes connected via a capillary. Continuous flow of the protein solution from one syringe to another through a narrow constriction has been shown to produce shear and

extensional forces leading to protein aggregation and particle formation[27]. The flow device apparatus was also used to investigate the role of hydrolyzed PS80 on the protein's propensity for aggregation during mechanical stress. We analytically characterized the stressed samples for protein aggregation and particle formation, as these are the key parameters affected by mechanical stress.

Materials and methods

Materials

A monoclonal antibody (humanized IgG1) at a concentration 50 mg/ml in 12 mM L-histidine (pH 6.0) and 250 mM sucrose was donated by Janssen. For each experiment in this study the IgG was diluted with formulation buffer to 5 mg/ml. PS80 of multicompendial grade (MC-PS80) was purchased from J.T. Baker (Avantor, USA) and PS80 compliant the with Chinese pharmacopeia (ChP-PS80) was obtained from Croda International Plc (Snatih, United Kingdom). Sucrose and acetonitrile were purchased from VWR Chemicals (Radnor, USA) and L-histidine from Sigma Aldrich (Taufkirchen, Germany). All other excipients used in the study were purchased from Merck (Darmstadt, Germany) unless otherwise stated. Highly purified water (conductivity: 18.2 mΩ·cm) obtained from a Milli-Q® Advantage A10 system (Merck, Germany) was used throughout the study.

Chemical degradation of PS80

Hydrolytic degradation of PS80 was performed by incubating 2% (w/v) PS80 (MC-PS80 and ChP-PS80) in methanol with 1 M NaOH at 40 °C for 21 hours. After incubation, the solution was neutralized with 10% (w/v) formic acid. Methanol was removed by using a RCV 2-18 CD plus SpeedVac (Marin Christ) operating at 37 °C over 2 hours with 1,400 rounds per minute (rpm). The obtained fully hydrolyzed dry material was stored at -80 °C and resuspended in 500 µl of formulation buffer prior to use.

Different levels of hydrolyzed PS80 were prepared by mixing solutions of neat PS80 with solutions of fully hydrolyzed PS80. Levels of degradants described throughout the paper correspond to % (w/v) of neat PS submitted to complete hydrolysis. PS solutions containing

fully hydrolyzed PS80 were not filtered prior to usage, to enable the assessment of the impact of both insoluble and soluble PS80 degradants on protein stability.

Sample preparation

The IgG was thawed at room temperature and further diluted to approximately 7 mg/ml with PS80-free formulation buffer. The intermediate IgG formulations were filtered by using a 0.2-µm Millex-VV syringe filter unit (Millipore, Germany). PS80-MC and PS80-ChP stock solutions were prepared at 2% (w/v) by weighing 1 g of neat PS80 in a 50-ml volumetric flask, followed by the addition of the required amount of highly purified water. PS80 stock solutions were filtered by using a 0.2-µm Millex-VV syringe filter unit and stored at -80 °C. Intermediate PS80 stock solutions, at 1% and 0.01%, were prepared freshly from PS80 stock solution and an appropriate amount was added to the IgG formulation to reach the desired PS80 concentrations described in the results section. Finally, formulation buffer was added to the IgG formulations in order to reach a target protein concentration of 5 mg/ml.

Mechanical stress methods

Shaking stress was performed by constant agitation of vertically placed 2R glass vials at 500 rpm at 25 °C by using an IC 4000 shaker (IKA, Germany). Vials were filled with sample to 50% of their maximum volumetric capacity, closed with 13-mm rubber stoppers (bromobutyl, FluoroTec B2-40 coating) and standard aluminum crimp camps, and protected from light during stress. Analysis of the formulations was performed after 0 h, 72 h and 360 h of shaking.

Free-fall stress was carried out by using an in-house designed apparatus which meets the ISO specifications[26]. 2R glass vials filled with sample to 50% of their total volume and crimped with 13-mm rubber stoppers (bromobutyl, FluoroTec B2-40 coating) and standard aluminum crimp camps, were subjected to repetitive free falls from a height of 1 m. The vial lands on a smooth surface made of hard, 3-mm thick rigid steel, backed by a wooden board of 20 mm in thickness. A custom 3D printed vial holder ensures a constant angle of the vial (45°) during and at the end of the fall. The fixed vial travels through a tube to ensure a non-turbulent fall. Formulations were analyzed after 0, 1, 2, 5, 10 and 20 free falls.

Pumping conditions, present during protein manufacturing, were mimicked by using a neMESYS apparatus[28] equipped with glass Hamilton-Gastight syringes and polytetrafluoroethylene (PTFE) plungers (Hamilton, Switzerland) placed in custom 3D printed holders. Formulations were stressed for a defined number of passes through a 20-cm PEEK capillary (inner diameter: 1 mm; Thermo Scientific, USA) at a fixed velocity of 8.84 ml/min. Prior to submitting each sample to stress, a control sample consisting of only formulation buffer (with or without PS80) was passed 20 times and analyzed for particle content to ensure cleanliness of the system. Each sample was passed 100 times through the capillary, corresponding to ca. 50 min of pumping of the sample solution, at room temperature. Each sample tested with the syringe pump method was prepared and stressed in triplicate, unless otherwise stated.

Analytical methods

Ultra performance size-exclusion chromatography (SEC)

An Acquity UPLC I-Class (Waters Corporation, USA) system equipped with a titanium cell UV detector was employed for analysis. Ten μg of protein was injected into a TSK gel UP-SW3000, 4.6 x 150 mm column (Tosoh Bioscience, Japan). Separation was achieved by using isocratic conditions with a mobile phase consisting of 150 mM sodium sulfate and 100 mM sodium phosphate dihydrate at pH 6.8 with a flow rate of 0.22 ml/min. UV detection was performed at a wavelength of 215 nm. Monomer content and total recovery (based on the area under the curve (AUC) of stressed sample relative to that of non-stressed (reference) sample) were determined.

High performance liquid chromatography coupled with a charged aerosol detector (LC-CAD)

Characterization and quantification of PS80 and its degradation products was performed by using the method developed by Kranz *et al*[19]. A Dionex Ultimate 3000 HPLC system hyphenated with a Corona Veo CAD (Thermo Scientific, USA) was used. Separation was achieved by using a BEH C18 column, 50 x 2.1 mm (Waters, USA) at 60 °C. A 6-point calibration curve was generated for quantification of PS80 supplemented to the IgG formulations that were investigated in this study. Data integration and processing was

performed with Chromeleon V6.8, where composition of PS80 was grouped into POE, monoesters and polyesters.

UV spectroscopy

A Tecan Safire² plate reader (Tecan, Austria) was used for the determination of the protein content at 280 nm (A280nm) and assessment of turbidity/optical density at 350 nm (OD350nm). Triplicate measurement of 200 µl sample in a 96-well plate was performed. The absorbance of the respective formulation buffer was subtracted from each sample measurement. A280nm values were corrected for light scattering by subtracting absorbance at 320 nm. Undiluted protein concentration was acquired after correction with the dilution factor. Optical density of undiluted samples was determined at 350 nm to assess turbidity. Presented turbidity values were determined from the difference between OD350nm of stressed samples and that of identical unstressed samples.

Dynamic light scattering (DLS)

DLS was performed by using a Zetasizer APS 2000 plate reader (Malvern Instruments, UK) equipped with a 633-nm He-Ne laser set at an angle of 90°. Individual wells within a 96-well plate (Corning Costar, United States) were filled with 150 µl of sample. The attenuator was set automatically. Samples were equilibrated to a working temperature of 25 °C for 60 s prior to each analysis. The Z-average diameter (Z-ave), polydispersity index (PDI) and intensity-weighted size distribution were derived from the autocorrelation function using the default settings for protein solutions in sucrose solution (10% w/v). Each measurement was performed in triplicate.

Flow imaging microscopy (FIM)

MFI 5200 (ProteinSimple, USA) was used for characterization and quantification of particles ≥2 µm in equivalent circular diameter. The system was equipped with a silane-coated high-resolution 100-µm flow cell. Formulation buffer was used to perform optimization of illumination and 0.28 ml of IgG formulation was analyzed within each measurement. Data was processed by using MVAS V2.3 software and the concentrations

of particles ≥ 2, 5, 10, and 25 µm as well as exemplary particle images of particles ≥ 25 µm were reported. Each sample was measured once.

Backgrounded membrane imaging (BMI)

BMI for micrometer-sized particle characterization and quantification was performed by using Horizon (Halolabs, USA). Under laminar air flow conditions 30 µl of sample was transferred on a polycarbonate 96-well membrane filter plate (Halolabs, USA) with a 0.4-µm pore size. Vacuum of 350 mbar was applied after filling 6 wells to allow a flow of liquid through the membrane and entrapment of particles. Subsequently, 90 µl of highly purified water was used to wash each well after sample transfer to remove any soluble material. Each sample was measured in triplicate.

Results

Shaking stress

The IgG formulations without PS80 and with three different concentrations of MC-PS80 or ChP-PS80 (0.04%, 0.004% and 0.0004% (w/v)) were subjected to vertical shaking for 72 h and 360 h at 25°C (Figure 1). The formulation without PS80 showed a significant increase in turbidity (UV), Z-average diameter (DLS), and micrometer-sized particle concentration (FIM) after 72 h of shaking, at which point the stress was discontinued. On the contrary, no substantial changes occurred even after 360 h of shaking when formulating the IgG with 0.04% and 0.004% w/v PS80, independent of the PS80 grade. However, at lower concentrations of PS80 a small increase in particle concentration was observed at T0. Interestingly, stressed IgG formulations with the lowest MC-PS80 or ChP-PS80 concentration of 0.0004% (w/v) showed a larger decrease in monomer content than the PS80-free formulation. In addition, an increase in high-molecular-weight species occurred to a greater extent than in the PS80-free formulation (data not shown).
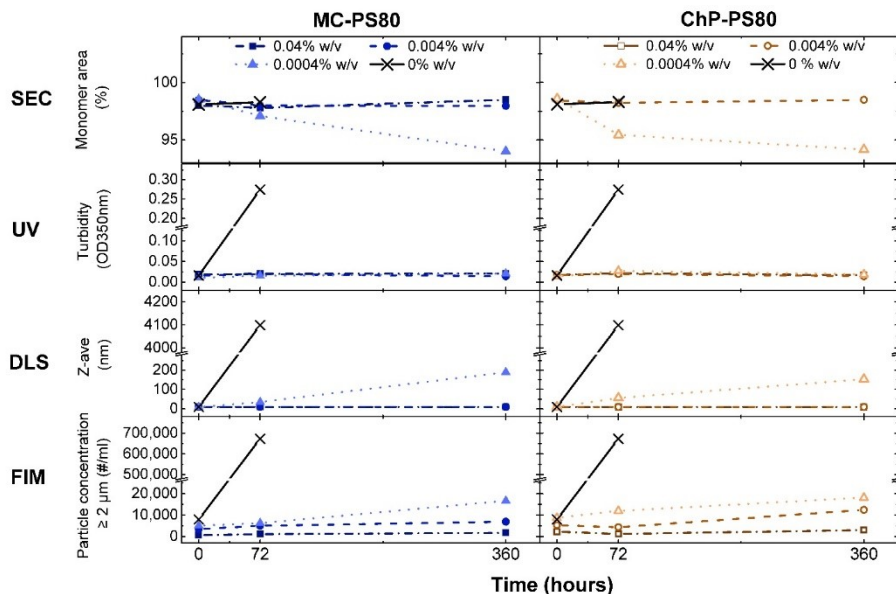
Figure 1: Aggregation over time of 5 mg/ml IgG formulated with different amounts of MC-PS80 or ChP-PS80, stressed by shaking in 2R glass vials at RT, as analyzed by SEC, UV (OD350nm), DLS and FIM.

Free-fall stress

2R glass vials filled with 1.5 ml of IgG formulation were dropped (0 to 20 falls) on a rigid surface to induce stress. With an increasing number of falls, a consecutive increase in the Z-average diameter (DLS) and concentration of micrometer-sized particles (FIM) was observed in IgG formulations without PS80 (Figure 2). IgG in presence of MC-PS80 or ChP-PS80 was well protected, and even after 20 falls no clear increase in micrometer-sized particle content was observed. IgG formulations with 0.0004% (w/v) PS80 of either grade did show a slight increase in Z-average diameter. No changes after stress were observed in SEC and turbidity analyses (data not shown). Similarly as in shaking stress, no difference between the functionality of the two grades of PS80 was observed.
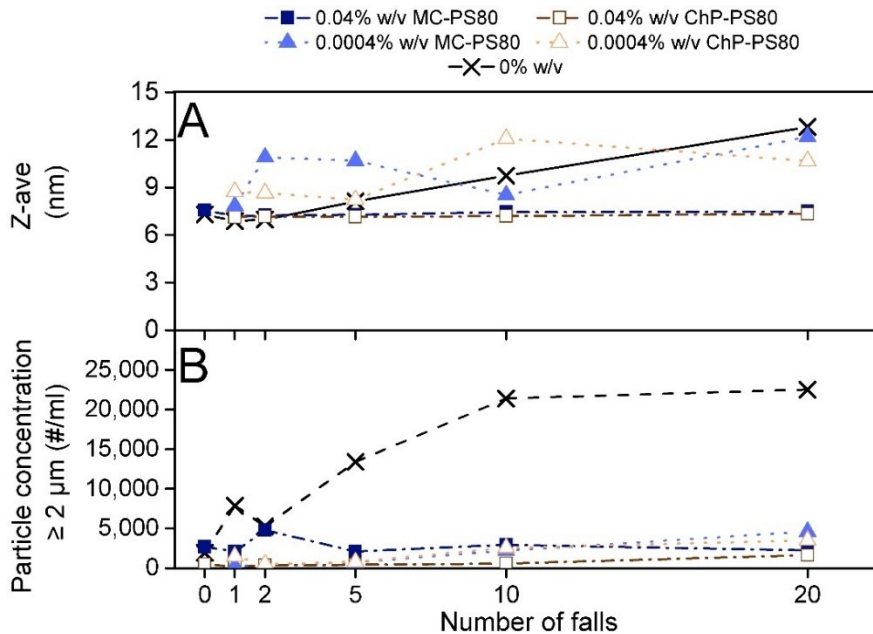
Figure 2: (A) Z-average diameter (DLS) and (B) micrometer-sized particle concentration (FIM) in 5 mg/ml IgG formulations (PS80-free and supplemented with MC-PS80 or ChP-PS80 at target concentrations 0.04% and 0.0004% (w/v)) exposed to free-fall stress as function of number of falls.

Syringe pump stress

Syringe pump stress induced a high concentration of micrometer-sized particles, which made DLS analysis unfeasible. Therefore, we focused on the characterization of soluble aggregates (SEC), sample turbidity (OD350nm) and particles sized ≥ 2 µm (FIM and BMI).

The formation of high-molecular-weight species and fragments after stress was negligible (< 0.5%). Therefore, the protein recovery by SEC practically equaled the monomer recovery. A slight decrease in protein recovery was observed with the two lowest PS80 concentrations, whereas the lowest recovery was obtained for IgG formulations without PS80 (Figure 3 A). At each tested PS80 concentration, the protein recovery for ChP-PS80 compared to formulations with MC-PS80 was statistically similar (T-test, two-sided, p>0.41), indicating a comparable protective effect of the two PS80 grades. After stress, the OD350 nm taken as measure for turbidity was slightly increased (OD350 values for all unstressed formulations were 0.011 ± 0.003), which was more pronounced with decreasing amount of

PS80 (Figure 3 B). Nevertheless, based on turbidity data no significant difference between the protective effect of the two PS80 grades could be observed (T-test, two-sided, p>0.07).
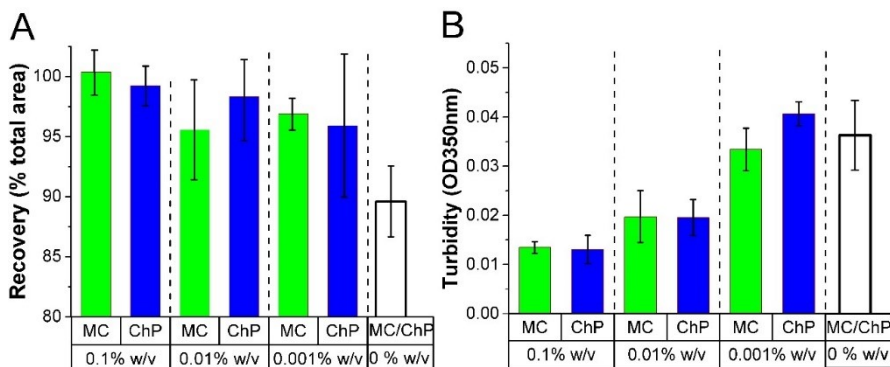

Figure 3: (A) Protein recovery (SEC) and (B) turbidity (OD 350nm UV spectroscopy) in IgG formulations after exposure to syringe pump stress in absence (no PS80) and presence of 0.1%, 0.01% and 0.001% (w/v) of MC-PS80 and ChP-PS80. Turbidity values present the difference between OD350nm of stressed samples and that of identical unstressed samples. Error bars represent standard deviation of mean values from triplicate stressed IgG formulations.

Figure 4 A-D presents the micrometer-sized particle concentration determined by FIM and BMI in stressed formulations of IgG in absence and presence of PS80 over a range from 0 to 0.1% (w/v). For each stressed sample, most of the measured particles were in the size range 2-25 μm (FIM and BMI). Both, MC-PS80 and ChP-PS80 at concentrations 0.1% and 0.01% (w/v) suppressed the formation of particles in IgG formulations during syringe pump stress. No significant difference was found between the number of particles measured in stressed formulations with MC-PS80 and ChP-PS80 for all three concentrations (T-test, two-sided, p>0.23). However, the cumulative number of particles (sized ≥2 μm) per ml in stressed formulations at the two higher PS80 concentrations (0.01% and 0.1%) was at least 2-fold lower compared to formulations without PS80. Formulations with the highest concentration of PS80 had less particles ≥ 10 μm in size compared to all other tested formulations. Interestingly, the lowest concentration of both PS80 grades (0.001% (w/v)) showed modestly higher particle counts, in the size range 2-25 μm compared to the formulations without PS80. Nonetheless, highly similar particle size distributions were detected in the stressed formulations for both PS80 grades at the three tested

concentrations. A high proportion of particles formed during syringe pump stress were ≥10 µm in size, whereas the vast majority of particles found in IgG formulations after shaking and free-fall stress were 2-10 µm in size. Overall, the measured particle concentrations within each size range by FIM and BMI were highly similar for the two techniques. Lower numbers of particles in samples with PS80 at 0.001% (w/v) were detected by BMI compared to FIM, which could be explained by exceeding the recommended higher limit of quantification for BMI[29]. Particle levels measured by FIM in control samples (corresponding PS80 formulation without protein subjected to the same type of stress) did not exceed a concentration of 6,000 particles ≥2 µm/ml throughout the study.
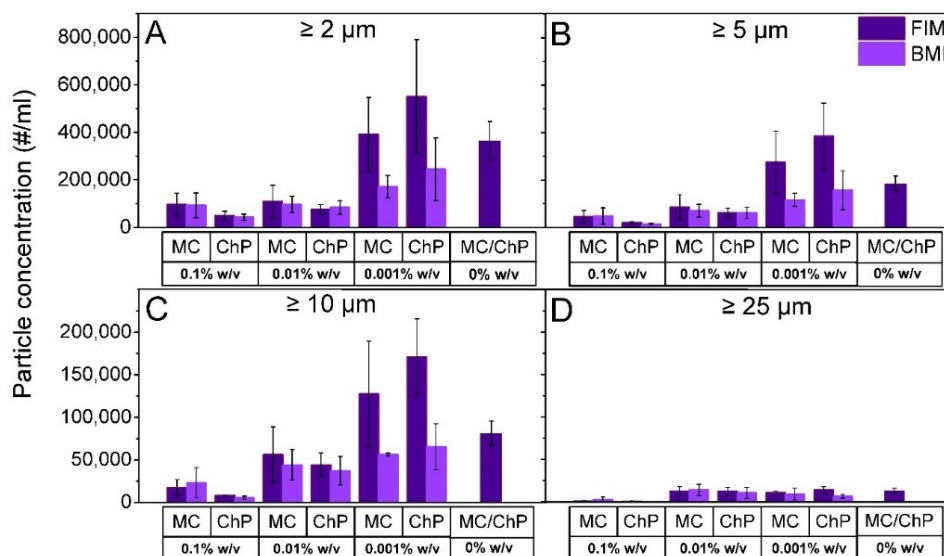
Figure 4: Micrometer-sized particle concentrations ≥ 2 µm (A), ≥ 5 µm (B), ≥ 10 µm (C) and ≥ 25 µm (D) in syringe pump stressed IgG formulations with MC-PS80 (MC), ChP-PS80 (ChP) and without PS80 (no PS80) determined by using FIM and BMI. Error bars represent standard deviation of mean values from triplicate stressed IgG formulations.

Characterization of syringe pump stress induced particles

Morphologies of exemplary particles formed after the three stress methods are presented in Figure 5. Clear differences between particle morphologies can be observed, depending on the type of mechanical stress used and on the presence of PS80. Differences in particle intensity depending on the presence of PS80 were especially apparent in formulations

submitted to syringe pump stress (Figure 5). Within the stressed PS80-containing IgG formulations, particles were dark and compact – independent of the PS80 grade. However, in stressed IgG formulations without PS80 a noticeable subpopulation of transparent, fibrous-like particles was observed. Light-microscopic imaging of the particles isolated by membrane filtration confirmed the presence of two distinct particle morphologies in syringe pump stressed IgG formulations without PS80: white 'flakes' and thin transparent ´foils´ (data not shown). The flake-like particles showed relatively high thickness (several microns) in images obtained by using scanning electron microscope (SEM), whereas the transparent foil-like particles could not be imaged because of the lack of reflectance.
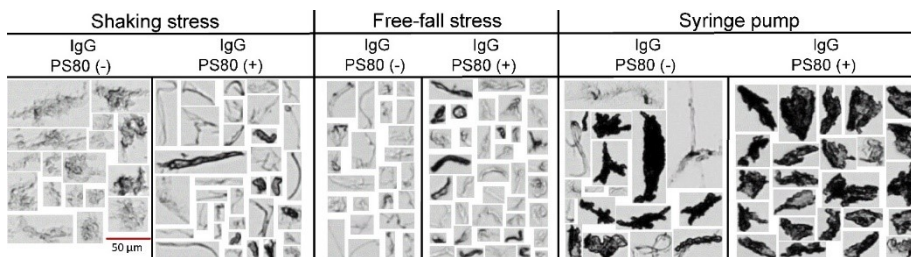
Figure 5: Representative FIM images of particles in stressed IgG formulations with the three mechanical stress methods. Particles are grouped into IgG formulation without PS80 and in presence of PS80 (no morphological differences were observed in particles formed in presence of MC-PS80 and ChP-PS80).

Attenuated total reflection Fourier transform infrared spectroscopy (ATR-FTIR) was performed on isolated particles from stressed IgG formulations to determine the nature of the particles formed during syringe pump stress. The obtained spectra of particles formed in presence (Figure 6 A) and absence (Figure 6 B) of PS80 showed typical protein bands (amide I between 1600 and 1700 cm^{-1}; amide II between 1510 and 1580 cm^{-1}). Additionally, SEM with energy dispersive X-ray spectroscopy showed that isolated particles consisted of solely carbon, oxygen, nitrogen and sulfur - an elemental composition consistent with protein. Therefore, we conclude that most of the formed particles are proteinaceous, most likely IgG, rather than contaminants from the syringe pump device.
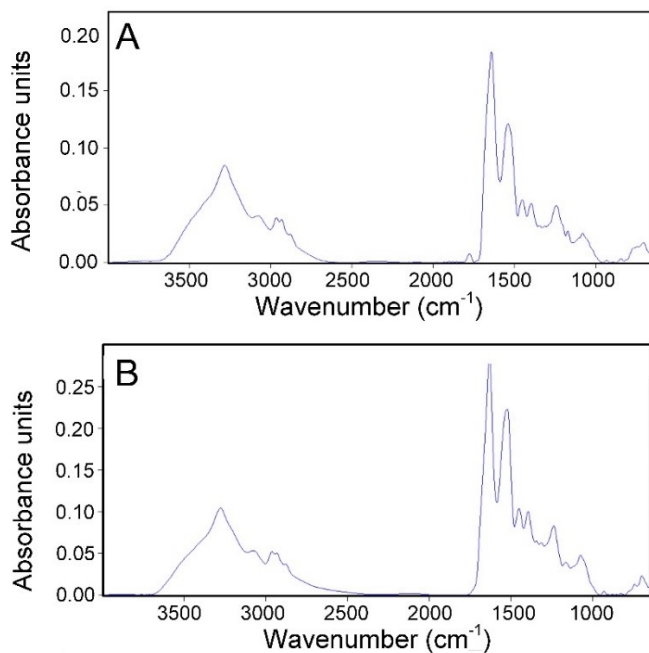
Figure 6: Average ATR-FTIR spectra performed on particles found within an area of 100 μm in the radius of filtration spot. Particles were generated during syringe pump stress in IgG formulation (A) with 0.01% w/v MC-PS80 and (B) without PS80.

Degradation of PS80 and impact of PS80 degradation products on IgG stability

Chemical hydrolysis of MC-PS80 and ChP-PS80 was performed, and the effect of different levels of surfactant degradation on the stability of the IgG during mechanical stress was examined.

LC-CAD analysis of intact PS80 showed three broad peaks eluting at 8.1, 8.9 and 9.4 min, which represent the majority of the monoester fraction (Figure 7 A). The polyester fraction eluted mainly between 11.5 and 12.5 min. The POE fraction was nearly absent in the intact PS. However, after hydrolysis the peak area of the free POE fraction (between 1 and 5 min) increased significantly, whereas the mono- and poly-ester peaks were practically absent. Therefore, we can conclude that the chemical degradation yielded fully hydrolyzed PS80.

Figure 7 B presents the concentration of particles ≥ 2 μm (FIM and BMI) in size present in samples with degraded PS80 (of different degree of hydrolysis; no IgG present) prior to stress. Especially high numbers of particles were measured in samples with a high degree of PS80 hydrolysis (90% and 100%). For samples with 50% or less degradants, the number of particles per ml was below 15,000. From the FIM particle images, it was obvious that mainly droplet-like particles were formed (Figure 7 C). Indeed, BMI measurements showed very low particle counts: it is expected that the droplets, being most likely composed of liquid oleic acids, were not retained on the membrane during sample preparation.
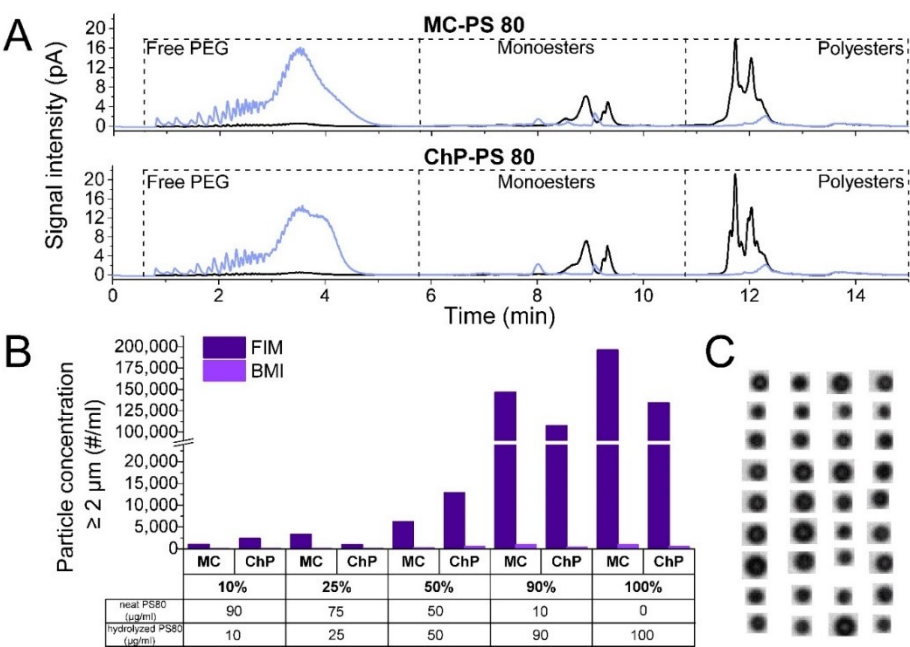
Figure 7: (A) RP-HPLC chromatograms of intact PS80 (black line) and fully hydrolyzed PS80 (light blue line). (B) Particle concentration in hydrolyzed PS80 samples measured by using FIM and BMI. Percentages indicate degree of PS80 hydrolysis. (C) Exemplary FIM images (≥ 5 μm) of a fully hydrolyzed MC-PS80 sample.

Samples of fully degraded MC-PS80 contained more particles compared to fully degraded ChP-PS80. Moreover, quantification of myristic, palmitic, stearic, oleic, and linoleic acids by using HPLC coupled with fluorescence detection supported the particle data and showed higher amounts of FFA in fully hydrolyzed MC-PS80 compared to ChP-PS80 (data not shown).

We utilized the syringe pump device to evaluate the impact of PS80 degradation on protein stability during mechanical stress. The stability of the IgG formulated with intact PS80 and hydrolyzed PS80 (10-100% hydrolysis) was examined (Figure 8 A-C). The PS80 concentration in stressed formulations was equal to 0.01% w/v and the degree of hydrolysis is described by the percentage of fully hydrolyzed PS80 mixed with neat PS80 (see Materials and Methods). For this part of the study, a single preparation and measurement was performed for each sample. Quantification of particles ≥ 2 µm showed an increasing particle concentration with increased extent of PS degradation for both PS80 grades. It must be noted that unstressed IgG formulations (controls), with PS80 hydrolyzed at 90% and 100%, contained a high background level of particles determined by FIM. Therefore, in IgG formulations with 90% and 100% degraded PS80 the particle levels in the controls were 11-15% (ChP-PS80) and 21-24% (MC-PS80) of the total particle concentration found in stressed formulations. However, most of the particles in unstressed IgG formulations were identified as droplets, originating from FFA present in the hydrolyzed material. For both PS80 grades the extent of surfactant hydrolysis on stressed IgG in terms of formed micron-sized particles was similar. An exception was the sample with 50% hydrolyzed PS80, where a clear difference in particle concentration was observed between MC-PS80 and ChP-PS80. Both unstressed IgG formulations containing partially (50%) degraded PS80 had low concentrations of particles sized ≥ 2 µm (below 10,000 #/ml). Therefore, the high number of measured particles in stressed formulations originates solely from the applied stress and reflects the functionality of PS80 (see discussion). The recovery in SEC was similar for all stressed IgG formulations with hydrolyzed PS80. A slight increase in turbidity was detected for formulations with a higher degree of hydrolyzed PS80, but no difference between formulations with different PS80 grades was observed.
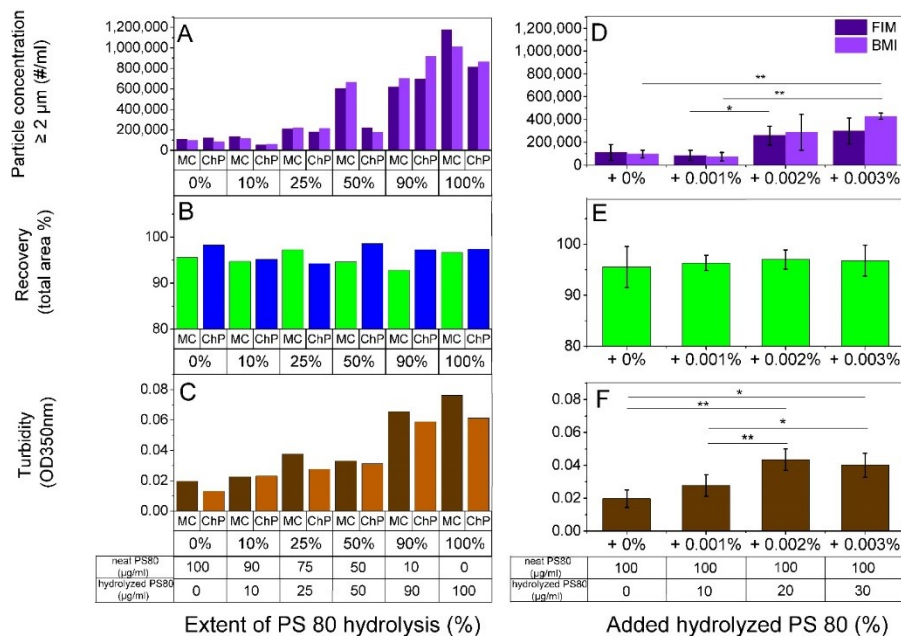
Figure 8: Syringe pump stressed IgG formulations with PS80. X-axes present extent of 0.01% (w/v) MC-PS80 and ChP-PS80 degradation (A-C) and amount of fully hydrolyzed MC-PS80 added to IgG formulations with 0.01% (w/v) (D-F). Extent of IgG aggregation was assessed by measuring micrometer-sized particle concentration (FIM and BMI, A and D), protein recovery (SEC, B and E) and turbidity (UV, C and F). Error bars represent standard deviation of mean values from triplicate stressed formulations. *p < 0.05 was considered statistically significant and **p < 0.01 highly significant.

Next, we investigated the impact of PS80 degradants on protein stability during mechanical stress. For this purpose, the IgG formulation with 0.01% (w/v) MC-PS80 was spiked with degradants from fully hydrolyzed MC-PS80. The amounts of MC-PS80 degradants spiked into the IgG formulation were equivalent to fully hydrolyzed MC-PS80 at 0.001%, 0.002% and 0.003% (w/v). Therefore, IgG formulations contained degradants at three different concentrations on top of the 0.01% (w/v) intact PS80. Micrometer-sized particle concentration, protein recovery and turbidity data of stressed formulations is presented in Figure 8 D-F. A significant difference (T-test, two-sided, p<0.05) in concentration of particles ≥2 μm in size after stress was observed for formulations with additional 0.002% and 0.003% (w/v) of degradants compared to formulations with no or 0.001% (w/v) of spiked-in hydrolyzed PS80 degradants. The latter two formulations showed a highly similar particle content after stress. No apparent loss of protein after stress had occurred according to the

SEC data. However, optical density at 350 nm was significantly higher (T-test, two-sided, p<0.05) for stressed IgG formulations containing 0.02% and 0.03% (w/v) spiked-in degradants compared to formulations with 0% or 0.01% (w/v) of degradants. The increase in particle concentration and optical density in stressed IgG formulations with degradation products originating from MC-PS80 hydrolysis show the apparent destabilizing properties of PS80 degradants.

Discussion

Choosing the optimum PS type and concentration to be used in protein-based pharmaceuticals is an integral part of formulation development programs. Up until now, there has been only one published study evaluating the functional properties of different PS80 grades in IgG formulations, where the focus was placed on chemical degradation of the IgG[30]. In our study we report for the first time the effectiveness of both PS80 grades (multicompendial vs Chinese Pharmacopoeia) in inhibiting protein aggregation in formulations exposed to various types of mechanical stress.

We characterized IgG formulations with MC-PS80 or ChP-PS80 at three different concentrations, as well as without PS80, exposed to shaking stress up to two weeks. Shaking increases the contact area of proteins with air-liquid interfaces. Furthermore, it causes mechanical perturbation of the interface, thereby increasing the probability of intermolecular protein-protein interactions as well as desorption of aggregated species into bulk solution[31,32]. The propensity of protein molecules to accumulate at phase boundaries makes the air-liquid interfacial stress the predominant stress factor during shaking. Nevertheless, cavitation and solid-liquid interfaces are also detrimental to the physical stability of proteins[4]. The IgG formulation without PS80 was highly unstable during shaking stress: it was visibly turbid and presented high numbers of nano- and micrometer-sized particles after three days of shaking. Thus, our model IgG was highly sensitive to mechanical stress if formulated without any surfactants. On the contrary, even after 14 days of shaking, IgG formulations supplemented with either PS80 grade showed modest to no changes in terms of turbidity and particulate content. However, a concentration dependent effect for MC-PS80 and ChP-PS80 was observed. Elevated number of particles ≥ 2 μm and > 5%

monomer loss after 14 days of shaking stress was observed in IgG formulations with PS80 of both grades at the lowest concentration (0.0004% w/v), which is below PS80's CMC of 0.0017% (w/v)[33]. A PS concentration dependent destabilization was also observed by Kiese et al., who observed an increase in high molecular weight species (HMWS) in stressed formulations consisting of 0.0025% (w/v) PS 20 (CMC of 0.011% w/v[33]) compared to formulations with 2-fold or 4-fold higher concentrations[34]. Nonetheless, we found MC-PS80 and ChP-PS80 to have a highly similar protective effect at equal surfactant:protein molar ratio and surfactant:interface area ratio[35].

Mechanical shock can result from inappropriate handling of biopharmaceutical products where a vial or syringe is dropped in its primary or secondary package. It was reported that mechanical shock treatment results in cavitation leading to formation and collapse of short-lived bubbles[24,25,36]. Consequences of these events are free radicals, local high temperatures and high-pressure shock waves, which may lead to localized oxidative and/or conformational changes of proteins. Furthermore, formation of bubbles increases the transiently available air-liquid interfaces[36]. In agreement with the cited studies, we observed an increase in concentration of nano- and micrometer-sized particles present in IgG formulations without PS80 after free fall stress and the formed mechanical shock. PS80 of both grades inhibited the formation of particles after mechanical drops, which became more apparent when the IgG formulations were dropped ≥ 5 times. PS80 was reported neither to have an effect on the thermostability of IgGs[37] nor to inhibit oxidation in IgG formulations[19]. Therefore, the inhibition of particle formation seen in formulations containing PS80 suggests interface-mediated aggregation as the predominant factor causing aggregation in dropped vials. Particle formation in formulations exposed to free-fall stress was suppressed in presence of PS80; and even at low PS80 concentrations (below CMC) solely a very small increase of micron-sized particles could be observed. Similarly, as observed after shaking stress, no difference in functionality of PS80 was determined between the two grades.

By using our customized syringe pump device, with multiple cycles we observed significant particle formation in IgG formulations with and with no PS80. The extensive protein

aggregation could have been the result of multiple stress factors, such as shear in the capillary, extensional flow at the exit of the capillary and interfacial stresses within the syringe barrels (PTFE and glass surfaces). Previously, it was reported that exposure of globular proteins to a "pure" shear stress of 10^7 s^{-1} should not cause unfolding or aggregation[38]. However, a combination of shear and solid-liquid or air-liquid interfaces had a detrimental effect on the structural integrity of investigated globular proteins[39,40]. Furthermore, adsorption and desorption of (un-)folded protein and nanometer-sized proteinaceous particles to syringe surfaces may result in remarkably higher counts in protein particles after stress, as demonstrated by Torisue et al.[24]. Therefore, the concomitant stresses during syringe pumping could allow for assessment of the functionality of PS80 grades with respect to adsorption of surfactant molecules onto the protein via hydrophobic interactions as well as competitive adsorption to interfaces.

Similarly, as with the two previous stress methods, in syringe pump stress both PS80 grades at 0.1% and 0.01% (w/v) reduced the number of micron-sized particles to a similar degree. The PS80 concentration effect on particle formation for both grades is clearer for particles ≥10 μm in size where an increase in particle concentration is correlated with a decreasing PS80 content (Figure 4 C and D). The relative size distributions for protein particles in IgG formulations with MC-PS80 and ChP-PS80 are highly similar. Independent of the grade, the highest tested PS80 concentration resulted in the lowest number of particles sized ≥ 25 μm, indicating the best properties in inhibiting formation of large particles.

At the lowest tested PS80 concentration (0.001% (w/v)), stressed formulations after syringe pump stress contained slightly higher micron-sized particle concentrations compared to IgG formulations without PS80. The destabilizing effect at low PS concentrations was also observed in our shaking stress study and previously by Kiese et al.[34]. The mechanism of the PS concentration dependent destabilization effect is currently unclear. However, the effect was observed only with PS concentrations below the CMC, suggesting specific protein:surfactant ratios to show this behavior.

The FIM images revealed a heterogeneous mixture of particles in each stressed formulation (Figure 5). The presence of PS80 in the IgG formulations and the type of mechanical stress

applied had a substantial impact of the morphology of the particles. The formation of distinct particle appearances may result from one or more predominant aggregation pathways leading to specific assembly of IgG molecules into non-native aggregates[41]. Our results correlate with the existing literature, i.e., the type of stress applied to a protein formulation has a clear impact on the morphology of formed particles[42-46]. Furthermore, particles formed in our stressed IgG formulations (independent of the type of mechanical stress) presented irregular and elongated structures, which are associated with disruption of interfacial protein gel layers formed at interfaces[43,44]. Even though PS80 at 0.001% (w/v) did not exhibit any protective role with respect to particle concentrations in IgG formulations submitted to syringe pump stress, all formulations with PS80 contained one predominant particle population regarding the morphology. In contrast, particle populations of two distinct morphologies were present in stressed IgG formulations without PS80. Therefore, even minute amounts of surfactant may inhibit certain aggregation pathways. Nonetheless, no direct connection has been found between molecular interactions and the resulting particle morphology on the micrometer scale[42]; and studying this further was beyond the scope of this study.

The two main degradation pathways for PS80 include oxidation and hydrolysis. Hydrolytic cleavage of the ester bond in PS80 can be enzymatically or chemically (low or high pH) catalyzed. Whereas chemically driven hydrolysis is generally not a concern for products stored at 5 °C or 25 °C, residual host cell proteins (HCPs) may enhance the rate of PS hydrolysis during a product's shelf life[38,39]. The presence of these enzymatic proteins is a result of insufficient downstream purification processes and can result in issues during formulation development. For both chemical and enzymatic hydrolysis, POE and FFA are the main degradation products. To avoid complexity by introducing an enzyme to the IgG formulations, the PS degradants used in our study were obtained from a base catalyzed hydrolysis reaction.

Several authors have reported the potential impact of PS 80 degradation products on the stability of therapeutic proteins during stress and storage[12,20,47,48]. IgG formulations containing FFA originating from PS20 showed particle formation upon long-term storage at

2-8°C; PS20 with fatty acid esters of variable lengths showed higher destabilizing properties compared to PS20 with only lauric acid[49]. Furthermore, Kishore et al. observed an increase in opalescence and soluble aggregate content in shake stressed IgG formulations with free lauric acid and PS20 in contrast to statically stored samples[20].

In our study, fully hydrolyzed PS80 samples, of both grades, contained high numbers of spherical, oil-drop like particles in the size range 2-5 µm (FIM). Oleic acid– the main product of PS80 hydrolysis – is liquid at room temperature and therefore the droplets can be attributed to oleic acid droplets. The presence of oil droplets could explain the significant difference in concentration of micrometer-sized particles between PS80 samples with 50% and 90% degradation products (Figure 7). For samples with the amount of PS80 degraded below 50%, the free oleic acid is most likely incorporated into micelles composed of neat PS80 and droplets are not expected to form. For particle characterization of the stressed IgG formulations used in this study, FIM and BMI were used as orthogonal methods to allow for the differentiation between proteinaceous particles induced by stress and fatty acid droplets originating from PS80 degradation. A hydrolytic 10% loss of MC-PS80 and ChP-PS80 resulted in no change in PS80 functionality, when comparing the formation of proteinaceous particles during syringe pump stress to formulations with 0.01% PS80 (Figure 8 A). A slight increase in proteinaceous particle concentration after stress was observed for formulations with 25% hydrolyzed PS80. At 50% PS80 hydrolysis, ChP-PS80 partially retained its functionally, whereas MC-PS80 showed minimal protective role in mechanical stress. This difference could be the result of different amount of FFA in the nominal 50% degraded MC-PS80 compared to ChP-PS80. In fact, the total (soluble and particulate form) free fatty acids concentration in fully hydrolyzed MC-PS80 was approximately 2-fold higher compared to the ChP-PS80 (data not shown), which could result in an overall higher concentration of FFA in the preparations at 50% nominal PS80 hydrolysis. Although FIM and BMI showed comparable results for both PS80 grades at 50% hydrolysis in absence of protein (Figure 7), it is possible that more FFA particles of different nature (e.g., stearic or palmitic acid derived particles) were present in MC-PS80 and promoted aggregation of the IgG during syringe pump stress.

Furthermore, we showed that the loss of PS80 functionality may not be related solely to the lower amount of available intact PS80 but also to the presence of PS80 degradants. When spiking a small amount of degraded MC-PS80 (0.002% and 0.003% w/v) to an IgG formulation consisting of MC-PS80 at 0.01% (w/v), we observed an increase in particle concentration and turbidity after stress. No loss of protein or formation of HMWS was observed, which is in agreement with previous results where an addition of 0.03% (w/v) of PS80 degradants did not induce HMWS in shaked IgG formulations containing 0.01% w/v of PS80[20]. No significant effect on protein stability was observed for IgG formulations spiked with 0.001% (w/v) of degraded MC-PS80. This suggests a certain threshold for the amount of degradants which must be reached in the IgG formulation to see pronounced destabilizing effects of hydrolyzed PS80.

Conclusions and outlook

The presented work shows that MC-PS80 and ChP-PS80 similarly inhibit the formation of aggregates and micrometer-sized particles in IgG formulations upon mechanical stress, pointing towards a similar functionality of the two grades. A comparable PS80 concentration dependent effect for both PS80 grades was observed, irrespective of the mechanical stress method applied: shaking, free-fall or syringe pump stress. Furthermore, very low PS80 concentrations (below the CMC values) showed minimal protection or even had destabilizing properties to the IgG during mechanical stress. The syringe pump stress had stronger destabilizing effects on the IgG than the other two stress methods; therefore, it was used to evaluate the impact of PS80 degradants on IgG stability. We found that PS80 exposed to hydrolytic degradation is no longer capable of sufficiently stabilizing the IgG during syringe pump stress. Additionally, hydrolytic degradants (of MC-PS80) may destabilize the IgG and promote particle formation. Functionality of both PS80 grades after long-term storage was not investigated, but should be considered given the recently described differences in stability of MC-PS80 and ChP-PS80[19]. Further studies would also be necessary to evaluate if the "harsh" syringe pump stress conditions correlate with current Fill&Finish manufacturing conditions. Our study points out that it is important to monitor

PS during drug product formulation development and stability testing of therapeutic proteins.

References:

1. Mahler H-C, Fischer S, Randolph TW, Carpenter JF. Protein Aggregation and Particle Formation: Effects of Formulation, Interfaces, and Drug Product Manufacturing Operations. In: Wang W, Roberts CJ, eds. *Aggregation of Therapeutic Proteins*, John Wiley & Sons, Inc.; 2010:301-331.

2. Carpenter J, Cherney B, Lubinecki A, Ma S, Marszal E, Mire-Sluis A, Nikolai T, Novak J, Ragheb J, Simak J. Meeting report on protein particles and immunogenicity of therapeutic proteins: Filling in the gaps in risk evaluation and mitigation. Biologicals 2010; 38(5):602-611.

3. Wang W, Roberts CJ. Protein aggregation – Mechanisms, detection, and control. Int. J. Pharm 2018; 550(1):251-268.

4. Li J, Krause ME, Chen X, Cheng Y, Dai W, Hill JJ, Huang M, Jordan S, LaCasse D, Narhi L, Shalaev E, Shieh IC, Thomas JC, Tu R, Zheng S, Zhu L. Interfacial Stress in the Development of Biologics: Fundamental Understanding, Current Practice, and Future Perspective. The AAPS Journal 2019; 21(3):44.

5. Kapp SJ, Larsson I, Van De Weert M, Cárdenas M, Jorgensen L. Competitive Adsorption of Monoclonal Antibodies and Nonionic Surfactants at Solid Hydrophobic Surfaces. J Pharm Sci 2015; 104(2):593-601.

6. Agarkhed M, O'Dell C, Hsieh M-C, Zhang J, Goldstein J, Srivastava A. Effect of Surfactants on Mechanical, Thermal, and Photostability of a Monoclonal Antibody. AAPS PharmSciTech 2018; 19(1):79-92.

7. Khan TA, Mahler H-C, Kishore RSK. Key interactions of surfactants in therapeutic protein formulations: A review. Eur. J. Pharm. Biopharm 2015; 97:60-67.

8. Bam NB, Cleland JL, Yang J, Manning MC, Carpenter JF, Kelley RF, Randolph TW. Tween protects recombinant human growth hormone against agitation-induced damage via hydrophobic interactions. J Pharm Sci 1998; 87(12):1554-1559.

9. Lee HJ, McAuley A, Schilke KF, McGuire J. Molecular origins of surfactant-mediated stabilization of protein drugs. Adv. Drug Deliv. Rev 2011; 63(13):1160-1171.

10. Liu L, Qi W, Schwartz DK, Randolph TW, Carpenter JF. The Effects of Excipients on Protein Aggregation During Agitation: An Interfacial Shear Rheology Study. J Pharm Sci 2013; 102(8):2460-2470.

11. Thirumangalathu R, Krishnan S, Ricci MS, Brems DN, Randolph TW, Carpenter JF. Silicone Oil- and Agitation-Induced Aggregation of a Monoclonal Antibody in Aqueous Solution. J Pharm Sci 2009; 98(9):3167-3181.

12. Martos A, Koch W, Jiskoot W, Wuchner K, Winter G, Friess W, Hawe A. Trends on Analytical Characterization of Polysorbates and Their Degradation Products in Biopharmaceutical Formulations. J Pharm Sci 2017; 106(7):1722-1735.

13. Koo O. 2016. Pharmaceutical excipients: Properties, functionality, and applications in research and industry. ed. p 1-334.

14. Hoffmann C, Blume A, Miller I, Garidel P. Insights into protein–polysorbate interactions analysed by means of isothermal titration and differential scanning calorimetry. Eur Biophys J 2009; 38(5):557-568.

15. Deechongkit S, Wen J, Narhi LO, Jiang Y, Park SS, Kim J, Kerwin BA. Physical and biophysical effects of polysorbate 20 and 80 on darbepoetin alfa. J Pharm Sci 2009; 98(9):3200-3217.

16. Singh SM, Bandi S, Jones DNM, Mallela KMG. Effect of Polysorbate 20 and Polysorbate 80 on the Higher-Order Structure of a Monoclonal Antibody and Its Fab and Fc Fragments Probed Using 2D Nuclear Magnetic Resonance Spectroscopy. J Pharm Sci 2017; 106(12):3486-3498.

17. McShan AC, Kei P, Ji JA, Kim DC, Wang YJ. Hydrolysis of Polysorbate 20 and 80 by a Range of Carboxylester Hydrolases. PDA J Pharm Sci Technol 2016; 70(4):332-345.

18. Zhang R, Wang Y, Tan L, Zhang HY, Yang M. Analysis of Polysorbate 80 and its Related Compounds by RP-HPLC with ELSD and MS Detection. J Chromatogr Sci 2012; 50(7):598-607.

19. Kranz W, Wuchner K, Corradini E, Berger M, Hawe A. Factors Influencing Polysorbate's Sensitivity Against Enzymatic Hydrolysis and Oxidative Degradation. J Pharm Sci 2019; 108(6):2022-2032.

20. Kishore RSK, Kiese S, Fischer S, Pappenberger A, Grauschopf U, Mahler H-C. The Degradation of Polysorbates 20 and 80 and its Potential Impact on the Stability of Biotherapeutics. Pharm Res 2011; 28(5):1194-1210.

21. Hall T, Sandefur SL, Frye CC, Tuley TL, Huang L. Polysorbates 20 and 80 Degradation by Group XV Lysosomal Phospholipase A2 Isomer X1 in Monoclonal Antibody Formulations. J Pharm Sci 2016; 105(5):1633-1642.

22. Eppler A, Weigandt M, Hanefeld A, Bunjes H. Relevant shaking stress conditions for antibody preformulation development. Eur. J. Pharm. Biopharm 2010; 74(2):139-147.

23. Nejadnik MR, Randolph TW, Volkin DB, Schöneich C, Carpenter JF, Crommelin DJA, Jiskoot W. Postproduction Handling and Administration of Protein Pharmaceuticals and Potential Instability Issues. J Pharm Sci 2018; 107(8):2013-2019.

24. Torisu T, Maruno T, Yoneda S, Hamaji Y, Honda S, Ohkubo T, Uchiyama S. Friability Testing as a New Stress-Stability Assay for Biopharmaceuticals. J Pharm Sci 2017; 106(10):2966-2978.

25. Randolph TW, Schiltz E, Sederstrom D, Steinmann D, Mozziconacci O, Schöneich C, Freund E, Ricci MS, Carpenter JF, Lengsfeld CS. Do Not Drop: Mechanical Shock in Vials Causes Cavitation, Protein Aggregation, and Particle Formation. J Pharm Sci 2015; 104(2):602-611.

26. ISO/TC 11608-1:2014: Devices for administration of medicinal products and catheters. Needle-based injection systems for medical use —Requirements and test methods. Available at: https://www.iso.org/standard/65021.html. Accessed August 1, 2019.

27. Dobson J, Kumar A, Willis LF, Tuma R, Higazi DR, Turner R, Lowe DC, Ashcroft AE, Radford SE, Kapur N, Brockwell DJ. Inducing protein aggregation by extensional flow. PNAS USA 2017; 114(18):4673.

28. Heinzelmann U, Garidel P, Kern H-J, Langer A, Weber J. Apparatus for quantifying shear stress on a formulation comprising biomolecules. 2007; *US20100326200A1.* Available at: https://patents.google.com/patent/US20100326200. Accessed August 1,2019.

29. Helbig C, Ammann G, Menzen T, Friess W, Wuchner K, Hawe A. Backgrounded Membrane Imaging (BMI) for High-Throughput Characterization of Subvisible Particles During Biopharmaceutical Drug Product Development. J Pharm Sci 2019.

30. Singh SR, Zhang J, O'Dell C, Hsieh M-C, Goldstein J, Liu J, Srivastava A. Effect of polysorbate 80 quality on photostability of a monoclonal antibody. AAPS PharmSciTech 2012; 13(2):422-430.

31. Serno T, Hartl E, Besheer A, Miller R, Winter G. The role of polysorbate 80 and HPbetaCD at the air-water interface of IgG solutions. Pharm Res 2013; 30(1):117-130.

32. Couston RG, Skoda MW, Uddin S, van der Walle CF. Adsorption behavior of a human monoclonal antibody at hydrophilic and hydrophobic surfaces. MAbs 2013; 5(1):126-139.

33. Patist A, Bhagwat SS, Penfield KW, Aikens P, Shah DO. On the measurement of critical micelle concentrations of pure and technical-grade nonionic surfactants. J Surfactants Deterg 2000; 3(1):53-58.

34. Kiese S, Papppenberger A, Friess W, Mahler HC. Shaken, not stirred: mechanical stress testing of an IgG1 antibody. J Pharm Sci 2008; 97(10):4347-4366.

35. Chou DK, Krishnamurthy R, Randolph TW, Carpenter JF, Manning MC. Effects of Tween 20 and Tween 80 on the stability of Albutropin during agitation. J Pharm Sci 2005; 94(6):1368-1381.

36. Duerkop M, Berger E, Durauer A, Jungbauer A. Impact of Cavitation, High Shear Stress and Air/Liquid Interfaces on Protein Aggregation. Biotechnol J 2018; 13(7):e1800062.

37. Agarkhed M, O'Dell C, Hsieh M-C, Zhang J, Goldstein J, Srivastava A. Effect of polysorbate 80 concentration on thermal and photostability of a monoclonal antibody. AAPS PharmSciTech 2013; 14(1):1-9.

38. Bee JS, Stevenson JL, Mehta B, Svitel J, Pollastrini J, Platz R, Freund E, Carpenter JF, Randolph TW. Response of a concentrated monoclonal antibody formulation to high shear. Biotechnol Bioeng 2009; 103(5):936-943.

39. Biddlecombe JG, Smith G, Uddin S, Mulot S, Spencer D, Gee C, Fish BC, Bracewell DG. Factors influencing antibody stability at solid-liquid interfaces in a high shear environment. Biotechnol Prog 2009; 25(5):1499-1507.

40. Maa YF, Hsu CC. Protein denaturation by combined effect of shear and air-liquid interface. Biotechnol Bioeng 1997; 54(6):503-512.

41. Chi EY, Krishnan S, Kendrick BS, Chang BS, Carpenter JF, Randolph TW. Roles of conformational stability and colloidal stability in the aggregation of recombinant human granulocyte colony-stimulating factor. Protein Sci 2003; 12(5):903-913.

42. Schack MM, Moller EH, Carpenter JF, Rades T, Groenning M. A Platform for Preparing Homogeneous Proteinaceous Subvisible Particles With Distinct Morphologies. J Pharm Sci 2018; 107(7):1842-1851.

43. Wiesbauer J, Prassl R, Nidetzky B. Renewal of the Air–Water Interface as a Critical System Parameter of Protein Stability: Aggregation of the Human Growth Hormone and Its Prevention by Surface-Active Compounds. Langmuir 2013; 29(49):15240-15250.

44. Mehta SB, Lewus R, Bee JS, Randolph TW, Carpenter JF. Gelation of a monoclonal antibody at the silicone oil-water interface and subsequent rupture of the interfacial gel results in aggregation and particle formation. J Pharm Sci 2015; 104(4):1282-1290.

45. Joubert MK, Luo Q, Nashed-Samuel Y, Wypych J, Narhi LO. Classification and characterization of therapeutic antibody aggregates. J Biol Chem 2011; 286(28):25118-25133.

46. Mahler H-C, Friess W, Grauschopf U, Kiese S. Protein aggregation: Pathways, induction factors and analysis. Journal of Pharmaceutical Sciences 2009; 98(9):2909-2934.

47. Kishore RSK, Pappenberger A, Dauphin IB, Ross A, Buergi B, Staempfli A, Mahler H-C. Degradation of polysorbates 20 and 80: Studies on thermal autoxidation and hydrolysis. J Pharm Sci 2011; 100(2):721-731.

48. Labrenz SR. Ester Hydrolysis of Polysorbate 80 in mAb Drug Product: Evidence in Support of the Hypothesized Risk After the Observation of Visible Particulate in mAb Formulations. J Pharm Sci 2014; 103(8):2268-2277.

49. Jones MT, Mahler HC, Yadav S, Bindra D, Corvari V, Fesinmeyer RM, Gupta K, Harmon AM, Hinds KD, Koulov A, Liu W, Maloney K, Wang J, Yeh PY, Singh SK. Considerations for the Use of Polysorbates in Biopharmaceuticals. Pharm Res 2018; 35(8):148.

50. Dwivedi M, Blech M, Presser I, Garidel P. Polysorbate degradation in biotherapeutic formulations: Identification and discussion of current root causes. Int. J. Pharm 2018; 552(1):422-436.

51. Siska CC, Pierini CJ, Lau HR, Latypov RF, Matthew Fesinmeyer R, Litowsk JR. Free Fatty Acid Particles in Protein Formulations, Part 2: Contribution of Polysorbate Raw Material. J Pharm Sci 2015; 104(2):447-456.

Chapter 6

Particulate impurities in cell-based medicinal products traced by flow imaging microscopy combined with deep learning for image analysis

Adam D. Grabarek[1,2], Enes Senel[1], Tim Menzen[1], Karin H. Hoogendoorn[3], Karin Pike-Overzet[3], Andrea Hawe[1], Wim Jiskoot[1,2*]

[1] *Coriolis Pharma, Fraunhoferstrasse 18 b, 82152 Martinsried, Germany*

[2] *Leiden Academic Centre for Drug Research, Leiden University, The Netherlands*

[3]*Department of Immunology, Leiden University Medical Center, Leiden, The Netherlands.*

*corresponding author

Abstract

Cell-based medicinal products (CBMPs) are rapidly gaining importance in the treatment of life-threatening diseases. However, the analytical toolbox for characterization of CBMPs is limited. The aim of our study was to develop a method based on flow imaging microscopy (FIM) for the detection, quantification and characterization of subvisible particulate impurities in CBMPs. Image analysis was performed by using an image classification approach based on a convolutional neural network (CNN). Jurkat cells and Dynabeads were used in our study as a representation of cellular material and non-cellular particulate impurities, respectively. We demonstrate that FIM assisted with CNN is a powerful method for the detection and quantification of Dynabeads and cells with other process related impurities, such as cell agglomerates, cell-bead adducts and debris. By using CNN we achieved an over 50-fold lower misclassification rate compared to the utilization of output parameters from the FIM software. The limit of detection was ca. 15,000 beads/ml in the presence of ca. 500,000 cells/ml, making this approach suitable for the detection of these particulate impurities in CBMPs. In conclusion, CNN-assisted FIM is a powerful method for the detection and quantification of cells, Dynabeads as well as other subvisible process impurities potentially present in CBMPs.

Introduction

Technological advancements in the past decades have profoundly revolutionized the area of biotherapeutics[1]. Cell-based medicinal products (CBMPs), an important category of medicinal products based on cells or tissues, are rapidly gaining significance as they can serve as an effective cure for patients where no other treatment option is available. Examples of CBMPs include stem cells, (genetically modified) T-cells and (antigen loaded) dendritic cells[2]. More than a thousand of clinical trials with CBMPs are completed or underway (as of January 2020, www.clinicaltrials.gov) and regulatory agencies are expecting an increasing number of market approvals in the coming years[3]. A recent breakthrough in this field was the approval of two genetically engineered T-cells (chimeric antigen receptor [CAR] T-cells) in the USA in 2017 and Europe in 2018. Despite their clinical success, challenges with respect to manufacturing and quality control (QC) must be faced in order to make CBMPs commercially viable[4].

Manufacturing of CBMPs, such as the current generation of CAR T-cells, is a much more complex and labor intensive process compared to the production of classical protein-based biologics[2,5]. For instance, the production of CAR T-cells involves collection of cells from the patient via leukapheresis, *ex vivo* transduction with a viral vector, encoding the CAR transgene, T-cell activation and expansion, formulation, fill & finish, storage and QC prior to intravenous infusion. Moreover, the manufacturing processes involve the addition of raw materials, such as media, vector, cytokines or antibody-coated magnetic beads. Some of the raw materials can diminish the safety of the final drug product and are considered as impurities. An example are monoclonal antibody-coupled magnetic beads, which must be removed from the process to acceptable levels and need to be measured as part of product QC testing[6].

Most CBMPs consist of a suspension of living cells with a size between typically 10-30 µm. Lymphocytes, including T-cells, are generally smaller in diameter and can range from 7 up to 18 µm in diameter[7]. Therefore, only large-pore filters (≥ 70 µm pore size) can be used during manufacture. Such filtration is not capable of removing particulate impurities within

the micron and submicron size range. Ineffective removal of these particulates, derived either from raw materials or from manufacturing processes, may potentially lead to adverse reactions in patients[8]. Micrometer sized extrinsic particles (e.g., glass particles, metal particles, fibers) may result in occlusion of small capillaries of the circulatory system[9]. Moreover, proteins can adsorb to such non-proteinaceous particles, which may result in unwanted immunogenicity[10]. Furthermore, micro- and submicron-sized proteinaceous particles, which may originate from cells or cell culture medium, have been shown to increase the risk of unwanted immunogenicity[11]. In addition, necrotic cells and cell debris tend to have a smaller diameter compared to healthy cells[12]. Therefore, monitoring the size of cells and other particulate matter may aid in assessing the quality of CBMPs.

For CBMPs, because of their particulate nature, it is very challenging to fulfil specific pharmacopeial testing requirements. The compedial specifications set limits for the number of visible and subvisible (micrometer-sized) particles (USP <790> and <788>, respectively) in injectable drug products[13,14]. The current pharmacopeial methods include visual inspection and light obscuration or microscopic particle count test for visible and subvisible particles, respectively. Visual inspection may not consistently and reliably detect visible particles in CBMPs, as these products may be highly opalescent and viscous because of the high cell concentration (e.g., 10^5-10^7 cells/ml). Furthermore, CBMPs are often supplied as a single-dose, low-volume (µL-ml range) sterile suspension in a (cryo)vial, which has a relatively thick wall making visual inspection difficult. In addition, subvisible particle analysis by light obscuration is very challenging because light obscuration cannot differentiate cells from foreign and particulate impurities. Despite the above considerations, from a quality, safety and potentially efficacy perspective it is prudent that subvisible particles in CBMPs are adequately tested[15].

Flow imaging microscopy (FIM) techniques have been widely used for the characterization of subvisible particles in protein-based drugs[16]. Using these techniques, one can derive concentration, size and morphological parameters of particles within the micrometer size range from microscopic images. Different particle populations can be discriminated based on particle structure and appearance[17,18]. Recently, FIM has been applied to study cell viability and confluency in cell culture as well as quality of CBMPs[12,19-21]. However,

comprehensive particle characterization reaches a limit when using the morphological parameters derived from the instruments´ operating software because of the complexity of CBMPs, which may consist of multiple particulate populations of highly heterogeneous morphologies.

Deep learning for image analysis is an alternative approach, offering more insight into the collected data and potentially allowing for a better discrimination of particle populations. The increasing computing power and advancements in algorithms for pattern recognition have made the deep learning methods, such as convolutional neural networks (CNN), useful tools in many fields, including the biopharmaceutical industry[22]. Deep learning refers to a multi-layered neural network consisting of hidden layers as well as an input and output layer. It can be exceptionally effective in extracting intricate structures in raw (pre-processed) data and recognition of representative features that allow categorization of images with minimum error[23]. For example, protein aggregates formed upon different stress methods were imaged by using FIM and successfully discriminated with the aid of CNN, based on the distinct particle morphology resulting from each stress method[24]. In the area of cell biology, CNN have brought microscopy to a new level, where features such as the type of intracellular structures or the cell cycle and type of cells, previously requiring immunohistochemistry, can now be recognized without fluorescent labeling[25].

In our study, we utilized a flow imaging microscope, FlowCam, to collect images of subvisible particulate matter in T-cell samples and developed an automated image classification method based on CNN for the analysis of the raw images (further referred to as FlowCam-CNN). As a model system, we used suspensions of Jurkat cells (8-16 µm in diameter) and CD3/CD28 Dynabeads (4.5 µm in diameter); the latter are commonly used for T-cell activation and purification. We show that the developed FlowCam-CNN method enables the detection, quantification and characterization of process-related particulate impurities (e.g., Dynabeads, cell-bead adducts) as well as product-related particulates (e.g., cells, cell agglomerates and debris).

Materials and Methods

Materials

T-cell leukemia cells (Jurkat, Clone E6-1, ATCC® TIB152™) were provided by Leiden University Medical Centre (LUMC) as frozen 1-ml aliquots at a total cell concentration of 10^7 cells/ml, and were stored at -140 °C in the freezer prior to usage. The Jurkat cells were formulated in high-glucose RPMI 1640 (RPMI medium; ThermoFisher, Waltham, USA) supplemented with 10% fetal bovine serum (Life Technologies, USA) and 10% dimethyl sulfoxide (DMSO) (Life Technologies, USA). Dynabeads Human T-Activator CD3/CD28 for T Cell Expansion and Activation and low-protein binding collection tubes were purchased from ThermoFisher (Waltham, USA). Sterile 5-ml Eppendorf tubes were purchased from VWR (Ismaning, Germany).

Sample preparation

Jurkat cells used in this study as model T- cells were thawed and freshly prepared in RPMI medium prior to analysis. Frozen cell aliquots were thawed at 36°C and resuspended in ca. 40 ml of RPMI medium. To remove residual fetal bovine serum and DMSO, the cell suspension was centrifuged at 300 rcf for 10 minutes at 20°C. The supernatant was removed and the pellet was resuspended in 10 ml of RPMI medium, unless otherwise stated. The mean concentration of (live and dead) cells was 477,188 ± 85,914 per ml with a mean viability of 81% ± 9% (n=8) as determined by hemocytometry (described below), unless otherwise stated. Cell containing samples were measured up to 4 hours post thawing, a time window during which the cell viability was not affected (data not shown).

Dynabeads were diluted to an intermediate stock concentration of 10^6 beads/ml (based on the dilution factor of the nominal Dynabead concentration) in RPMI medium and stored at 2-8 °C for up to 1 month. The required volume of the intermediate stock was added to cell samples to reach the desired Dynabead concentrations. Reference concentration of Dynabeads stated in the results section is the expected concentration of Dynabeads in the sample derived from dilution calculations and the original bead concentration stated by the manufacturer. It must be noted that the manufacturer does

not use FlowCam for quantification of Dynabeads; therefore, a systematic deviation between reference concentrations and measured concentrations should be anticipated.

Hemocytometry

Cell viability and total cell concentration were determined by using a Bright-Line hemocytometer glass (Merck, Darmstadt, Germany) and an Axiostar Plus microscope (Zeiss, Jena, Germany) with 10x magnification (Zeiss, Jena, Germany). The washed cell suspension was diluted 2-fold with a sterile-filtered 0.4% trypan blue solution (Merck, Darmstadt, Germany). Next, 10 µl of the mixture was placed in the hemocytometer and at least 100 cells were counted (both viable – not stained, and non-viable – stained cells), following the manufacturer´s recommendations.

Flow imaging microscopy (FIM)

For characterization of micron-sized particles, a FlowCam 8100 (Fluid Imaging Technologies, Scarborough, USA) equipped with an 80-µm flow cell and a 10x objective was used. The instrument was operated by using a VisualSpreadsheet software (v4.10.8). Analysis was performed by using a flowrate of 0.18 ml/min and the detection thresholds were set to 17 for dark pixels and 15 for light pixels. Images were taken with a high-resolution CMOS camera (1920x1200 pixels) at 27 frames per second. In total, a sample volume of 0.5 ml was analyzed with an efficiency of approximately 70% (i.e., the measured sample volume was ca. 0.35 ml). Cleaning steps between sample measurements involved thorough flushing of the flow cell with 2% Hellmanex III and highly purified water. Diameters are reported as equivalent spherical diameter (ESD) and filters were not applied for imaging pre-processing. Samples were measured in triplicate or sextuplicate, unless otherwise stated.

Samples measured within this study contained particles of five distinct populations, which are: "single cells", "doublet cells", "Dynabeads", "adducts" (defined as a combination of at least one bead with at least one cell) and "debris" (any other cellular and non-cellular types of particles). For reporting the total determined concentration of cells, we summed the counts of single cells, adducts and 2x doublet cells. The determined concentration of

Dynabeads in measured samples was derived from the summed counts of Dynabeads and adducts.

Generation of particle images for population discrimination

Establishment of threshold values and training of the CNN was performed on manually selected images (4,000-4,500) of each population class, which was shown to be sufficient for training our model to a reach high classification accuracy (>0.99). In order to facilitate the selection process for debris and adducts, samples with elevated numbers of the respective particles were generated prior to FlowCam analysis. Samples enriched in particles representing debris were obtained by submitting freshly resuspended (cryoprotectant free) cell suspensions to two freeze-thaw cycles (-140 $°C$ – 36 $°C$). Samples with high numbers of adducts were generated by incubation of cells (ca. 500,000 cells/ml) in presence of Dynabeads in a number ratio of 1:1 for 1.5 hours at 37 $°C$ and 5% CO_2.

Development of morphological filters for FlowCam

The VisualSpreadsheet software of the FlowCam system outputs 30 morphological parameters for each detected particle within the measured sample. Five of these available parameters, i.e., intensity, sigma intensity, convexity, compactness and aspect ratio, were found to have the highest resolving power for particle populations. Values of particle properties for each population class were further clustered into 1-µm sized bins and are presented in box plots (Figure 1). For the development of threshold values used to assign each particle to its class, a similar approach as previously reported for the discrimination of silicone oil and protein aggregate particles was used[17]. Briefly, a step-wise approach was followed, as described below.

Firstly, Dynabeads and adducts were separated from cells (singlets and doublets) and debris, based on mean particle intensity values. For each size bin of 1 µm, average values of the 10th quartile of "low transparent" particles (Dynabeads and adducts) and of the 90th quartile of "highly transparent" particles (cells and debris) were calculated as a function of size. For size regions where only one population was present, the cutoff threshold was adjusted manually below or above of the 95th quartile parameter value. Furthermore, a 4-

degree polynomial function was fitted to these points from 3 to 35 µm and tested particles of a certain diameter falling above or below the threshold value set were assigned to either group. Secondly, threshold values for compactness, convexity and sigma intensity were derived in a similar manner, which allowed for separation of adducts from Dynabeads and cells from debris. For separation of single cells and doublet cells, the aspect ratio parameter was applied. Therefore, each tested particle must have fulfilled at least three criteria to be assigned to a specific population class. All particles with a diameter below 3 µm were assigned to the debris population.
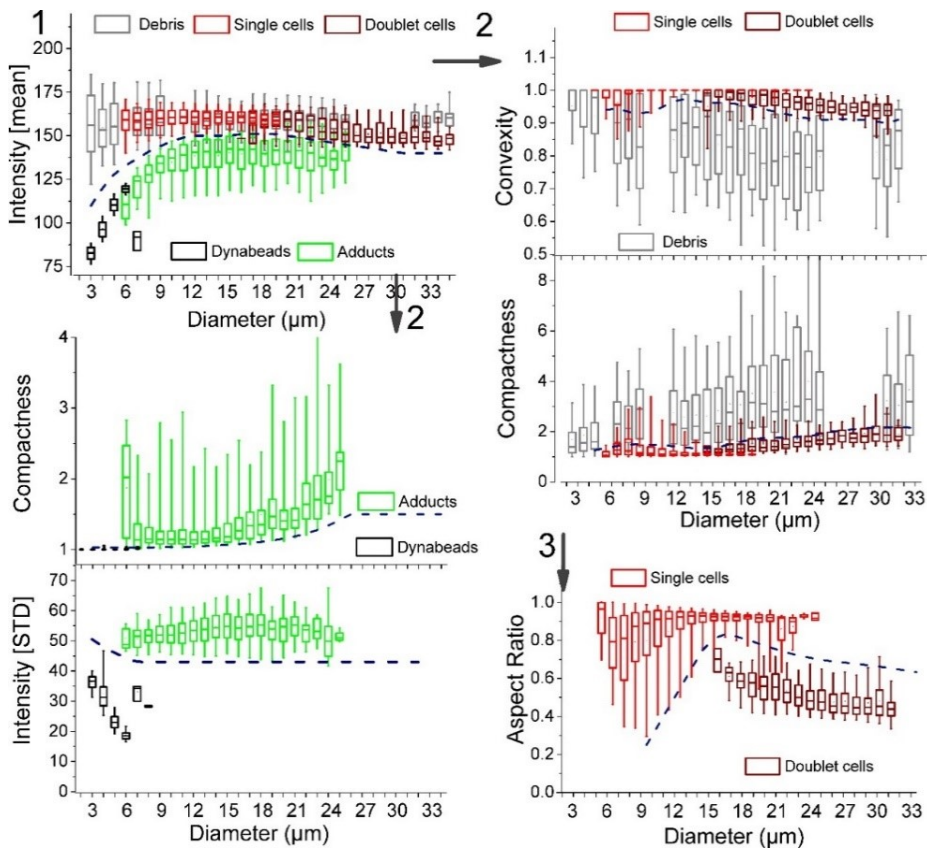
Figure 1: Clustered morphological parameters utilized to discriminate the five particle populations (see text) by using the output data from the FlowCam software. Arrows with accompanying numbers show the order in which the separation of particle populations was carried out.

Deep convolutional neural networks (CNN)

The VGG-19 architecture was used as the foundation for our CNN[26]. This architecture includes 19 convolutional (weight) layers and it can capture a large range of visual object features. The network weights are optimized by reformulating convolutional layers as learning residual functions, taking the input to layers as reference. The VGG-19 network used in our studies has been pre-trained on the open source ImageNet dataset found in[27]. By fine-tuning only the last two fully-connected layers, the feature complexity of the pre-trained model can be optimized for the particle classification task. For fine-tuning the image dataset was split into test, validation and training sets at a 0.1, 0.1 and 0.8 ratio, respectively. Such division of the dataset was aimed to maintain the classes balanced and so the fine-tuning would not be biased towards a specific class. The deep learning model was fine-tuned with 30 epochs with the Adam optimization algorithm. The machine learning model was implemented in the Keras (2.2.4)-Tensorflow (1.13.1) Python (3.7.3) library and ran on a Nvidia Turing GPU with 11 GB of VRAM. A simplistic workflow for image analysis by using CNN is presented in Figure 2.
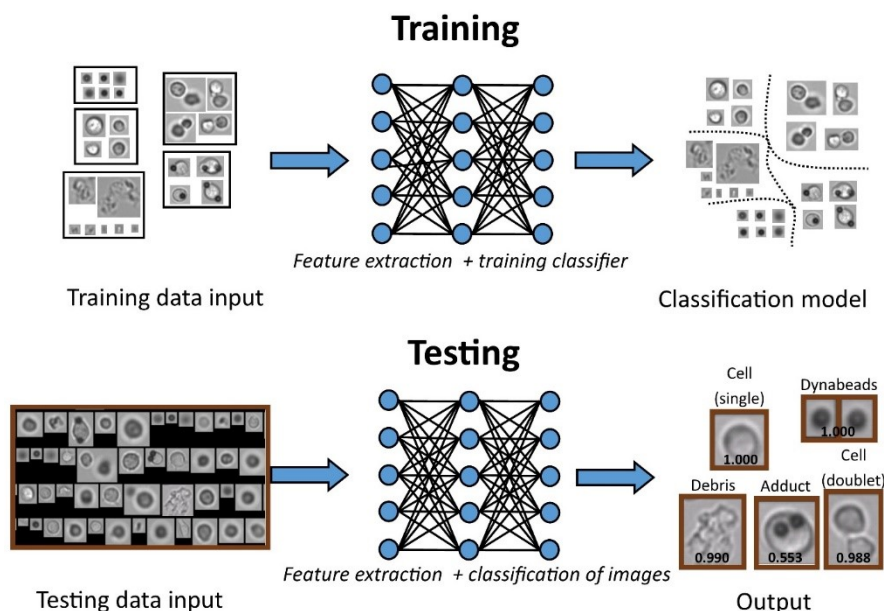
Figure 2: Illustration of the CNN work flow. Firstly, a collection of 4,000-4,500 images from each particle class is manually selected for training with the VGG-19 network. During training, kernels of weights in the two last layers of our network are updating weight parameters and extracting representative image descriptors based on the input data. Once training is completed, the network can be used to predict particle classes of new (not used during training) images. Output is given as a probability of an image assigned to the stated class. A detailed description of the VGG-19 network can be found in[26].

Data analysis

Statistical analysis of data was performed in Origin 2016 (OriginLab Corporation, Northampton, USA). Box plots represent the distribution of data where central rectangles span from the first to the third quartile and whiskers range from the 5th up to the 95th percentile values. For comparison of mean values, a 2-sided student T-test with α= 0.05 (95% confidence interval) was used.

The limit of detection (LOD) and limit of quantification (LOQ) were determined by using values of the entire tested range for Dynabeads, where six measurement replicates were performed for each bead concentration. LOD and LOQ were calculated by using Eq. 1 and Eq. 2[28]:

$$LOD = (3.3 * \sigma) / S \qquad\qquad\qquad\text{(Eq. 1)}$$

$$LOQ = (10 * \sigma) / S \qquad\qquad\qquad\text{(Eq. 2)}$$

where σ is the standard error of the y-intercept and S is the slope of the linear regression line.

Results

Identification of particle populations in cell suspensions

Analysis of cell suspensions supplemented with Dynabeads was performed by using FlowCam and representative examples of generated images of the five distinct particle populations are shown in Figure 3. Besides single cells, debris and Dynabeads, we observed a noticeable number of images with two captured cells (doublet cells) as well as cells with one or more adjacent Dynabeads (adducts). Particle size distributions of samples containing cells (without beads), Dynabeads (without cells) and a mixture of cells and Dynabeads are shown in Figure 3. Samples containing cells showed a broad peak between 10 and 16 µm, representing the Jurkat cells (Figure 3 A). Furthermore, a sharp peak at the lower size limit of detection was observed and assigned to debris. Dynabeads showed a bimodal peak with maxima at 3.5 and 6.0 µm (Figure 3 B). These values represent the measured size of beads from in-focus (sharp) and out-of-focus (blurred) images, and are close to the mean bead diameter of 4.5 µm stated by the manufacturer. Particle size distributions of mixtures of Dynabeads and cells looked like a summation of the cells and the beads (Figure 3 C). Although these samples were found to contain adducts (see Figure 3, top panel), which obviously were not present in the other samples, the number of adducts was relatively small and did not substantially affect the overall size distribution.
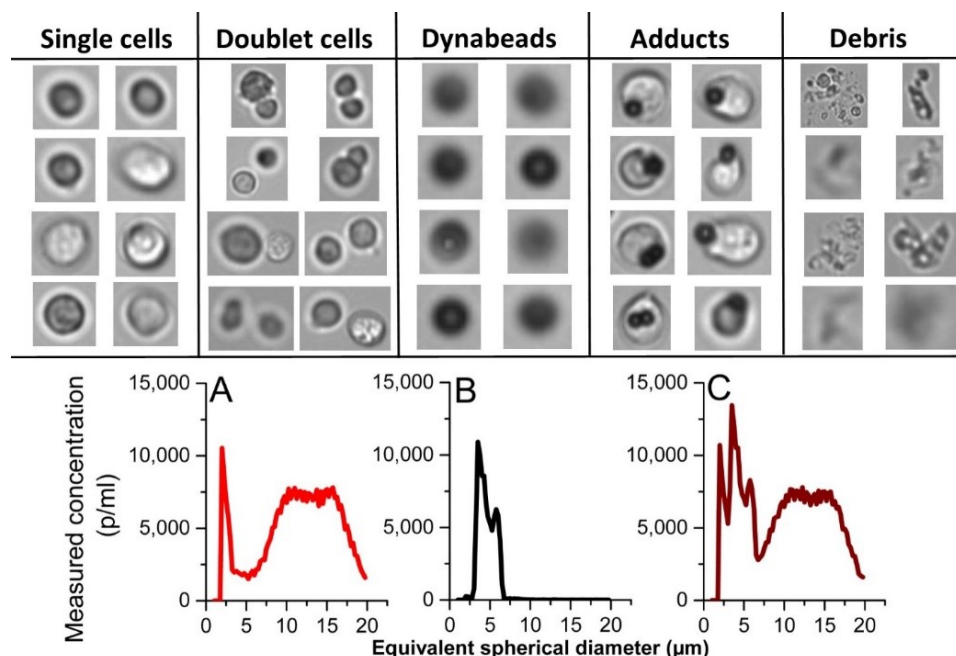
Figure 3: Representative images of each population class obtained by using FlowCam (top). All images were enlarged for presentation and actual size is not represented. Particle size distributions of samples containing (A) Jurkat cells (375,000 cells/ml), (B) Dynabeads (68,000 beads/ml) and (C) Jurkat cells + Dynabeads (bottom).

Morphological parameters for particle classification

For beads suspended in the RPMI medium, a linear relation was found between the measured Dynabead concentration and the expected Dynabead concentration derived from the dilution factor, with a linearity of $r^2 = 0.95$ (Supplementary figure S1 A), based on the selected morphological parameters with the FlowCam software (cf. Figure 1). Measurements of beads in the presence of cells (ca. 500,000 total cells/ml by using a hemocytometer) resulted in a similar linear correlation ($r^2 = 0.98$). However, unexpectedly high numbers of unclassified particles (i.e., particles with morphological parameters not falling into any of the 5 classes) were found. The coefficient of variation for measured concentrations of Dynabeads in presence of cells was noticeably higher as compared to the control samples. Additionally, the recovery of Dynabeads in cell suspensions at the lowest three reference concentrations was above 100%, suggesting a number of debris and other particles were misclassified as Dynabeads (or adducts) when using this

approach. Dynabeads suspended in RPMI medium showed recovery rates from 25% (lowest Dynabead concentration) up to 85% (highest Dynabead concentration) (data not shown). Altogether, using the morphological particle parameters output from the FlowCam software resulted in a good correlation between detected concentrations and reference concentrations of Dynabeads. However, the high numbers of unclassified particles and the noticeable variation in determined particle concentrations illustrate the friability of this classification approach.

CNN for particle classification

Since accurate discrimination of particle populations, present in cell suspensions, was not satisfactory with conventional morphological filters, we applied CNN for analysis of raw FlowCam images. The fine-tuned FlowCam-CNN model with the pre-selected datasets (see methods section above and Figure 2) was used to classify on average 140,000 images per sample into individual particle classes.

Detection and quantification of Dynabeads

In contrast to the results based on the morphological particle parameters output described above, FlowCam-CNN analysis resulted in classification of all particles present cell suspensions (500,000 cell/ml counted by using a hemocytometer) with or without Dynabeads (Figure 4). Linearity over the entire tested Dynabead concentration range was > 0.95 for both sample sets and slope values were about 0.8. Samples containing cells and >50,000 beads/ml had recovery values above 80% and a coefficient of variation below 15%. The relative error of the determined bead concentration was apparently random and showed a uniform distribution around 0 for samples with cells, except for the lowest bead concentrations measured (data not shown). Dynabeads suspended in cell-free RPMI medium at reference concentrations below 60,000 beads/ml showed lower recoveries compared to samples containing cells, which exceeded a recovery rate of 75% within the tested range. The coefficient of variation of determined Dynabead concentrations was >10% for samples with less than 50,000 beads/ml and below 10% for the higher tested bead concentrations. Therefore, the optimal Dynabead concentration for quantification of

beads by using FlowCam-CNN was determined to be from ca. 45,000 beads/ml to at least 200,000 beads/ml.
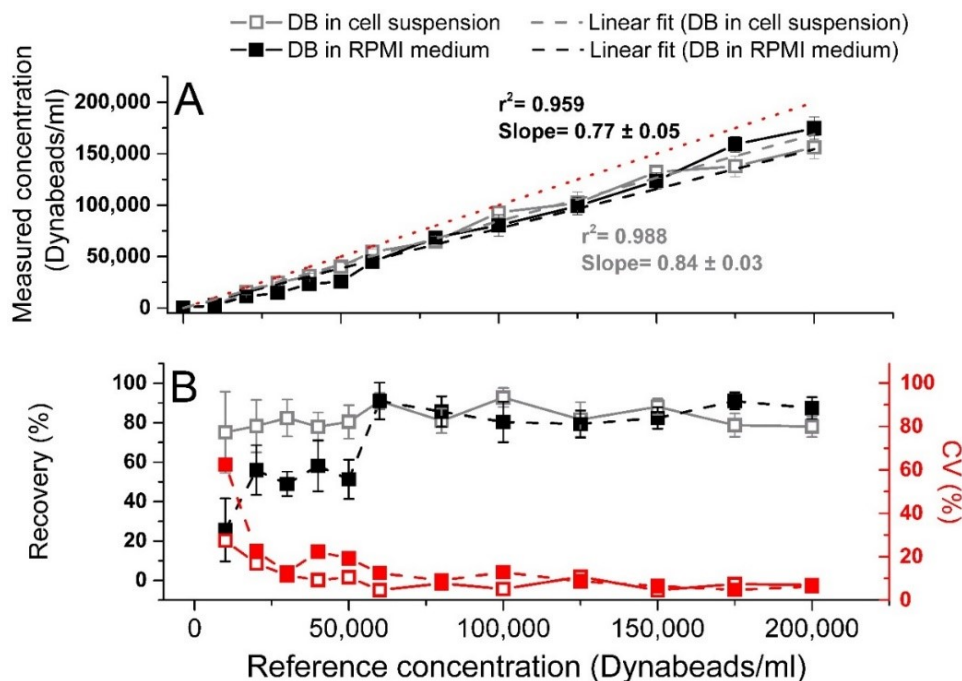
Figure 4. Presented data on classified Dynabeads (DB) by using CNN. (A) Determined concentration of Dynabeads in a concentration series of Dynabeads suspended in RPMI medium (DB ctrl, gray) and in Jurkat cell suspensions (DB + cells, black). (B) Recovery (left y-axis, black) and corresponding coefficient of variation (CV; right y-axis, red) of Dynabeads in RPMI medium (open squares) and Jurkat cell suspensions (closed squares). Error bars represent the standard deviation of mean values of six replicates. The coefficient of variation values (%) were calculated from the six replicate measurements.

The FlowCam method assisted with automated image classification (FlowCam-CNN) was examined in alignment with the ICH Q2 (R1) guideline for validation of analytical procedures. Accuracy, precision, LOD, LOQ and linear relationship for Dynabeads detection in absence and presence of cells were evaluated and the results are presented in Table 1.

The LOD and LOQ were about 15,000 and 45,000 beads/ml, respectively, where slightly higher values were found for Dynabead suspensions in absence of cells.

Accuracy and precision (repeatability) were calculated for Dynabead concentrations above the LOQ and the values present averages of two intra-day sets of triplicate measurements. Accuracy was determined as the recovery of spiked in Dynabeads with respect to the reference concentrations (Recovery%). Accuracy was found to be substantially lower for beads in absence of cells at reference concentrations below 50,000 beads/ml. Above this concentration, the presence of cells did not have an impact on the accuracy of quantification. Furthermore, precision of Dynabeads concentration determination was evaluated as the coefficient of variation (CV%) and overall values were <10%.

Table 4. Parameters determined by FlowCam-CNN based on mean values of two inter-day triplicate measurements. The LOD and LOQ were deteremined for Dynabead concentrations tested in the study and presented in Figure 4. Accuracy and precision were determined for Dynabead concentrations above the LOQ. Cell concentration was ca. 375,000 cells per ml.

Parameter	Dynabeads (in cell suspension)	Dynabeads (in RPMI 1640 medium)
Accuracy (Recovery%)	86.9 ± 5.4	80.5 ± 12.6
Precision (CV%)	4.7 ± 0.9	8.0 ± 3.2
LOD (beads/ml)	15,229	13,661
LOQ (beads/ml)	46,149	41,396
Linearity (R^2)	0.988	0.959

Characterization of cellular particulate matter

In addition to developing a method for characterization of non-cellular particles, we aimed to quantify debris (a potential impurity) as well as cells and adducts.

The tested concentrations of Dynabeads in Jurkat cell suspensions, presented in Figure 4, were studied at a constant cell concentration (385,711 ± 59,337 cells per ml as determined with FlowCam). The presence of Dynabeads did not have a significant impact on the number of quantified total number of cells (T-test, 2-sided, $p > 0.17$; Supplementary figure S2 A). Moreover, the numbers of detected particles classified as debris in cell samples without and with Dynabeads were highly comparable. Furthermore,

as expected, the number of detected adducts increased with higher concentrations of beads present in cell samples (Supplementary figure S2 B and S2 C).

Misclassifications

The misclassification rate was calculated in an indirect manner because of the large number of acquired images per measurement (>100,000 per measurement). Debris particles were present in all measured samples (Dynabeads and cell suspensions); therefore, we did not consider the misclassification rate for this population. Figure 5 A represents the rates of erroneously detected cells (singlets, doublets and adducts) and of unclassified particles within Dynabead suspensions of different reference concentrations. Figure 5 B presents the error rates of detected Dynabeads and adducts as well as unclassified particles within cell only suspensions at a cell concentration of approximately 375,000 cells/ml (as measured by FlowCam). In both cases, the misclassification rates were very low (< 2%) when the data was processed by using CNN. Furthermore, the error rate was independent of the spiked-in amount of Dynabeads, as the fraction of misclassified particles was similar for each of the tested concentration of beads in cell suspensions. Particles analyzed by using morphological parameters showed a much higher inaccuracy and unclassified fraction, which is reflected by the relatively high error rates (up to 50-fold higher compared to CNN).
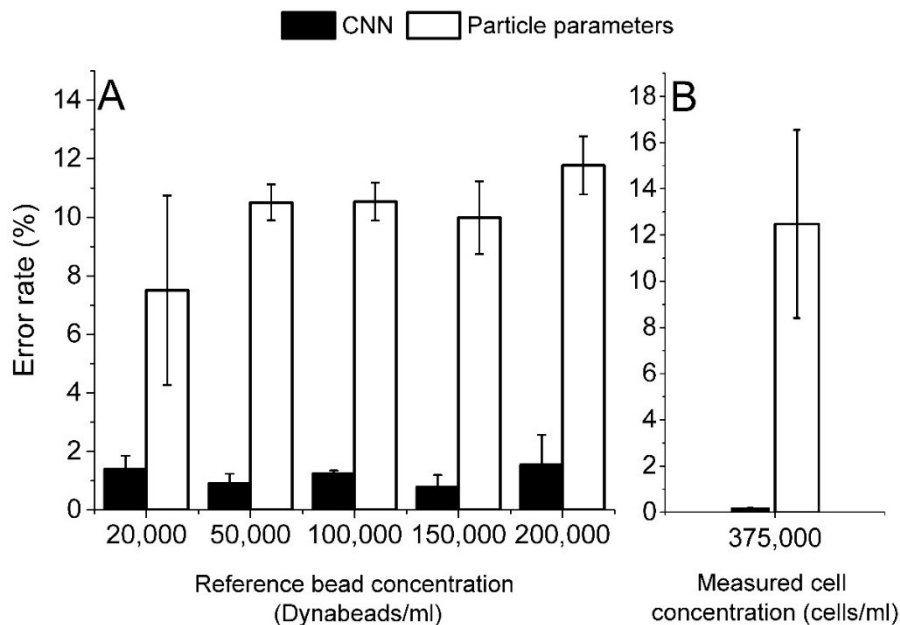
Figure 5. Error rates of particles classified as (A) cells or adducts in Dynabead suspensions with different Dynabead target concentrations (x-axis) and (B) Dynabeads and adducts in cell suspensions at 375,000 cells/ml (as determined by using FlowCam). Error rates are based on misclassified particles by using CNN (filled bars), and on mis- and unclassified particles by using particle morphological parameters (empty bars). Error bars are standard deviations of mean values of six replicates.

Figure 6 presents the probability distribution, as determined by deep learning classification, of particle images classified as Dynabeads. Particle images were collected during FlowCam measurements of Dynabeads (80,000 beads/ml) in presence and absence of cells. In our classification network the Softmax regression function was integrated, which is an activation function converting calculated weights into probability distributions and rejecting all cases with probabilities below 0.2. For the sample with suspended Dynabeads in RPMI medium, the vast majority of images classified to the bead class had a probability equal to 1, which confirmed that the network made the assignment with very high confidence. Moreover, this high confidence was not impacted by the presence of cellular material in the sample, as similar counts of beads with a probability of 1 were found in samples containing Jurkat cells. In conclusion, these data demonstrate that image classification by using FlowCam-CNN is highly accurate.
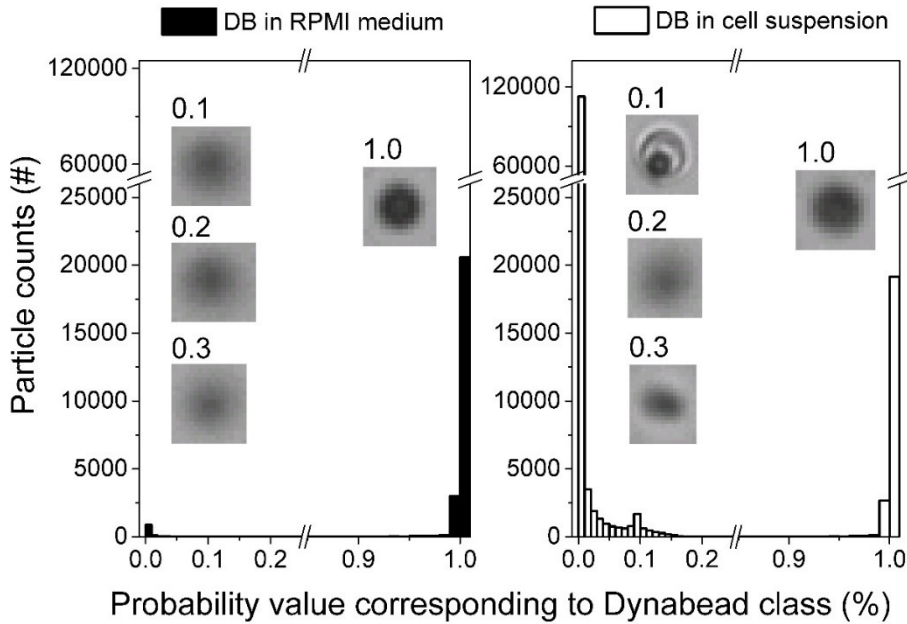
Figure 6. Probability distribution (binned in units of 0.01) of classified particle images determined by FlowCam-CNN for Dynabead suspension (filled) and cell suspension suplemented with Dynabeads (empty) at a concentration of 80,000 beads per ml. Representative images are shown with their asssgned probability of belonging to the Dynabead class.

Effect of cell concentration on measurement

The impact of the Jurkat cell concentration on the quantification of Dynabeads in cell suspensions by FlowCam-CNN was investigated and the results are presented in Figure 7. Dynabeads spiked into samples with cell concentrations up to ca. 500,000 cells/ml (as determined by using a hemocytometer) resulted in similar measured bead concentrations in presence of cells. At the highest tested cell concentration (900,000 cells/ml), we observed an underestimation of detected beads at reference Dynabead concentrations of 50,000 and 100,000 beads/ml. Such an underestimation was not observed for the lowest tested Dynabead concentration (20,000 beads/ml). Furthermore, control samples showed lower Dynabead recoveries compared to samples with cell suspensions.
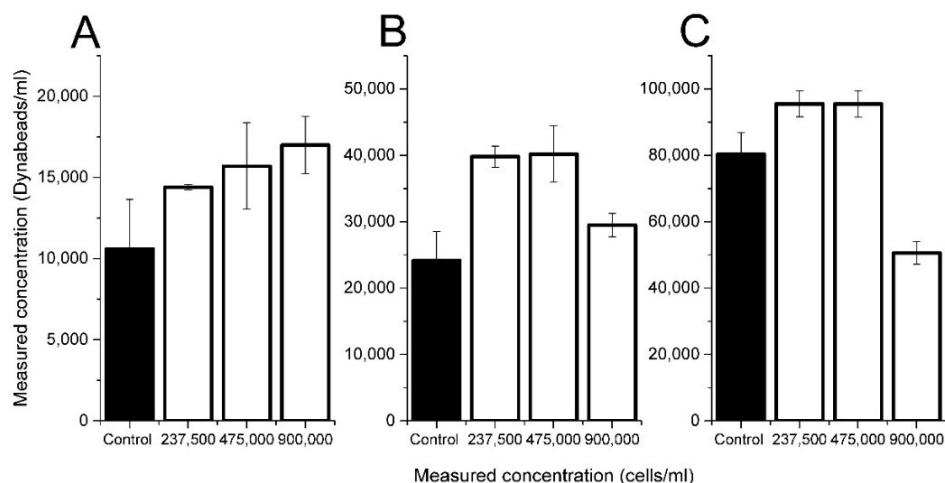
Figure 7. Determined concentration of Dynabeads in RPMI medium (control; filled bars) and cell suspensions (empty bars). Three different cell concentrations (x- axis; determined by using hemocytometry) were tested with reference concentrations of Dynabeads of A) 20,000, B) 50,000 and C) 100,000 Dynabeads/ml. Error bars represent standard deviations of triplicate measurements of Dynabeads in cell suspensions and of nonuplet measurements of Dynabeads in RPMI medium.

Discussion

Characterization of cellular and non-cellular (i.e., foreign) particulate matter in CBMPs is important to guarantee a good quality and safe product[8]. Additionally, with the limited time available for analytical testing of some cell products, straightforward, rapid and comprehensive methods are urgently needed[5].

In this study we used a model system containing Jurkat cells, serving as a surrogate for T-cells, such as CAR-T cells[29], and Dynabeads CD3/CD28, serving as a representative potential process-related particulate impurity in CAR-T cell products[30]. These super-paramagnetic beads coupled to CD3 and CD28 monoclonal antibodies are used in the production of CBMPs[31]. However, their removal prior to the final formulation step remains difficult[32]. More importantly, taking into consideration reports on the potential toxicity of Dynabeads[30], methods showing effective and consistent removal of these impurities in the manufacturing process are required. Therefore, in our study, we assessed the feasibility of FIM for the discrimination of Dynabeads and cells, and for the assessment of the

Dynabead concentration. We hypothesized this should be possible, because Dynabeads differ in size and morphological properties from T cells. It must be noted that the full production protocol, where beads are present in cell medium for days/weeks, was not mimicked here and Dynabeads were spiked into cell suspensions shortly before analysis. Therefore, monitoring the stability of beads in the suspension and their interactions with cells over time was beyond the scope of this study.

The FIM-based method may offer advantages for characterizing CBMPs, as it is a high-throughput technique capable of rapid measurements of high sample numbers without laborious preparative steps. The two most commonly used FIM systems are FlowCam and Micro-Flow Imaging (MFI). Previously, it has been shown that FIM techniques have the potential in determination of cell concentration and viability[12]. For our study FlowCam was chosen because of its capability of recording images of high quality and its high accuracy and precision in particle concentration determination[33]. A downside of the FlowCam technique can be the relatively inaccurate particle sizing, resulting from a narrow depth of focus within the field of the imaging system. As a result, particles of a homogenous diameter may show a bimodal distribution[34], which was also observed in the present study (Figure 3). Accurate sizing was not of key importance in our study. However, blurry and non-blurry images should both be assigned to the same particle class, implying an increase in complexity of the classification process.

The verification of viability and total concentration of cells used in our study was performed by using a hemocytometer. As shown in previous studies[12,21], cell concentrations determined by using FlowCam were lower compared to manual counting and in our case the difference was ca. 20%. Furthermore, the concentration of Dynabeads detected by FlowCam deviated from the reference concentrations stated by the manufacturer, i.e., the recovery was always below 100% especially for Dynabeads at lower concentrations. This, however, can be most likely ascribed to a loss of beads during sample preparation, as measurements with a Multisizer 4e Coulter-Counter analyzer (method used by the manufacturer for quantification) showed similar results (data not shown). Moreover, preliminary studies showed a significant impact of used lab

disposables (e.g., low-protein binding materials, volume-to-surface ratios) on the determined concentration of Dynabeads. The high affinity of the antibody coated beads to surfaces resulted most probably to adherence of Dynabeads to polypropylene tubes and tips used for sample handling. Interestingly, a more consistent and higher recovery rate was observed for Dynabeads in presence of cells compared to Dynabeads in cell-free RPMI buffer (control) over the measured concentration range. In particular, a pronounced loss of beads at low concentrations (< 60,000 beads/ml) was observed in our cell-free control samples, resulting in a recovery below 50%. Such high losses of Dynabeads were not observed in the cell-containing samples, in which most likely debris and other cell-related materials occupied free surfaces and competitively decreased bead adsorption. Because the bead-to-T-cell ratio is critical for T cell activation or T-cell purificiation[35], bead-preparative steps where dilutions in cell-free media are involved should be carefully considered to reach the desired bead concentration and assure a consistent manufacturing process.

When using FIM, a capable demarcation approach is required for accurate quantification of specific particle populations found within highly heterogeneous samples. Output parameters by the instruments' operating software can be helpful in discriminating particles based on morphology, but may be prone to high error rates[18]. The uniformity of Dynabead images resulted in similar values of each particle parameter and developed filters had close to no misclassifications and 5% of unclassified particles for Dynabead-only samples. However, the morphological nature of cells, cell aggregates and debris is highly heterogeneous and the distribution of each of these particle parameters was highly disperse (Figure 1). Furthermore, adducts and cells had in many cases interchangeable values for most particle parameters. The error rates (misclassifications and unclassified particles) for images containing only cells were approximately 20% with datasets used for developing morphological filters. Error rates for cell and Dynabead suspensions were ca. 10% with testing datasets. The lack of a high capability in discrimination of different particle population groups by using morphological parameters prompted us to use an automated image classification method based on CNN.

In comparison with other machine learning techniques, deep learning is straightforward in usage and achieves high accuracies with minimal refinements to the network layers[22]. The high performance of neural networks is in most cases based on large data sets to train the networks. For successful training of an entire CNN, such as VGG-19, several million of labeled images per class are required. Although FIM techniques are well suited for applications where comparably large numbers of images can be collected within a relatively short period of time and with low sample consumption, cleaning and labeling a high-quality training dataset remains a challenge. Because the pre-trained VGG-19 was able to differentiate features on the ImageNet dataset very efficiently, fine-tuning of the last two fully-connected layers by using a relatively small number of labeled FlowCam images resulted in a powerful CNN for differentiation and quantification of Dynabeads. The misclassification rate was significantly reduced with the CNN and was only 0.2% for cell samples spiked with Dynabeads. FlowCam-CNN was capable of quantifying a wide concentration range of Dynabeads in cell suspensions, demonstrating a large dynamic range. Furthermore, the high precision (CV% < 5%) in determination of Dynabead concentration in cell suspensions above the LOQ presents this method as a robust approach for quantification of process-related particulates.

The determined total cell and debris concentration was not impacted by the number of Dynabeads spiked into the suspension (Supplementary figure S2). As expected, the number of detected adducts increased with increasing concentration of Dynabeads in the sample because of the higher probability of beads interacting with cells. Furthermore, a concentration of 500,000 cells/ml showed to have no impact on the quantification of Dynabeads in cell suspensions. However, at the highest cell concentration tested, we observed a clear decrease in recovery of Dynabeads which were spiked to a target concentration 50,000 and 100,000 beads/ml. This loss in recovery was not observed for the lowest Dynabead concentration of 20,000 beads/ml. A possible explanation could be the approach for counting Dynabead(s) attached to a single cell. Cases in which a particle was classified as "adduct" were considered to consist of a single cell and a single Dynabead, which was true in the majority of cases. However, with increasing number of cells or Dynabeads, the probability of capturing a cell with two or more adhering

Dynabeads per image becomes higher. Therefore, the underestimation of Dynabeads could have been related to the inaccurate counting of beads in dense cell populations.

Conclusions and Outlook

In our study we developed a reliable method based on FIM coupled with CNN for detection, characterization and quantification of relevant particulate impurities, specifically Dynabeads. We showed that small amounts of Dynabeads can be detected in cell suspensions and a high precision in counting is achieved if the bead concentration is above the determined LOQ. Moreover, cells and cellular impurities, such as cell aggregates and adducts, can be easily classified by using CNN. Quantification of these particles can assist in monitoring manufacturing processes of CBMPs and assist in process and product characterization, such as stability testing.

Further work is being carried out to enhance the capabilities of the method for other cell lines, the identification of multiple beads adhering to cells, as well as to characterize other populations of particulates potentially present in CBMPs, such as leachables, extractables and beads used as carriers for the *ex vivo* expansion of adherent cells. In addition, further evaluation of the presented method by using orthogonal methods could endorse the results obtained from the currently opaque processing algorithm, such as CNN[36]. This would increase confidence and understanding of FlowCam-CNN, presumably supporting in-process and quality control analyses at first, and potentially becoming a critical release test. Currently, we are not aware of other methods with similar performance and we believe that CBMP development can benefit from FlowCam-CNN in its current state.

References:

1. La G de Torre B, Albericio F. The Pharmaceutical Industry in 2018. An Analysis of FDA Drug Approvals from the Perspective of Molecules. Molecules. 2019;24(4). doi:10.3390/molecules24040809.

2. Roh K-H, Nerem RM, Roy K. Biomanufacturing of Therapeutic Cells: State of the Art, Current Challenges, and Future Perspectives. Annu Rev Chem Biomol Eng. 2016;7:455-478. doi:10.1146/annurev-chembioeng-080615-033559.

3. Holzinger A, Abken H. Advances and Challenges of CAR T Cells in Clinical Trials. In: Theobald M, ed. Current Immunotherapeutic Strategies in Cancer. Cham: Springer International Publishing; 2020:93-128.

4. Jönsson B, Hampson G, Michaels J, Towse A, Schulenburg J-MG von der, Wong O. Advanced therapy medicinal products and health technology assessment principles and practices for value-based and sustainable healthcare. Eur J Health Econ. 2019;20(3):427-438. doi:10.1007/s10198-018-1007-x.

5. Kaiser AD, Assenmacher M, Schröder B, et al. Towards a commercial process for the manufacture of genetically modified T cells for therapy. Cancer Gene Ther. 2015;22(2):72-78. doi:10.1038/cgt.2014.78.

6. European Medicines Agency. Guideline on quality, non-clinical and clinical aspects of medicinal products containing genetically modified cells. 2018. https://www.ema.europa.eu/en/documents/scientific-guideline/draft-guideline-quality-non-clinical-clinical-aspects-medicinal-products-containing-genetically_en.pdf. Accessed 01.Dec.2019.

7. Rosenberg G. Microscopic haematology : a practical guide for the laboratory. Amsterdam: Harwood Academic Publishers; 1997.

8. Clarke D, Stanton J, Powers D, et al. Managing particulates in cell therapy: Guidance for best practice. Cytotherapy. 2016;18(9):1063-1076. doi:10.1016/j.jcyt.2016.05.011.

9. Narhi LO, Corvari V, Ripple DC, et al. Subvisible (2-100 μm) Particle Analysis During Biotherapeutic Drug Product Development: Part 1, Considerations and Strategy. Journal of Pharmaceutical Sciences. 2015;104(6):1899-1908. doi:10.1002/jps.24437.

10. Jiskoot W, Kijanka G, Randolph TW, et al. Mouse Models for Assessing Protein Immunogenicity: Lessons and Challenges. Journal of Pharmaceutical Sciences. 2016;105(5):1567-1575. doi:10.1016/j.xphs.2016.02.031.

11. Moussa EM, Panchal JP, Moorthy BS, et al. Immunogenicity of Therapeutic Protein Aggregates. Journal of Pharmaceutical Sciences. 2016;105(2):417-430. doi:10.1016/j.xphs.2015.11.002.

12. Sediq AS, Klem R, Nejadnik MR, Meij P, Jiskoot W. Label-Free, Flow-Imaging Methods for Determination of Cell Concentration and Viability. Pharm Res. 2018;35(8):150. doi:10.1007/s11095-018-2422-5.

13. General Chapter. <788> Particulate Matter in Injections. The United States Pharmacopeial Convention. 2013;USP36,NF32:350–353.

14. General Chapter. <790> Visible Particulates in Injections. The United States Pharmacopeial Convention. 2014;USP37,NF32:6393-6394.

15. Levine BL, Miskin J, Wonnacott K, Keir C. Global Manufacturing of CAR T Cell Therapy. Mol Ther Methods Clin Dev. 2017;4:92-101. doi:10.1016/j.omtm.2016.12.006.

16. Corvari V, Narhi LO, Spitznagel TM, et al. Subvisible (2-100 μm) particle analysis during biotherapeutic drug product development: Part 2, experience with the application of subvisible particle analysis. Biologicals : journal of the International Association of Biological Standardization. 2015;43(6):457-473. doi:10.1016/j.biologicals.2015.07.011.

17. Weinbuch D, Zölls S, Wiggenhorn M, et al. Micro-flow imaging and resonant mass measurement (Archimedes)--complementary methods to quantitatively differentiate protein particles and silicone oil droplets. Journal of Pharmaceutical Sciences. 2013;102(7):2152-2165. doi:10.1002/jps.23552.

18. Akhunzada ZS, Hubert M, Sahin E, Pratt J. Separation, Characterization and Discriminant Analysis of Subvisible Particles in Biologics Formulations. Curr Pharm Biotechnol. 2019;20(3):232-244. doi:10.2174/1389201020666190214100840.

19. Farrell CJ, Cicalese SM, Davis HB, et al. Cell confluency analysis on microcarriers by micro-flow imaging. Cytotechnology. 2016;68(6):2469-2478. doi:10.1007/s10616-016-9967-0.

20. Wu L, Martin T, Li Y, et al. Cell aggregation in thawed haematopoietic stem cell products visualised using micro-flow imaging. Transfus Med. 2012;22(3):218-220. doi:10.1111/j.1365-3148.2012.01147.x.

21. Vollrath I, Mathaes R, Sediq AS, et al. Subvisible Particulate Contamination in Cell Therapy Products-Can We Distinguish? Journal of Pharmaceutical Sciences. 2019. doi:10.1016/j.xphs.2019.09.002.

22. LeCun Y, Bengio Y, Hinton G. Deep learning. Nature. 2015;521(7553):436-444. doi:10.1038/nature14539.

23. Schroff F, Kalenichenko D, Philbin J. FaceNet: A Unified Embedding for Face Recognition and Clustering. 2015. Cornell University. doi:10.1109/CVPR.2015.7298682

24. Calderon CP, Daniels AL, Randolph TW. Deep Convolutional Neural Network Analysis of Flow Imaging Microscopy Data to Classify Subvisible Particles in Protein Formulations. Journal of Pharmaceutical Sciences. 2018;107(4):999-1008. doi:10.1016/j.xphs.2017.12.008.

25. Christiansen EM, Yang SJ, Ando DM, et al. In Silico Labeling: Predicting Fluorescent Labels in Unlabeled Images. Cell. 2018;173(3):792-803.e19. doi:10.1016/j.cell.2018.03.040.

26. Simonyan K, Zisserman A. Very Deep Convolutional Networks for Large-Scale Image Recognition; 2014. http://arxiv.org/pdf/1409.1556v6. Accessed 01. Feb. 2020

27. Russakovsky O, Deng J, Su H, et al. ImageNet Large Scale Visual Recognition Challenge. Int J Comput Vis. 2015;115(3):211-252. doi:10.1007/s11263-015-0816-y.

28. Borman P, Elder D. Q2(R1) Validation of Analytical Procedures. In: Teasdale A, Elder D, Nims R, editors. ICH Quality Guidelines: An Implementation Guide., Wiley Online Books; 2017, p. 127-166

29. Baeuerle PA, Ding J, Patel E, et al. Synthetic TRuC receptors engaging the complete T cell receptor for potent anti-tumor response. Nat Commun. 2019;10(1):2087. doi:10.1038/s41467-019-10097-0.

30. Tiwari A, Punshon G, Kidane A, Hamilton G, Seifalian AM. Magnetic beads (Dynabead) toxicity to endothelial cells at high bead concentration: implication for tissue engineering of vascular prosthesis. Cell Biol Toxicol. 2003;19(5):265-272.

31. Wang X, Rivière I. Clinical manufacturing of CAR T cells: foundation of a promising therapy. Mol Ther Oncolytics. 2016;3:16015. doi:10.1038/mto.2016.15.

32. Iyer RK, Bowles PA, Kim H, Dulgar-Tulloch A. Industrializing Autologous Adoptive Immunotherapies: Manufacturing Advances and Challenges. Front Med (Lausanne). 2018;5:150. doi:10.3389/fmed.2018.00150.

33. Werk T, Volkin DB, Mahler H-C. Effect of solution properties on the counting and sizing of subvisible particle standards as measured by light obscuration and digital imaging methods. Eur J Pharm Sci. 2014;53:95-108. doi:10.1016/j.ejps.2013.12.014.

34. Zölls S, Weinbuch D, Wiggenhorn M, et al. Flow imaging microscopy for protein particle analysis--a comparative evaluation of four different analytical instruments. The AAPS journal. 2013;15(4):1200-1211. doi:10.1208/s12248-013-9522-2.

35. Kalamsz D, Long SA, Taniguchi R, Buckner J, Berenson R, Bonyhadi M. Optimization of Human T-Cell Expansion Ex Vivo Using Magnetic Beads Conjugated with Anti-CD3 and Anti-CD28 Antibodies. J Immunother. 2004;(27):405-418. doi:10.1097/00002371-200409000-00010.

36. Price WN. Big data and black-box medical algorithms. Sci Transl Med. 2018;10(471). doi:10.1126/scitranslmed.aao5333.

Supplementary materials
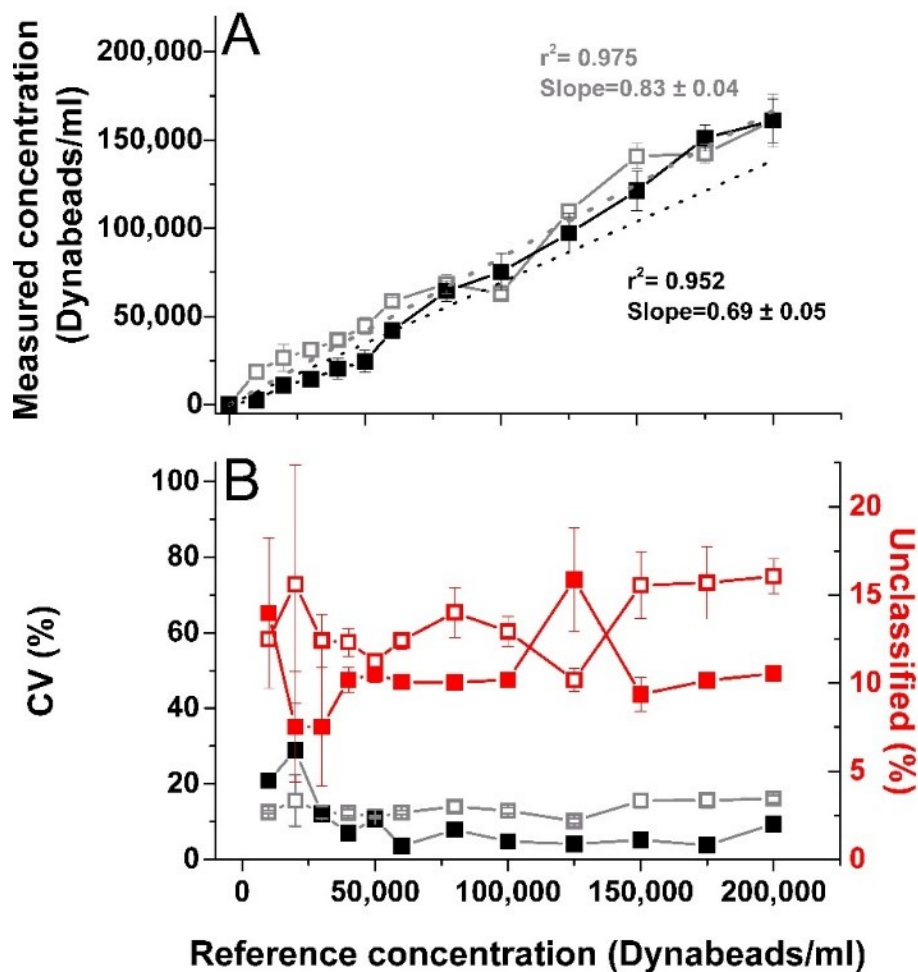
Supplementary figure S1: Presented data on classified Dynabeads by using morphological parameters output from the FlowCam software. (A) Determined concentration of Dynabeads in a concentration series of Dynabeads suspended in RPMI buffer (DB ctrl, gray) and in cell suspensions (DB + cells, black). (B) Recovery (left y-axis) and coefficient of variation (right y-axis) of Dynabeads in RPMI buffer (gray) and cell suspensions (black). Error bars represent the standard deviation of mean values of six replicates. Coefficients of variation (%) were calculated from six replicate measurements.
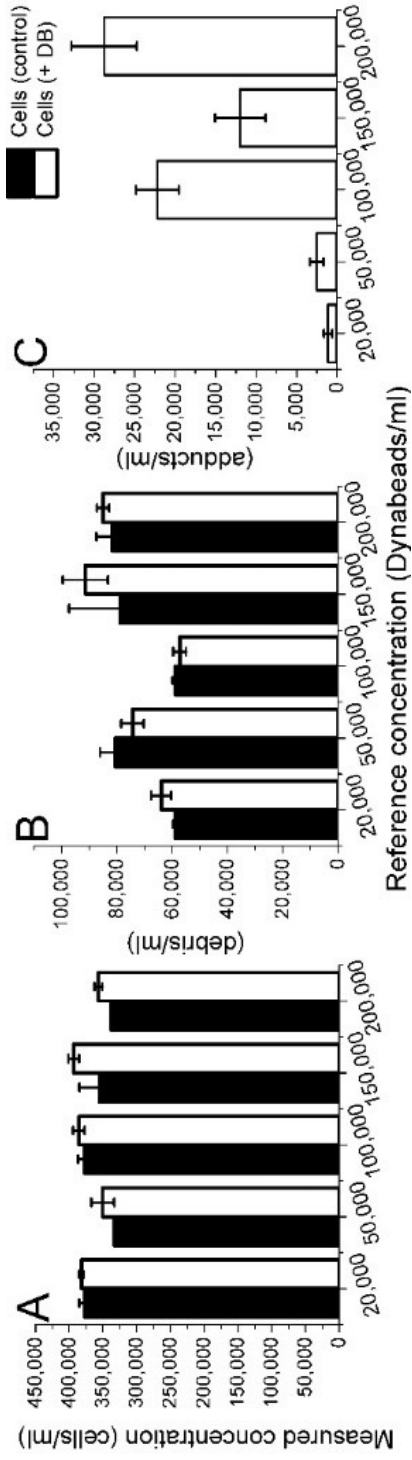
Supplementary figure S2: (A) Cell concentrations determined by using automated image classification in samples consisting of only cells (filled bars) and cells with different concentrations of spiked Dynabeads (empty bars). (B) Debris concentrations determined by using automated image classification in samples consisting of only cells (filled bars) and cells with different concentrations of spiked Dynabeads (empty bars). (C) Adduct concentrations determined by using automated image classification in samples consisting of cells with different concentrations of spiked Dynabeads (empty bars). Error bars represent standard deviations of mean concentrations from intra-day triplicate measurements.

Chapter 7

Forced degradation of cell-based medicinal products guided by flow imaging microscopy: explorative studies with Jurkat cells

Adam D. Grabarek[1,2], Wim Jiskoot[1,2*], Andrea Hawe[2], Karin Overzet-Pike[3], Tim Menzen[2*]

[1]*Coriolis Pharma, Fraunhoferstraße 18 b, 82152 Martinsried, Germany*

[2]*Leiden Academic Centre for Drug Research, Leiden University, The Netherlands*

[3]*Department of Immunology, Leiden University Medical Center, Leiden, The Netherlands.*

*corresponding author

Abstract

Cell-based medicinal products (CBMPs) offer ground-breaking opportunities to treat diseases with limited or no therapeutic options. However, the intrinsic complexity of CBMPs results in great challenges with respect to analytical characterization and stability assessment. In our study, we submitted Jurkat cell suspensions to forced degradation studies mimicking conditions to which CBMPs might be exposed from procurement of cells to administration of the product. Flow imaging microscopy assisted by machine learning was applied for determination of cell viability and concentration, and quantification of debris particles. Additionally, orthogonal cell characterization techniques were used. Thawing of cells at 5 $^{\circ}$C was detrimental to cell viability and resulted in high numbers of debris particles, in contrast to thawing at 37 °C or 20 °C which resulted in better stability. After freezing of cell suspensions at -18 °C in presence of dimethyl sulfoxide (DMSO), a DMSO concentration of 2.5% (v/v) showed low stabilizing properties, whereas 5% or 10% was protective. Horizontal shaking of cell suspensions did not affect cell viability, but led to a reduction in cell concentration. Fetal bovine serum (10% [v/v]) protected the cells during shaking. In conclusion, forced degradation studies with application of orthogonal analytical characterization methods allow for CBMP stability assessment and formulation screening.

Introduction

The number of cell-based medicinal products (CBMPs) entering clinical trials and being approved by major regulatory bodies for commercial use is consistently increasing each year[1]. Despite the promising clinical data emerging from the use of these innovative therapeutic products, many challenges remain in the areas of manufacturing, formulation development and analytical characterization[2,3].

Most CBMPs consist of living cells, which are intrinsically fragile and much more susceptible to unfavourable conditions compared to other biotherapeutics, such as protein-based products. Nonetheless, irrespective of the type of the CBMP (e.g., autologous or allogenic, genetically modified or not), they often undergo multiple and complex manufacturing steps before being administered to the patient. The main processing steps CBMPs undergo during their production include isolation of cells from a healthy donor or patient, *ex-vivo* cell manipulation, formulation, storage, and quality control prior to release and administration[4]. Furthermore, between each of the above listed steps, transportation, freeze-thawing or manual handling of CBMPs occurs. With clinical site-specific handling procedures, differences in processing and administration of the product will also occur[5]. Such diverse and multistep production and handling processes expose cells to a range of intended and/or accidental environmental stress factors, such as freeze-thawing, surface related stress (i.e., mechanical stress), thermal and oxidative stress. Each of these kinds of stresses may result in accidental cell death or alterations in cell activity. Therefore, examination of the impact of formulation parameters on cell stability under these stress conditions should be considered to better understand the sensitivity of the product to the stress factors involved. This will likely contribute to new insights that can be employed to mitigate the potential risk of therapeutic failure and the occurrence of serious adverse effects due to poor product quality[6,7].

Introduction or formation of particulate impurities in CBMPs is one of the potential risks associated with manufacturing and handling of these drug products[3,8,9]. Particles found in CBMPs can originate from either the process or the cell product itself. Process-related

particulate impurities may include ineffectively removed antibody coated magnetic beads used for activation and expansion of cells, viral vectors utilized in a cell transduction step, extrinsic particles (glass, cellulose, rubber), or leachables derived from primary containers[10-13]. Sterile filtration of cell suspensions is not possible because of the inherent size of cells; therefore, unwanted micrometer-sized particles will remain in the product if their removal is not complete[14]. Cell-based impurities, on the other hand, comprise materials originating from cells. These may be non-viable or non-therapeutic cells[15], as well as cell agglomerates and cellular debris[9,16]. For example, necrosis induced in cells exposed to extreme physiological conditions (pyroptosis) leads to plasma membrane rupture, release of intracellular contents and formation of debris particles[17]. In contrast to apoptotic (programmed) cell death, where cellular components are packaged into vesicles and digested by appropriate caspases for facilitated removal by the immune system[18], necrosis produces debris with potent inflammatory properties. One of the results from these debris particles may be an adverse immune response upon administration[19]. Furthermore, if larger micrometer-sized particles are introduced into the smaller blood vessels, they may result in tissue damage from thromboembolism[20].

Forced degradation studies are commonly included in the development of any pharmaceutical product as part of establishment of analytical methods and formulation screenings[21,22]. Alongside real time stability studies at the intended storage conditions, forced degradation studies are applied to estimate the shelf-life of products as well as define suitable storage and handling conditions[23]. Moreover, this type of studies can simulate accidental exposure of drug products to deleterious conditions and assist in the evaluation of potential risks occurring to drug products throughout their product life-cycle. These studies also assist in selecting appropriate excipients during formulation development where the aim is to determine a component mixture achieving maximum stability for the active pharmaceutical ingredient. Even though the manufacturability, critical quality attributes (CQAs), degradation pathways and product degradants in CBMPs will vary substantially from, e.g., protein-based therapeutics, the same concept of forced degradation studies can be highly relevant in process and product development of CBMPs.

Extensive testing of a CBMP prior to administration to a patient is a regulatory obligation to assure the product is safe, efficacious and of good quality. The testing parameters include identity, purity, activity and potency of cells. However, also cellular and non-cellular materials must be identified and qualified[15,24]. For this purpose, reliable analytical methods for characterization of product quality and stability testing are necessary[25]. In this study we utilized flow imaging microscopy coupled with convolutional neural networks (FIM-CNN) to establish a high-throughput and label free method for quantification of viable and necrotic cells as well as debris particles in the size range from 1 to 50 µm. We submitted Jurkat cells to external stress factors, which allowed us to define the impact of thawing temperature, freeze-thaw stress and shaking stress on the stability of Jurkat cells. In addition to FIM-CNN, we measured cell quality attributes, including cell membrane integrity and cell metabolism, after exposure of the cells to the same stress stimuli.

Materials and methods

Materials

T-cell leukemia cells (Jurkat, Clone E6-1, ATCC® TIB152™) were donated by Leiden University Medical Centre (LUMC) as frozen 1-ml aliquots at a total cell concentration of 1×10^7 cells/ml (cells counted using NucleoCounter3000 [Chemometec]), and were stored at -145 °C prior to usage. Jurkat cells were formulated in high-glucose RPMI 1640 (RPMI medium; ThermoFisher, Waltham, USA) supplemented with 10% (v/v) fetal bovine serum (FBS; Life Technologies, USA) and 10% (v/v) dimethyl sulfoxide (DMSO) (Life Technologies, Carlsbad, USA). For washing and dilution steps RPMI medium, 1x phosphate buffered saline (Gibco™, pH, 7.4; ThermoFisher, Waltham, USA) or fetal bovine serum stain buffer (FisherScientific, New Hampshire, USA) was used. FBS (heat inactivated, sterile-filtered) and DMSO (suitable for hybridoma, ≥ 99.7%) were purchased from Sigma-Aldrich (St. Louis, USA). Dead Cell Apoptosis Kit (annexin V, fluorescein isothiocyanate [FITC] and propidium iodide [PI]), calcein AM dye and CyQUANT™ LDH kit were purchased from (ThermoFisher, Waltham, USA).

Forced degradation studies

Jurkat cells were exposed to three types of forced degradation studies, as described below. Each of the three types of stress conditions were carried out in duplicate on different days.

Thawing as stress factor

Single 1-ml frozen cell aliquots were transferred from storage at -145 ^{o}C on dry ice to a water bath (GFL, Burgwedel, Germany) for thawing at 37 ^{o}C for 1 min 30 sec (the default thawing condition). For investigation of other thawing temperatures, cells were also thawed in a water bath at 25 °C for 2 min 40 sec and at 5 °C for 4 min 25 sec. Thawing in the water bath was performed to solely dissolve the ice adhering to the walls of the cryovials. Further, the 1-ml aliquot of the partially frozen cell suspension was transferred into 40 ml of RPMI medium equilibrated to the thawing temperature, where the remaining of the ice nucleus dissolved within seconds. The cell suspension was centrifuged at 350 x g for 10 minutes at 20 ^{o}C, after which the supernatant was discarded and the pellet was resuspended in 5 ml of RPMI medium. Total cell concentration and viability were assessed by using a CASY counter (Bremen, Germany) and dilution to $1x10^{6}$ cells/ml was performed by addition of the required volume of RPMI medium (containing DMSO or FBS where stated).

Freeze-thaw stress

DMSO, cooled on wet ice, was slowly added to cell suspensions (placed on wet ice) to reach a target concentration 1%, 2.5%, 5% and 10% (v/v) at a cell concentration of $1x10^{6}$ cells/ml. Further, five 1-ml aliquots were prepared in 1.8-ml Nalgene cryovials, which were submitted to freezing at -18 ^{o}C for 3 hours. This period of time was sufficient for complete freezing of the aliquots. Prior to analysis, the samples were thawed for 2 min at 37 ^{o}C, pooled and washed with fresh RPMI medium. Control samples were stored at 20 ^{o}C for 3 hours and were otherwise treated identically as the freeze-thawed samples.

Shaking stress

Cells at a concentration of $1x10^6$ cells/ml (without or with FBS at 10% [v/v]) were filled (1 ml) into five Nalgene cryovials (ThermoScientific, Waltham, USA) with a 1.8 ml volume capacity. The cryovials were submitted to shaking by constant horizontal agitation at 185 rpm at 25 ^{o}C by using an IC 4000 shaker (IKA, Germany). Analysis of cell suspensions of pooled cell aliquots was performed following 3 hours of shaking. Control samples were stored statically and protected from light at 25 ^{o}C in cryovials, and subsequently pooled.

Flow imaging microscopy (FIM)

Cells (viable and necrotic) and debris particles were quantified by using a FlowCam 8100 (Fluid Imaging Technologies, Scarborough, USA) equipped with a 50-μm flow cell. The objective used resulted in a 20x magnification and sample imaging was performed by a high-resolution CMOS camera (1920x1200 pixels) at 27 frames per second. In total, a sample volume of 140 μl was measured with an efficiency of approximately 63% (i.e., the imaged sample volume was ca. 87 μl). Particles imaged within the flow cell were detected with intensity thresholds of 12 for light and dark pixels. Cleaning steps between sample measurements involved thorough flushing of the flow cell with Terg-a-zyme® enzyme detergent (1% [w/v]) and highly purified water. Collected images were not sorted by using any morphological filters and samples were measured in triplicate, unless otherwise stated.

Image analysis using convolutional neural networks

Particle images captured with a FlowCam were analyzed by using convolutional neural networks (CNN). The CNN was based on the VGG-19 architecture described in our previous study[26]. Briefly, the VGG-19 network using rectified linear unit activation functions, punctuated with max-pooling and dropout layers, was pre-trained on a ImageNet dataset discussed in detail elsewhere[27]. The re-training of the network was performed with the first ten layers frozen in order to save computation time and improve accuracy of the model by preserving its pre-learned feature recognition capabilities. For fine-tuning we split our dataset into an 8:1:1 ratio for training, validation and testing,

respectively. The model was optimized by running 19 epochs with a stochastic gradient descent optimization algorithm and a 0.001 learning rate. The machine learning model was performed by using Keras (2.2.4), Tensorflow (1.13.1) and Python (3.7.3) libraries, and ran on a Nvidia Turing GPU with 11 GB of VRAM.

Generation of particle images for population discrimination

The CNN was fine-tuned on manually labeled images (4,000-4,500) of each of the three populations: viable cells, necrotic cells and debris particles.

Images of viable cells were manually selected from measured samples consisting of Jurkat cells with a viability of 86.8% (based on PI assay). For selection of necrotic cells, two separate methods were used to induce cell necrosis. Firstly, FlowCam images of cell suspensions treated by heat (55 °C for 90 min) were collected, which showed a viability of 7.6% (based on PI assay). Secondly, cells were imaged after incubation with ethanol (10% (v/v)) for 90 min at 37 °C and had a determined viability of 12.8% (based on PI assay). In order to further define image populations of viable and necrotic cells for the network fine-tuning, morphological parameters, such as aspect ratio, circle fit, convexity, sigma intensity and symmetry, of the two populations were used. Only particles (cells) of morphological parameter values falling between the 10th and 90th percentile of the manually selected population as viable and necrotic cells were taken for input to the training of the model. Images of debris particles were manually selected from measured suspensions of cells submitted to vortexing for approximately 2 min or two freeze-thaw cycles (-140 °C – 37 °C).

Automated cell counting

A CASY TTC 150 (Omni Life Science, Bremen, Germany) cell counter equipped with a 150-µm capillary was used for automated cell counting. Cells were diluted 100-fold in CASYton (Omni Life Science, Bremen, Germany) shortly before analysis. Samples were measured in duplicate and each measurement consisted of 5 sub-runs of 400 µl, resulting in more than 5,000 events counted per analysis.

Imaging flow cytometry

To assess cell viability based on cell metabolism, imaging flow cytometry was used in combination with the membrane-permeable dye calcein-AM (calcein-AM assay), at a final concentration of 6.3 nM in the sample to be analyzed. After dye addition, cells were incubated at room temperature for 30 minutes (in the dark) and further washed with 200 µl of stain buffer (with FBS; BD Bioscience, New Jersey, USA). Subsequently, samples were analyzed by using an Amnis FlowSight imaging flow cytometer (Luminex, Seattle, USA) and data were analyzed by using IDEAS 6.2.183 (Luminex, Seattle, USA) image analysis software. Sample measurements were carried out by using a 20x magnification objective in medium-sensitivity mode (132 mm/sec). The side scatter laser was set to 10 mW and the 488-nm fluorescence excitation laser was set to 12 mW. Images of the calcein-AM stained cells were recorded in channel 02 (532/55 nm). Brightfield acquisition was set to channel 9 (582/25 nm) with automatically set intensities. Only particles with a Gradient RMS >30 were collected as true events. Appropriate morphological filters were applied to discriminate between cells and debris particles, in order to assess cell viability/necrosis on the cell population only. Cell viability was calculated based on the proportion of viable cells from the total population shown in Figure S1. Each measurement was performed in duplicate.

Cell apoptosis and necrosis were determined by imaging flow cytometry after labelling of the cells with annexin V-FITC and PI assays. Sample preparation was carried out according to the Dead Cell Apoptosis Kit instructions. After incubation for 15 min in the dark at room temperature samples were kept on wet ice until analysis. After adjusting the excitation power of the FlowSight imaging flow cytometer to 4 mW, the same instrument settings as described in for the calcein-AM assay above was used. Brightfield as well as fluorescence images in channels 02 (532/55 nm) for annexin V-FITC and channel 04 (610/30 nm) for PI were recorded. Appropriate morphological filters based on mean intensity, area, aspect ratio and modulation from channel 09 were applied to discriminate between single cells and cell aggregates or debris particles. Once single cells were selected based on brightfield images, mean intensity values from channel 02 (fluorescence) were plotted against the

particle area (erode mask) where the positively stained cells were classified as viable. Cell viability was calculated based on the proportion of viable cells from the total population shown in Figure S1.

Lactate dehydrogenase release assay

Cell membrane integrity was assessed by using a lactate dehydrogenase (LDH) release assay (CyQUANT; ThermoFisher, Waltham, USA). Loss of cell integrity was measured based on the level of LDH released upon damage to the plasma membrane. The assay is based on the conversion of lactate to pyruvate, which is catalyzed by LDH and results in formation of $NADH^+$. The tetrazolium salt included in the kit is reduced to formazan in presence of $NADH^+$ and can be quantified by absorbance measurements at 490 nm with a reference absorbance of 680 nm. Measurements were performed by using a Tecan Spark plate reader (Tecan, Männedorf, Switzerland). The total cell concentration was adjusted to ca. 150,000 cells/ml with RPMI medium (cell concentration to be within the linear range for this assay (data not shown)). Cells were incubated at 37 ^{o}C and 5% CO_2 for 45 min (with spiked water or Triton X-100) before the assay was carried out according to the manufacturer´s protocol. Release of the amount of LDH in the medium was calculated according to Eq. 1:

$$LDH \text{ release } (\%) = \left(\frac{Spontanous \; LDH \; activity}{Maximum \; LDH \; activity}\right) * 100 \qquad \text{(Eq. 1)}$$

Spontaneous LDH activity was based on measurements of cell suspensions spiked with water and maximum LDH activity values were derived from cell suspensions spiked with Triton X-100 to a target concentration of 10% (v/v). The results for each sample are based on measurements of four replicate wells.

Results

Jurkat cell suspensions were submitted to thawing at three defined temperatures, freeze-thawing in the presence of different DMSO concentrations and shaking in absence and presence of FBS. The stressed samples were characterized by using orthogonal methods for evaluation of the quality of cell suspensions.

FIM-CNN for measurement of cell counts, cell viability and debris particle concentration

We used FlowCam images of viable and necrotic cells as well as debris particles (Figure 1 A) to train a CNN for image classification. The recall value (proportion of positive identifications of all true positives present in the population) for classification of debris particles with our model was 99.5%, proving a high confidence of this classification approach (Figure 1 B). Similar recall values were achieved for the viable and necrotic cell populations (94.0% and 96.6%, respectively). For evaluation of the classification model performance, the F1 score is an additional metric used to assess the weighted average of the precision and recall. Here, the F1 score for debris, viable cells and necrotic cells was determined to be 0.991, 0.933 and 0.919, respectively. Such high values confirm the low number of incorrectly classified images during the testing phase of the network´s fine-tuning. Therefore, FIM-CNN is presented in this study as a novel method for determination of the concentration of viable and necrotic cells, as well as for quantification of debris particles with a heterogeneous size distribution (Figure 1C).
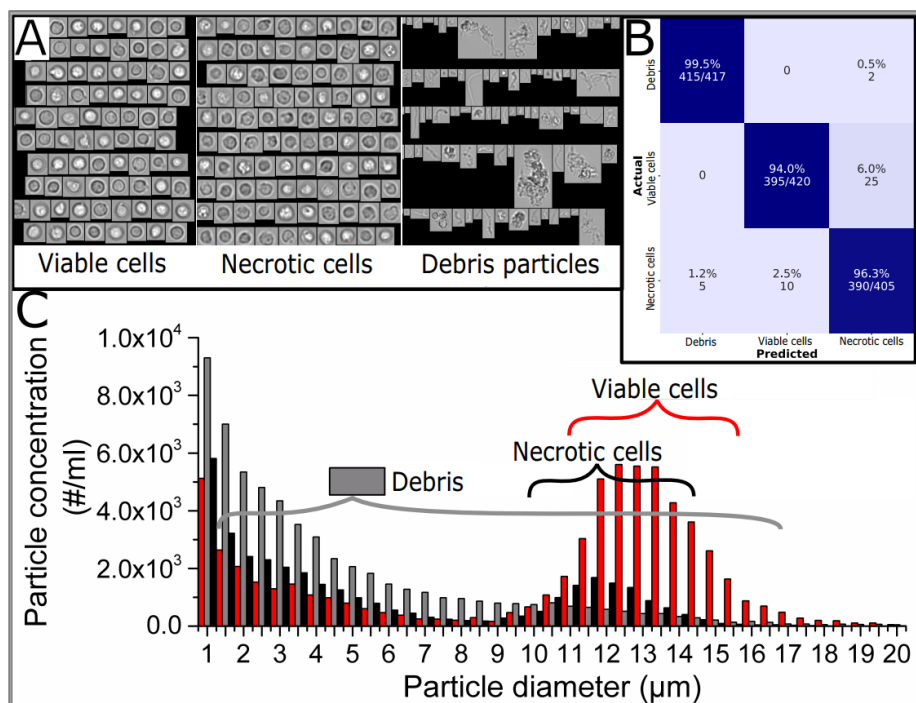
Figure 1: (A) Examplery FlowCam images selected for training of the CNN model, (B) confusion matrix obtained from cross-validation analysis on image datasets not used during model training, (C) particle size distribution of cell suspensions vortexed (enriched in debris particles), heat treated (enriched in necrotic cells) and freshly thawed (viable cells) determined by using FlowCam.

Effect of thawing temperature

Frozen Jurkat cell suspensions were thawed at 5 °C, 25 °C and 37 °C to evaluate the impact of thawing temperature on cell quality (Figure 2 A). FIM-CNN and automated cell counting showed an increase in recovery of viable cells with increasing thawing temperatures. Comparable concentrations of viable cells were obtained from both methods; however, the counts for necrotic cells and debris particles differed substantially. FIM-CNN measured a higher number of necrotic cells in samples thawed at 5 °C, as well as an increasing concentration of debris particles with decreasing thawing temperature. At the lowest tested thawing temperature of 5 °C, cell suspensions contained over 4×10^6 debris particles/ml (i.e., 4-fold higher than the initial cell concentration), including dark and dense particles which were not observed in cell suspensions thawed at 37 °C and 20 °C (Supplementary figure S2).

High cell viability was recorded for aliquots thawed at 37 °C and 20 °C (Figure 2 B). The two fluorescence-based methods showed a viability between 86% and 91%, whereas with FIM-CNN values were between 63% and 71%. However, a clear decrease in cell viability to 43%, 50% and 22% was observed for aliquots thawed at 5 °C according to the calcein-AM, PI and FIM-CNN assays, respectively. For all three thawing temperatures, there was a discrepancy in the absolute values of determined cell viability, when comparing the two fluorescence-based assays and FIM-CNN.

The annexin V-FITC assay suggests that cells are more likely to undergo apoptosis when thawed at lower temperatures (Figure 2 C). In particular, a marked increase in apoptotic cells can be observed in cell suspensions thawed at 5 °C. A similar trend was observed with the LDH release assay, albeit less pronounced (Figure 2 FigureD).
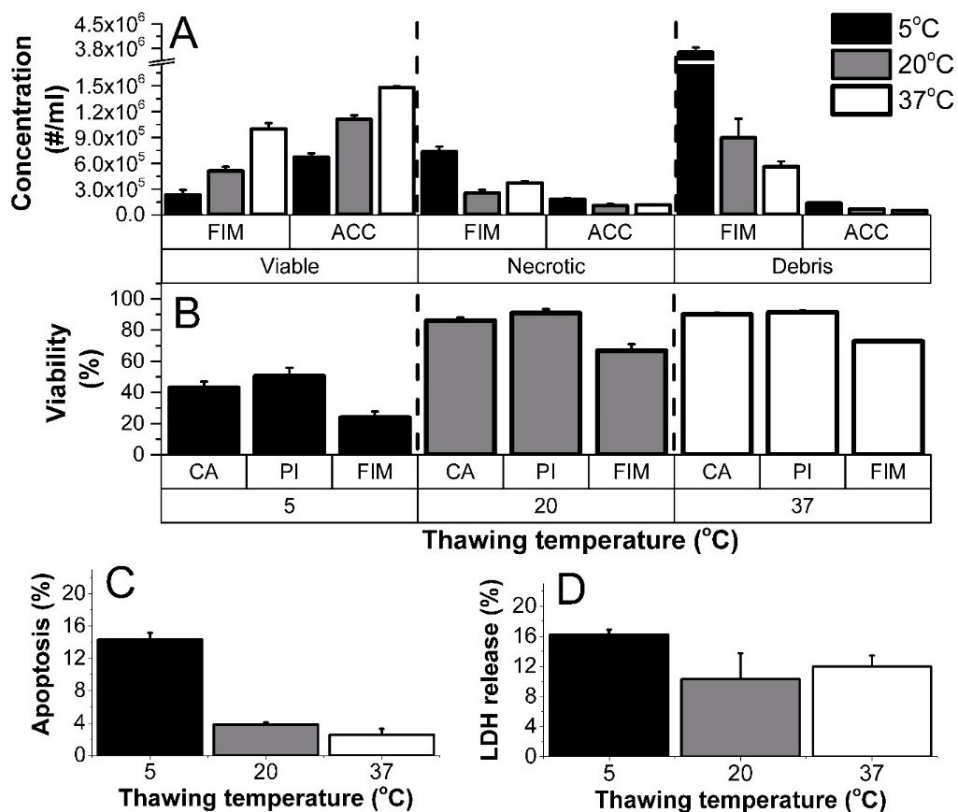
Figure 2: Measurements of cell aliquots after thawing at 5 °C, 25 °C and 37 °C. (A) Determination of concentration of cellular debris, viable and necrotic cells measured by using FIM-CNN (FIM) and automated cell counting (ACC). (B) Measurement of cell viability by performing calcein-AM (CA), propiodium iodide (PI) and FIM-CNN assays. Assessment of (C) cell apoptosis with annexin V-FITC assay and (D) LDH release. Error bars represent standard deviations of mean values.

Effect of freeze-thawing

Jurkat cells formulated in RPMI medium and DMSO (0%, 1%, 2.5%, 5% and 10% [v/v]) were submitted to one freeze-thaw cycle, which included storage of the cell suspensions at -18 °C for three hours and 2 min of thawing at 37 °C. Freeze-thawing of cell suspensions with 0% and 1% (v/v) DMSO led to a reduction of cell counts by >98%, indicating that under these conditions practically all cells lose their viability (data not shown).

Concentrations of cells (viable and necrotic) and debris particles were determined by using FIM-CNN (Figure 3 A and B). With higher DMSO concentrations, higher total cell concentrations were observed after one freeze-thaw cycle, compared to lower tested

cryoprotectant concentrations. Furthermore, cell suspensions with 10% (v/v) DMSO contained the lowest number of debris particles after freeze-thawing. Total cell concentrations prior to freezing (T0) and after three hours of storage at room temperature (Ctrl) were comparable for each tested DMSO concentration. However, control cell suspensions with 10% (v/v) DMSO showed slightly elevated debris contents compared to T0 and cell suspensions with lower DMSO content.

Interestingly, cell viability determined after freeze-thawing was heavily dependent on the assay used (Figure 3 C). The calcein-AM assay suggested the smallest changes of cell viability, with 85-90% cell viability, irrespective of DMSO content and time point. In contrast, PI and FIM-CNN assays showed noticeable (ca. 20%) losses in viability for cell suspensions frozen with 2.5% (v/v) DMSO, indicating that this concentration of cryoprotectant is insufficient for cell stabilization upon freezing. The PI assay also showed a smaller drop of ca. 10% in cell viability for cell suspensions with 5% and 10% (v/v) DMSO for freeze-thawed and control samples compared to T0, whereas FIM showed such a decrease in cell viability only for cell formulations containing 10% (v/v) DMSO. The toxic effects of DMSO was demonstrated by loss of cell viability after an exposure of 3 hours at RT for each tested concentration according to the PI assay, and at 10% (v/v) based on FIM. Based on the results from PI and FIM, the best cell-stabilizing effect of DMSO was achieved at 5% (v/v).

Figure 3: Cell suspensions supplemented with DMSO at three different concentrations before (T0) and after a single freeze-thaw step following a storage for 3 hours at either -18 °C (T1) or storage for 3 hours at RT (Ctrl). FIM was used to measure the concentration of (A) total (viable + necrotic) cells and (B) debris particles. (C) Cell viability was deteremined by using calcein-AM (CA), propiodium iodide (PI) and FIM-CNN (FIM) assays. Error bars represent standard deviation of mean values.

An increase in LDH release in the medium was observed in cell suspensions which underwent freeze-thawing or were stored at room temperature in presence of DMSO (Figure 4 A). Only small differences in LDH concentration were observed in cell formulations with different DMSO concentrations. However, cells frozen with 5% (v/v) DMSO showed less LDH release compared to suspensions with 2.5% and 10% (v/v). Similarly, the fraction of apoptotic cells was smallest for cell suspensions with 5% (v/v) upon freeze-thawing (Figure 4 B).
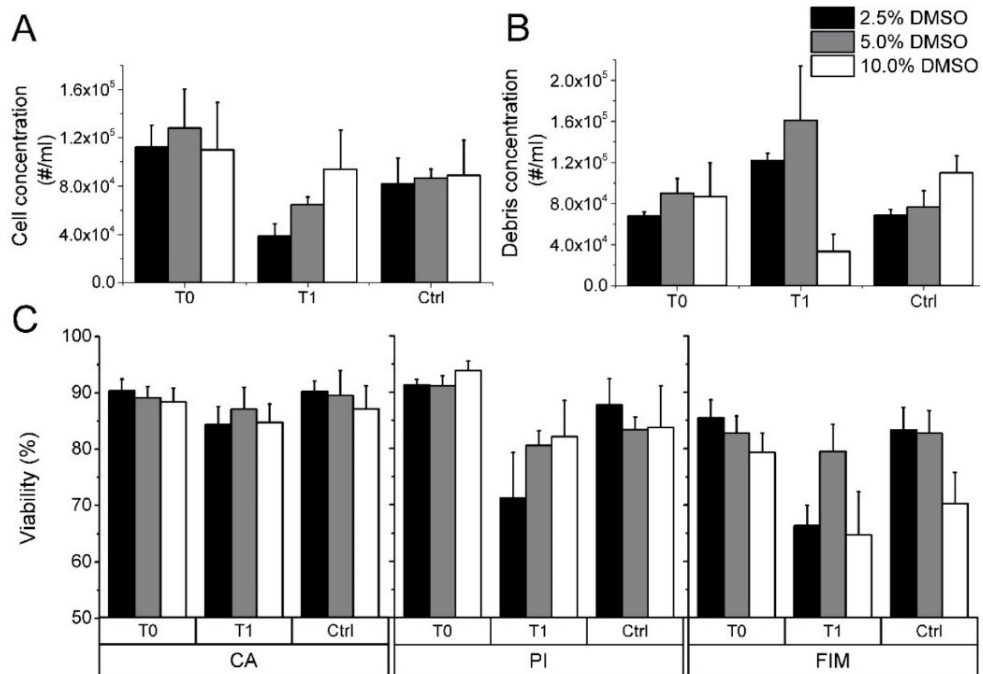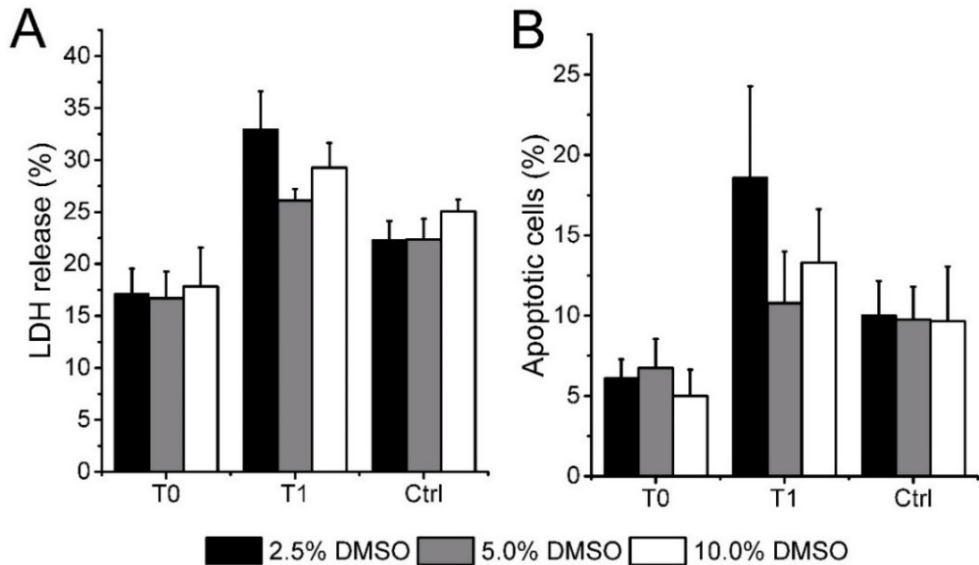
Figure 4: Cell suspensions supplemented with DMSO at three different concentrations befire (T0) and after a single freeze-thaw step following a storage for 3 hours at either -18 ºC (T1) or storage for 3 hours at RT (Ctrl). (A) LDH release assay and (B) apoptotic cell fraction quantified by using imaging flow cytometry (annexin V-FITC assay) at given time points. Error bars represent standard deviation of mean values.

Effect of shaking stress

Jurkat cell suspensions were submitted to horizontal shaking in presence and absence of 10% (v/v) FBS. Figure 5 A presents the total concentration of viable and necrotic cells, as well as debris particles measured by FIM-CNN in the two cell formulations at given time points. Following shaking stress, a substantial decrease in the total number of cells was observed in formulations without FBS compared to cell suspensions containing FBS. A remarkable increase in concentration of debris particles was observed for both formulations. Notably, debris present in stressed cell suspensions supplemented with FBS originated not only from ruptured cells but also from aggregated proteins present in FBS (observed in stressed RPMI medium with 10% [v/v] FBS, data not shown). Cell viability after shaking stress and quiescent storage was very similar to the viability of cells at T0 according to all three methods used (Supplementary figure S3).

The LDH release in stressed cell suspensions was higher compared to T0 or control cell suspensions, irrespective of FBS content. The increase in LDH release in the formulation with FBS was unexpected, given the observation that cell viability and cell concentration remained unchanged at all sampling points. A slight increase in the apoptotic cell fraction was observed after shaking in formulations with and without FBS, but a similar increase was observed in the unshaken control. Thus, shaking stress did not have a detectable impact on cell apoptosis in our study.

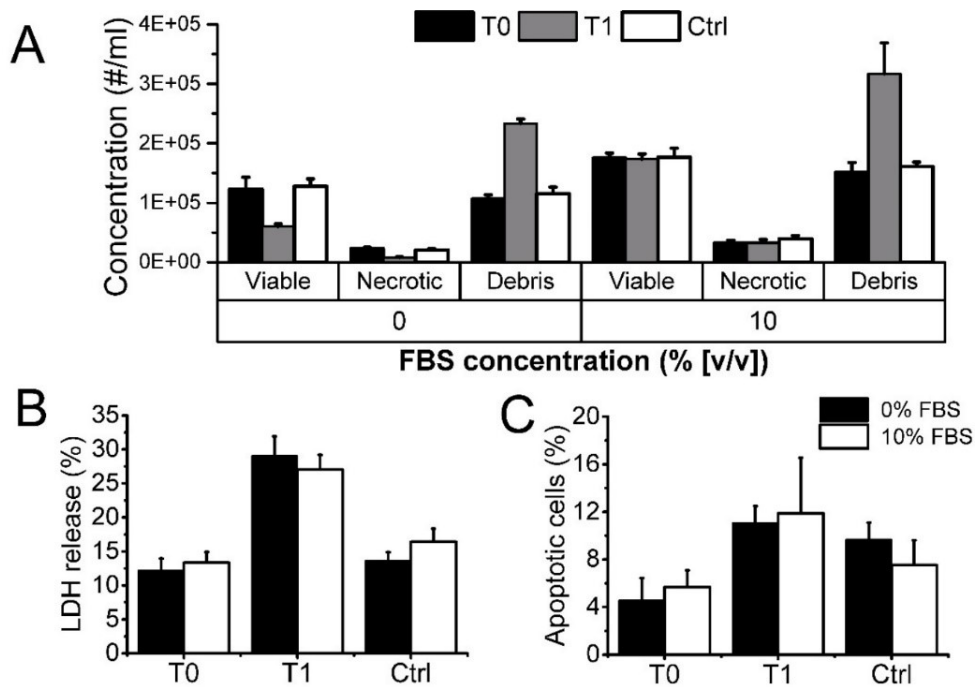Figure 5: Cell suspensions without or with FBS (10% (v/v)) before (T0) and after shaking (T1) or quiescent storage (Ctrl) at room temperature. (A) Total concentration of cells (viable and necrotic) and debris particles by using FIM. (B) LDH release and (C) apoptotic cell fraction quantified by using imaging flow cytometry (annexin V-FITC assay) at given time points. Error bars represent standard deviation of mean values.

Discussion

Currently approved CBMPs are either stored in a cryopreserved (frozen liquid) or a non-frozen (liquid) state[25]. In both cases, cells may be exposed to all kind of stress factors, e.g., resulting from freeze-thawing or handling in the clinic prior to administration. This may cause cell damage, loss in quality and potential clinical implications, such as serious adverse effects or lack of drug efficacy. Cells have developed mechanisms to handle certain stress stimuli by activating signalling pathways and stress response proteins[6]. However, when the threshold of deleterious factors is surpassed, cells can abruptly lose membrane integrity or undergo programmed death[28]. Within human bodies, macrophages and dendritic cells of the innate immune system are equipped with appropriate mechanisms for removal of dying cells[17,23]. However, in CBMPs any cell degradants that may be formed, such as dead cells and cell debris, will remain within the product and might accelerate further cell degradation[25]. Furthermore, debris particles originating from abruptly ruptured cells are deficient in "eat-me" signals of apoptotic cells[29]. After administration, such necrotic cells and debris particles may trigger the immune system potentially resulting in inflammatory responses[17].

Viable cell concentration is considered as one of the most important quality attributes of CBMPs. A manifold of viability assays, based on the integrity of cell membrane or cellular metabolism, is available[30]. However, common viability assays involve fluorescent staining which encompass expensive fluorescent dyes and multistep preparation procedures with incubation times. Additionally, manual gating in flow cytometers is heavily biased and difficult to reproduce between different operators[31,32]. Thus, the drawbacks of these assays limit their capabilities to be robust and high-throughput methods for quantification of necrotic cells. Furthermore, classic trypan blue exclusion exhibits cytotoxic effects to cells[33], whereas other colorimetric assays can be affected by the pH of the culture medium or particular enzymes[30]. These drawbacks may compromise assay accuracy and precision.

In our study we applied FIM-CNN to accurately determine the number of viable and necrotic cells in suspensions of up to 200,000 cells/ml based on morphological appearance of cells. Necrosis is manifested by several morphological changes to the cell appearance,

including rounding of the cell and cytoplasmic swelling[34]. These are not obvious in the FlowCam images to a human eye and are difficult to discriminate with the use of morphological parameters output by the FlowCam software[35]. However, pattern recognition algorithms implemented in CNN models have been shown to successfully discriminate between complex fingerprints, i.e., protein aggregate structures formed upon different stress conditions[36], and proved to be successful in classification of cell-related particles in our study.

The characterization of particulate matter in parenterals is described in pharmacopeial monographs and products should meet the acceptance limits for subvisible particle impurities sized above 10 µm and 25 µm[19]. However, given the particulate nature of cells, it is challenging to fulfil specific particle testing requirements applicable to injectable products, as human cells fall within the subvisible size range (typically 7-30 µm)[37]. One of the standard pharmacopeial methods for quantification of subvisible particle impurities, light obscuration, will not discriminate between cells and other particulates. Hence, high-throughput microscopy methods providing morphological data on particles within several hundred µl are promising tools for evaluation of particulates in cell-based products. Previously, the FIM approach was utilized to identify and quantify Dynabeads, which are commonly used during cell activation, in cell suspensions[26]. Moreover, FIM has also found its use in detection of other particulates, such as process impurities in CBMPs[13]. Here, by using FIM-CNN, reliable numbers on the concentration of debris particles sized 1–50 µm could be obtained (Figure 1). Debris particles consist of a mixture of lipids, proteins, nucleic acids and potentially other extrinsic particles, and thus are particulate impurities in CBMPs. Nevertheless, the commonly applied cell characterization methods do not report on the debris content within cell suspensions, likely omitting relevant information on the potential implications for product quality (consistency and stability) and safety of these drug products (see discussion above). In addition, debris content imaged by using a bright-field microscope in cell suspensions was previously used to assess the level of late-stage apoptotic primary human hepatocytes and MDCK cells[38]. Similarly, we observed that exposure of cells to stress conditions led to an increase in cellular debris which correlated well with loss in cell viability and total cell count.

The unique supply chain of some CBMPs, where at least one freeze-thaw cycle is included, makes cryopreservation crucial in conserving the integrity of the product. Cryopreservation of human cells has been widely studied and multiple factors have been found critical in this process[39-42]. The freezing and thawing rates are two of the most critical parameters to be optimized to achieve high recovery of functional cells post-thawing. However, the optimal conditions are different for each cell suspension, and the impact of the thawing rate is less understood compared to the effect of freezing rate on cells[39]. Jurkat cells used in our study were submitted to controlled freezing with 10% (v/v) DMSO at a rate of 1 ^oC min^{-1}. Subsequent thawing at 5 ^oC in a water bath had deleterious effect on the viability and apoptotic rate of cells (Figure 2). The negative impact of slow thawing on cells may result from recrystallization of ice. Metastable ice crystals formed during freezing may have formed larger crystals upon thawing at 5 ^oC, leading to denaturation of cellular proteins and disruption of membranes[43]. Similar observations were made by Thorpe et al., who reported that decreasing the thawing temperature led to a lower survival of mouse lymphocytes[44]. On the other hand, our results are in disagreement with another study in which the thawing temperature had minimal effects on the survival of T cells[39]. In addition to reduced viability, we observed an increase in concentration of debris particles at lower thawing temperatures with dense and irregular particles formed at the lowest thawing temperature (Supplementary figure S2). Such debris particles were not observed in cell suspensions thawed at 20 ^oC or 37 ^oC.

The presence of cryoprotectants is important for the cryopreservation of cells stored at ultra-low temperatures (vapour phase of liquid nitrogen [< 120 ^oC]). DMSO is currently the most widely used cryoprotectant in cryobiology[40]. Its amphiphilic and water-binding properties allow for a ready pass through cell membranes, thereby avoiding the efflux of water from the cytoplasm and thus preventing cellular dehydration upon freezing. At commonly used DMSO concentrations, such as 5-10% (v/v), formation of large intracellular and extracellular crystalline lattices is prevented by interfering with water molecules[45]. Formation of ice crystals and preservation of cell viability will also depend on the cooling rate, where the preferred very slow cooling rates (0.1 ^oC min^{-1}) produce fine dendritic ice structures and fast cooling rates (10 ^oC min^{-1}) generate large ice crystals [39]. In

our study, Jurkat cells were subjected to passive (uncontrolled) freezing at -18 °C in presence of DMSO at a concentration ranging from 0% to 10% to mimic unintentional freezing. In agreement with previously reported data[46], the lowest tested DMSO concentrations (i.e., 0% and 1%) did not show any cryoprotection towards cells upon freeze-thawing as nearly a complete loss in cell viability was observed (data not shown). In contrast, the highest tested DMSO concentration of 10% (v/v) showed the highest cell recovery after one freeze-thaw cycle with the lowest number of debris particles present in cell suspensions (Figure 3). Although, control samples (stored at RT) with the highest tested DMSO concentration showed an increase in debris particle over time, most likely due to its cytotoxic effect on cells.

Interestingly, the three viability assays used in our study did not provide conclusive results on the degree of protection against freeze-thawing at each tested DMSO concentration. The calcein-AM assay showed to be least sensitive in detecting changes in cell viability after freeze-thaw, whereas the PI and FIM assays detected a substantial drop in viability in suspensions with 2.5% (v/v) DMSO. However, for cell suspensions with 5% and 10% (v/v) DMSO, a reduced viability was observed with the PI assay for freeze-thawed and control samples, whereas FIM suggested minimal impact of freeze-thawing on cell viability with 5% (v/v) DMSO. It should be noted that each of the viability assays used may result in different outcomes given the different assay principles. For example, when using the calcein-AM assay, some apoptotic cells would be metabolically active and show positive staining, whereas others may be classified as necrotic. In the PI assay, only PI positive cells were classified as necrotic and cells undergoing early apoptosis did not show fluorescence, thus were regarded as viable. However, it is not currently possible to discriminate apoptotic cells by using FIM-CNN, therefore these cells may be classified to either the viable or necrotic population. In addition, post-thawed cell suspensions with 5% (v/v) DMSO showed the smallest fraction of apoptotic cells (based on annexin V-FITC assay) and the lowest LDH release, compared to the two other tested DMSO concentrations (Figure 4). Similar observations were made for peripheral blood stem cells[47,48]. After cryopreservation with 5% DMSO, less apoptotic and necrotic peripheral blood stem cells compared to suspensions with 10% DMSO were measured[48]. The apoptosis-inducing

effect of DMSO, via interaction with the PD-1 receptor and their ligands[40], was observed in our control group where a nearly 2-fold increase in apoptotic cell content was recorded. Taking into consideration the toxicity of DMSO and its potential to cause adverse effects upon administration[47], optimization of the DMSO concentration, or its replacement by a less cytotoxic alternative, should be an important focus during formulation development of cryopreserved CBMPs. Furthermore, effects of freeze-thawing on the functionality of cells and cellular biochemical pathways was beyond the scope of this study, but should also be tested during the development of CBMPs[25,49].

Mechanical stress is potentially the most frequent stress factor to which biopharmaceutical products are exposed to during processing, transportation and handling[50]. Solid-liquid and air-liquid interfaces play a crucial role in the formation of particles in protein-based formulations during agitation[51]. Thereby, amphiphilic, non-ionic surfactants (e.g., polysorbate 20 or 80) are commonly used in order to reduce protein aggregation upon interfacial stress and mechanical shock[52]. Unfortunately, such an approach may not be successful for CBMPs, as polysorbates have lytic effects on cells even at low concentrations[53]. Up to date, mild shaking conditions were applied to cell suspensions mainly for the purpose of cell expansion or to induce formation of cell aggregates for creation *ex vivo* tissue models[54,55]. In our study, we instigated harsher stress conditions to mimic potential "real-life" mechanical stress which has been shown to have detrimental effects on protein-based therapeutics[50,51]. Cell suspensions filled into cryovials and positioned vertically were unaffected by shaking speeds up to 500 rpm. However, positioning of the cryovials horizontally led to a dramatic loss (ca. 50%) of total cell concentration after relatively short shaking stress at 185 rpm (Figure 5). Although the cell viability was unaffected by the mechanical stress according to the two fluorescence-based methods and FIM-CNN, LDH release and apoptosis were markedly increased compared to control samples. The increase in free LDH content suggests compromised cell quality and illustrates the value of using orthogonal cell characterization techniques. Furthermore, FBS demonstrated a protective effect towards cells upon shaking. While FBS is a commonly used supplement in cell culture and may be protective towards cells against mechanical stress, it is considered as a process-related impurity that is difficult to remove

in the downstream processing steps[4]. Additionally, FBS is of non-human origin, which is associated with safety and immunogenicity concerns. Moreover, bovine serum proteins are also susceptible to aggregation and may form particulate species, which add another unwanted complexity with respect to particulate impurities in CBMPs[19]. Ultimately, a wider array of formulation excipients should be tested in cell suspensions submitted to forced degradation studies in order to allow for a decision-based formulation strategy of CBMPs.

Conclusions

To the best of our knowledge, this study is the first to demonstrate the application of systematic forced degradation studies in the evaluation of cell stability and formulation, using Jurkat cells as model. The uniform cell line of immortalized cells may not fully reflect the behaviour of cell samples used in clinics. The aging of primary human cells will introduce a much greater heterogeneity on morphological cell features and pose greater challenges for acquisition of quality parameters. However, application of CNN for image classification allowed us to utilize FIM as a robust and fast analytical tool for characterization of cell suspensions, which has the potential for translation into assessment of "real-life" samples. Cell viability was assessed by using FIM-CNN in addition to other established approaches and a good correlation between the methods was observed. In addition, quantification of debris particles in CBMPs was only possible with FIM-CNN, highlighting the method's ability to monitor particulate impurities in cell suspensions. Overall, our study shows that thermal, freeze-thaw and shaking stresses are relevant tools for CBMP formulation studies. Moreover, it illustrates the importance of choosing a broad range of analytical methods to better understand the impact of each stress factor on CBMP quality.

Acknowledgment

References:

1. Walsh G. Biopharmaceutical benchmarks 2018. Nat Biotechnol. 2018;36(12):1136-1145. doi:10.1038/nbt.4305.

2. Eyles JE, Vessillier S, Jones A, Stacey G, Schneider CK, Price J. Cell therapy products: focus on issues with manufacturing and quality control of chimeric antigen receptor T-cell therapies. J Chem Technol Biotechnol. 2019;94(4):1008-1016. doi:10.1002/jctb.5829.

3. Jere D, Sediq AS, Huwyler J, Vollrath I, Kardorff M, Mahler H-C. Challenges for Cell-Based Medicinal Products From a Pharmaceutical Product Perspective. J Pharm Sci. 2020. doi:10.1016/j.xphs.2020.11.040.

4. Levine BL, Miskin J, Wonnacott K, Keir C. Global Manufacturing of CAR T Cell Therapy. Mol Ther Methods Clin Dev. 2017;4:92-101. doi:10.1016/j.omtm.2016.12.006.

5. Iancu EM, Kandalaft LE. Challenges and advantages of cell therapy manufacturing under Good Manufacturing Practices within the hospital setting. Curr Opin Biotechnol. 2020;65:233-241. doi:10.1016/j.copbio.2020.05.005.

6. Fulda S, Gorman AM, Hori O, Samali A. Cellular stress responses: cell survival and cell death. Int J Cell Biol. 2010;2010:214074. doi:10.1155/2010/214074.

7. Woods EJ, Thirumala S, Badhe-Buchanan SS, Clarke D, Mathew AJ. Off the shelf cellular therapeutics: Factors to consider during cryopreservation and storage of human cells for clinical use. Cytotherapy. 2016;18(6):697-711. doi:10.1016/j.jcyt.2016.03.295.

8. Clarke D, Harati D, Martin J, et al. Managing particulates in cellular therapy. Cytotherapy. 2012;14(9):1032-1040. doi:10.3109/14653249.2012.706709.

9. Clarke D, Stanton J, Powers D, et al. Managing particulates in cell therapy: Guidance for best practice. Cytotherapy. 2016;18(9):1063-1076. doi:10.1016/j.jcyt.2016.05.011.

10. Marín Morales JM, Münch N, Peter K, et al. Automated Clinical Grade Expansion of Regulatory T Cells in a Fully Closed System. Front Immunol. 2019;10:38. doi:10.3389/fimmu.2019.00038.

11. Neurauter AA, Bonyhadi M, Lien E, et al. Cell isolation and expansion using Dynabeads. Adv Biochem Eng Biotechnol. 2007;106:41-73. doi:10.1007/10_2007_072.

12. Iyer RK, Bowles PA, Kim H, Dulgar-Tulloch A. Industrializing Autologous Adoptive Immunotherapies: Manufacturing Advances and Challenges. Front Med (Lausanne). 2018;5:150. doi:10.3389/fmed.2018.00150.

13. Vollrath I, Mathaes R, Sediq AS, et al. Subvisible Particulate Contamination in Cell Therapy Products-Can We Distinguish? J Pharm Sci. 2019. doi:10.1016/j.xphs.2019.09.002.

14. Morgan RA, Boyerinas B. Genetic Modification of T Cells. Biomedicines. 2016;4(2). doi:10.3390/biomedicines4020009.

15. European Medicines Agency. Guideline on quality, non-clinical and clinical requirements for investigational advanced therapy medicinal products in clinical trials. 2019

https://www.ema.europa.eu/ documents/ scientific-guideline/draft-guideline-quality-non-clinical-clinical-requirements-investigational-advanced-therapy_en.pdf. Accessed 05.Mar.2021

16. Herberts CA, Kwa MSG, Hermsen HPH. Risk factors in the development of stem cell therapy. J Transl Med. 2011;9(1):29. doi:10.1186/1479-5876-9-29.

17. Westman J, Grinstein S, Marques PE. Phagocytosis of Necrotic Debris at Sites of Injury and Inflammation. Front Immunol. 2019;10:3030. doi:10.3389/fimmu.2019.03030.

18. Green DR, Ferguson T, Zitvogel L, Kroemer G. Immunogenic and tolerogenic cell death. Nat Rev Immunol. 2009;9(5):353-363. doi:10.1038/nri2545.

19. Carpenter JF, Randolph TW, Jiskoot W, et al. Overlooking subvisible particles in therapeutic protein products: gaps that may compromise product quality. J Pharm Sci. 2009;98(4):1201-1205. doi:10.1002/jps.21530.

20. Bukofzer S, Ayres J, Chavez A, et al. Industry Perspective on the Medical Risk of Visible Particles in Injectable Drug Products. PDA J Pharm Sci Tech. 2015;69(1):123. doi:10.5731/pdajpst.2015.01037.

21. Hawe A, Wiggenhorn M, van de Weert M, Garbe JHO, Mahler H-C, Jiskoot W. Forced Degradation of Therapeutic Proteins. J Pharm Sci. 2012;101(3):895-913. doi:10.1002/jps.22812.

22. Halley J, Chou YR, Cicchino C, et al. An Industry Perspective on Forced Degradation Studies of Biopharmaceuticals: Survey Outcome and Recommendations. J Pharm Sci. 2020;109(1):6-21. doi:10.1016/j.xphs.2019.09.018.

23. Ammann C. Stability studies needed to define the handling and transport conditions of sensitive pharmaceutical or biotechnological products. AAPS PharmSciTech. 2011;12(4):1264-1275. doi:10.1208/s12249-011-9684-0.

24. European Medicines Agency. Guideline on quality, non-clinical and clinical aspects of medicinal products containing genetically modified cells. 2020. https://www.ema.europa.eu/documents/scientific-guideline/guideline-quality-non-clinical-clinical-aspects-medicinal-products-containing-genetically-modified_en.pdf. Accessed 03.Mar.2021.

25. Hoogendoorn KH, Crommelin DJA, Jiskoot W. Formulation of Cell-Based Medicinal Products: A Question of Life or Death? J Pharm Sci. 2020. doi:10.1016/j.xphs.2020.07.002.

26. Grabarek AD, Senel E, Menzen T, et al. Particulate impurities in cell-based medicinal products traced by flow imaging microscopy combined with deep learning for image analysis. Cytotherapy. 2020. doi:10.1016/j.jcyt.2020.04.093.

27. Russakovsky O, Deng J, Su H, et al. ImageNet Large Scale Visual Recognition Challenge. Int J Comput Vis. 2015;115(3):211-252. doi:10.1007/s11263-015-0816-y.

28. Green DR, Llambi F. Cell Death Signaling. Cold Spring Harb Perspect Biol. 2015;7(12):a006080. doi:10.1101/cshperspect.a006080.

29. Sachet M, Liang YY, Oehler R. The immune response to secondary necrotic cells. Apoptosis. 2017;22(10):1189-1204. doi:10.1007/s10495-017-1413-z.

30. Kepp O, Galluzzi L, Lipinski M, Yuan J, Kroemer G. Cell death assays for drug discovery. Nat Rev Drug Discov. 2011;10(3):221-237. doi:10.1038/nrd3373.

31. Lippeveld M, Knill C, Ladlow E, et al. Classification of Human White Blood Cells Using Machine Learning for Stain-Free Imaging Flow Cytometry. Cytometry A. 2019. doi:10.1002/cyto.a.23920.

32. Grant R, Coopman K, Medcalf N, et al. Quantifying Operator Subjectivity within Flow Cytometry Data Analysis as a Source of Measurement Uncertainty and the Impact of Experience on Results. PDA J Pharm Sci Tech. 2021;75(1):33. doi:10.5731/pdajpst.2019.011213.

33. Chan LL-Y, Rice WL, Qiu J. Observation and quantification of the morphological effect of trypan blue rupturing dead or dying cells. PLoS ONE. 2020;15(1):e0227950. doi:10.1371/journal.pone.0227950.

34. Vanden Berghe T, Vanlangenakker N, Parthoens E, et al. Necroptosis, necrosis and secondary necrosis converge on similar cellular disintegration features. Cell Death Differ. 2010;17(6):922-930. doi:10.1038/cdd.2009.184.

35. Sediq AS, Klem R, Nejadnik MR, Meij P, Jiskoot W. Label-Free, Flow-Imaging Methods for Determination of Cell Concentration and Viability. Pharm Res. 2018;35(8):150. doi:10.1007/s11095-018-2422-5.

36. Gambe-Gilbuena A, Shibano Y, Krayukhina E, Torisu T, Uchiyama S. Automatic Identification of the Stress Sources of Protein Aggregates Using Flow Imaging Microscopy Images. J Pharm Sci. 2020;109(1):614-623. doi:10.1016/j.xphs.2019.10.034.

37. Rosenberg G. Microscopic haematology : a practical guide for the laboratory. Amsterdam: Harwood Academic Publishers; 1997.

38. Ölander M, Handin N, Artursson P. Image-Based Quantification of Cell Debris as a Measure of Apoptosis. Anal Chem. 2019:5548-5552. doi:10.1021/acs.analchem.9b01243.

39. Baboo J, Kilbride P, Delahaye M, et al. The Impact of Varying Cooling and Thawing Rates on the Quality of Cryopreserved Human Peripheral Blood T Cells. Sci Rep. 2019;9(1):3417. doi:10.1038/s41598-019-39957-x.

40. Baust JM, Campbell LH, Harbell JW. Best practices for cryopreserving, thawing, recovering, and assessing cells. In Vitro Cell Dev Biol Anim. 2017;53(10):855-871. doi:10.1007/s11626-017-0201-y.

41. Hughes SM, Shu Z, Levy CN, et al. Cryopreservation of Human Mucosal Leukocytes. PLoS ONE. 2016;11(5):e0156293. doi:10.1371/journal.pone.0156293.

42. Hornberger K, Yu G, McKenna D, Hubel A. Cryopreservation of Hematopoietic Stem Cells: Emerging Assays, Cryoprotectant Agents, and Technology to Improve Outcomes. Transfus Med Hemother. 2019;46(3):188-196. doi:10.1159/000496068.

43. Mazur P, Seki S. Survival of mouse oocytes after being cooled in a vitrification solution to -196°C at 95° to 70,000°C/min and warmed at 610° to 118,000°C/min: A new paradigm for cryopreservation by vitrification. Cryobiology. 2011;62(1):1-7. doi:10.1016/j.cryobiol.2010.10.159.

44. Thorpe P, Knight S, Farrant J. Optimal conditions for the preservation of mouse lymph node cells in liquid nitrogen using cooling rate techniques. Cryobiology. 1976;13:126-133.

45. Brayton CF. Dimethyl sulfoxide (DMSO): a review. Cornell Vet. 1986;76(1):61-90.

46. Giugliarelli A, Sassi P, Urbanelli L, et al. Cryopreservation of cells: FT-IR monitoring of lipid membrane at freeze-thaw cycles. Biophys Chem. 2016;208:34-39. doi:10.1016/j.bpc.2015.08.001.

47. Mitrus I, Smagur A, Fidyk W, et al. Reduction of DMSO concentration in cryopreservation mixture from 10% to 7.5% and 5% has no impact on engraftment after autologous peripheral blood stem cell transplantation: results of a prospective, randomized study. Bone Marrow Transplant. 2018;53(3):274-280. doi:10.1038/s41409-017-0056-6.

48. Abrahamsen, J. et al. Cryopreserving human peripheral blood progenitor cells with 5-percent rather than 10-percent DMSO results in less apoptosis and necrosis in CD34+ cells.

49. Panch SR, Srivastava SK, Elavia N, et al. Effect of Cryopreservation on Autologous Chimeric Antigen Receptor T Cell Characteristics. Mol Ther. 2019:1275-1285. doi:10.1016/j.ymthe.2019.05.015.

50. Nejadnik MR, Randolph TW, Volkin DB, et al. Postproduction Handling and Administration of Protein Pharmaceuticals and Potential Instability Issues. J Pharm Sci. 2018;107(8):2013-2019. doi:10.1016/j.xphs.2018.04.005.

51. Das TK, Narhi LO, Sreedhara A, et al. Stress Factors in mAb Drug Substance Production Processes: Critical Assessment of Impact on Product Quality and Control Strategy. J Pharm Sci. 2020;109(1):116-133. doi:10.1016/j.xphs.2019.09.023.

52. Grabarek AD, Bozic U, Rousel J, et al. What Makes Polysorbate Functional? Impact of Polysorbate 80 Grade and Quality on IgG Stability During Mechanical Stress. J Pharm Sci. 2019. doi:10.1016/j.xphs.2019.10.015.

Supplementary information
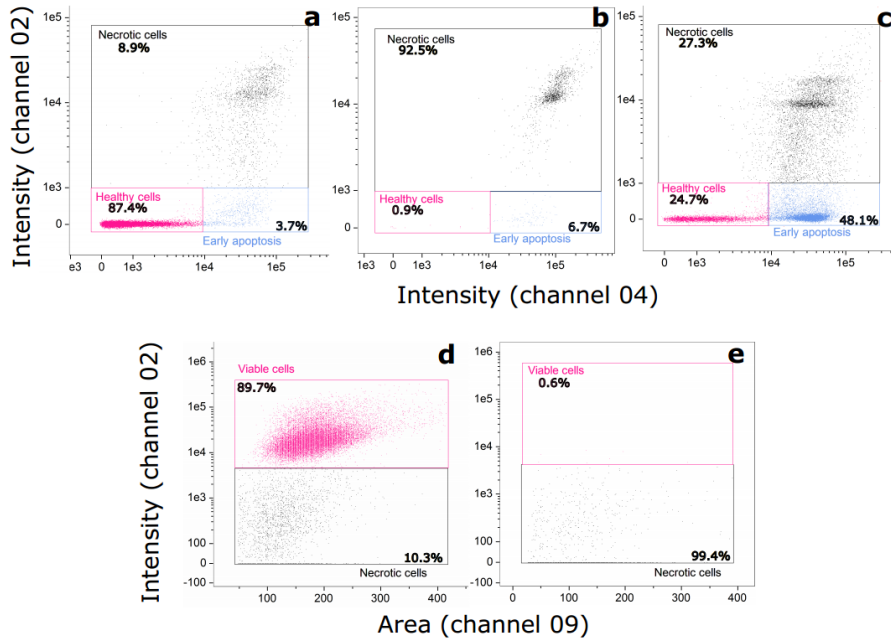
Supplementary figure S1: Manual gating of (a) freshly thawed cells, (b) heat treated cells, (c) camptothecin treated cells measured by using annexin V-FITC and PI assay. Viable cells consist of healthy and apoptotic cells. Manual gating of (d) freshly thawed cells and (e) digitonin treated cells measured by using calcein-AM assay.
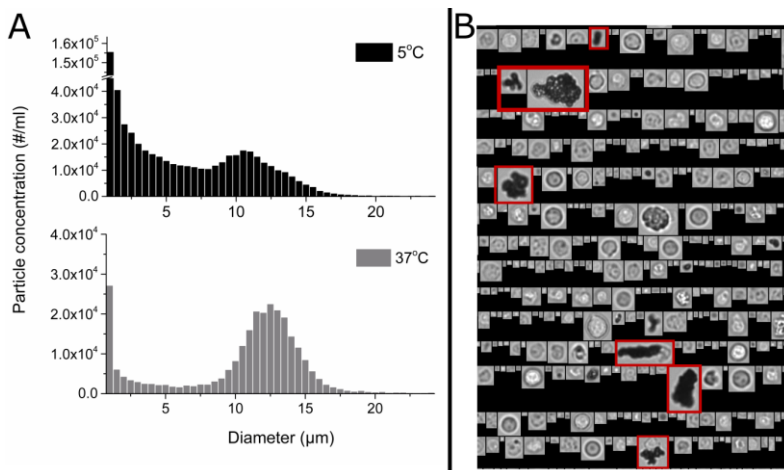
Supplementary figure S2: (A) Size distribution of Jurkat cells measured by using FIM after thawing at 5 °C and 37 °C. (B) Exemplary images of particles detected in Jurkat cell suspensions after thawing at 5 °C. Particles highlighted in the red boxes were not present in thawed suspensions at 20 °C and 37 °C
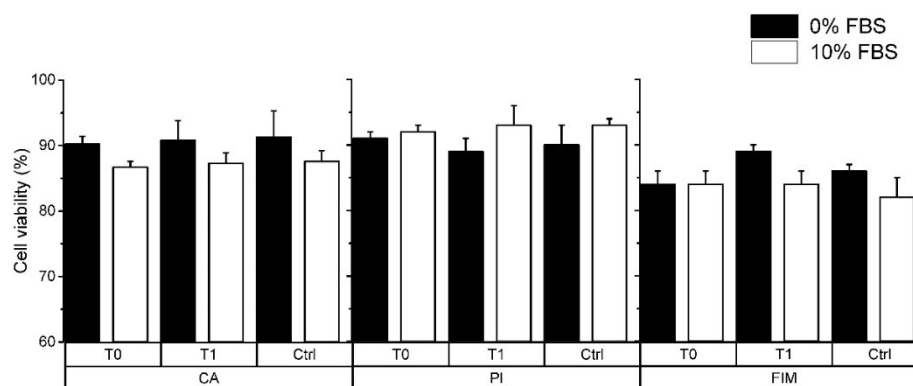
Supplementary figure S3: Measurements of cell viability by performing calcein-AM (CA), propiodium iodide (PI) and FIM-CNN (FIM) assays after horizontal shaking in absence and presence of 10% (v/v) FBS. (A). Error bars represent standard deviation of mean values.

Chapter 8

Summary, conclusions and perspectives

Summary and conclusions

The establishment of analytical methods for characterization of particles in biopharmaceutical products is of critical importance during drug product development. Early assessment of particulate impurities and degradation pathways in protein-based formulations during (accelerated) storage and forced degradation conditions can decrease the chances of clinical failures at later stages of development and support the quality assessment of drug products. Furthermore, cell-based medicinal products (CBMPs), an emerging class of therapeutics, are comprised of heterogeneous mixtures of particulates and require analytical methods with advanced data processing approaches for comprehensive product characterization.

In **Chapter 2**, we investigated the advantages and limitations of a recently developed nanoparticle characterization technique – microfluidic resistive pulse sensing (MRPS). The single particle analysis technique was compared to other more established particle characterization techniques, including dynamic light scattering (DLS), nanoparticle tracking analysis (NTA) and resonant mass measurement (RMM), with respect to particle sizing and counting. To this end, samples comprising polystyrene beads, liposomes, bacteria and protein aggregates were measured. MRPS was shown to have the widest measurable concentration range amongst all tested techniques. This would make MRPS superior in quantification of drug products with high particle loads, such as virus- or liposomal-based products, as no dilution of the sample is required. MRPS, RMM and NTA are single particle counting techniques, thus their sizing resolution of samples with heterogeneous particle populations is superior to that of DLS. More in-depth examination of size resolution revealed that MRPS slightly outperforms RMM, whereas NTA demonstrated the poorest capabilities in resolving two distinct particle populations. However, the requirement of a relatively high electrical conductivity for samples measured by using MRPS can be a limitation of the technique, as shown in the next chapter.

Chapter 3 describes a follow-up study on nanoparticle characterization techniques for the analysis of proteinaceous particles within a mAb formulation. In particular, the impact of spiking electrolytes into mAb formulations was investigated. Measurements with tunable

resistive pulse sensing (TRPS) and MRPS require samples to have sufficient electrical conductivity. For commonly used protein formulations with low electrical conductivity, samples must be spiked with electrolytes prior to analysis. However, by using RMM and NTA we found a substantial increase in nano-meter sized particles in heat stressed monoclonal antibody (mAb) formulations that were spiked with sodium chloride or histidine. Such a change upon spiking was not observed for unstressed protein samples. Therefore, the impact of adding electrolytes to protein formulations for resistive pulse sensing measurements requires prior assessment with respect to the stability of protein monomers and aggregates.

In **Chapter 4,** we investigated the immunogenicity of previously discovered nanoparticle impurities (NPIs) present in sugars of pharmaceutical grade[1,2]. NPIs isolated from pharmaceutical-grade sucrose, a commonly used formulation excipient, were found to contain β-glucans that can act as adjuvants in the presence of immunogenic agents (e.g., protein aggregates). In contrast to previous studies, trastuzumab formulations incubated for several hours in presence of NPIs showed only a minor increase in the concentration of nano-meter sized particles and no substantial increase in the levels of micro-meter sized particles. NPIs alone at a high concentration (10^{10} p/ml) or in the presence of trastuzumab at 1 mg/ml did not activate monocyte-derived dendritic cells (moDC). These results suggest that, in contrast to our expectations, NPIs in the presence or absence of protein are not immunogenic in the tested *in vitro* model.

Chapter 5 focused on the role of the grade polysorbate 80 (PS80), another important excipient, on its protein-stabilizing effect during mechanical stress. Exposure of protein formulations to mechanical stress is known to lead to particle formation[3,4]. Two grades of PS80, i.e., specified by the United States Pharmacopeia (USP) and the Chinese Pharmacopeia (ChP), were tested for their stabilizing properties towards a model mAb under three mechanical stress conditions: shaking, free-fall and pumping. UV spectroscopy, DLS, backgrounded membrane imaging (BMI) and flow imaging microscopy (FIM) were used for assessing the stability of the mAb under these conditions. Despite the higher purity of ChP PS80 (content of oleic acids >98%) compared to USP PS80 (content of

oleic acids 50-60%), no clear differences in terms of functionality were observed between the two grades. Taking into consideration the lower chemical stability of ChP PS80 compared to USP PS80[5], high purity grade polysorbate may not provide greater stability towards mAbs upon long-term storage.

The focus of the studies described in **chapters 6 and 7** was the analytical characterization of CBMPs. The research aimed to expand the currently limited analytical toolbox for the characterization of cell suspensions. In **chapter 6,** we developed a method based on FIM assisted with convolutional neural networks (FIM-CNN) for image analysis to detect and quantify particulate impurities in CBMPs. The focus was set on the identification of Dynabeads, antibody coated magnetic beads used for cell activation, in the presence of Jurkat cells at a concentration up to 500,000 cells per ml. The standard morphological parameters obtained from the instrument's software were not sufficient for discrimination between Dynabeads, cells, cellular debris and adducts (Dynabeads attached to cells). Thus, machine learning for image classification was implemented in this study. By using FIM-CNN, the error rate in classification of Dynabeads dropped by 50-fold compared to using the standard morphological parameter approach. Furthermore, a limit of quantification (LOQ) was determined at 50,000 beads/ml with a high recovery and low variability in concentration determination above the LOQ. The work performed in chapter 6 paved the way to study the stability of Jurkat cell suspensions submitted to forced degradation conditions. **Chapter 7** described the characterization of cell suspensions submitted to different stress conditions: thawing at various temperatures, freeze-thawing and shaking. Analysis of cells was performed by using the newly developed FIM-CNN alongside more established fluorescence-based cell characterization techniques. FIM-CNN was applied to determine the concentration of cells (viable and necrotic) and debris particles. The viability results obtained from FIM-CNN compared well to the read-outs of calcein-AM and propidium iodide assays. Thawing of frozen cell aliquots at low temperature (5 $^{\circ}$C) showed to be detrimental to cell viability and count, compared to thawing at 20 and 37 $^{\circ}$C. Furthermore, cells were formulated with different DMSO concentrations (0 - 10% [v/v]) and submitted to one freeze-thaw cycle (-20 $^{\circ}$C – 37 $^{\circ}$C). The lowest DMSO concentration tested (1% [v/v]) showed no protective effects upon freeze-

thawing, whereas the best cell-stabilizing properties of DMSO were achieved at 5% (v/v). Horizontal shaking of cell suspensions did not affect the cell viability at the tested conditions, but rather led to a substantial decrease in total cell counts. The drop in cell concentration after shaking stress was mitigated by addition of FBS (10% [v/v]) to the cell suspension. Our findings show the usefulness of the three types of forced degradation studies for CBMP formulation studies, as well as the importance of including orthogonal analytical techniques for cell characterization.

Perspectives

Characterization of particles within the nano- and micro-meter size range is an important aspect in the development of novel biopharmaceutical drug products. The work in this thesis aimed to strengthen the knowledge on current analytical techniques and methods used for the assessment of particle populations in protein- and cell-based formulations. New approaches utilizing artificial intelligence were introduced, which in future studies should be further developed in order to maximize the information obtained from data produced by particle characterization methods. Other objectives of upcoming research should attempt to further increase the fundamental understanding of the quality of current and prospective excipients in relation to their functionality in drug products.

Particulates in drug products

One of the main concerns with respect to the quality and stability of biopharmaceuticals is the presence of particulate impurities in drug products. The industry is currently showing great interest in the identification and characterization of impurities in raw materials in order to improve their quality through better manufacturing and purification processes. For example, Merck has recently released an improved multi-compendial grade of sucrose (Emprove Expert) that is low in nanoparticle content. The eliminated nanoparticulate impurities from sucrose have been shown to destabilize mAbs[1,2]. However, for excipients of a more complex chemical nature than sucrose, higher purity may not always translate into better performance and stability. Manufacturers of surfactants are keen to improve the quality of their products by producing polysorbate 20 (PS20) and polysorbate 80

(PS80) of higher purity grades. Unexpectedly, the increased content of lauric acid and oleic acid in PS20 and PS80, respectively, has shown to considerably exacerbate the risk of oxidative degradation[5]. The instability of polysorbates in protein formulations may result in the formation of insoluble fatty acid particles which pose a threat to protein stability[6]. Furthermore, as demonstrated in this thesis, the functionality of PS80 in mAbs formulations did not improve with increased content of oleic acid.

In recent years, a manifold of new structural formats of therapeutic antibodies, as well as other proteins, nucleic acids, viruses and cells have been designed to exhibit potential therapeutic effects[7-10]. In contrast, the list of excipients used to maintain the stability and efficacy of drug products remained relatively constant. Out of the vast number of chemical entities available, only 57 are used as excipients in marketed biopharmaceutical products[11]. With the support from academia, industry and regulatory authorities, further research should look for novel excipients that are able to better stabilize biopharmaceuticals and/or are more stable themselves. In any case, the quality and stability of excipients should be carefully evaluated in future work where new and/or commonly used stabilizing agents are incorporated into formulations.

Particles in drug products can also serve a positive role and act as the active pharmaceutical ingredient (API), a drug delivery vehicle or a (viral) vector for gene therapies. For example, the recently approved mRNA-based COVID-19 vaccines use lipid nanoparticles (LNPs) to deliver the nucleic acids into the cells where the expression of the encoded virus spike protein can take place[12]. The efficacy of mRNA-LNP vaccines is heavily dependent on the composition, size distribution and quantity of the nanoparticle population[13]. The same holds true for gene therapy products utilizing recombinant viral vectors for achieving the desired therapeutic effect. For instance, unwanted immunotoxicity and altered biodistribution resulting in inconsistent *in vivo* functionality can result from instability of virus particles and formation of aggregates[14]. Furthermore, the cells in CBMPs are micro-meter sized API particles. Demonstrating the integrity and concentration of these particles requires robust and accurate particle (cell) characterization techniques.

Particle characterization techniques

Characterization of particles in biopharmaceutical products has been an active field of research in the past decade[15-19]. Despite the significant advancements made in technologies used for the detection, sizing, counting and characterization of particles in the nano- and micro-meter size range, several challenges remain.

Techniques based on particle-light interactions play a major role in the detection and analysis of nanoparticles. Examples include dynamic and static light scattering (DLS and SLS, respectively), and nanoparticle tracking analysis (NTA). These techniques can be used for early detection of the onset of protein aggregation and particle formation[20-22]. NTA has additionally been validated by several research groups for the sizing of polydisperse nanoparticles, showing high accuracy and precision in the determination of the mean size for distinct particle populations[23-25]. However, not all samples may be suitable for these techniques; high background noise arising from formulation components can disturb the analysis and the presence of larger particles scattering more light will overshadow particles of smaller size. Alternative techniques have been developed to cover the "sub-micron gap" and overcome some of the challenges encountered with light scattering-based techniques. Examples include resonant mass measurement (RMM) and resistive pulse sensing (RPS), both of which provide some advantages with respect to sizing resolution and elimination of artefacts arising from light scattering events. Nonetheless, the microfluidic systems employed within these techniques require laborious cleaning procedures or can result in blockages, which compromises sample throughput. Furthermore, the precision with respect to quantification of nanoparticles remains low, especially for inter-laboratory experiments (Benkstein et al., in preparation). The reason for the imprecise quantification is related to the minuscule volume analyzed per measurement. For example, a single measurement performed by NTA processes ca. 0.08 nl of sample, and RMM or RPS can process up to several hundred nanolitres. Given the absolute concentration is provided in particles per millilitre, the extremely high extrapolation factors lead to high deviations in cases where small differences in particle counts are measured. Technical improvements in design to increase the volume of analyte

measured would increase the reliability and robustness of nanoparticle characterization techniques.

Several orthogonal techniques for characterization of micro-sized particles were developed within the past few years and include holographic video microscopy (HVM)[26], backgrounded membrane imaging (BMI)[27] and imaging flow cytometry (IFC)[28] . One advantage of HVM and BMI, compared to light-based techniques, is that results are unaffected by the differences in refractive indices between measured particles and formulation buffer. Both techniques can therefore be considered for measurements of formulations with high protein or sugar concentrations. In addition, BMI results should not be affected by air bubbles or silicone oil droplets, because these will pass through the porous membrane. BMI and IFC techniques include fluorescence detection systems offering chemical identification of particles based on the selectivity of fluorescent probes used for staining particles of interest. The currently established light obscuration and flow imaging microscopy (FIM) techniques have been compared and critically evaluated with respect to size and concentration determination by several research groups[29-36]. More recently, advanced computational methods, such as machine learning (ML), have been utilized in processing images derived from FIM[19,37-39]. In this way, the limitations of standard particle classification approaches, which are based on morphological particle parameters derived from the instrument´s software, were overcome[40,41]. The intrinsic morphological features extracted from bright-field images by using machine learning allowed for recognition of minute differences in particle morphologies. Thereby, discrimination of particles highly similar in appearance, but of different origins, was possible to achieve. Integration of machine learning for image segmentation in a newly developed FIM instrument was also suggested by Krause et al.[42]. An oil-immersed objective embodied into the FIM device allows for detection of particles in the sub-micron and low micron range (0.3 – 10 µm). The current limitations of this method include low image contrast of particles and light-scattering, both of which can be potentially resolved by application of more sophisticated thresholding algorithms. Advancements in computer vision and image processing algorithms should be applied in future work on characterization of particles in the nano- and micro-meter size range in order to derive

more information from captured images as well as from other parameters (e.g., fluorescence data).

Development of cell-based medicinal products (CBMPs)

The current preliminary stage of cell therapy approaches as well as the limited number of analytical techniques applied for the characterization of CBMPs makes this field highly attractive for future research. Application of new analytical techniques, such as FIM, for the characterization of cells and particulate impurities in cell suspensions is necessary to help ensuring the quality of CBMPs[43]. Some of the analytical methods being examined for cell characterization have been originally developed for small molecules or protein-based therapeutics. Therefore, applying them to cells may not be straightforward and multi-analytical based approaches may be required for accurate product characterization[19,44-46]. In contrast to mAbs and other therapeutic proteins, therapeutic cells exhibit high levels of heterogeneity originating from patient/donor, harvesting and processing methods and storage/transportation conditions[47-49]. Therefore, repeatable and robust analytical methods are essential for defining quality attributes and decision making at all stages of a CBMP´s life cycle. On the one hand, especially for autologous products, for which the amount of material usually is very limited and the time available for testing is short, it is crucial to develop analytical methods that are fast and require very low sample volumes. On the other hand, comprehensive analysis of CBMPs requires the assessment of numerous attributes such as sterility, cellular or process impurities, cell viability, cell concentration, potency, and functionality. For this reason, the applicability of statistical methods should be explored in experiment design and data interpretation, where the impact of multiple parameters can be individually assessed and correlated with the product's CQAs[50].

Present formulations of CBMPs are at an early stage of development and are usually limited to several isotonic multi-electrolyte solutions with few types of cryoprotectant agents (CPAs)[51]. Currently the most widely used CPA with best cell stabilizing properties upon freezing is dimethyl sulfoxide (DMSO). However, alternative plausible CPAs are needed, as DMSO at the used concentrations is toxic to cells in a non-frozen state and has

the potential to cause adverse effects in patients[52]. Thus, further research is required in this arena in order to understand cell-excipient interactions, demonstrate cell-stabilizing properties of novel (preferably not of human or animal origin) excipients and recognize degradation pathways occurring at different stress conditions. An important consideration is that the active ingredients in CBMPs are living cells that secrete various cytokines, metabolites or growth factors into the media, adding an additional layer of complexity. Selection of primary packaging materials is another consideration for CBMPs due to the potential interactions of cells with the primary packing material[53]. Some CBMPs are submitted to extreme environmental conditions (i.e., freezing at ultra-low temperatures) during product processing, transportation and storage. Such conditions not only may affect the cells but also can alter the properties of primary packaging materials, such as vials, stoppers and (cryo)bags, consequently compromising container closure integrity[54]. Taking advantage of the lessons learned and experiences gained during development of protein-based products, further research should focus on establishing comprehensive analytical techniques and formulation strategies for CBMPs.

References:

1. Weinbuch D, Cheung JK, Ketelaars J, et al. Nanoparticulate Impurities in Pharmaceutical-Grade Sugars and their Interference with Light Scattering-Based Analysis of Protein Formulations. Pharm Res. 2015;32(7):2419-2427. doi:10.1007/s11095-015-1634-1.

2. Weinbuch D, Ruigrok M, Jiskoot W, Hawe A. Nanoparticulate Impurities Isolated from Pharmaceutical-Grade Sucrose Are a Potential Threat to Protein Stability. Pharm Res. 2017;34(12):2910-2921. doi:10.1007/s11095-017-2274-4.

3. Randolph TW, Schiltz E, Sederstrom D, et al. Do not drop: mechanical shock in vials causes cavitation, protein aggregation, and particle formation. J Pharm Sci. 2015;104(2):602-611. doi:10.1002/jps.24259.

4. Li J, Krause ME, Chen X, et al. Interfacial Stress in the Development of Biologics: Fundamental Understanding, Current Practice, and Future Perspective. The AAPS journal. 2019;21(3):44. doi:10.1208/s12248-019-0312-3.

5. Kranz W, Wuchner K, Corradini E, Berger M, Hawe A. Factors Influencing Polysorbate's Sensitivity Against Enzymatic Hydrolysis and Oxidative Degradation. J Pharm Sci. 2019;108(6):2022-2032. doi:10.1016/j.xphs.2019.01.006.

6. Kishore RSK, Kiese S, Fischer S, Pappenberger A, Grauschopf U, Mahler H-C. The degradation of polysorbates 20 and 80 and its potential impact on the stability of biotherapeutics. Pharm Res. 2011;28(5):1194-1210. doi:10.1007/s11095-011-0385-x.

7. Wang D, Tai PWL, Gao G. Adeno-associated virus vector as a platform for gene therapy delivery. Nat Rev Drug Discov. 2019;18(5):358-378. doi:10.1038/s41573-019-0012-9.

8. Sahin U, Karikó K, Türeci Ö. mRNA-based therapeutics--developing a new class of drugs. Nat Rev Drug Discov. 2014;13(10):759-780. doi:10.1038/nrd4278.

9. Lu R-M, Hwang Y-C, Liu I-J, et al. Development of therapeutic antibodies for the treatment of diseases. J Biomed Sci. 2020;27(1):1. doi:10.1186/s12929-019-0592-z.

10. Holzinger A, Abken H. Advances and Challenges of CAR T Cells in Clinical Trials. In: Theobald M, ed. Current Immunotherapeutic Strategies in Cancer. Cham: Springer International Publishing; 2020:93-128.

11. Tosstorff A, Menzen T, Winter G. Exploring Chemical Space for New Substances to Stabilize a Therapeutic Monoclonal Antibody. J Pharm Sci. 2020;109(1):301-307. doi:10.1016/j.xphs.2019.10.057.

12. Chung YH, Beiss V, Fiering SN, Steinmetz NF. COVID-19 Vaccine Frontrunners and Their Nanotechnology Design. ACS Nano. 2020;14(10):12522-12537. doi:10.1021/acsnano.0c07197.

13. Tyagi P, Subramony JA. Nanotherapeutics in oral and parenteral drug delivery: Key learnings and future outlooks as we think small. J. Control. Release. 2018;272:159-168. doi:10.1016/j.jconrel.2018.01.009.

14. Rodrigues GA, Shalaev E, Karami TK, Cunningham J, Slater NKH, Rivers HM. Pharmaceutical Development of AAV-Based Gene Therapy Products for the Eye. Pharm Res. 2018;36(2):29. doi:10.1007/s11095-018-2554-7.

15. Gross-Rother J, Blech M, Preis E, Bakowsky U, Garidel P. Particle Detection and Characterization for Biopharmaceutical Applications: Current Principles of Established and Alternative Techniques. Pharmaceutics. 2020;12(11). doi:10.3390/pharmaceutics12111112.

16. Carpenter JF, Randolph TW, Jiskoot W, et al. Overlooking subvisible particles in therapeutic protein products: gaps that may compromise product quality. J Pharm Sci. 2009;98(4):1201-1205. doi:10.1002/jps.21530.

17. Zölls S, Tantipolphan R, Wiggenhorn M, et al. Particles in therapeutic protein formulations, Part 1: overview of analytical methods. J Pharm Sci. 2012;101(3):914-935. doi:10.1002/jps.23001.

18. Das TK. Protein particulate detection issues in biotherapeutics development--current status. AAPS PharmSciTech. 2012;13(2):732-746. doi:10.1208/s12249-012-9793-4.

19. Calderon CP, Daniels AL, Randolph TW. Deep Convolutional Neural Network Analysis of Flow Imaging Microscopy Data to Classify Subvisible Particles in Protein Formulations. J Pharm Sci. 2018;107(4):999-1008. doi:10.1016/j.xphs.2017.12.008.

20. Tian X, Nejadnik MR, Baunsgaard D, Henriksen A, Rischel C, Jiskoot W. A Comprehensive Evaluation of Nanoparticle Tracking Analysis (NanoSight) for Characterization of Proteinaceous Submicron Particles. J Pharm Sci. 2016;105(11):3366-3375. doi:10.1016/j.xphs.2016.08.009.

21. Jarand CW, Reed WF. On the Reproducibility of Early-Stage Thermally Induced and Contact-Stir-Induced Protein Aggregation. J Phys Chem B. 2018;122(40):9361-9372. doi:10.1021/acs.jpcb.8b07820.

22. Amin S, Barnett GV, Pathak JA, Roberts CJ, Sarangapani PS. Protein aggregation, particle formation, characterization & rheology. Curr. Opin. Colloid Interface Sci2014;19(5):438-449. doi:10.1016/j.cocis.2014.10.002.

23. Sauvain J-J, Suarez G, Edmé J-L, et al. Method validation of nanoparticle tracking analysis to measure pulmonary nanoparticle content: the size distribution in exhaled breath condensate depends on occupational exposure. J Breath Res. 2017;11(1):16010. doi:10.1088/1752-7163/aa56dd.

24. Kim A, Ng WB, Bernt W, Cho N-J. Validation of Size Estimation of Nanoparticle Tracking Analysis on Polydisperse Macromolecule Assembly. Sci Rep. 2019;9(1):2639. doi:10.1038/s41598-019-38915-x.

25. Kestens V, Bozatzidis V, Temmerman P-J de, Ramaye Y, Roebben G. Validation of a particle tracking analysis method for the size determination of nano- and microparticles. J Nanopart Res. 2017;19(8):271. doi:10.1007/s11051-017-3966-8.

26. Winters A, Cheong FC, Odete MA, et al. Quantitative Differentiation of Protein Aggregates From Other Subvisible Particles in Viscous Mixtures Through Holographic Characterization. J Pharm Sci.2020;109(8):2405-2412. doi:10.1016/j.xphs.2020.05.002.

27. Helbig C, Ammann G, Menzen T, Friess W, Wuchner K, Hawe A. Backgrounded Membrane Imaging (BMI) for High-Throughput Characterization of Subvisible Particles During Biopharmaceutical Drug Product Development. J Pharm Sci. 2020;109(1):264-276. doi:10.1016/j.xphs.2019.03.024.

28. Probst C, Zayats A, Venkatachalam V, Davidson B. Advanced Characterization of Silicone Oil Droplets in Protein Therapeutics Using Artificial Intelligence Analysis of Imaging Flow Cytometry Data. J Pharm Sci. 2020;109(10):2996-3005. doi:10.1016/j.xphs.2020.07.008.

29. Kiyoshi M, Shibata H, Harazono A, et al. Collaborative Study for Analysis of Subvisible Particles Using Flow Imaging and Light Obscuration: Experiences in Japanese Biopharmaceutical Consortium J Pharm Sci. 2019;108(2):832-841. doi:10.1016/j.xphs.2018.08.006.

30. Zölls S, Weinbuch D, Wiggenhorn M, et al. Flow imaging microscopy for protein particle analysis--a comparative evaluation of four different analytical instruments. The AAPS journal. 2013;15(4):1200-1211. doi:10.1208/s12248-013-9522-2.

31. Sharma DK, King D, Oma P, Merchant C. Micro-flow imaging: flow microscopy applied to subvisible particulate analysis in protein formulations. The AAPS journal. 2010;12(3):455-464. doi:10.1208/s12248-010-9205-1.

32. Matter A, Koulov A, Singh S, et al. Variance Between Different Light Obscuration and Flow Imaging Microscopy Instruments and the Impact of Instrument Calibration. J Pharm Sci. 2019;108(7):2397-2405. doi:10.1016/j.xphs.2019.02.019.

33. Werk T, Volkin DB, Mahler H-C. Effect of solution properties on the counting and sizing of subvisible particle standards as measured by light obscuration and digital imaging methods. Eur J Pharm Sci. 2014;53:95-108. doi:10.1016/j.ejps.2013.12.014.

34. Ripple DC, Hu Z. Correcting the Relative Bias of Light Obscuration and Flow Imaging Particle Counters. Pharm Res. 2016;33(3):653-672. doi:10.1007/s11095-015-1817-9.

35. Zölls S, Weinbuch D, Wiggenhorn M, et al. Flow imaging microscopy for protein particle analysis--a comparative evaluation of four different analytical instruments. The AAPS journal. 2013;15(4):1200-1211. doi:10.1208/s12248-013-9522-2.

36. Ripple DC, Montgomery CB, Hu Z. An interlaboratory comparison of sizing and counting of subvisible particles mimicking protein aggregates J Pharm Sci. 2015;104(2):666-677. doi:10.1002/jps.24287.

37. Farrell CJ, Cicalese SM, Davis HB, et al. Cell confluency analysis on microcarriers by micro-flow imaging. Cytotechnology. 2016;68(6):2469-2478. doi:10.1007/s10616-016-9967-0.

38. Daniels AL, Calderon CP, Randolph TW. Machine learning and statistical analyses for extracting and characterizing "fingerprints" of antibody aggregation at container interfaces from flow microscopy images. Biotechnol Bioeng. 2020;117(11):3322-3335. doi:10.1002/bit.27501.

39. Schuster J, Koulov A, Mahler H-C, et al. Particle Analysis of Biotherapeutics in Human Serum Using Machine Learning. J Pharm Sci. 2020;109(5):1827-1832. doi:10.1016/j.xphs.2020.02.015.

40. Weinbuch D, Zölls S, Wiggenhorn M, et al. Micro-flow imaging and resonant mass measurement (Archimedes)--complementary methods to quantitatively differentiate protein particles and silicone oil droplets. J Pharm Sci. 2013;102(7):2152-2165. doi:10.1002/jps.23552.

41. Strehl R, Rombach-Riegraf V, Diez M, et al. Discrimination between silicone oil droplets and protein aggregates in biopharmaceuticals: a novel multiparametric image filter for sub-visible particles in microflow imaging analysis. Pharm Res. 2012;29(2):594-602. doi:10.1007/s11095-011-0590-7.

42. Krause N, Kuhn S, Frotscher E, et al. Oil-Immersion Flow Imaging Microscopy for Quantification and Morphological Characterization of Submicron Particles in Biopharmaceuticals. The AAPS journal. 2021;23(1):13. doi:10.1208/s12248-020-00547-9.

43. Jere D, Sediq AS, Huwyler J, Vollrath I, Kardorff M, Mahler H-C. Challenges for Cell-Based Medicinal Products From a Pharmaceutical Product Perspective. J Pharm Sci. 2020. doi:10.1016/j.xphs.2020.11.040.

44. Rangan S, Schulze HG, Vardaki MZ, Blades MW, Piret JM, Turner RFB. Applications of Raman spectroscopy in the development of cell therapies: state of the art and future perspectives. Analyst. 2020;145(6):2070-2105. doi:10.1039/c9an01811e.

45. Giugliarelli A, Sassi P, Urbanelli L, et al. Cryopreservation of cells: FT-IR monitoring of lipid membrane at freeze-thaw cycles. Biophys Chem. 2016;208:34-39. doi:10.1016/j.bpc.2015.08.001.

46. Goldrick S, Umprecht A, Tang A, et al. High-Throughput Raman Spectroscopy Combined with Innovate Data Analysis Workflow to Enhance Biopharmaceutical Process Development. Processes. 2020;8(9):1179. doi:10.3390/pr8091179.

47. Moutsatsou P, Ochs J, Schmitt RH, Hewitt CJ, Hanga MP. Automation in cell and gene therapy manufacturing: from past to future. Biotechnol Lett. 2019;41(11):1245-1253. doi:10.1007/s10529-019-02732-z.

48. Kang I, Lee B-C, Choi SW, et al. Donor-dependent variation of human umbilical cord blood mesenchymal stem cells in response to hypoxic preconditioning and amelioration of limb ischemia. Exp Mol Med. 2018;50(4):1-15. doi:10.1038/s12276-017-0014-9.

49. Biendarra-Tiegs SM, Secreto FJ, Nelson TJ. Addressing Variability and Heterogeneity of Induced Pluripotent Stem Cell-Derived Cardiomyocytes. In: Turksen K, ed. Cell Biology and Translational Medicine, Volume 6: Stem Cells: Their Heterogeneity, Niche and Regenerative Potential. Cham: Springer International Publishing; 2020:1-29.

50. Lipsitz YY, Timmins NE, Zandstra PW. Quality cell therapy manufacturing by design. Nat Biotechnol. 2016;34(4):393-400. doi:10.1038/nbt.3525.

51. Hoogendoorn KH, Crommelin DJA, Jiskoot W. Formulation of Cell-Based Medicinal Products: A Question of Life or Death? J Pharm Sci. 2020. doi:10.1016/j.xphs.2020.07.002.

52. Awan M, Buriak I, Fleck R, et al. Dimethyl sulfoxide: a central player since the dawn of cryobiology, is efficacy balanced by toxicity? Regenerative Medicine. 2020;15(3):1463-1491. doi:10.2217/rme-2019-0145.

53. Wang M, Li Y, Srinivasan P, et al. Interactions Between Biological Products and Product Packaging and Potential Approaches to Overcome Them. AAPS PharmSciTech. 2018;19(8):3681-3686. doi:10.1208/s12249-018-1184-z.

54. Zuleger B, Werner U, Kort A, Glowienka R, Wehnes E, Duncan D. Container/Closure Integrity Testing and the Identification of a Suitable Vial/Stopper Combination for Low-Temperature Storage at −80 °C. PDA J Pharm Sci Technol. 2012;66(5):453. doi:10.5731/pdajpst.2012.00884.

Samenvatting en conclusies

Het ontwikkelen van analytische methoden voor de karakterisering van deeltjes is van groot belang tijdens de ontwikkeling van biofarmaca. Vroegtijdige bepaling van deeltjesonzuiverheden en degradatieprocessen in therapeutische eiwitformuleringen tijdens (versnelde) opslag en geforceerde degradatieomstandigheden kan de kans op klinische mislukkingen in latere ontwikkelingsstadia verkleinen en de stabiliteits- en kwaliteitsbeoordeling van deze geneesmiddelen ondersteunen. Daarnaast zijn op cellen gebaseerde geneesmiddelen (*cell-based medicinal products*; CBMPs) in opkomst, welke gebaseerd zijn op heterogene suspensies van verschillende deeltjes. Hiervoor zijn analytische methodes nodig in combinatie met geavanceerde dataverwerking om een uitgebreide productkarakterisering mogelijk te maken.

In **hoofdstuk 2** onderzochten we de voordelen en beperkingen van een recentelijk ontwikkelde techniek om nanodeeltjes te karakteriseren: *microfluidic resistive pulse sensing* (MRPS). Deze analysetechniek die in staat is individuele deeltjes in een oplossing te analyseren was vergeleken met bestaande deeltjesanalysetechnieken, waaronder *dynamic light scattering* (DLS), *nanoparticle tracking analysis* (NTA) en *resonant mass measurement* (RMM), met betrekking tot het bepalen van de deeltjesgrootte en het deeltjesaantal. Hiervoor werden monsters gemeten met polystyreennanodeeltjes, liposomen, bacteriën en eiwitaggregaten. MRPS bleek van alle geteste technieken het breedste meetbare concentratiebereik te hebben. Dit zou MRSP superieur maken voor het kwantificeren van medicamenten met hoge deeltjesaantallen, zoals formuleringen op basis van virussen en liposomen, aangezien er geen verdunning van het monster nodig is. MRPS, RMM en NTA zijn technieken voor het tellen van individuele deeltjes, waardoor de resolutie bij het bepalen van de deeltjesgrootte in monsters met heterogene deeltjespopulaties superieur is aan die van DLS. Uit verder onderzoek naar de resolutie voor de deeltjesgrootte bleek dat MRPS ietwat beter presteerde dan RMM, terwijl NTA het slechtst in staat was om onderscheid te maken tussen twee groepen deeltjes met elk een andere grootte. Het feit dat metingen via MRPS een relatief hoge elektrische geleiding

van monsters vereisen kan echter een beperkende factor zijn van deze techniek, zoals in het volgende hoofdstuk is beschreven.

Hoofdstuk 3 beschrijft een vervolgstudie over nanodeeltjesanalysetechnieken voor het analyseren van eiwitdeeltjes in een oplossing van een monoclonaal antilichaam (*monoclonal antibody*; mAb). In het bijzonder werd het effect van de toevoeging van elektrolyten op de stabiliteit van de mAb onderzocht. Metingen met *tunable resistive pulse sensing* (TRPS) en MRPS vereisen dat de monsters genoeg elektrische geleiding hebben. Voor algemeen gebruikte eiwitformuleringen met een lage geleiding moeten elektrolyten worden toegevoegd voordat een monster gemeten kan worden. Door gebruik te maken van RMM en NTA werd echter een substantiële verhoging van het aantal nanometerdeeltjes gevonden in aan hitte blootgestelde mAb-formuleringen waaraan natriumchloride of histidine was toegevoegd. Een dergelijke verandering werd niet vastgesteld in verhitte eiwitmonsters zonder zulke toevoegingen. Daarom dient voorafgaand aan metingen met *resistive pulse sensing* het effect van de toevoeging van elektrolyten aan eiwitformuleringen op de eiwitstabilititeit, met name aggregatie, vooraf bepaald te worden.

In **hoofdstuk 4** onderzochten wij de immunogeniciteit van eerder vastgestelde nanodeeltjesonzuiverheden (*nanoparticulate impurities*; NPIs) in suikers van farmaceutische kwaliteit. NPIs geïsoleerd uit sucrose van farmaceutische kwaliteit, een veelgebruikte hulpstof in eiwitformuleringen, bleken β-glucanen te bevatten die als adjuvantia kunnen fungeren in de aanwezigheid van immunogene stoffen (zoals eiwitaggregaten). In tegenstelling tot eerder onderzoek werd in trastuzumabformuleringen die gedurende enkele uren waren geïncubeerd met NPIs slechts een geringe toename in de concentratie van nanodeeltjes en geen substantiële toename in microdeeltjes vastgesteld. NPIs in een hoge concentratie (10^{10} p/ml), al dan niet in combinatie met 1 mg/ml trastuzumab, zorgde niet voor de activatie van *monocyte-derived dendritic cells*. Deze resultaten suggereren dat, in tegenstelling tot onze

verwachting, NPIs in zowel de aan- als afwezigheid van eiwitten niet immunogeen zijn in het gebruikte *in vitro* model.

Hoofdstuk 5 richtte zich op de rol van de zuiverheid van polysorbaat 80 (PS80), een ander belangrijke hulpstof, op het eiwit-stabiliserend effect tijdens blootstelling aan mechanische stress, waarvan bekend is dat dit kan leiden tot de vorming van eiwitaggregaten in de vorm van deeltjes. Twee soorten PS80, gespecificeerd door de *United States Pharmacopeia* (USP) en de Chinese Farmacopee (ChP), werden getest op hun stabiliserende werking op een model mAb onder drie mechanische-stressomstandigheden: schudden, vrije val en pompen. UV-spectroscopie, DLS, *backgrounded membrane imaging* (BMI) en *flow imaging microscopy* (FIM) werden gebruikt ter bepaling van de stabiliteit van de mAb onder deze omstandigheden. Ondanks de hogere zuiverheid van ChP PS80 (gehalte aan oliezuur >98%) in vergelijking met USP PS80 (gehalte aan oliezuur 50-60%), werden geen duidelijke verschillen in functionaliteit waargenomen. Rekening houdend met de lagere chemische stabiliteit van ChP PS80 in vergelijking met USP PS80, biedt ChP PS80 ondanks de hogere zuiverheid wellicht geen voordelen voor de stabilisatie van mAbs.

De nadruk van de in de **hoofdstukken 6 en 7** beschreven studies lag op de analytische karakterisering van een innovatieve, op cellen gebaseerde geneesmiddelencategorie, CBMPs. Het onderzoek was gericht op het uitbreiden van de momenteel beperkte analytische gereedschapskist voor de karakterisering van celsuspensies.

In **hoofdstuk 6** ontwikkelden we een op FIM gebaseerde methode, in combinatie met convolutionele neurale netwerken (FIM-CNN) voor beeldanalyse, voor het detecteren en kwantificeren van de deeltjesonzuiverheden in CBMPs. De focus werd gelegd op de identificatie van Dynabeads, met antilichamen gecoate magnetische microdeeltjes die worden gebruikt voor celactivering, in aanwezigheid van Jurkat-cellen in een concentratie tot 500,000 cellen per ml. De morfologische standaardparameters afkomstig van de software van het gebruikte instrument (FlowCam) waren onvoldoende om onderscheid te maken tussen Dynabeads, cellen, celresten en adducten (aan cellen gehechte Dynabeads). Daarom werd in deze studie gebruik gemaakt van *machine learning* voor beeldclassificatie.

Door gebruik te maken van FIM-CNN daalde het foutenpercentage bij de classificatie van Dynabeads met het 50-voudige in vergelijking met de standaard morfologische parameterbenadering. Bovendien werd een *limit of quantification* (LOQ) vastgesteld bij 50,000 Dynabeads/ml met een hoge nauwkeurigheid en een lage variabiliteit in de concentratiebepaling boven de LOQ.

Het in **hoofdstuk 6** verrichte werk legde de basis voor het bestuderen van de stabiliteit van Jurkat-celsuspensies die worden onderworpen aan geforceerde degradatieomstandigheden in **hoofdstuk 7**: ontdooien bij verschillende temperaturen, vriezen-dooien en schudden. De analyse van cellen werd uitgevoerd door gebruik te maken van de nieuw ontwikkelde FIM-CNN, naast meer conventionele op fluorescentie gebaseerde celkarakteriseringstechnieken. FIM-CNN werd toegepast om de concentratie van cellen (levensvatbare en necrotische) en overige deeltjes (waaronder celdebris) te bepalen. De met FIM-CNN verkregen resultaten inzake levensvatbaarheid waren goed te vergelijken met die van calceine-AM- en propidiumjodide-assays. Het ontdooien bij lage temperatuur (5 $^{\circ}$C) van bevroren cellen bleek nadelig te zijn voor de levensvatbaarheid en het aantal cellen, vergeleken met ontdooien bij 20 en 37 $^{\circ}$C. Bovendien werden cellen geformuleerd met verschillende dimethylsulfoxide (DMSO)-concentraties (0 - 10% [v/v]) en onderworpen aan één vries-dooicyclus (van -20 $^{\circ}$C naar 37 $^{\circ}$C). De laagste geteste DMSO-concentratie (1% [v/v]) vertoonde geen beschermende effecten, terwijl de beste celstabiliserende eigenschappen van DMSO werden bereikt bij 5% (v/v). Horizontaal schudden van celsuspensies had geen invloed op de levensvatbaarheid van de cellen onder de onderzochte omstandigheden, maar leidde wel tot een aanzienlijke daling van het totale aantal cellen. De daling van de celconcentratie na schudden werd verminderd door toevoeging van foetaal kalfsserum (10%[v/v]) aan de celsuspensie. Onze bevindingen tonen het nut aan van de drie types van geforceerde-degradatiestudies voor CBMP-formuleringsontwikkeling, alsook het belang van orthogonale analysetechnieken voor celkarakteriserin

Abbreviations

%	Percent
°C	Degree Celsius
µg	Microgram
µl	Microliter
µm	Micrometer
ABD	Area based diameter
AM	Acetoxymethyl
ANN	Artificial neuronal networks
APC	Antigen-presenting cell
API	Active pharmaceutical ingredient
ATR	Attenuated total reflection
AU	Absorbance unit
AUC	Area under the curve
BMI	Backgrounded membrane imaging
BSA	Bovine serum albumin
CAR-T	Chimeric antigen receptor T cells
CBMP	Cell-based medicinal product
CD3	Cluster of differentiation 3
CD4	Cluster of differentiation
ChP	Chinese Pharmacopeia
cMFI	Corrected mean fluorescence intensity
CNN	Convolutional neural network
CPA	Cryoprotectant agent
CQA	Critical quality attribute
DLS	Dynamic light scattering
DNA	Deoxyribonucleic acid
DMSO	Dimethylsulfoxide
DP	Drug product
DS	Drug substance
ECD	Equivalent circular diameter
ESD	Equivalent spherical diameter
ESZ	Electric sensing zone
Exp.	Expiration date
FBS	Fetal bovine serum
FDA	Food and Drug Administration
FFA	Free fatty acid

FIM	Flow imaging microscopy
FITC	Fluorescein isothiocyanate
FSC	Forward scatter
FTIR	Fourier transform infrared spectroscopy
g	Gram
h	Hour
HCl	Hydrogen chloride
His	Histidine
HVM	Holographic video microscopy
HSA	Human serum albumin
HMW	High molecular weight
HPLC	High performance liquid chromatography
ICH	International Council for Harmonisation
IEP	Isoelectric point
IgG	Immunoglobulin G
IgG1	Immunoglobulin G1
IgM	Immunoglobulin M
IL	Interleukin
INF	Interferon
kDa	Kilodalton
LNP	Lipid nanoparticle
LO	Light obscuration
LOD	Limit of detection
LOQ	Limit of quantification
LPS	Lipopolysaccharide
mAb	Monoclonal antibody
MC	Multicompendial
MFI	Micro-Flow Imaging
mg	Milligram
MHC	Major histocompatibility complex
min	Minute
ml	Milliliter
ML	Machine learning
mM	Millimolar
mm	Millimeter
moDC	Monocyte-derived dendritic cell
MRPS	Microfluid resistive pulse sensing

NaCl	Sodium chloride
ng	Nanogram
nl	Nanoliter
NIST	National Institute of Standards and Technology
NK	Natural killer
nm	Nanometer
NPI	Nanoparticulate impurity
NTA	Nanoparticle tracking analysis
p/ml	Particles per milliliter
PBMC	Peripheral blood mononuclear cell
PBS	Phosphate buffered saline
PDI	Polydispersity index
PDMS	Polydimethylsulfoxane
Ph.Eur.	European Pharmacopeia
PI	Propidium iodide
POE	Polyoxyethylene
PS	Polystyrene
PS20	Polysorbate 20
PS80	Polysorbate 80
PTFE	Polytetrafluoroethylene
PVDF	Polyvinylidene fluoride
QC	Quality control
R	Resistance
R^2	Coefficient of determination
RFI	Relative fluorescence intensity
RI	Refractive index
RMM	Resonant mass measurement
RNA	Ribonucleic acid
RPS	Resistive pulse sensing
rpm	Rounds per minute
RPMI	Roswell Park Memorial Institute
RT	Room temperature
s	Second
SEC	Size-exclusion chromatography
SEM	Scanning electron microscopy
SLS	Static light scattering
SMR	Suspended microchannel resonator

SSC	Side scatter
SVP	Subvisible (micro-meter sized) particle
T_{agg}	Aggregation temperature
TCR	T cell receptor
TFF	Tangential flow filtration
Tg	Glass transition temperature of the frozen state
TNF	Tumor necrosis factor
TRPS	Tunable resistive pulse sensing
UPLC	Ultra performance liquid chromatography
USP	United States Pharmacopeia
UV	Ultraviolet
V	Voltage
v/v	Volume per volume
w/v	Weight per volume
w/w	Weight per weight
λ	Wavelength

List of publications

1. **Grabarek AD**, Jiskoot W, Hawe A, et al. Forced degradation of cell-based medicinal products guided by flow imaging microscopy: explorative studies with Jurkat cells: Eur J Pharm Biopharm 2021; 167: 38-47. doi: 10.1016/j.ejpb.2021.07.004

2. **Grabarek AD**, Nabhan M, Turbica I, et al. Immunological Evaluation In Vitro of Nanoparticulate Impurities Isolated From Pharmaceutical-Grade Sucrose. J Pharm Sci. 2021;110(2):952-958. doi: 10.1016/j.xphs.2020.11.011

3. Sekulovic A, Verrijk R, Rades T, **Grabarek AD**, et al. Simultaneous automated image analysis and Raman spectroscopy of powders at an individual particle level. J Pharm Biomed Anal. 2021;193:113744. doi: 10.1016/j.jpba.2020.113744

4. **Grabarek AD**, Senel E, Menzen T, et al. Particulate impurities in cell-based medicinal products traced by flow imaging microscopy combined with deep learning for image analysis. Cytotherapy 2021; 23: 339-347. doi:10.1016/j.jcyt.2020.04.093

5. **Grabarek AD**, Bozic U, Rousel J, et al. What Makes Polysorbate Functional? Impact of Polysorbate 80 Grade and Quality on IgG Stability During Mechanical Stress. J Pharm Sci. 2020; 109(1):871-880. doi: 10.1016/j.xphs.2019.10.015

6. **Grabarek AD**, Weinbuch D, Jiskoot W, Hawe A. Critical Evaluation of Microfluidic Resistive Pulse Sensing for Quantification and Sizing of Nanometer- and Micrometer-Sized Particles in Biopharmaceutical Products. J Pharm Sci. 2019;108(1):563-573. doi: 10.1016/j.xphs.2018.08.020

7. Kwok PC, **Grabarek AD**, Chow MY, et al.(2015) Inhalable spray-dried formulation of D-LAK antimicrobial peptides targeting tuberculosis. Int. J. Pharm.; 491(1-2):367-74. doi: 10.1016/j.ijpharm.2015.07.001

Curriculum Vitae

Adam Grabarek was born on the 9th of December 1990 in Warsaw, Poland. After graduating from XXI Liceum Ogólnokształcące im. Hugonna Kołłątaja in Warsaw, he started his studies in Pharmacy at University College London. In 2013, Adam completed a research placement for his master research project at Hong Kong University where he obtained an academic mention with his thesis in peptide formulation entitled "Inhalable spray-dried formulation of D-LAK antimicrobial peptides targeting tuberculosis". He obtained his Pharmacy degree (Second Class Honours, Upper Division) in 2015. In the subsequent year, after completing a pre-registration placement at Boots UK, Adam registered as a qualified pharmacist in the UK.

In September 2016, he started his PhD research at Leiden University under the supervision of Prof. Dr. Wim Jiskoot (LACDR, Leiden University) and Dr. Andrea Hawe at Coriolis Pharma in Munich, Germany, which resulted in this thesis. During his PhD he worked part time as a formulation scientist and represented Coriolis Pharma at international conferences on several occasions. He is currently working as a Scientist at Coriolis Pharma.